

UNCLASSIFIED



AD NUMBER

**AD-617 182**

CLASSIFICATION CHANGES

TO **UNCLASSIFIED**

FROM **CONFIDENTIAL**

AUTHORITY

TID-1263; DEC 12, 1961

THIS PAGE IS UNCLASSIFIED

UNCLASSIFIED



AD NUMBER

**AD-617 182**

NEW LIMITATION CHANGE

TO

**DISTRIBUTION STATEMENT - A**

Approved for public release;  
distribution is unlimited

**LIMITATION CODE: 1**

FROM

**NO PRIOR DISTR ST'MT ASSIGNED**

AUTHORITY

HQ FLD CMD, AFSWP; JUN 26, 1963

THIS PAGE IS UNCLASSIFIED

~~CONFIDENTIAL~~  
**UNCLASSIFIED**

THIS REPORT HAS BEEN APPROVED FOR OPEN PUBLICATION.

WT-1109

OPERATION TEAPOT—PROJECT 1.10

Report to the Test Director

**AIRBLAST OVERPRESSURE AND DYNAMIC  
PRESSURE OVER VARIOUS SURFACES**

**UNCLASSIFIED**

D.C. Sachs  
L.M. Swift  
F.M. Sauer

Stanford Research Institute  
Menlo Park, California

CLASSIFICATION CANCELLED  
OR CHANGED TO **UNCLASSIFIED**  
BY AUTHORITY OF 7.10.12.63  
BY J2C DATE 12/19/63

Issuance Date: September 9, 1957

CONFIDENTIAL

**CONFIDENTIAL**  
Handwritten notes and stamps, including "CONFIDENTIAL" and "UNCLASSIFIED".

THIS REPORT HAS BEEN APPROVED FOR OPEN PUBLICATION.

**UNCLASSIFIED**

AD 617122

WT-1109

This document consists of 194 pages

No. 197 of 250 copies, Series A

UNCLASSIFIED

# Operation TEAPOT

NEVADA TEST SITE

9/18/65

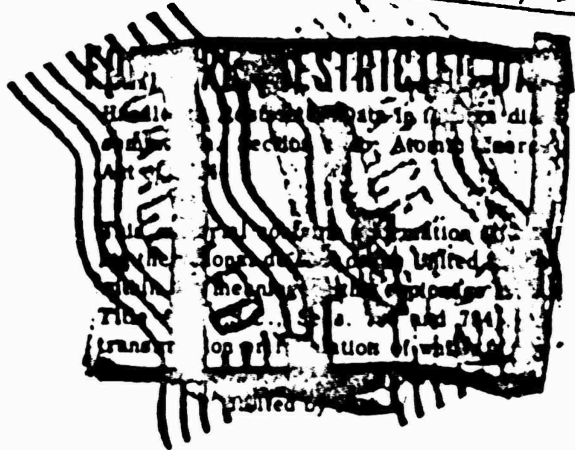
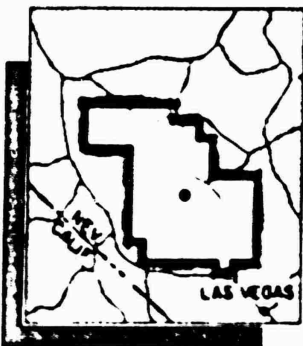
February - May 1955

UNCLASSIFIED

Project 1.10

AIRBLAST OVERPRESSURE AND DYNAMIC  
PRESSURE OVER VARIOUS SURFACES

COPY	1	OF	1
MICROFORM			



HEADQUARTERS FIELD COMMAND, ARMED FORCES SPECIAL WEAPONS PROJECT  
SANDIA BASE, ALBUQUERQUE, NEW MEXICO

43898

UNCLASSIFIED

RECEIVED

EVALUATION COPY

OCT 10 1957

PROCESSING COPY

USAEC HEADQUARTERS  
TECHNICAL REPORTS

ARCHIVE COPY



## **REPRODUCTION QUALITY NOTICE**

**This document is the best quality available. The copy furnished to DTIC contained pages that may have the following quality problems:**

- **Pages smaller or larger than normal.**
- **Pages with background color or light colored printing.**
- **Pages with small type or poor printing; and or**
- **Pages with continuous tone material or color photographs.**

**Due to various output media available these conditions may or may not cause poor legibility in the microfiche or hardcopy output you receive.**

☐

**If this block is checked, the copy furnished to DTIC contained pages with color printing, that when reproduced in Black and White, may change detail of the original copy.**

# SUMMARY OF SHOT DATA, OPERATION TEAPOT

Shot	Code Name	Date	Time*	Area	Type	Latitude and Longitude of Zero Point
1	Wasp	18 February	1200	T-7-4†	762-ft Air	37° 05' 11.0" N 118° 01' 10.1200" W
2	Moth	22 February	0545	T-3	300-ft Tower	37° 03' 52.254" N 118° 01' 19.2907" W
3	Teala	1 March	0530	T-3b	300-ft Tower	37° 01' 51.077" N 118° 03' 51.0077" W
4	Turk	7 March	0520	T-3	500-ft Tower	37° 02' 18.044" N 118° 07' 00.0079" W
5	Hornet	12 March	0520	T-3a	300-ft Tower	37° 03' 25.042" N 118° 01' 51.2074" W
6	Bee	22 March	0505	T-7-1a	500-ft Tower	37° 06' 41.2000" N 118° 01' 25.2474" W
7	ESS	23 March	1230	T-10a	67-ft Underground	37° 10' 00.1253" N 118° 03' 27.7010" W
8	Apple	29 March	0455	T-4	500-ft Tower	37° 06' 05.0300" N 118° 00' 00.0000" W
9	Wasp	29 March	1000	T-7-4‡	740-ft Air	37° 06' 11.2000" N 118° 01' 15.7200" W
10	HA	1 April	1000	T-5§	36,820-ft MSL Air	37° 01' 43.2542" N 118° 03' 20.2534" W
11	Post	9 April	0430	T-3c	300-ft Tower	37° 01' 19.0000" N 118° 02' 00.2000" W
12	MET	15 April	1115	FF	400-ft Tower	36° 07' 52.0007" N 113° 05' 04.0000" W
13	Apple 2	5 May	0510	T-1	500-ft Tower	36° 03' 11.0000" N 118° 00' 00.0000" W
14	Zucchini	15 May	0500	T-7-1a	500-ft Tower	37° 06' 41.2000" N 118° 01' 25.2474" W

\* Approximate local time, PST prior to 24 April, PDT after 24 April.

† Actual zero point 36 feet north, 436 feet west of T-7-4.

‡ Actual zero point 94 feet north, 62 feet west of T-7-4.

§ Actual zero point 36 feet south, 397 feet west of T-5.

## ABSTRACT

Project 1.10 measured static overpressure and dynamic pressure versus time over surfaces possessing different physical properties on two tower shots, 6 and 12. On Shot 12, three surfaces were provided: the natural desert, a water surface consisting of a flooded area, and an asphalt surface. On Shot 6, desert and asphalt areas only were available. There were 123 channels of instrumentation installed for Shot 12, and 24 for Shot 6.

Although some instrumental difficulties were encountered, usable records were obtained on 141 of the 147 total gage channels. In contrast with previous tests, no gage tower or mount failures were experienced.

From the data, a system of wave-form classification was devised for overpressure and dynamic-pressure-versus-time measurements. Incorporation of this system into data analysis indicates that it is possible for an ideal peak pressure to be identified with a nonideal wave form. Introducing both variables, wave form and peak pressure, into analyses reduces ambiguities associated with comparing results of different nuclear tests.

The data show the effect of the nature of the surface upon airblast phenomena from a nuclear explosion. Although the indication is that the Shot 12 water line did not provide entirely ideal conditions over its whole length, the measured disturbances were markedly less than those observed on the desert line. The results from the asphalt line show most severe deviation from classical behavior.

The effects of surface conditions upon shock phenomena are made more understandable by a review of temperature computations, using shock wave parameters in addition to an analysis based upon the arrival time of the thermal pulse. A phenomenological discussion of precursor formation is presented, and comparisons are made using data from all known precursor-forming nuclear shots.

Two Shot 12 drag-force measurements on the H Beams are presented and discussed.

## FOREWORD

This report presents the final results of one of the 56 projects comprising the Military Effects Program of Operation Teapot, which included 14 test detonations at the Nevada Test Site in 1955.

For overall Teapot military-effects information, the reader is referred to the "Summary Report of the Technical Director, Military Effects Program," WT-1153, which includes the following: (1) a description of each detonation including yield, zero-point location and environment, type of device, ambient atmospheric conditions, etc.; (2) a discussion of project results; (3) a summary of the objectives and results of each project; (4) a listing of project reports for the Military Effects Program.

## PREFACE

The planning and execution of Project 1.10 were under the direction of L. M. Swift, with L. H. Inman serving as field party chief. Other members of the field party included F. Hempy, C. C. Hughes, D. C. Knirck, V. E. Krakow, R. V. Ohler, C. T. Vincent, and C. M. Westbrook. E. J. Wells and Mrs. S. R. Hornig assisted in the data analysis.

The excellent planning and cooperation of CDR W. M. McLellan, USN, and Major H. T. Bingham, USAF, Directorate of Weapons Effects Tests, Field Command, AFSWP, are gratefully acknowledged.

# CONTENTS

ABSTRACT .....	5
FOREWORD .....	6
PREFACE .....	6
CHAPTER 1 INTRODUCTION .....	13
1.1 Objective .....	13
1.2 Background .....	13
CHAPTER 2 PROCEDURE .....	15
2.1 Description of Tests .....	15
2.2 Gage Layouts .....	15
2.2.1 Shot 6 .....	15
2.2.2 Shot 12 .....	15
2.3 Predictions .....	16
2.4 Gage Coding .....	21
2.5 Instrumentation .....	21
2.5.1 Gages .....	24
2.5.2 Gage Mounting .....	24
2.5.3 Instrument Response .....	26
2.5.4 Calibration .....	26
2.5.5 Accuracy .....	28
CHAPTER 3 OPERATIONS .....	29
3.1 Shot 6 .....	29
3.2 Shot 12 .....	29
CHAPTER 4 RESULTS .....	32
4.1 Instrumentation Performance .....	32
4.1.1 Shot 6 .....	32
4.1.2 Shot 12 .....	32
4.2 Definition of Measured Quantities .....	33
4.3 Record Reading and Data Reduction .....	37
4.3.1 Pitot-Tube Corrections .....	37
4.4 Gage Records .....	40
4.5 Wave Forms .....	40
4.5.1 Wave-Form Classification .....	40
4.5.2 Effects of Surface Characteristics on Wave Form .....	42
4.5.3 Effects of Gage Mount on Wave Form .....	43
4.6 Tables of Results .....	43
CHAPTER 5 DISCUSSION .....	87
5.1 Arrival-Time Data .....	87
5.1.1 Time of Arrival and Shock Velocity .....	87
5.1.2 Wave-Front Orientation .....	90

5.2 Overpressure Measurements $p$ (pitot) .....	92
5.2.1 Effects of Surface Characteristics .....	93
5.2.2 Additional Surface Effects and Cross-Feed .....	96
5.2.3 Overpressure Decay Behind Shock Front .....	104
5.2.4 Comparisons with Previous Data .....	108
5.3 Dynamic Pressure Measurements $q^*$ (pitot) .....	113
5.3.1 Effects of Surface Characteristics $q^*$ (pitot) .....	114
5.3.2 $q^*$ (pitot) Positive Impulse .....	118
5.3.3 Comparisons with Previous Data .....	113
5.4 Precursor Phenomena .....	120
5.4.1 Background .....	120
5.4.2 Measured and Computed Preshock Temperature .....	122
5.4.3 Precursor Development .....	134
5.4.4 Precursor Arrival-Time and Velocity Characteristics .....	140
5.5 Measurements on Beam Device .....	144
5.5.1 Background and Definitions .....	146
5.5.2 Beam-Device Results .....	148
CHAPTER 6 CONCLUSIONS AND RECOMMENDATIONS .....	153
6.1 Conclusions .....	153
6.1.1 Instrumentation Performance .....	153
6.1.2 Wave-Form Classification .....	153
6.1.3 Shock Velocity and Computed Preshock Temperature .....	153
6.1.4 Surface Effects .....	154
6.1.5 Precursor Phenomena .....	154
6.1.6 Correlation with Damage .....	155
6.2 Recommendations .....	155
REFERENCES .....	156
APPENDIX A ACCELERATION RESPONSE OF WIANCKO PRESSURE GAGES .....	158
APPENDIX B GAGE RECORDS .....	160
APPENDIX C GAGE CALIBRATION DATA .....	189
FIGURES	
2.1 Gage layout, Shot 6 .....	17
2.2 Gage layout, Shot 12, water and asphalt lines .....	18
2.3 Gage layout, Shot 12, desert line and area layout .....	19
2.4 Detailed gage layout, Shot 12 .....	20
2.5 Instrument shelter, Shot 6 .....	22
2.6 Instrument shelter, Shot 12 .....	23
2.7 Pitot-static tube construction .....	25
2.8 Pitot-tube installation on 10-foot tower .....	27
2.9 Side-on baffle and pitot-tube installation on 10-foot tower .....	27
2.10 Beam device, general view .....	28
3.1 General view, Shot 12, desert line .....	30
3.2 General view, Shot 12, water line .....	30
3.3 General view, Shot 12, test area .....	31
4.1 Schematic of detached shock and impact tube shock in front	



5.10	Maximum overpressure versus ground range, desert and asphalt, Shot 12-----	100
5.11	Maximum overpressure versus ground range, surface level, Shot 12-----	101
5.12	Maximum overpressure versus ground range, 3-foot level, Shot 12-----	101
5.13	Maximum overpressure versus ground range, 10-foot level, Shot 12-----	103
5.14	Results from BRL measurements on gage-arc, Shot 12-----	105
5.15	Area layout of Shot 12 test area, showing stabilized areas-----	105
5.16	Post-Shot 12, desert line, looking northeast toward ground zero-----	106
5.17	Post-Shot 12, water line, looking south toward ground zero-----	107
5.18	Post-Shot 12, asphalt line, looking north toward ground zero-----	107
5.19	Decay of overpressure behind shock front, water line, Shot 12-----	109
5.20	Decay of overpressure behind shock front, desert and asphalt lines, Shot 12-----	110
5.21	Wave form comparisons (A-scaled), Teapot Shot 6, Upshot- Knothole Shot 10, Tumbler Shot 4, and Upshot- Knothole Shot 11-----	111
5.22	Wave form comparisons (A-scaled), Teapot Shot 12, and Upshot-Knothole Shot 1-----	112
5.23	Wave form comparisons (A-scaled), Upshot-Knothole Shots 1 and 10-----	113
5.24	Wave form comparisons (A-scaled), Teapot Shot 12 and Upshot- Knothole Shot 9-----	114
5.25	A-scaled maximum overpressure, surface level, Teapot Shots 6 and 12, previous shots, desert line-----	115
5.26	A-scaled positive phase duration versus A-scaled maximum overpressure, Teapot Shots 6 and 12, previous shots-----	117
5.27	A-scaled positive impulse versus A-scaled maximum overpressure, Teapot Shots 6 and 12, previous shots-----	119
5.28	Maximum $q^*$ (pitot) pressure versus ground range, water line, Shot 12-----	121
5.29	Maximum $q^*$ (pitot) pressure versus ground range, desert line, Shot 12-----	121
5.30	Maximum $q^*$ (pitot) pressure versus ground range, asphalt line, Shot 12-----	123
5.31	Maximum $q^*$ (pitot) pressure versus ground range, 3-foot level, Shot 12-----	123
5.32	Maximum $q^*$ (pitot) pressure versus ground range, 10-foot level, Shot 12-----	125
5.33	Maximum $q^*$ (pitot) pressure versus ground range, Shot 6-----	125
5.34	$q^*$ (pitot) impulse versus time, 1,250 feet-1,500 feet-1,750 feet, Shot 12-----	127
5.35	$q^*$ (pitot) impulse versus time, 2,000 feet-feet-2,250 feet- Shot 12-----	129
5.36	$q^*$ (pitot) impulse versus time, 2,500 feet, Shot 12-----	131
5.37	$q^*$ (pitot) impulse versus time, 3,000 feet, Shot 12-----	133
5.38	$q^*$ (pitot) impulse versus time, 1,300 feet, Shot 6-----	133
5.39	A-scaled maximum $q^*$ (pitot) pressure, 10-foot level, Teapot Shots 6 and 12, previous shots-----	135



5.40 Shock front diagram for pressure calculation of preshock temperature----	137
5.41 Wave front diagram for angle-of-front calculation of preshock temperature-----	137
5.42 Computed preshock temperature versus ground range, Shot 12-----	139
5.43 Computed preshock temperature versus arrival time, Shot 12-----	141
5.44 Schematic diagram of propagation velocity versus ground range-----	143
5.45 Schematic diagram of arrival time versus ground range in region of rapidly changing velocity-----	143
5.46 A-scaled time of arrival versus slant range, Teapot Shot 12-----	145
5.47 A-scaled time of arrival versus slant range, Teapot Shot 6-----	147
5.48 A-scaled ( $V_x t G/R^2$ ) versus slant range, Teapot Shot 12-----	149
5.49 A-scaled ( $V_x t G/R^2$ ) versus slant range, Upshot-Knothole Shots 1 and 10 compared with Teapot Shot 12-----	149
5.50 A-scaled ( $V_x t G/R^2$ ) versus slant range, Teapot Shot 6 compared with Teapot Shot 12-----	149
5.51 Records of force versus time from H-beam devices, Shot 12-----	151
5.52 Computed drag coefficient versus time for H-beam devices, Shot 12-----	151
A.1 Schematic diagram of Wiancko pressure transducer system-----	158
A.2 Effects of acceleration; Wiancko gage-----	159
B.1 Original records, Shot 12, water line, 750-1,500 feet-----	161
B.2 Original records, Shot 12, water line, 1,500-2,000 feet-----	163
B.3 Original records, Shot 12, water line, 2,000-2,500 feet-----	165
B.4 Original records, Shot 12, water line, 2,500-3,000 feet-----	167
B.5 Original records, Shot 12, desert line, 750-1,500 feet-----	169
B.6 Original records, desert line, 1,750-2,000 feet-----	171
B.7 Original records, Shot 12, desert line, 2,250-2,750 feet-----	173
B.8 Original records, Shot 12, desert line, 2,750-4,500 feet-----	176
B.9 Original records, Shot 12, asphalt line, 750-1,500 feet-----	178
B.10 Original records, Shot 12, asphalt line, 1,750-2,250 feet-----	180
B.11 Original records, Shot 12, asphalt line, 2,500-3,000 feet-----	182
B.12 Original records, Shot 6, desert line-----	184
B.13 Original records, Shot 6, asphalt line-----	186

## TABLES

2.1 Description of Tests-----	16
4.1 Symbols and Notation-----	33
4.2 Overpressure Wave-Form Classification-----	41
4.3 Dynamic Pressure Wave-Form Classification-----	45
4.4 A-Scaling Factors-----	45
4.5 Overpressure, Shot 12 Water Line-----	46
4.6 Dynamic Pressure, Shot 12 Water Line-----	47
4.7 Overpressure, Shot 12 Desert Line-----	48
4.8 Dynamic Pressure, Shot 12 Desert Line-----	49
4.9 Overpressure, Shot 12 Asphalt Line-----	50
4.10 Dynamic Pressure, Shot 12 Asphalt Line-----	51
4.11 Overpressure, Shot 6 Desert Line-----	51
4.12 Dynamic Pressure, Shot 6 Desert Line-----	52
4.13 Overpressure, Shot 6 Asphalt Line-----	52
4.14 Dynamic Pressure, Shot 6 Asphalt Line-----	52
5.1 Wave Front Orientation Data-----	93

5.2 Cross-Feed Data. Shot 12 -----	102
5.3 Shot Descriptions for Data Comparisons-----	108
5.4 Desert-Line Computed Temperatures for Shot 12 -----	132
5.5 Asphalt-Line Computed Temperatures for Shot 12 -----	138
5.6 Water-Line Computed Temperatures for Shot 12 -----	150
C.1 Shot 6 Pressure Gages -----	189
C.2 Shot 12 Pressure Gages -----	190
C.3 Shot 12 Strain Gages (H-Beam)-----	192

**CONFIDENTIAL**

## Chapter 1

## INTRODUCTION

### 1.1 OBJECTIVE

The objective of Project 1.10 was to obtain data on the variation with ground range of static overpressure (side-on) and dynamic pressure from a nuclear explosion over a dust-free water surface, an asphalt surface, and a natural desert surface.

Particular attention was given to the relationship between overpressure and dynamic pressure in the regions of expected perturbed wave forms. These data were to be used for the modification and reinforcement of theory of blast effects and precursor formation. Accurate theory would permit establishment of damage criteria under a variety of burst conditions, when correlated with measurements of other blast phenomena. Specific data were also to be furnished to Programs 3 and 5 for use in analyzing structural effects.

## 1.2 BACKGROUND

Prior to 1952, the optimum height of burst for maximum area of desired ground level peak overpressure was obtained from Reference 1. This information was based on theoretical considerations and extrapolation from small-scale experiments, and on limited nuclear-explosion data from Bikini Able and a few tower shots. The Buster shots in 1951 indicated considerable disparity between predicted and observed pressures both in amplitude and wave form (Reference 2). The Tumbler shots in 1952 were planned to resolve some of these differences; the results confirmed that at certain relatively low-scale heights of burst these discrepancies were real (Reference 3). On Tumbler Shot 4 (particularly at pressure levels above approximately 8-psi peak) amplitudes were reduced, rise times were increased, and the velocity of propagation of the first effects was increased. These effects were shown to be associated with the thermal radiation acting jointly on the earth's surface and on surface-produced dust clouds to produce a thermal layer. Evidence indicated the existence of severe turbulence in these regions of interest, which complicated the problem of delineating the behavior of the blast wave by point measurements. At this time a rather satisfactory qualitative analysis of these phenomena was formulated. However, the quantitative data from Tumbler were insufficient to permit development of analytical techniques that would allow predictions of the magnitude of these disturbing effects under a given set of conditions other than for a desert-like surface.

The Upshot-Knothole shots in 1953, particularly Shots 1, 10, and 11, provided a great deal of quantitative data on these phenomena (References 4 and 5). Data from these and previous shots permitted the development of analytical techniques for prediction of overpressure to a satisfactory degree of accuracy, but it became increasingly obvious that the correlation between peak overpressure and damage effects was not satisfactory in these regions of distorted wave forms. This was particularly true on Upshot-Knothole Shot 10, where damage to several types of targets at some ground ranges was far greater than that expected on the basis of the peak overpressure observed. A number of measurements of dynamic pressure were planned and conducted, but the rather unexpected damage to the gage mountings themselves reduced the usefulness of the data (Reference 6).

Program 1 of Operation Teapot was therefore planned to give primary emphasis to measurement of dynamic pressures in those regions where the relationship between dynamic pressure and overpressure remained questionable. Analysis of earlier data had also indicated that the magnitude of these unpredicted effects probably depended on the nature of surfaces involved; Teapot, therefore, included an investigation of the effects of different types of surface upon blast phenomena.

Prior to Teapot, experimental data seemed to indicate that formation of the precursor was due to refraction of the incident shock wave by a layer of heated air near the ground surface. It was believed that if the temperature of the heated layer were sufficiently high with respect to the ambient air above it, the velocity of this refracted shock wave would be increased so that it would reach a ground radius station sooner than would the incident (undisturbed) shock wave. The refracted wave, as it was propagated through the heated air layer, also sent another shock wave into the ambient air above the thermal layer (Reference 7). Although few dynamic-pressure measurements had been obtained in the precursor region, the data available indicated that the dynamic pressures in the region of disturbed blast waves were equal to or greater than ideal and much greater than would be calculated from the measured overpressures using the classical Rankine-Hugoniot relationship applicable across a shock front.

These abnormally high dynamic-pressure measurements were at least partially explained when laboratory tests indicated that the pitot-static tube measurement is sensitive to dust or other particulate matter carried along by the shock wave. Differential pressures measured in the precursor region are therefore believed to represent the dynamic pressure of the air plus some portion of the dynamic pressure associated with dust.

Before Teapot, very little data was available for determining the effect of the physical properties of the ground surface upon precursor wave formation and development. A few measurements of disturbed blast waves over land and water and the results of the smoke experiments on Upshot-Knothole (Reference 7) indicated that conditions which altered the physical characteristics at or near a surface could have a profound effect upon measured pressures and wave forms. Furthermore, since it has become apparent that pressure measurements are influenced by such parameters as dust density, near-surface temperatures, and wind direction, the determination of these quantities assumes a greater importance than previously realized. For this reason, the Teapot program included extensive measurements of some of the more-fundamental blast parameters for which presumably dependable instrumentation had been developed previously, and included a limited number of exploratory measurements of the more-important physical parameters.

Finally, a limited program of drag-force measurement on simple shapes was included. These measurements, when coupled with the pressure measurements at the same locations, could permit later correlation with wind-tunnel and shock-tube experiments designed to investigate the drag forces developed by a precursor.

## Chapter 2

# PROCEDURE

### 2.1 DESCRIPTION OF TESTS

The two Operation Teapot Shots with which this report is concerned are Shots 6 and 12 (see Table 2.1).

Blast measurements on Shot 6, although limited in number, were included to explore the effects of different types of ground surface (desert and asphalt). In addition, it was thought that Teapot Shot 6 data could help clarify the results obtained on Upshot-Knothole Shot 10 (Reference 4), which was detonated at approximately the same burst height.

Shot 12 measurements, taken over three different surfaces (desert, asphalt, and water), were designed to obtain detailed information on the effects due to surface properties in the region of disturbed blast waves. Also, it was hoped that the measurements would yield definitive data on pitot-tube dynamic pressure, few of which were available from nuclear tests prior to Teapot.

### 2.2 GAGE LAYOUTS

2.2.1 Shot 6. The gage layout for Shot 6 (Figure 2.1) was designed to obtain maximum information practicable with the 24 available gage channels. Since ground zero was located near the northern edge of the paved area in Area T-7-1, blast lines were extended both north over the desert area and south over the paved area. The availability of these surfaces, similar to two of those used on Shot 12, was the basis of the decision to instrument this shot. However, the desert surface in this area was rough and boulder-strewn, in contrast with the smooth surface of the Frenchman Flat area of Shot 12. Also, the asphalt surface was broken and ridged in places, but still provided a definite contrast to the desert surface and was much greater in length and span than the Shot 12 asphalt line. On each line, gage stations were located to concentrate on the region of probable transition between precursor and normal wave forms. Ground ranges of 1,300, 1,650, and 2,000 feet in each direction were chosen as those most likely to produce the critical information, based on the pretest estimate of yield and on the results of Upshot-Knothole Shot 10.

It was decided that measurements of surface-level overpressure, and of overpressure and dynamic pressure (using a pitot-tube gage) at 10-foot elevation at each station would provide maximum useful information. To compute corrections to the measured dynamic pressure corresponding to variations in pitch angle of flow, pitch gages at 10 feet were included at each gage station. (The angle of pitch is defined as the flow angle measured in that vertical plane which is determined by the pitch gage and ground zero.)

2.2.2 Shot 12. The gage layout for Shot 12 (Figures 2.2 and 2.3) was a complex problem. The general concept of Program 1 for this shot was to instrument three different blast lines: one over a water surface, one over an asphalt surface, and the third over the natural desert. An effort was made to locate gages on each line to obtain the maximum information of interest and the maximum correlation between lines. A number of projects participated, and the resultant gage layout for Project 1.10 represented, in

some instances, a compromise between interests for the best overall program results.

The general principle followed in instrument layout was as follows. Surface-level air pressures were measured at sufficient stations along each line to provide correlation with other shots and general information as to pressure level versus radius. Above-ground (10-foot) overpressure was measured at a few stations on each line for further correlation with other shots and for determination of any pressure gradients which might be detectable. Dynamic pressures with their associated overpressures were measured at 3- and 10-foot heights at intervals determined partly by practicability of towers and partly by the usefulness of this information to other projects and programs. At one sta-

TABLE 3.1 DESCRIPTION OF TESTS

Shot	Code Name	Date	Location (Area)	Blast-Line Surface	Yield	Height	Atmos. Press		Air Temp	
							GZ	Burst Ht	GZ	Burst Ht
					kt	ft	mb	mb	°C	°C
6	Bee	Mar 22, 1955	T-7-1a (Yucca)	Desert Asphalt	7.76	500 Tower	876	871	1.0	5.0
12	Met	Apr 15, 1955	Frenchman Flat	Water Desert Asphalt	22.0	400 Tower	908	895	19.5	18.9

tion on each line, investigation was made of the variation of dynamic pressures with heights up to 40 feet. At two stations (1,500 and 2,500 feet) on the water line, the pitot-tube measurements were made at locations which were displaced from the main blast line (see Figure 2.4). It was hoped that these measurements would aid in determining the extent and time of feed-in of disturbances from the desert surface. Measurements on the water and asphalt lines were restricted in radius to that of the lines themselves. In general, for each gage measuring dynamic pressure, associated measurement of pitch was made by Project 1.11 (Sandia Corporation) for correction of measured pressures and for study of flow characteristics. Full detail of the gage layouts can be obtained from Figures 2.2 through 2.4. In conjunction with this project, seven instrument channels were supplied to Project 3.6 for their direct use, not connected with free-field phenomenology. Two channels were used for measurements of loading on beams under Project 3.2. These beam devices were located at 200- and 2,500-foot ground range on the desert line.

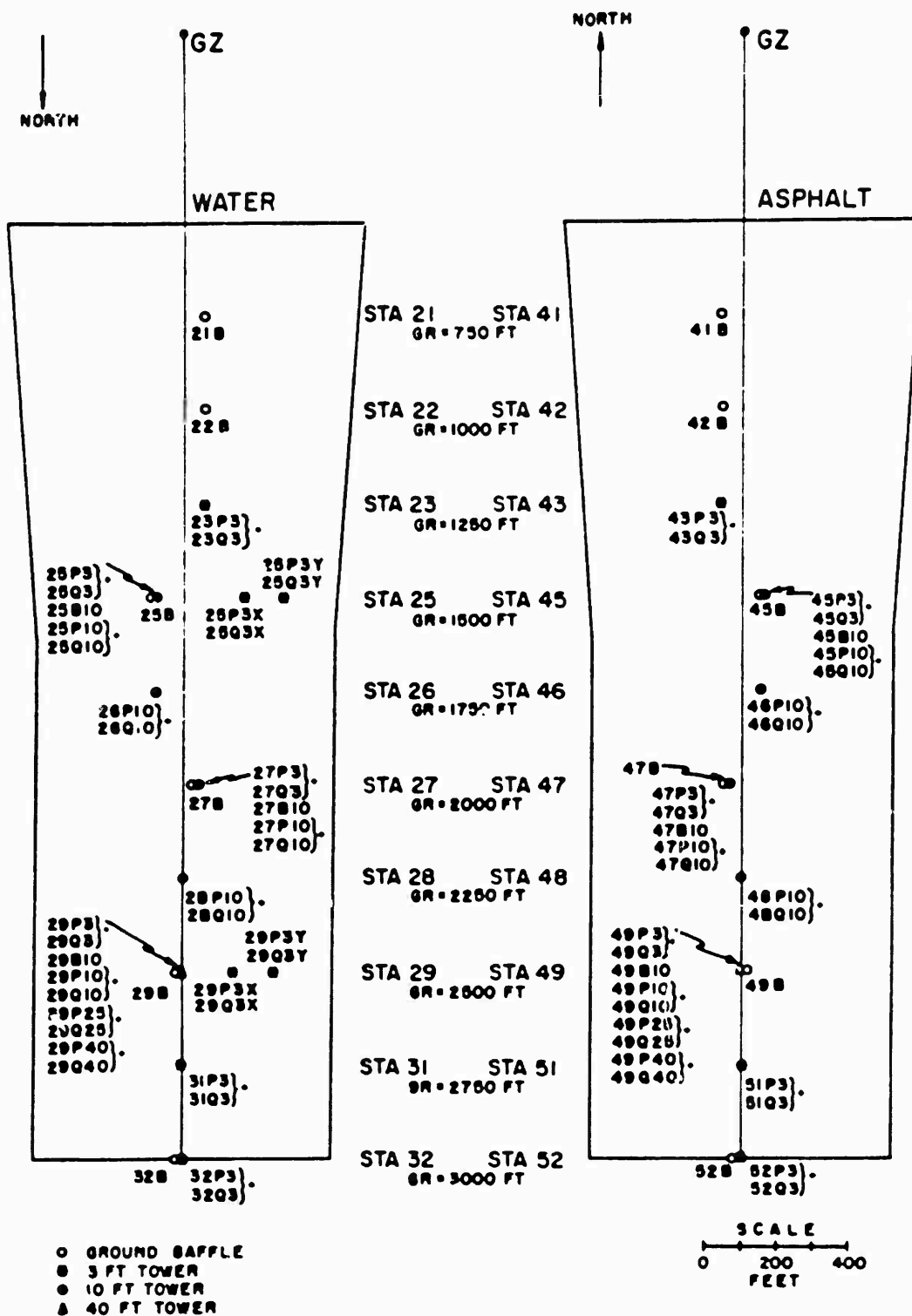
## 2.3 PREDICTIONS

In planning an experiment of this type, it is necessary to predict the values of the functions to be measured with an accuracy sufficient to allow the sensitivity of each channel to be set closely enough so that satisfactory deflections will be recorded. For best results, these should be within a factor of two from the true values.

Sufficient data were available (References 3, 4, and 5) from shots at similar heights of burst over desert soil to permit reasonably dependable predictions of peak overpressure versus radius for the desert lines of both shots. These same predictions were used for the asphalt lines, under the assumption that thermal effects would be similar to those on the desert lines. For prediction purposes, an ideal curve was constructed for the water-line of Shot 12, based on the free-air curve and assumed reflection factors.

Predictions of dynamic pressure on the desert lines were based largely on data from Upshot-Knothole Shots 1, 10, and 11 (References 4 and 6). While not as complete as overpressure data, they were sufficient to permit reasonably dependable predictions. For the water line, predictions were based on the theoretical relationships between overpressure and dynamic pressure, using the ideal curve of overpressure as a basis for calculation.





• ANGLE OF PITCH VS TIME (SANDIA CCRP PROJECT 1.11)

Figure 2.2 Gage layout, Shot 12, water and asphalt lines.



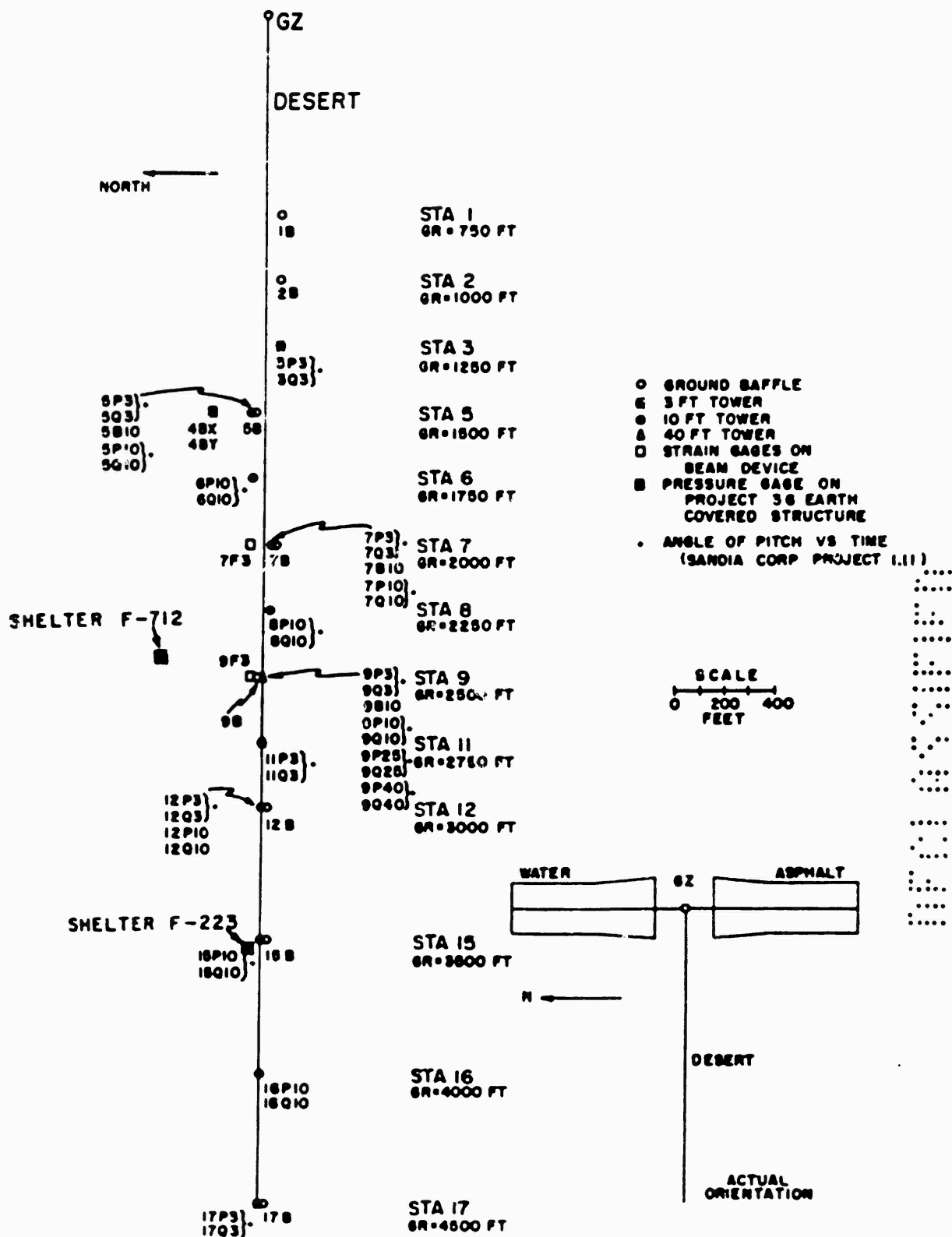


Figure 2.3 Gage layout, Slot 12, desert line and area layout.

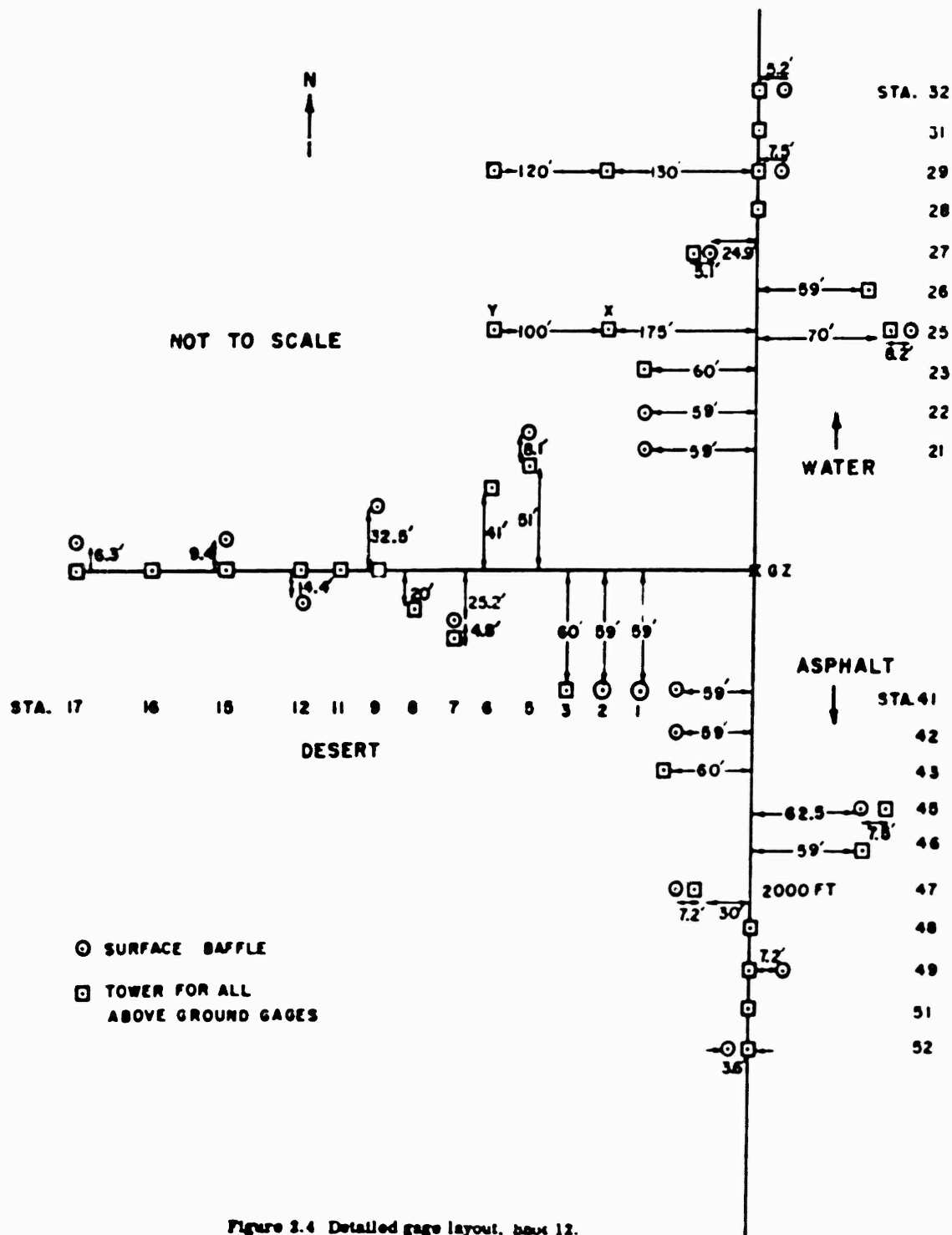


Figure 2.4 Detailed gage layout, box 12.

For the asphalt lines, no specific method of prediction could be agreed upon. It was generally agreed, however, that dynamic pressures on these lines should fall between those on the desert line and those in the ideal case, thus establishing a lower and upper limit. Predictions for range setting, then, were based on a logarithmic mean between those for the desert and water lines.

These predictions for Shot 12 were prepared by Directorate of Weapons Effects Tests, Field Command, AFSWP, and distributed at FCWET/54-1589-0 on 26 October 1954.

## 2.4 GAGE CODING

For identification of channels and recorded traces with their proper gages, a systematic coding was adopted for nomenclature. Station numbers were assigned to each gage range on each line. These numbers were used as the first part of the gage code. The second part of the gage code was a letter indicating the nature of the measurement. In this project, these letters were B for air blast measured by conventional baffle-mounted gages, P for air blast measured as the side-on (overpressure) component of the pitot-tube gage, Q for measured dynamic pressures, and Y for pitch. A third part of the code, where necessary, indicated the height of a gage above the surface in feet. Typical gage code numbers might be 61B10, a baffle gage at Station 61, 10 feet high; or 2B, a baffle gage at Station 2, baffle flush with ground surface; or 47P3, an overpressure gage at the static orifice of a pitot-tube at Station 47, 3 feet high; or 31Q3, a pressure gage at the nose of a pitot-tube at Station 31, 3 feet high.

## 2.5 INSTRUMENTATION

All channels of instrumentation were essentially identical to those described in previous reports (Reference 3). Wiancko balanced, variable-reluctance pressure transducers were connected through modified Wiancko equipment to William Miller Corporation oscillograph recorders. Provisions were included for applying automatically a synthetic calibrating signal to each channel immediately prior to zero time to compare final deflection on the record with the deflection produced by the same signal at the time of calibration. A highly accurate timing signal of 100 cps and 1,000 cps was also applied to all recorders simultaneously from a single source. This signal had a time accuracy of better than 10 parts per million and provided means for accurate time correlation of records.

The prime power supply for all instruments during actual shots was a bank of storage batteries. Suitable converters were used to produce 115 volts for components requiring this type of supply. An individual converter was used for each rectifier power supply, thus minimizing the probability of gross failure due to converter failure.

On Shot 12, there were 132 gage channels connected. Of these, 72 were connected to dual recording systems consisting of one galvanometer on each of two recorders. These dual channels were assigned to those gages which were considered to be most important, to minimize loss of important data due to any possible single recorder failure. On 32 of those 72 channels, one of the galvanometers had a natural frequency of 200 cps, whereas the remaining galvanometers were of 300-cps natural frequency. The channels incorporating one 200-cps galvanometer were used on gages where the uncertainty of the predicted peak was greatest and where the expected signal would not be degraded appreciably by the reduced frequency response of the lower-frequency galvanometer. Since there was an appreciable difference in the sensitivity of the two galvanometers thus used on a single channel, a wider range of input signal could be accommodated without loss of data (provided both recorders operated properly).

On Shot 12, two recording shelters were used, F-223, and F-712. The former contained 84 channels of terminal equipment, the latter 48. This separation was made because of limitations in space in existing recording shelters and because a saving in total cable and ditch lengths could be achieved.

On Shot 6, 24 gage channels were connected and fed to two recorders. Each of these channels used dual recording as described above. Eight used galvanometers of two frequencies as a protection against recorder failure. For this shot all terminal instruments and recorders were mounted in a single shelter, F-235, located about 1,700 feet from ground zero (Figure 2.1).

Instruments were powered at suitable times before zero time by Edgerton, Germeshausen, and Grier (EG & G) relay circuits, with lock-in relays controlled by a time-delay

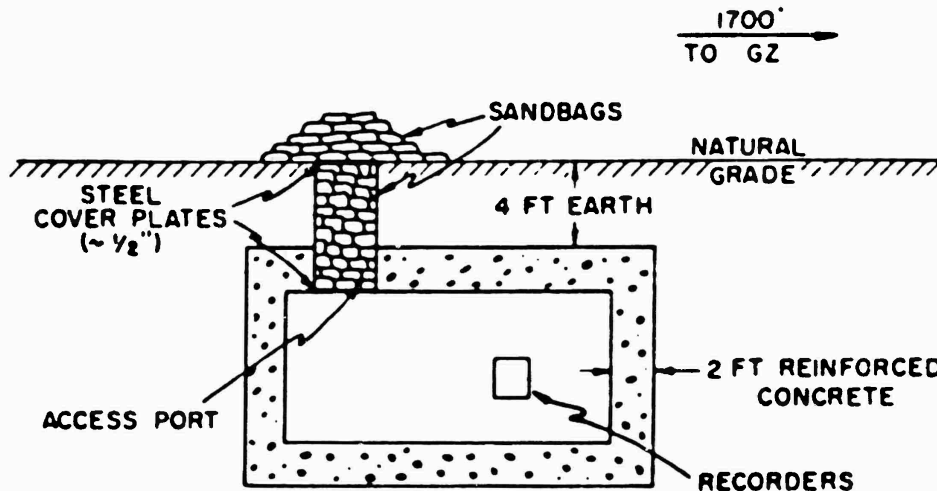


Figure 2.5 Instrument shelter, Shot 6.

relay in order to continue operation for approximately one minute after zero time, even though the EG & G relays dropped out sooner. Utmost attention was paid to circuitry and procedures to ensure maximum reliability of operation. Dual relay contacts or dual relays were used wherever feasible. A separate recording was made of the output voltage of each power oscillator supplying the carrier power to a group of 12 gages. Thus, correction might be made in the final data reduction for any change in output voltage due to shorted cables or other mishaps during the shot. A multipen recorder was connected to provide a record of operating time and sequence of various elements so that any failure might be traced to its source in a post-test study.

Schematic diagrams of the recording shelters used on Shots 6 and 12 are shown in Figures 2.5 and 2.6. It should be noted that, while the Shot 6 shelter and the rear shelter of Shot 12 were completely buried, most of the Shot 12 front shelter (2400 feet from ground zero) was above the natural grade. This necessitated an earth cover over the shelter for protection of the recording paper against radiation fogging (see Figure 2.6). From previous experience, it was decided that shielding which reduced the integrated radiation dosage within the shelter to below 10 roentgens would be acceptable. Using the prompt- and residual-radiation data obtained on Upshot-Knothole and the 10-roentgen limit, it was possible to compute the necessary shielding thickness required. It was further assumed that earth shielding was approximately 60 percent as effective as concrete of the same thickness. The calculation for the Shot 12 front shelter yielded the requirement of about 40 inches of earth covering the shelter. As shown in Figure 2.6,

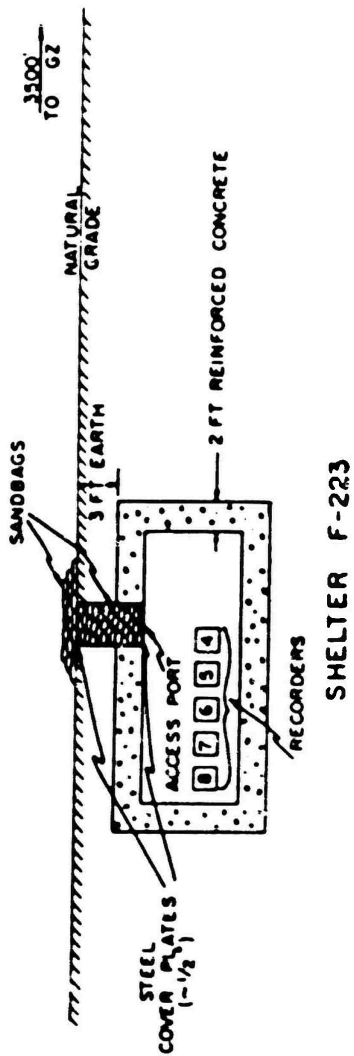
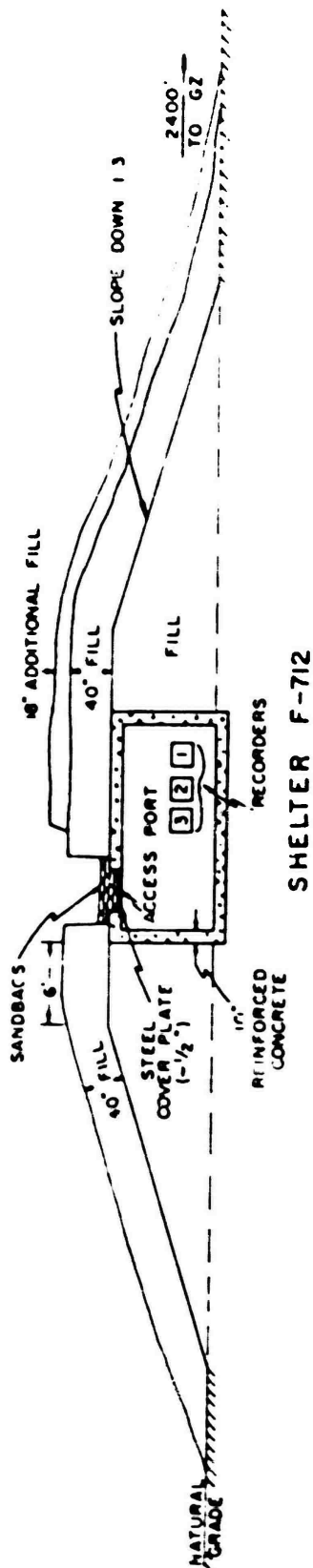


Figure 2.6 Instrument shelter, Shot 12.

DECLASSIFIED

an additional 18 inches of earth cover was added on the ground-zero side of the shelter as a safety factor. The natural earth cover over the other two shelters was adequate for shielding.

Before each shot, the access holes into each shelter were covered with a heavy steel plate (about one-half inch thick) and covered with sandbags, as illustrated in the figures. Post-shot observations on recording-paper fogging will be discussed in Chapter 4.

**2.5.1 Gages.** The Wiancko pressure gages used to measure overpressure were identical with those used in previous operations (References 3 and 4). Damping of all gages was checked prior to operation and was adjusted to provide a maximum of damping consistent with a minimum rise time. Since the damping of these gages is slightly non-linear, this procedure results in a value of damping which permits an appreciable overshoot at the natural frequency of the gage, which varies from 1,400 to 1,800 cps. However, since the frequency response of the recording system was limited by the characteristics of the galvanometers, this overshoot did not appear on the final record (see Section 2.5.3).

The instruments used as differential gages in the pitot-tube assemblies were similar to those used for measurement of overpressure, except that all damping was removed. This procedure had been found desirable because the sensitive element of the gage in this use is exposed to a certain amount of dust which passes the filter. When grease is used as a damping element, this dust collects on the grease and introduces the danger of blocking the gage mechanism for a portion of the record. These and the associated overpressure gages were mounted in a pitot-tube housing essentially identical to those developed and previously described by Sandia Corporation (Reference 8). The general construction of this pitot-tube head is shown in Figure 2.7.

Because the gage which measures dynamic pressure in a pitot tube operates as a differential sensor, arrival times of the shock wave determined by this gage are not considered reliable. The arrival-time data used in this report are therefore taken from the pitot-tube overpressure gage and overpressure baffle-gage measurements.

Actual pressures at the total- and static-pressure inlets of the pitot-tube depend upon the angle between the direction of flow and the axis of the tube, as well as upon the Mach number of the flow. This will be discussed more fully in Chapter 4. Also, for this series of measurements (since only a head-on dynamic pressure was measured) no attempt was made to determine dynamic pressures in the negative phase. For this reason, the positive-phase-duration of the pitot-tube dynamic pressure is not considered reliable.

**2.5.2 Gage Mounting.** All baffle-mounted pressure gages were mounted with their inlets at the center of a 17-inch-diameter cast-aluminum baffle. Where the gage was at ground level, this baffle was cemented flush with the earth surface and held in place by a buried anchor. Where it was above the surface, the baffle was oriented in a vertical plane passing through ground zero and offset from the gage tower about 14 inches.

All pitot-tube gages were mounted in a special adapter mount which projected forward from the mounting tower so that the side opening of the pitot-tube gage was approximately 30 inches ahead of the vertical portion of the tower. The mounting was tapered to provide additional strength and to provide a degree of fairing between the small-diameter gage and the large-diameter tower.

A standardized mounting was adopted for all gages, including the pitch and yaw gages used by Sandia Corporation. This basic mount consisted of a heavy flange (8 inches in diameter) onto which any type of gage mount could be bolted.

The towers supporting aboveground gages were designed by the personnel of the

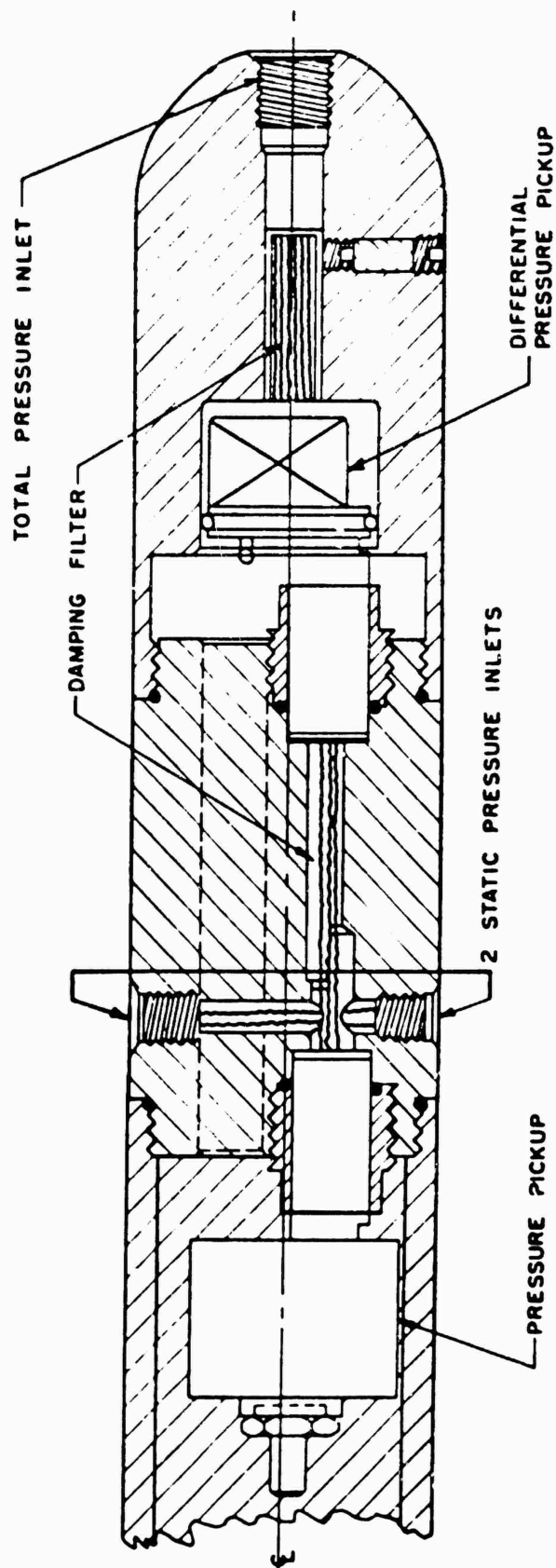


Figure 2.7 Pitot-static tube construction.

DECLASSIFIED

office of the Director, Program 1. In the design of these towers, as well as that of the gage mounts, every effort was made to ensure maximum resistance to damage by overpressure and dynamic pressures. This was particularly true for those towers which were installed at relatively short ground ranges. These precautions were considered necessary because of the extensive gage and tower damage experienced on Upshot-Knothole Shot 10 and other similar shots. Typical gage installations on towers are shown in Figures 2.8 and 2.9.

The two beam devices, 3.2d1 and 3.2d2 recorded on channels 7F3 and 9F3, were designed to provide information on the drag factor of a standard cross section under conditions of high drag loading. Figure 2.10 shows a general view of one of these structures. The 12-inch H-beam was mounted to provide a simple beam of 10-foot length with two 1-foot end sections to eliminate end effects. A Wiancko strain gage was mounted between short straps welded to the back edges of the flanges at the center. From the deflection of the strain gage, the loading on the beam could be calculated.

**2.5.3 Instrument Response.** The response time of the pressure-gage recording system was determined by the characteristics of the recording galvanometers used. The 300-cps (nominal) galvanometers had an undamped natural frequency of 315 to 340 cps and were damped to have an overshoot of approximately 7.5 percent. This corresponds to a damping factor of approximately 0.65 and provides a nominal rise time (to 90 percent of final amplitude) of 1.3 msec. The nominal 200-cps galvanometers had an actual undamped natural frequency of 200 to 230 cps and were similarly damped to give a nominal rise time of approximately 1.8 msec. Since the rise time of the Wiancko gages when properly adjusted was appreciably smaller than either of these galvanometer rise times, it is evident that the response of the galvanometer was the limiting feature of the response of the system.

The Wiancko gage with its associated recording system is basically flat down to steady-state conditions. However, to avoid drift due to changes in temperature or ambient pressure, the cases of the lower-range gages are provided with a bleed plug. Thus, any pressure difference between the inside and outside of the case will be equalized over a period of time. The time constant of this bleed plug was adjusted to a minimum of 30 seconds so that it would have no effect on the recording of a blast wave of normal duration. As a consequence, the low-frequency response of the gage system may be considered as completely flat.

**2.5.4 Calibration.** Each pressure gage was calibrated in the field by the application of several values of static overpressure after the gage had been installed in its final location and connected to its associated equipment for the shot. After each shot, a post-shot calibration was performed to check stability of the system. Calibrations for specific gages will be found in Appendix C.

In the calibration procedure, several pressures ranging from zero to well above the expected peak were applied to the gage in sequence. For each pressure, the galvanometer deflection was noted and recorded; in addition, the deflection caused by a signal of known magnitude injected into the gage circuit was recorded. From the former deflection, a calibration curve of deflection versus pressure was constructed; the latter deflection served to correct for any changes in sensitivity of the recording system between calibration and the final tests, since an identical signal was injected on the final record about four seconds before zero time.

The strain-gage-H-beam system was calibrated in the field using a hydraulic jack to provide a static load. The jack loaded the beam at the span center with the assumption



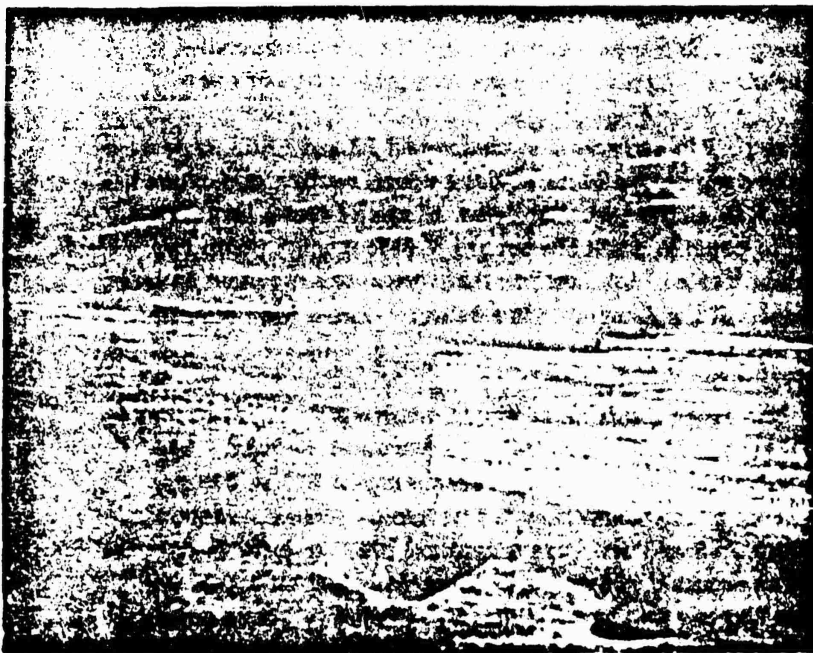


Figure 2.8 Pitot-tube installation on 10-foot tower.

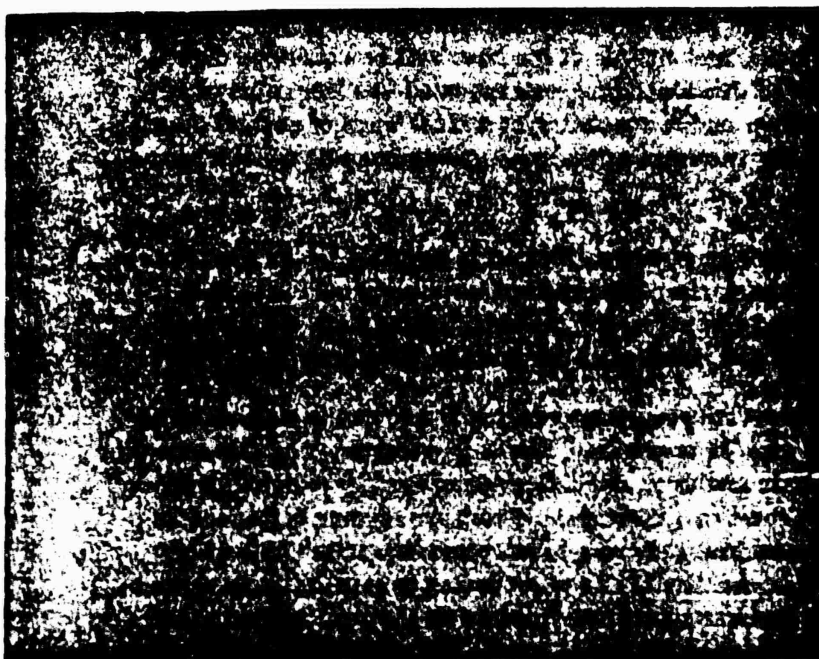


Figure 2.9 Side-on baffle and pitot-tube installation on 10-foot tower.

that this type of loading was equivalent to a distributed load of double the applied magnitude.

**2.5.5 Accuracy.** In the absence of excessive acceleration and/or high temperature, it is believed that the calibration procedure assures that the Wiancko gage measurements are reliable to within  $\pm 5$  percent of the actual pressures. Low-pressure measurements, far below nominal gage rating, may be somewhat less accurate. Moreover, in regions of disturbed blast waves, where drag forces on gage towers are large and gage internal temperature may be high, it is difficult to assign an overall accuracy.

Subsequent to Teapot, a program of laboratory testing was undertaken to determine the effect of gage acceleration upon pressure sensing. The conclusion was that acceleration imposed while the gage was recording pressure could have a significant effect upon



Figure 2.10 Beam device, general view.

the measurement. Details of these tests and the discussion of the results are included in Appendix A. In the absence of actual acceleration-versus-time data for the gage mounts, it is necessary to look into indirect means for determining the effects of gage acceleration upon pressure measurements. One such method is described in Appendix A; namely, any response to transverse or vertical acceleration of the pitot-tube mount should be in the same sense (i. e., positive or negative) on both pitot gages. Careful examination of the gage records from Shots 6 and 12 show high-frequency disturbances, but there appears to be no phase relationship between disturbances observed on the p (pitot) and q (pitot) records. For this reason, it appears that the accuracy of the Project 1.10 pressure measurements is not significantly affected by gage-mount acceleration.

## Chapter 3

# OPERATIONS

### 3.1 SHOT 6

At the start of field operations, Shot 6 was scheduled after Shot 12. When this order was changed, it became necessary to remove terminal equipment from Shot 12 temporarily. This equipment (gage cables and the gages) was installed beginning 1 March 1955, and was ready on 15 March. No unusual difficulties were caused by weather or other conditions. The shot was fired on 22 March, and all terminal equipment was removed for reinstallation in Frenchman Flat on the same day. No post-test calibration was conducted, and gage installations were removed on 6 April.

### 3.2 SHOT 12

Work was begun on the installation of project equipment for Shot 12 on 12 February 1955. Cables were first laid to gage stations on the water line from Shelter F-712. A leak in the reservoir dike adjacent to the water line had flooded a portion of the cable trenches, and a few cables were of necessity laid in very wet trenches. During the laying of the cables and before all trenches were back-filled, a severe rain on 16-17 February flooded the entire area so that much of the cable-trench back-fill was severely waterlogged. Although special care had been taken in insulation of cable splices and although plastic-insulated cable was used in runs extending under the water line, some cases of cable leakage to ground resulted from the flood. The majority of these dried out eventually, but some undue leakage remained. Although this cable leakage alters the channel sensitivity, the procedure of pre- and post-test calibration eliminated any possible ambiguities in the data.

The open cable trenches for the desert and asphalt lines were almost completely filled by this flood, which was followed by a severe freeze, hampering efforts to pump out the water. Cables from Shelter F-223 to the desert and asphalt lines were first laid alongside these trenches and placed in the trenches only after a major part of the water had dried out.

In the meantime, terminal equipment had been installed in Shelters F-712 and F-223. The cable entries of the latter (underground) shelter were open at the time of the flood, but suitable earth fill was placed in the trenches and no damage resulted.

By 1 March, essentially all gages had been placed and circuits checked. (A few gage installations were delayed pending completion of construction.) At this time, it was necessary to remove all recorders, as well as a portion of the Wiancko equipment, for use on Project 1.7 (Shot 7) and on Shot 6.

All of the equipment was returned to the shelters by 28 March, calibration of all gage channels was performed, final installations were made, and a condition of readiness was attained by 4 April. Figures 3.1 and 3.2 show general pre-shot views of the Shot 12 desert and water lines, respectively. A more comprehensive view of the Shot 12 test area is shown in Figure 3.3.

Final check-outs and "button-up" were first made on 7 April, but were repeated on 14 April for the shot on 15 April. Records were recovered on 15 April, and post-test

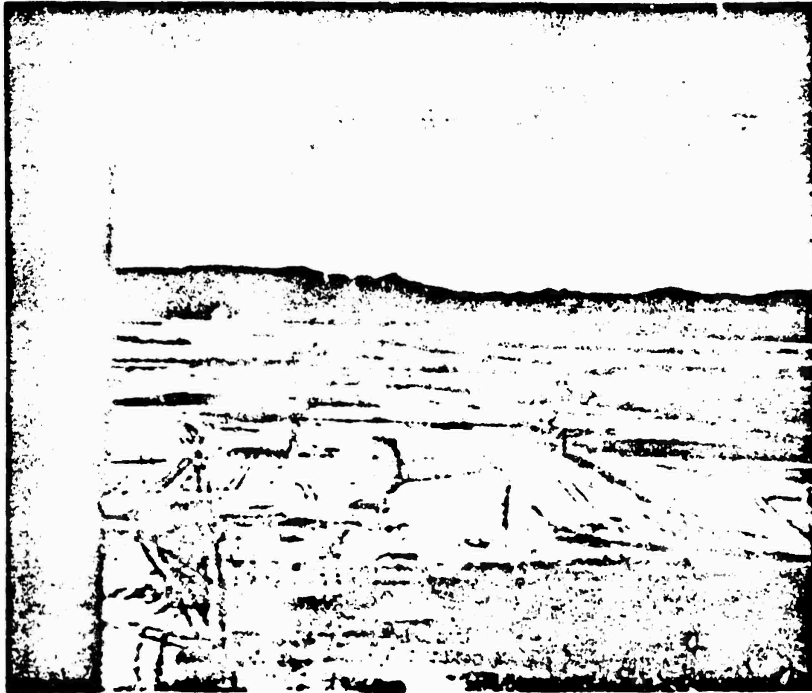


Figure 3.1 General view, Shot 12, desert line.

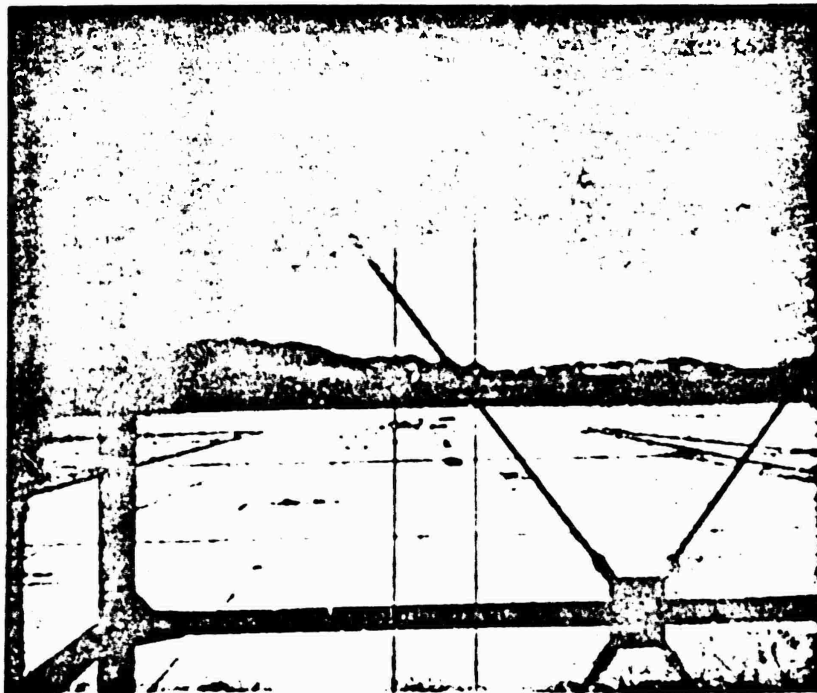
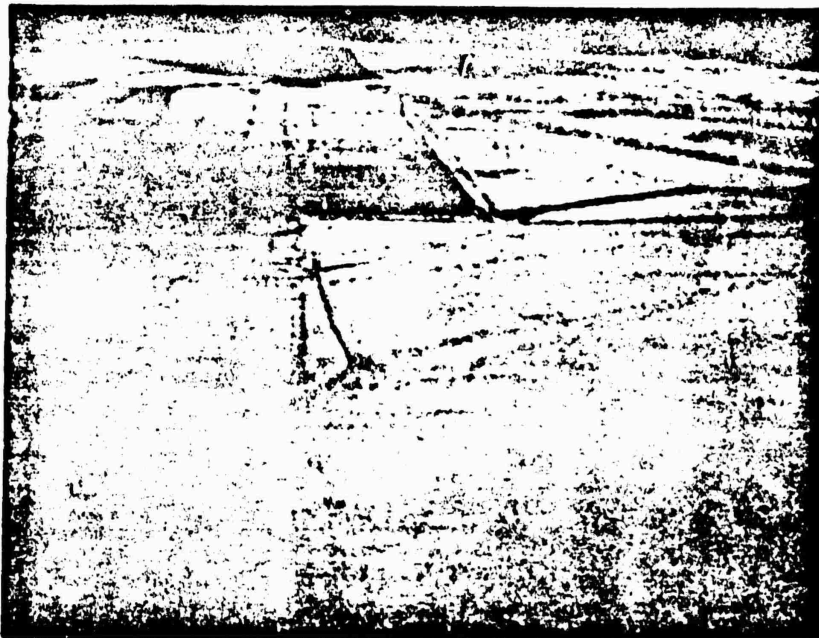


Figure 3.2 General view. Shot 12, water line.



**Figure 3.3 General view, Shot 12, test area.**

calibrations started on 18 April. Equipment was recovered on 20-21 April, and the field crew left the Nevada Test Site at that time.

CONFIDENTIAL

## Chapter 4

# RESULTS

### 4.1 INSTRUMENTATION PERFORMANCE

**4.1.1 Shot 6.** Of the 24 gage channels installed on this shot, two failed to produce records due to electrical gage failure at approximately zero time. This failure was apparently caused by the electromagnetic induction signal, in spite of the protective circuits used. Examination of one of these gages, a pitch gage, showed the potentiometer element completely burned out. The other, the differential pressure gage in one pitot tube, showed an arc-over of one coil, causing severe unbalance.

The remaining 22 channels gave completely satisfactory records, with no cable breaks or other trouble, except that the photographic records were slightly fogged by radiation. There is little evidence to show whether this was due to direct prompt, back-scattered prompt, or residual radiation, except that the steel cover plate near the ground surface was highly radioactive when the records were recovered at about H + 5 hours. Thus, the radiation fogging was very probably due to back-scattered prompt or residual radiation—the direct prompt component is virtually ruled out by the geometry (see Figure 2.5).

**4.1.2 Shot 12.** Of the 132 channels installed on Shot 12, four were lost at zero time due to gage damage similar to that experienced on Shot 6. In addition, the electrical failure of three of the four gages caused a combination of grounded connections which resulted in the loss of synchronization of one of the power oscillators in Shelter F-223 (rear shelter). This, in turn, introduced a beat signal on many of the 84 channels recorded at that shelter station. This beat, superimposed on the recorded traces, increased considerably the difficulty of reading the amplitudes and reproducing the wave forms of the records.

At the conclusion of the field operation, the recording equipment was set up at SRI, and the beat signal was purposely reproduced and studied. By replacing the gage which shorted to ground with a variable resistor and inductance, it was possible to establish indefinitely that the shorted gage gave rise to the beats. The laboratory tests also established the type and magnitude of the corrections which had to be applied to eliminate the effects of the variations in the zero-input traces (base lines) on the oscillograph records. As a result of these extensive laboratory tests and the care taken in correcting each trace, it is believed that the accuracy of the records was not seriously impaired.

The records from the three recorders located in the front shelter on Shot 12 (F-712) all showed radiation fogging, while those located in the rear shelter (F-223) showed no such effect. Also, it was apparent that the records from Camera 3 were more severely fogged than those from Cameras 1 and 2. This fact and reference to Figure 2.6 indicates that the fogging radiation probably entered the shelter through the access port, which was not sufficiently covered with sandbags. This supports the belief that the principal cause of radiation fogging was back-scattered prompt radiation.

The two beam devices of Project 3.2 (Channels 7 F3 and 9 F3) gave readable records with no severe ringing present. The records exhibit a gradual but large displace-

ment starting at zero time. This peculiar behavior and the significance of the measurement will be discussed in Chapter 5.

The data obtained for Project 3.6 have been turned over to the project officer.

## 4.2 DEFINITIONS OF MEASURED QUANTITIES

To clarify further discussions of the measurements obtained, it is worthwhile to define and explain, as follows, the measured quantities as used in this report (see also Table 4.1 for the symbols and notations used throughout).

TABLE 4.1 SYMBOLS AND NOTATION

$a$	speed of sound	$q^*$ (pitot)	pitot tube dynamic pressure corrected for pitch angle and/or Mach number
$A$	cross sectional area or projected area	$Q_n$	total thermal energy (normal)
$C$	sonic velocity	$R$	blast range
$C_d$	drag coefficient	$R_g$	gas constant
$F$	force	$Re$	Reynolds number
$G$	ground range	$t$	time
$K$	surface constant	$t_m$	time to second thermal maximum
$L$	length	$S$	rate of heat release per unit area
$M$	Mach number, $u/a$	$T$	absolute temperature $^\circ$
$p$	pressure $^\dagger$	$u$	velocity of flow
$p_o$	reservoir or stagnation pressure in continuous flow	$v$	velocity of shock front
$p_o'$	reservoir or stagnation pressure for shock wave flow	$W$	radiochemical yield
$p_t$	local reservoir pressure behind shock front measured by impact tube	$\alpha$	pitch angle, angle in plane defined by gage and ground zero
$p$ (pitot)	pressure measured at the static orifice of a pitot tube	$\gamma$	ratio of specific heats, $C_p/C_v$
$p^*$ (pitot)	pitot tube pressure corrected for pitch angle and/or Mach number	$\eta$	kinematic viscosity
$q$	dynamic pressure	$\mu$	absolute viscosity
$q$ (pitot)	dynamic pressure measured by a differential gage pitot tube instrument	$\rho$	mass density $^\dagger$

$^\dagger$  Without subscripts,  $p$ ,  $\rho$ , and  $T$  denote static pressure, static density, and static temperature, respectively.

In aerodynamic theory, under certain conditions, the air density may vary sufficiently to cause the flow behavior to depart appreciably from that predicted by the incompressible-fluid theory. The new flow behavior may be computed, in some cases, in terms of corrections or alterations to known incompressible fluid flow solutions; in other cases, entirely new types of flow solutions are necessary. For aerodynamics, compressibility effects generally become of engineering importance when speed changes (i. e., relative speeds) of the fluid, or of bodies relative to the fluid, become appreciably large compared with the speed of sound in the fluid (of the order one half or more).

Many of the characteristic features of the flow of a compressible fluid may be studied by investigating motion in one dimension. The general one-dimensional flow problem is to find the pressure  $p$ , velocity  $u$ , and density  $\rho$  distribution in a channel or stream tube. For steady flow of an isentropic compressible fluid, Bernoulli's equation becomes:

$$\frac{u^2}{2} + \frac{\gamma}{\gamma - 1} \frac{p_0}{\rho_0} \left( \frac{p}{p_0} \right)^{\gamma-1} = \frac{\gamma}{\gamma - 1} \frac{p_0}{\rho_0} \quad (4.1)$$

The pressure  $p_0$  is sometimes called the reservoir or stagnation pressure for the flow, since it corresponds to the pressure in a reservoir out of which flow would issue and accelerate isentropically (i. e., without change in entropy) to speed  $u$  and pressure  $p$ . In compressible fluid flow,  $p_0$  corresponds to the total head; however, Equation 4.1 indicates that for compressible flow, the dynamic pressure, defined by Equation 4.2, is no longer the difference between the local free stream pressure  $p$  and the total head  $p_0$ .

$$q = \frac{1}{2} \rho u^2 \quad (4.2)$$

At any point in a real fluid flow, a fictitious reservoir pressure, i. e., the stagnation pressure, may be defined if the flow at that point is imagined to be decelerated isentropically to zero speed. If the flow as a whole is nonisentropic, this reservoir pressure will vary from place to place in the flow.

The local speed of sound,  $a$ , is related to the pressure and density by the relation:

$$a^2 = \frac{p}{\rho} = \gamma R_g T \quad (4.3)$$

The ratio  $u/a$  is the Mach number ( $M$ ) of the flow. Since the speed of sound is an index of the compressibility of the gas, the Mach number will be an indication of the extent to which density changes may be important in the flow. In addition, the term  $u^2$  is proportional to the local kinetic energy of the flow, whereas  $a^2$  is proportional to the temperature  $T$  and therefore to the local thermal energy of the gas. Thus,  $M^2$  is proportional to the ratio between local kinetic and thermal energies in the gas.

The dynamic pressure,  $\frac{1}{2} \rho u^2$ , is related to the overpressure and to the Mach number very simply:

$$q = \frac{1}{2} \rho u^2 = \frac{\gamma p}{2} \frac{\rho u^2}{\gamma p} = \frac{\gamma p}{2} M^2 \quad (4.4)$$

For isentropic channel flow:

$$\frac{p_0}{p} = \left( 1 + \frac{\gamma - 1}{2} M^2 \right)^{\gamma/(\gamma-1)} \quad (4.5)$$

Combining Equations 4.4 and 4.5 yields the equation for the difference between reservoir or stagnation pressure and the overpressure:

$$\frac{p_0 - p}{q} = \frac{p_0 - p}{p} \frac{2}{\gamma M^2} = \frac{2}{\gamma M^2} \left[ \left( 1 + \frac{\gamma - 1}{2} M^2 \right)^{\gamma/(\gamma-1)} - 1 \right] \quad (4.6)$$

For values of  $M$  less than  $\sqrt{2/\gamma-1}$ , this may be expanded in a power series:



$$\frac{p_0 - p}{\gamma} = 1 + \frac{1}{4} M^2 + \frac{2 - \gamma}{24} M^4 + \frac{(2 - \gamma)(3 - 2\gamma)}{192} M^6 + \dots \quad (4.7)$$

Combining this last relation with Equation 4.4 yield:

$$\frac{2}{\gamma} \left( \frac{p_0 - p}{p} \right) = M^2 \left[ 1 + \frac{1}{4} M^2 + \frac{1}{40} M^4 + \frac{1}{1600} M^6 + \dots \right] \quad (4.8)$$

Therefore, for Mach numbers less than 1, an error of less than 0.1 percent is made if only three terms of the series are used. In an incompressible fluid, the Mach number must always be zero, since the speed of sound will be infinite. For this case, Equation 4.7 gives the usual result; i. e., the difference between stagnation and local pressure equals the dynamic pressure. Equation 4.7 is sometimes called the pitot-tube equation because of its application in correcting pitot-tube readings.

The foregoing discussion has been concerned with the continuous one-dimensional flow of a nonviscous fluid. It is now possible to proceed to consideration of normal shock waves, for which sudden and finite changes in velocity, pressure, and density can be shown to satisfy the basic equations of the motion. The analysis results in the familiar Rankine-Hugoniot relations for stationary shocks, which can be written:

$$\frac{p_2}{p_1} = \frac{(\gamma + 1) \rho_2 - (\gamma - 1) \rho_1}{(\gamma + 1) \rho_1 - (\gamma - 1) \rho_2} \quad (4.9)$$

Or:

$$\frac{\rho_2}{\rho_1} = \frac{u_1}{u_2} = \frac{(\gamma + 1) p_2 + (\gamma - 1) p_1}{(\gamma + 1) p_1 + (\gamma - 1) p_2} \quad (4.10)$$

These relations are different from the isentropic relation between pressure and density changes, which holds for continuous flow in a channel, and can be thought of as replacing it for this shock case. For a moving shock wave, which corresponds more exactly to the field-test condition, the Rankine-Hugoniot conditions lead to:

$$\frac{v^2}{a_1^2} = \frac{1}{2\gamma} \left[ (\gamma - 1) + (\gamma + 1) \frac{p_2}{p_1} \right] \quad (4.11)$$

And:

$$\frac{u}{v} = \frac{2 \left( \frac{p_2}{p_1} - 1 \right)}{(\gamma - 1) + (\gamma + 1) \frac{p_2}{p_1}} \quad (4.12)$$

Where:  $v$  = velocity of the shock front into the undisturbed medium  
 $a_1$  = sound velocity in that same medium

To determine the local dynamic pressure (see Equation 4.4) when the local reservoir pressure is not known, as behind a shock wave, for instance, an additional measurement must be made. An impact or total head tube is often used for this purpose. As stated previously, in subsonic flow it is generally assumed that the free-stream flow at Mach number  $M_1$  and pressure  $p$  is decelerated isentropically to the stagnation point of the impact tube; therefore, the pressure  $p_t$  measured there is the local reservoir pressure,  $p_0$ , of the flow.

The dynamic pressure is related to the difference between the total head and overpressure by Equation 4.7. Overpressure is often measured at an orifice located on the side of the total head tube (see Figure 2.7 for detailed diagram of pitot tube). Pitot tubes of standard design give satisfactory results up to the point where local shock waves begin to form around them.

When the free-stream Mach number  $M_1$  is greater than 1.0, the deceleration to the nose of the impact tube cannot be isentropic, for a shock wave must form in front of the impact tube as shown in Figure 4.1. Since the shock wave is normal immediately in front of such a body, the air on the streamline reaching the stagnation point has presumably passed through a normal shock wave. After the shock wave, the air may be assumed to decelerate isentropically to the stagnation point, so that the measured impact pressure  $p_t$  is equal to the reservoir pressure for the flow behind the normal shock  $p_0'$ . The change in reservoir pressure across the shock wave,  $p_0/p_0'$ , may be computed and, when combined with Equation 4.5, yields:

$$\frac{p}{p_0'} = \frac{p}{p_t} = \frac{\left[ \frac{2\gamma}{\gamma+1} M_1^2 - \frac{\gamma-1}{\gamma+1} \right]^{1/\gamma-1}}{\left[ \frac{\gamma+1}{2} M_1^2 \right]^{\gamma/\gamma-1}} \quad (4.13)$$

This equation relating the observed impact pressure and free stream static pressure is known as the supersonic pitot-tube equation. The equivalent relation below the speed of sound is given by Equation 4.5, which might be called the subsonic pitot-tube equation. At  $M = 1$ , Equations 4.5 and 4.13 become identical.

Overpressure measured in the vicinity of the impact tube in the supersonic case is in general not the free-stream static pressure; therefore the static orifice of a conventional pitot tube does not measure the free-stream static pressure, because the orifice is affected by the shock wave associated with the pitot tube. This factor will be discussed more fully in Section 4.3.1, which deals with corrections to be applied to pitot-tube measurements.

Because of the possible confusion between the definitions of dynamic pressure and overpressure (sometimes referred to as side-on or static pressure) and the measurements obtained with the pitot tube, a system of notation has been adopted for this report which may eliminate some of the ambiguity. The notation  $q(\text{pitot})$  and  $p(\text{pitot})$  will be used to designate the dynamic and free-stream pressure as measured by the gages mounted in the tube (see Figure 2.7), whereas  $q^*(\text{pitot})$  and  $p^*(\text{pitot})$  will designate these same quantities after correction for pitch angle of flow and/or Mach number.

### 4.3 RECORD READING AND DATA REDUCTION

Since the majority of the recorded traces were quite complex, it was found desirable to trace the records, one gage record per sheet, before any attempt was made to read amplitude versus time. Those traces which were disturbed by the beat were corrected for the resulting baseline shift in accordance with the laboratory tests described in Section 4.1.2.

After eliminating the beat disturbances where necessary, all records were smoothed to eliminate the unimportant traces and sharp peaks. Smoothing was effected upon those peaks which were of less than 10-msec duration at half-maximum. It was thought that

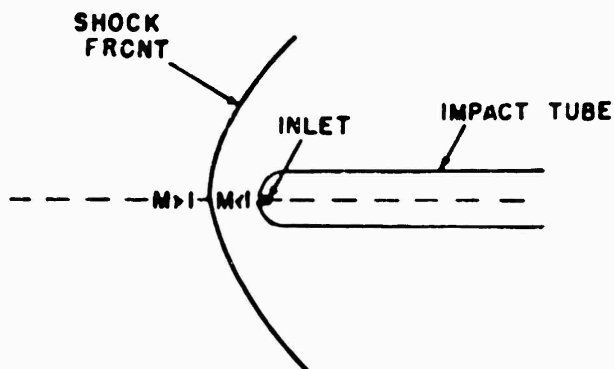


Figure 4.1 Schematic of detached shock and impact tube shock in front of impact tube for stationary flow.

this procedure would make record reading less ambiguous, while preserving the essential character of the gage measurement. The smoothed records were then read (inches deflection of trace versus time) using an electro-mechanical reader (Benson-Lehner "Oscar") which fed into an IBM card punch. These deflection-versus-time data cards, along with the appropriate calibration and pitot-tube correction cards for each gage, were processed by an IBM Card-Programmed Calculator (CPC). The final reduced data came out as corrected pressure-versus-time listings corresponding to each gage record. These listings were then plotted to yield data upon which the bulk of this report is based.

**4.3.1 Pitot-Tube Corrections.** The background with respect to the pitot-tube measurement of dynamic pressure and overpressure was presented in Section 4.2. To determine experimentally the Mach number and flow direction (pitch and yaw) corrections to be applied to pitot-tube measurements, the Cornell Aeronautical Laboratory (CAL), under contract to Sandia Corporation, undertook a testing program in their subsonic wind tunnel (Reference 6). A scale model of the pitot tube employed in the field was used; the results indicated that it was necessary to apply different correction factors to the  $p(\text{pitot})$  and  $q(\text{pitot})$  records. Unfortunately, since the CAL wind-tunnel flow did not exceed Mach 1.0, there is no information available on proper corrections to be applied to the several Teapot pressures measured in regions where the Mach number apparently exceeded unity. In addition, it must be emphasized that there is probably little evidence to support the assumption that pitot gage behavior under shock wave conditions (accelerated flow) will be the same as its behavior under conditions of continuous flow in a wind tunnel. The only available data indicate that, at low pressures, the peak  $q(\text{pitot})$  and  $p(\text{pitot})$  satisfy Rankine-Hugoniot relations.

Pitch-versus-time measurements were available at nearly every pitot-tube gage station for shots 6 and 12 (see Figures 2.1, 2.2, and 2.3); thus, to apply the proper corrections, it is necessary only to compute the Mach number as a function of time at each station. This calculation poses several problems.

Referring to Section 4.2, two ways of computing the instantaneous Mach number suggest themselves.

The first method is to substitute the pitot-tube overpressure measurement,  $p(\text{pitot})$ , and the ambient reservoir pressure,  $p_0$ , into the appropriate pitot-tube equation (Equation 4.5 for subsonic flow and Equation 4.13 for supersonic flow). This would yield the first approximation of the Mach number, which would then be used with the CAL data to correct  $p(\text{pitot})$  and  $q(\text{pitot})$ . Then, the new  $p(\text{pitot})$  values could be used to obtain a better approximation of  $M$  (using Equations 4.5 or 4.13, etc. This iterative method for obtaining  $M$  depends only on the assumption of steady adiabatic-flow.

The second method is to compute Mach number ( $M$ ) using Equation 4.4 with the measured  $q(\text{pitot})$  and  $p(\text{pitot})$ ; this is equivalent to using only the first term of the series in Equation 4.8 and assuming that  $p_0 - p$  is identical to  $q$ . This method is applied only to gas-phase subsonic flow; therefore, if the shock-wave flow contains suspended particulate matter and the conventional pitot-static tube is used for measurement, this computation will not yield the correct gas-phase Mach number.

Considering the first of these methods, it is obvious that the iterative nature of the calculation would be laborious, even for an electronic computer. Also, the CAL data include corrections for subsonic flow only. For these reasons, it was thought that the second method would be the more desirable. Figure 4.2 shows the errors resulting from using only the first term (instead of three terms) in the Equation 4.8 expansion. The maximum error in  $M$  is 10 percent which, for values of pitch angle less than 30 degrees, corresponds to about 3-percent maximum error in the correction to overpressure and impact pressure. Even the iterative method of Mach number calculation would contain some small errors. Thus, the second method was adopted for the Mach number determinations.

In some instances the Mach number as calculated from the pitot readings exceed unity; however, since the CAL tests (Reference 6) on the instrument were performed only for Mach numbers smaller than unity, it was necessary to consider this problem. As described previously, when the wind-tunnel Mach number exceeds unity a bow wave forms in the front of the pitot tube (Figure 4.1). However, the situation could be quite different for the case of a discontinuous, decaying flow encountered in the field measurement of blast. A short time would probably be required between initial shock arrival and the formation of the bow wave in front of the pitot tube. After the formation of the detached shock, the subsequent flow past the tube might tend to be much the same as for the wind-tunnel continuous-flow case.

In the absence of reasons for another course, it was decided to apply corrections corresponding to CAL data on highest Mach number (0.95) to all gage readings where the Mach number exceeded unity. Naturally this decision points up a serious weakness in the correction procedure, but it should be noted that the corrected  $p(\text{pitot})$  measurements at 3-foot height appear to agree well with surface level baffle gage measurements at the same stations. It is apparent that the CAL work has not solved the problem of correcting pitot-tube measurements for pitch, yaw, and Mach number, particularly for flows having Mach numbers larger than unity.

In addition, there is ample evidence to support the conclusion that the pitot-static tube used on Teapot was not an optimum design, even for subsonic flow behind a shock front. Reference 10 presents a pitot-static tube design which, when tested at subsonic and

transonic flow speeds and at large angles of pitch and yaw, requires corrections about one-tenth the magnitude of those indicated by the CAL work on a model of the Teapot field instrument. For supersonic flow behind the shock front, the free stream overpressure should be measured separate from and therefore undisturbed by the local shocks formed near the tube surface. It is recommended that the impact pressure (total head) be measured using a carefully designed supersonic tube in regions of flow where the Mach number is greater than unity, while the overpressure measurement should be made using a separate ground-level gage. The CAL report indicates that im-

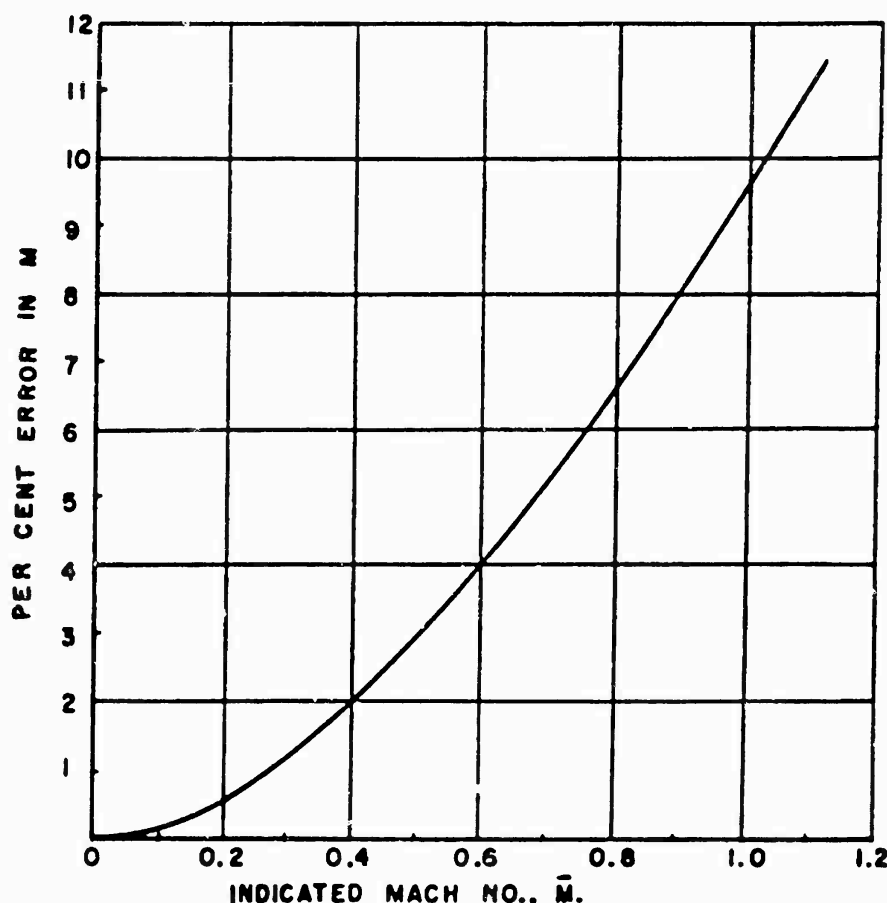


Figure 4.2 Error in M versus  $\bar{M}$ .

pitot-tube corrections (subsonic flow) are essentially independent of Mach number and straightforward to apply.

Also, since the pitot tube used registers a contribution to impact pressure due to particulate matter suspended in the flow, the apparent Mach number as calculated using Equations 4.4, 4.5, or 4.13 will be higher than the true Mach number of the air flow. This error will increase as the ratio of particle-to-air density increases. At present the corrections to be applied for this phenomenon are unknown; however, it can be assumed that such corrections are greatest at close-in stations. For this reason, it is apparent that pitot-tube gage corrections should be, as far as practical, independent of Mach number.

There has been some confusion as to the meaning of the pitch and yaw corrections as applied to field measurements. In the case of non-zero pitch and/or yaw, the axis of the measuring tube is inclined at an angle to the flow direction. Since the  $q$  (pitot) pressure is truly a vector quantity, the correction which is applied effectively yields the magnitude of  $q$  (pitot) in the direction of flow. This does not mean, as has sometimes been erroneously assumed, that the corrections give the component of  $q$  (pitot) in the direction of the tube axis. Thus, to obtain the component of  $q$  (pitot) along the tube axis, the corrected result must be multiplied by the cosine of the measured pitch and/or yaw angles.

#### 4.4 GAGE RECORDS

Figures 4.3 through 4.23 present the significant portions of the smoothed, corrected gage records obtained on Shot 12. The records are arranged first by blast line in the order water—desert—asphalt, then by ground range for each vertical gage height (surface level first). Auxiliary records (e. g., offset gage records) are introduced into the main sequence following the primary records at ground range. All records are plotted to the same time scale, and only two different pressure scales are used—the change in pressure scale is effected for all gage records beyond 2,000-foot ground range. Figures 4.24 through 4.27 include all usable smoothed and corrected records from Shot 6. The replotted gage records for these two shots represent the primary data upon which this report is based.

Reductions of tracings of the original gage records obtained on Shots 6 and 12 are presented in Appendix B. Also included with each record in the appendix is a corresponding smoothed record (dotted) from which were obtained the smoothed, corrected records of Figures 4.3 through 4.27.

#### 4.5 WAVE FORMS

Reference to the gage records of Figures 4.3 through 4.27 indicates that in a purely qualitative sense the forms of the records are pronouncedly different along the various blast lines and at the various ground ranges. Thus, before discussing the quantitative results of the measurements, wave forms will be investigated for evidence of effects of surface conditions and burst characteristics upon the blast wave.

4.5.1 Wave-Form Classification. The classification of the wave forms separates logically into two main groups: one dealing with the overpressure-versus-time measurements and the other with the dynamic pressure-versus-time data.

Examples of the overpressure (including  $p$  (pitot) and baffle-gage data) wave-form classifications are shown in Figures 4.28, 4.29, and 4.30. An explanation of the characteristics of each classification is included in Table 4.1. The  $q$  (pitot) wave-form classifications are illustrated in Figures 4.31 and 4.32, and their characteristics are explained in Table 4.2.

A number of  $q$  (pitot) gage records obtained on the water line were found to be incompatible with the best system of wave-form classification. Examples of these unclassified wave forms are shown in Figure 4.31. It was thought best to leave these forms unclassified rather than to change the entire system in an attempt to include them. As a matter of fact, the results obtained on the water line in the 2,000-to-2,500-foot ground range region are particularly strange and will be discussed more fully in Chapter 5.

TABLE 4.2 OVERPRESSURE WAVE-FORM CLASSIFICATION

Type	Description of Form	Relation to Previous Type	Examples
0	A sharp rise to a double-peaked maximum; peaks close together in time and approximately equal in amplitude.	In its ideal form it is the classical single-peaked shock wave, but is usually recorded as a double-peaked wave.	21B
1	A sharp rise to first low peak followed by either a plateau or a slight decay, then a higher second peak preceding the rapid decay. Time interval between first and second peaks can vary significantly; shock-like rises are evident.	The first low peak indicates the existence of a disturbance which travels faster than the main wave. This type is distinctly nonclassical.	22B; 23P3A; 2B; 3P3; 5B; 41B; 42B; 43P3
2	Same as Type 1 except that second peak is less than first.	The second peak has decayed to a lower value than the first and has become more rounded and less distinct. Second peak finally disappears.	25P3; 25P10; 45B; 46P10; 61B; 61P10
3	A first large rounded maximum followed by decay, then a later, usually smaller, second peak. Pressure rises may be slower than for Type 2.	The first peak of Type 3 has developed to become the rounded maximum, while the second peak has decreased in magnitude with respect to the first.	7R; 7P3; 7P10; 8P10
4	A long rise time, flat-topped form which exhibits a long decay time and much "hank".	The relatively sharp pressure rise of Type 3 has been replaced by a slow rise and the second peak has disappeared.	9B; 9P3; 47B; 47P3; 62B; 65P10
5	A pressure rise to a rounded plateau (desert) or peak (water) which is followed by a slow rise to a second higher peak.	The single-peaked hank form of Type 4 seems to develop a compression-type second peak, which may be the first indication of the return of the main wave.	9P10; 62B; 62P3; 62P10
6	A clear-cut double peak form with a rise to a plateau which slopes upward, then a shock rise to a peak.	This is clearly a cleaned-up Type 5, with the compression-type second peaks becoming shocks.	12B; 12P3; 38P10; 43B
7 (7R)*	A shock rise to a peak followed by either a slight gentle rise, a plateau, or, in later examples, a slow decay.	The second peak of Type 6 has overtaken the first peak, resulting in a wave form which is close to classic; sharp, single peak is not evident.	16P10; 17B; 29P3; 29B; 49P40
8 (8R)†	A classical wave form.	Sharp single-peaked form, followed by classic decay.	32P3; 32B

\* 7R refers to this form in region of regular reflection where a second (reflected) shock front is evident.

† 8R refers to classical wave form in region of regular reflection.

Overpressure wave-form classifications (Types 0 through 8) show a somewhat cyclic behavior. That is, Type 0 is very much like a classic form, and Types 1, 2, 3, and 4 indicate successively more-pronounced deviation from the classic. Types 5, 6, and 7 progressively lose the nonclassic characteristics. Finally, Type 8 is the classical wave form, observed at the last water-line station (3,000-foot) only. Types 3 and 5 can be considered as transition forms between the more-pure Types 2, 4, and 6.

The q (pitot) records fail to exhibit the same development as the overpressure results. Only for the later types (D, E, and F) are there corresponding static wave-form types, whereas Types B and C appear to have no definitive counterparts in the overpressure classifications (Table 4.2). Of course, the overpressure measurements were made at closer ground ranges on Shot 12 (750 and 1,000-foot) than were q (pitot) measurements (1,250-foot). Therefore, it should be expected that overpressure Types 2 and 3 would correspond closely to Types B and C; however, the similarity at best is rather tenuous.

**4.5.2 Effects of Surface Characteristics on Wave Form.** Comparisons of static overpressure wave forms over the various blast line surfaces for Shot 6 and Shot 12 are presented in Figures 4.33 through 4.35. One figure is devoted to each type of surface, in the order water—desert—asphalt.

The water-line wave-form summary shown in Figure 4.33 exhibits rather strange behavior. Measurements out to 1,500-foot ground range indicate the normal evolution of the precursor forms, i. e., Types 0, 1, and 2; however, at 2,000 feet, a wave form is observed (see Figure 4.5) which appears most similar to Type 1, but the rounded appearance suggests a Type 3 form. At greater ranges, the wave forms are approaching ideal. Thus, over the Shot 12 water line, the normal evolution breaks down near 2,000-foot range although the wave-form picture began in a conventional manner, and cleans up rapidly thereafter. In the wave forms of the offset-gage measurements (see layout in Figure 2.4), it is interesting that over the water there is some variation of wave form with distance from the main blast line at the same ground range; these aspects will be discussed more fully in Section 5.3.2.

For the desert surface (Figure 4.34), it is obvious that wave-form behavior is a sensitive function of surface characteristics. The two generalizations that can be made from the figure are: (1) wave-form evolution proceeds at a much slower rate (i. e., over a longer ground-range interval) over the desert than over the water; and (2) there is some indication (at 2,500 feet) that at one station the higher-gage records exhibit a more advanced form than does the surface-gage record. The Shot 6 wave-form data are plotted at ground range and gage heights which have been scaled to Shot 12 yield. The Shot 6 (approximately  $\frac{1}{3}$  yield of Shot 12) wave forms appear to fit into the picture quite well on this yield-scaling basis. The dashed line shown on Figure 4.34 indicates the approximate ground range extent of the Type 1 (classic precursor) wave form over the desert line on Shot 12. Further, it is significant that while a classic wave was observed at 3,000 feet on the Shot 12 water line, the data over the desert at this range are definitely nonclassical (Type 6). In addition, the wave forms even at 4,500 feet over the desert do not attain classical form. Thus, the properties of the surface may produce significant effects upon blast parameters in the pseudo-classical regime as well as in the precursor region.

The wave-form data from measurements over the asphalt surface are included in Figure 4.35; the behavior indicated is different from that encountered on the water or desert lines. In fact, the asphalt data require an even longer ground-range interval to go from Type 2 to Type 5 than the desert line. However, the presence of Type 7 forms at the 25- and 40-foot heights at 2,500 feet indicate that there is a pronounced height-of-gage effect upon wave forms over the asphalt surface. The Shot 6 data in Figure 4.35



(plotted at ranges scaled to Shot 12 yield) coincide well with those from Shot 12. As on the previous figure, the dashed line on Figure 4.35 shows the extent of the Type 1 wave form over the asphalt line. It is significant that the Type 1 form appears to disappear closer to ground zero on the asphalt line than over the desert. Thus, although the non-classical behavior persists to greater ranges over the asphalt, the precursor as a separate and distinct wave (Type 1 form) is observed at greater ranges over the desert surface.

The wave-form classifications of the q (pitot) gage records are summarized in Figure 4.36, which includes results from Shots 6 and 12 over three blast surfaces. The same general trends observed for overpressure wave forms hold for the q (pitot) classifications. The available data are admittedly meager, which necessarily makes any conclusions rather tentative. However, further reference will be made to the wave-form classifications in discussions of peak pressures and precursor phenomena.

**4.5.3 Effects of Gage Mount on Wave Form.** A comparison of the Shot 12 B 10 and P 10 gage records at same ground ranges in Figures 4.5, 4.8, 4.11, 4.12, 4.15, 4.20, and 4.21 reveals that these records may be quite dissimilar. Although the same type of Wiancko gage is used for both measurements, the method of gage mounting is quite different: the B 10 measurement originates from a baffle-mounted gage, while the P 10 gage is mounted at the static port of a pitot tube.

Comparisons can be made on the three Shot 12 blast lines at ground ranges of 1,500, 2,000, and 2,500 feet; only one record (asphalt line 49 P 10 at 2,500 feet) was lost. At the closest ground range (1,500 feet), the wave forms show poor agreement on all three blast lines; the B 10 records indicate negative pressures early in the pressure-time history—not recorded by the P 10 gages. At 2,000 feet, the wave forms are similar for the first 50 to 100 msec following blast arrival on the three blast lines; however, at this ground range, also, the B 10 records exhibit the negative pressure behavior referred to previously. Good agreement is evident at the water-line 2,500-foot station, and although the 9 B 10 and 9 P 10 (Figure 4.15) peak pressures correspond well, the wave-form comparison on the desert line at this ground range is poor.

To summarize, it must be concluded from available data that the baffle-type gage mount and the pitot-tube static port are not equivalent, particularly in the regions of high pressure and/or disturbed blast waves. If a thorough investigation is made of supersonic flow around obstacles of various shapes, this result is not completely unexpected. Such a survey of available wind-tunnel data reveals that for the baffle configuration used there is more tendency for complex interactions of secondary shocks in the vicinity of the gage port than is the case for a pitot tube. Also, it has been well established that secondary-shock interference effects are more pronounced for supersonic, rather than subsonic flows. It is probable that the negative pressures and other unpredicted variations in the B 10 records are caused by this secondary-shock interference phenomena.

These limitations imposed upon the baffle-type gage mount, coupled with the dearth of data on supersonic corrections for Mach number and pitch angle for the conventional pitot tube, point to the need for a comprehensive investigation to determine the best instrumentation for measuring the properties of high-pressure blast waves.

#### 4.6 TABLES OF RESULTS

The primary data obtained from all usable Project 1.10 records on Shots 6 and 12 are contained in Tables 4.5 through 4.14. Tables 4.11 through 4.14 include all Shot 6

data. All data are taken from the records after corrections for pitch and/or Mach number have been applied. The tables list the gage designation, ground range, gage height, arrival time, maximum pressure, time of maximum pressure, positive-phase duration (overpressure only) positive-phase impulse, and wave-form classification. Additional pressure data may be found by referring to the gage record tracings on Figures 4.3 through 4.27.

For comparison with other nuclear detonations, it is convenient to normalize the blast data for the Teapot shots to a common base by A-scaling. This procedure involves reducing data to a standard atmosphere at sea level for 1 kt of radiochemical yield. Conventional cube-root yield scaling is used in conjunction with Sachs' correction factors for atmospheric pressures and temperatures at burst heights. The following A-scaling relations apply:

$$\text{Pressure: } S_p = \frac{14.7}{p_0}$$

$$\text{Distance: } S_d = \left( \frac{p_0}{14.7} \right)^{1/3} \left( \frac{1}{W} \right)^{1/3}$$

$$\text{Time: } S_t = \left( \frac{T}{293} \right)^{1/2} \left( \frac{p_0}{14.7} \right)^{1/3} \left( \frac{1}{W} \right)^{1/3}$$

$$\text{Impulse: } S_i = \left( \frac{T}{293} \right)^{1/2} \left( \frac{14.7}{p_0} \right)^{2/3} \left( \frac{1}{W} \right)^{1/3}$$

Where:  $p_0$  = ambient pressure at burst height, psi  
 $T$  = absolute temperature at burst height, °C  
 $W$  = final total yield, kt.

The Sachs' burst-height correction factors have been specified for use by all test groups to permit direct comparison of the test results with those from previous test series which have been normalized in this manner. The pertinent normalizing factors for Shots 6 and 12 are listed in Table 4.4.

The A-scaled data for Teapot Shots 6 and 12 are presented with the as-read data in Tables 4.5 through 4.14.

TABLE 4.3 DYNAMIC PRESSURE WAVE - FORM CLASSIFICATIONS  
(See Figures 4.31 and 4.32)

Type	Description of Form	Relation to Previous Type	Examples
B	A shock rise to a broad single peak disturbance, characterized by serious pressure spikes.	Characteristic of previous type cannot be determined on basis of present data.	12Q2; 26Q3
C	A double-peaked form with second peak comparable in magnitude with the first. Exhibits shock-type initial rise in most cases.	Single prominent peak of Type B has become two distinct disturbances.	3Q2; 6Q2; 26Q16; 49Q3A; 49Q3
D	Transitional double-peaked form with longer initial rise-time; very hasty appearance and second peak somewhat indefinite.	More hasty than Type C; designation of the first and second peaks more tenuous.	8Q18; 8Q19; 47Q16A; 49Q3
E	More or less single-peaked form, characterized by a low-amplitude plateau having a slow, smooth rise at the beginning of record; very hasty.	The double-peaked form of Type D has become single-peaked; also, a low-amplitude plateau has been added to front of form.	8Q18; 8Q36; 49Q36; 49Q46A
F	A comparatively smooth record with shock rise followed by a plateau or slow steady rise, then another shock rise followed by a smooth decay. Corresponds to Type 6 (see Table 4.1).	The low-amplitude plateau of Type D has developed more definitely and is followed by a checked-up second peak.	12Q3A; 16Q16A; 21Q3
G	A smooth clean record possessing a shock rise followed by a relative smooth decay; slight rounding after initial rise represents deviation from classical form. Corresponds to Type 7 (see Table 4.1).	The checked-up second peak of Type F has become the initial and only peak. Some hush still present.	16Q16; 17Q3A; 23Q36; 28Q46
H	A classical wave form. Corresponds to Type 8 (see Table 4.1).	Strict single-peaked form, followed by classical decay.	22Q3

TABLE 4.4 A-SCALING FACTORS

Shot	Pressure ( $d_p$ )	Distance ( $d_d$ )	Time ( $d_t$ )	Impulse ( $d_i$ )
Shot 5	1.163	0.4983	0.4677	0.5440
Shot 12	1.122	0.3424	0.3418	0.2817

TABLE 4.6 OVERPRESSURE, SNOUT 13 WATER LINE

Gage	Ground Range	Gage Height	Arrival Time	Maximum Pressure	Time of Maximum Pressure	Positive Phase Duration	Positive Phase Impulse	Wave Form Type	Corr. for γ
	R	R	sec	psi	sec	sec	psi-sec		
As-Bored									
21BA	750	0	0.1105	170	0.135	0.50	11.0	1*	—
21B	1,000	0	0.1005	60.0	0.300	0.53	7.0	1	—
21P2A	1,250	3	0.343	70.3	0.300	0.43	0.10	1	Yes
26B	1,500	0	0.3045	34.5	0.400	0.44	4.30	2	—
26P2	1,500	3	0.273	41.0	0.300	0.42	4.64	3	Yes
26B10	1,500		0.270	37.3	0.300	0.55			
26P10	1,500	10	0.270	30.0	0.410	0.43	4.21	2	Yes
26P10A	1,750	10	0.403	25.1	0.500	0.30	3.00	7	Yes
27B	2,000	0	0.500	17.4	0.605	0.54	3.34	1	—
27P2	2,000	3	0.5045	20.1	0.605	0.50	2.03	1	Yes
27B10A	2,000		0.507	15.0	0.600	0.55			
27P10	2,000	10	0.5045	15.1	0.700	0.54	2.43	1	Yes
26P10	2,250	10	0.7455	15.2	0.775	0.57	3.17	0	No
26B	2,500	0	0.014	11.0	0.900	0.53	3.00	7	—
26P2	2,500	3	0.013	13.2	0.940	0.44	1.53	7	No
29B10	2,500		0.014	12.0	0.015	0.70			
29P10	2,500	10	0.013	12.0	0.900	0.55	3.00	7	Yes
29P20	2,500	20	0.013	12.7	0.015	0.53	3.11	7	No
29P40A	2,500	40	0.013	11.2	0.900	0.51	2.01	7	No
21P2	2,750	3	1.077	11.5	1.100	0.57	2.05	7	No
21BA	3,000	0	1.345	0.70	1.255	0.73	1.20	0	—
21P2	3,000	3	1.345	10.5	1.250	0.74	2.43	0	No
26P2X*	1,500	3	0.2715	45.3	0.300	0.45	4.44		No
26P2Y*	1,500	3	0.2075	25.5	0.425	0.23	3.05		No
29P2X*	2,500	3	0.063	14.7	0.065	0.37	1.55		No
29P2Y*	2,500	3	0.014	12.0	0.045	0.20	3.04		No
A-Sealed to 1 KT Radiochemical Release at Sea Level									
21BA	207	0	0.0405		0.0427	0.151	4.20	0*	—
21B	343	0	0.0470		0.0484	0.204	3.03	1	—
21P2A	430	1.0	0.0527		0.1025	0.144	1.05	1	Yes
26B	514	0	0.1253		0.1257	0.150	1.55	2	—
26P2	514	1.0	0.1275		0.1290	0.144	1.09	3	Yes
26P10	514	2.4	0.1205	43.3	0.1290	0.017			
26P10	514	2.4	0.1205		0.1401	0.147	1.01	2	Yes
26P10A	570	2.4	0.1005		0.1709	0.133	1.17	7	Yes
27B	505	0	0.2013		0.2370	0.105	1.27	1	—
27P2	505	1.0	0.2005		0.2370	0.101	1.50	1	Yes
27B10A	505	2.4	0.2005	17.0	0.2051	0.021			
27P10	505	2.4	0.2005		0.2303	0.105	1.21	1	Yes
26P10	775	2.4	0.2345		0.2640	0.105	1.21	0	No
29B	505	0	0.2194		0.2351	0.210	1.02	7	—
26P2	505	1.0	0.2121		0.2213	0.105	0.70	7	No
26B10	505	2.4	0.2194	14.0	0.2127	0.220			
26P10	505	2.4	0.2121		0.2201	0.223	1.17	7	Yes
26P20	505	5.0	0.2121		0.2127	0.213	1.10	7	No
29P40A	505	12.7	0.2121		0.2251	0.200	1.00	7	No
21P2	543	1.0	0.2001		0.2700	0.223	1.00	7	No
21BA	1,227	0	0.4250		0.4300	0.200	0.51	7	—
21P2	1,227	1.0	0.4254		0.4273	0.210	0.53	7	No
26P2X*	514	1.0	0.1270		0.1290	0.154	1.50		No
26P2Y*	514	1.0	0.1223		0.1453	0.113	1.17		No
29P2X*	505	1.0	0.2005		0.2200	0.092	0.53		No
29P2Y*	505	1.0	0.2124		0.2120	0.195	1.10		No

\* Gage offset from blast line; see Figure 2.4

TABLE 4.0 DYNAMIC PRESSURE, SHOT 13 WATER LOGS

Gage	Ground Range	Gage Height	Arrival Time	Maximum Pressure	Time of Maximum Pressure	Wave Form Type	Corr. for γ
	ft	ft	sec	psi	sec		
As-Read							
23Q3	1,250	3	0.253	273	0.273	B	Yes
25Q3A	1,500	3	0.3755	77.0	0.425	B*	Yes
25Q10A	1,500	10	0.375	63.0	0.440	C	Yes
26Q10	1,750	10	0.404	36.5	0.407	G	Yes
27Q3	2,000	3	0.5005	40.0	0.000		Yes
27Q10	2,000	10	0.5005	18.3	0.770		Yes
28Q10A	2,250	10	0.7445	5.0	0.772		No
29Q2A	2,500	3	0.9125	0.3	0.940	C	No
29Q10	2,500	10	0.9125	4.7	1.070	C	Yes
29Q25	2,500	25	0.913	4.0	0.515	G	No
29Q40A	2,500	40	0.913	5.05	0.925	G	No
31Q3	2,750	3	1.077	4.4	1.005	F	No
32Q3	3,000	3	1.945	2.1	1.247	M	No
25Q3X*	1,500	3	0.377	64.0	0.445	C	No
25Q3Y*	1,500	3	0.3725	200	0.400	B	No
29Q3X*	2,500	3	0.903	22.0	0.900	D	No
29Q3Y*	2,500	3	0.913	5.1	0.905	D	No
A-Sealed to 1 KY Radiochemical Reference at Sea Level							
23Q3	420	1.0	0.0072	200	0.0030		Yes
25Q3A	514	1.0	0.1203	05.3	0.1433	A	Yes
25Q10A	514	2.4	0.1251	70.0	0.1504	A	Yes
26Q10	599	2.4	0.1000	30.0	0.1009		Yes
27Q3	685	1.0	0.2007	54.4	0.2234		Yes
27Q10	685	2.4	0.2005	30.0	0.2038		Yes
28Q10A	770	2.4	0.2040	5.7	0.2030		No
29Q2A	854	1.0	0.2110	7.0	0.2201		No
29Q10	854	2.4	0.2110	5.2	0.2057		Yes
29Q25	854	5.0	0.2121	5.4	0.2127		No
29Q40A	854	12.7	0.2131	0.0	0.2103	E	No
31Q3	942	1.0	0.2061	5.0	0.2710	E	No
32Q3	1,027	1.0	0.4255	3.5	0.4303	E	No
25Q3X*	514	1.0	0.1200	02.3	0.1521	C	No
25Q3Y*	514	1.0	0.1277	200	0.1207	B	No
29Q3X*	854	1.0	0.2063	25.0	0.2250	D	No
29Q3Y*	854	1.0	0.2121	5.0	0.2003	D	No

\* Gages offset from blast line, see Figure 2.4.

TABLE 47 OVERPRESSURE, SHOT 13 DESERT LINE

Gage	Ground Range	Gage Height	Arrival Time	Maximum Pressure	Time of Maximum Pressure	Positive Phase Duration	Positive Phase Impulse	Wave Form Type	Corr. for y
	ft	ft	sec	psi	sec	sec	psi-sec		
As-Read									
1BA	750	0	0.104	164	0.133	>0.64	>14.3	1	—
2BA	1,000	0	0.145	88.8	0.234	0.361	8.38	1	—
3P3	1,250	3	0.203	36.3	0.365	0.256	3.06	1	Yes
5B	1,500	0	0.265	29.6	0.530	0.553	4.90	1	—
5P3	1,500	3	0.255	39.1	0.817	0.51	4.74	1	No
5B10	1,500	10	0.260			0.04			
5P10	1,500	15	0.263	27.8	0.830	0.55	4.30	1	Yes
5P19A	1,750	10	0.3455	12.8	0.730	0.641	3.90	1*	No
7B	2,000	0	0.4525	16.0	0.520	0.75	4.94	2	—
7P3	2,000	3	0.4625	18.5	0.830	0.78	5.51	2	Yes
7B10	2,000	10	0.455	21.5	0.560	0.11			
7P10	2,000	10	0.4645	15.8	0.530	0.67	4.30	3	Yes
5P16A	2,250	10	0.599	13.0	0.600	0.53	3.90	3	Yes
5B	2,500	0	0.701	7.44	0.645	0.77	3.74	4	—
5P3	2,500	3	0.780	5.0	0.865	0.5	2.30	4	Yes
5B10	2,500	10	0.785	0.0	0.930	0.44			
5P10	2,500	10	0.783	11.0	0.945	0.77	3.60	5	Yes
5P25	2,500	25	0.7885	5.5	0.865	0.76	3.11	5	Yes
5P40A	2,500	40	0.7815	7.9	1.030	0.71	2.74	5	Yes
11P3	2,750	3	0.907	7.25	1.150	0.77	2.76	5	No
12B	3,000	0	1.192	0.0	1.295	0.66	2.20	5	—
12P3	3,000	3	1.153	9.25	1.297	0.84	3.47	6	No
12P10	3,000	10	1.194	7.06	1.295	0.53	2.36	6	No
12B	3,500	0	1.5115	7.17	1.636	0.66	2.30	6	—
15P10	3,500	10	1.910	7.45	1.630	0.53	2.13	6	No
16P10	4,000	15	1.995	5.50	2.010	0.56	1.94	7	No
17B	4,500	0	2.3575	4.57	2.400	0.50	1.97	7	—
17P3	4,500	3	2.305	4.10	2.205	0.50	1.65	7	No
A-Sealed to 1 KT Radiochemical Release at Sea Level									
1BA	257	0	0.5355	106	0.6455	>0.210	>5.43	2	—
2BA	343	0	0.6500	77.7	0.9760	0.1234	3.61	2	—
3P3	430	1.0	0.6990	41.0	0.1340	0.0904	1.17	2	Yes
5B	514	0	0.9905	33.5	0.1777	0.1090	1.53	2	—
5P3	514	1.0	0.9905	44.3	0.1757	0.205	1.51	2	No
5B10	514	3.4	0.9910			0.014			
5P10	514	3.4	0.9910	31.5	0.1777	0.190	1.64	2	Yes
5P16A	599	3.4	0.1104	15.3	0.3495	0.3101	1.40	2	No
7B	685	0	0.1547	16.1	0.1777	0.307	1.89	3	—
7P3	685	1.0	0.1547	21.1	0.1813	0.267	2.10	3	Yes
7B10	685	3.4	0.1563	24.5	0.1814	0.030			
7P10	685	3.4	0.1560	17.0	0.1813	0.329	1.06	3	Yes
5P16A	770	3.4	0.3047	14.7	0.2324	0.284	1.51	3	Yes
5B	856	0	0.3050	8.4	0.3025	0.263	1.06	4	—
5P3	856	1.0	0.3050	10.3	0.3264	0.37	1.29	4	Yes
5B10	856	3.4	0.3057	0.1	0.3145	0.164			
5P10	856	3.4	0.3073	13.0	0.3230	0.263	1.37	5	Yes
5P25	856	0.0	0.3095	10.0	0.3264	0.260	1.34	5	Yes
5P40A	856	13.7	0.3705	0.0	0.3405	0.343	1.05	5	Yes
11P3	943	1.0	0.3374	5.2	0.3031	0.346	1.06	6	No
12B	1,027	0	0.4074	5.1	0.4426	0.294	0.91	6	—
12P3	1,027	1.0	0.4074	9.3	0.4433	0.287	0.94	6	No
12P10	1,027	3.4	0.4081	5.0	0.4430	0.280	0.90	6	No
15B	1,190	0	0.5305	0.1	0.5555	0.294	0.84	6	—
15P10	1,190	3.4	0.5503	5.4	0.5571	0.284	0.91	6	No
16P10	1,370	3.4	0.6910	0.33	0.6070	0.333	0.74	7	No
17B	1,541	0	0.5160	3.17	0.6203	0.304	0.64	7	—
17P3	1,541	1.0	0.5155	4.74	0.6185	0.333	0.93	7	No

TABLE 4.8 DYNAMIC PRESSURE, SHOT 12 DEBERT LINE

Gage	Ground Range	Gage Height	Arrival Time	Maximum Pressure	Time of Maximum Pressure	Wave Form Type	Corr. for $\gamma$
	ft	ft	sec	psi	sec		
As-Band							
3Q3	1,350	3	0.306	136	0.345	C	Yes
8Q3	1,500	3	0.307	100	0.278	C	No
8Q10	1,500	10	0.309	100	0.300	D	Yes
6Q10	1,750	10	0.347	145.0	0.416	D	No
7Q3	2,000	3	0.453	63.8	0.510	D	Yes
7Q10	2,000	10	0.450	67.3	0.526	E	Yes
8Q10A	2,250	10	0.600	30.0	0.640	E	Yes
8Q2A	2,500	3	0.781	13.0	0.875	E	Yes
8Q10	2,500	10	0.784	21.9	0.838	E	Yes
8Q30	2,500	30	0.7808	10.8	0.870	E	Yes
8Q40	2,500	40	0.792	14.3	1.000	E	Yes
11Q3	2,750	3	NR	NR	NR	NR	NR
13Q2A	3,000	3	1.1015	1.0%	1.207	F	No
13Q10	3,000	10	NR	NR	NR	NR	NR
16Q10A	3,500	10	1.010	1.30	1.626	F	No
16Q10	4,000	10	1.006	0.75	2.010	G	No
17Q2A	4,500	3	2.508	0.47	2.415	G	No
A-Sealed to 1 KT Radiological Release at Sea Level							
3Q3	420	1.0	0.0701	306	0.1170	C	Yes
8Q3	514	1.0	0.0813	304	0.0860	C	No
8Q10	514	2.4	0.0910	181	0.1026	D	Yes
6Q10	500	2.4	0.1106	104.8	0.1401	D	No
7Q3	686	1.0	0.1546	71.9	0.1743	D	Yes
7Q10	686	2.4	0.1640	52.8	0.1829	E	Yes
8Q10A	770	2.4	0.2061	26.0	0.2213	E	Yes
8Q2A	856	1.0	0.2000	18.4	0.2091	E	Yes
8Q10	856	2.4	0.2080	24.8	0.2196	E	Yes
8Q30	856	8.0	0.2096	22.4	0.2253	E	Yes
8Q40	856	12.7	0.2707	10.1	0.2736	E	Yes
11Q3	943	1.0	NR	NR	NR	NR	NR
13Q2A	1,027	1.0	0.4073	1.23	0.4423	F	No
13Q10	1,027	2.4	NR	NR	NR	NR	NR
16Q10A	1,190	2.4	0.6663	1.57	0.6664	F	No
16Q10	1,370	2.4	0.6810	0.88	0.6870	G	No
17Q2A	1,541	1.0	0.6166	0.53	0.8264	G	No

NR No record obtained.

TABLE 4-0 OVERPRESSURE, SHOT 13 ASPHALT LINE

Gage	Ground Range	Gage Height	Arrival Time	Maximum Pressure	Time of Maximum Pressure	Positive Phase Duration	Positive Phase Impulse	Wave Form Type	Corr. for γ
	ft	ft	sec	psi	sec	sec	psi-sec		
As-Read									
41BA	750	0	0.003	103	0.135	0.07	10.0	1	—
42BA	1,500	0	0.1335	78.1	0.230	>0.70	-0.2	1	—
43P3	1,500	3	0.183	36.8	0.370	0.48	5.00	1	Yes
46B	1,500	0	0.341	18.1	0.370	0.70°	4.1°	2	—
46P3	1,500	2	0.341	21.3	0.375	0.68°	4.0°	2	No
46B10	1,500		0.344	21.3	0.370	0.07			
46P10	1,500	10	0.3445	22.4	0.360	0.54	4.00	3	Yes
46P10	1,750	10	0.324	19.4	0.360	0.5°	4.5°	2	Yes
47B	2,000	0	0.418	12.0	0.440	1.0°	0.0°	4	—
47P3	2,025	2	0.418	14.3	0.455	—†	—†	4	Yes
47B10	2,000		0.421			0.27			
47P10	2,000	10	0.421	12.4	0.400	—†	—†	4	Yes
48P10	2,250	10	0.5205	10.2	0.505	1.2°	2.3°	4	No
49B	2,500	0	0.674	0.00	0.730	0.75	2.34	4	—
49P2	2,500	2	0.674	8.0	0.730	1.2°	4.2°	4	Yes
49B10	2,500	10	0.675	6.35	0.700	—†	—†	4	—
49P25	2,500	25	0.680	6.0	0.705	0.48	2.65	7	Yes
49P40	2,500	40	0.685	0.00	0.735	1.2°	2.0°	7	Yes
51F2A	2,750	2	0.843	0.30	0.885	0.0°	2.30°	4	No
52B	2,000	0	1.034	2.95	1.065	0.7	1.65	8	—
52P3	2,500	2	1.035	4.57	1.200	1.1°	2.0°	8	No
A-Scaled to 1 KT Radiochemical Balance at Sea Level									
41BA	367	0	0.0018	367	0.0461	0.125	4.12	1	—
42BA	343	0	0.0455	88.4	0.0705	>0.230	-2.1	1	—
43P3	430	1.0	0.0835	30.3	0.1265	0.164	1.94	1	Yes
46B	514	0	0.0834	30.0	0.0923	0.260°	1.0°	2	—
46P3	514	1.0	0.0834	34.1	0.0940	0.223°	1.0°	2	No
46B10	514	2.4	0.0834	34.0	0.0923	0.034			
46P10	514	2.4	0.0835	30.4	0.0900	0.191	1.55	3	Yes
46P10	500	2.4	0.1107	15.0	0.1230	0.27°	1.7°	2	Yes
47B	685	0	0.1429	15.7	0.1504	0.55°	2.5°	4	—
47P3	685	1.0	0.1429	10.1	0.1555	—†	—†	4	Yes
47B10	685	2.4	0.1430			0.002			
47P10	685	2.4	0.1430	15.2	0.1572	—†	—†	4	Yes
48P10	770	2.4	0.1644	11.5	0.2034	0.41°	1.0	4	No
49B	864	0	0.2304	7.5	0.3405	0.250	0.89	4	—
49P3	864	1.0	0.2304	9.0	0.3461	0.44°	1.0°	4	Yes
49B10	864	2.4	0.2301	7.2	0.3410	—†	—†	4	—
49P25	864	2.00	0.2303	7.0	0.3583	0.72	1.37	7	Yes
49P40	864	12.7	0.2370	7.7	0.3475	0.44°	1.4°	7	Yes
51F2A	942	1.0	0.3061	7.2	0.3925	0.21°	0.94°	4	No
52B	1,027	0	0.3534	4.44	0.3540	0.24	0.55	5	—
52P3	1,027	1.0	0.3527	5.31	0.4443	0.26°	0.86°	5	No

\* Data uncertain due to apparent instrumentation difficulties.

† Gage record does not return to zero



TABLE 4.10 DYNAMIC PRESSURE, SHOT 12 ASPHALT LANE

Gage	Ground Range	Gage Height	Arrival Time	Maximum Pressure	Time of Maximum Pressure	Wave Form Type	Corr. for γ
	ft	ft	sec	psi	sec		
As-Read							
43Q3A	1,350	2	0.100	300	0.340	C	Yes
43Q3A	1,500	2	0.240	92.0	0.300	C	No
43Q10	1,500	10	0.340	90.0	0.440	C*	Yes
43Q10A	1,750	10	0.220	50.0	0.430	D	Yes
47Q3A	2,000	2	0.410	20.0	0.430	D	Yes
47Q10A	2,000	10	0.423	17.3	0.700	D	Yes
48Q10A	2,200	10	0.0.95	10.0	0.640	D	No
49Q3	2,500	2	0.616	12.1	0.930	D	Yes
49Q10	2,500	10	0.379	10.3	0.900	E	Yes
49Q20	2,500	20	0.400	10.3	1.000	E	Yes
49Q40A	2,500	40	0.000	0.30	1.010	E	Yes
51Q3	2,750	2	NR	NR	NR	NR	NR
53Q3A	2,000	2	1.034	0.00	1.100	C	No
A-Sealed to 1 KT Radiological Release at Sea Level							
43Q3A	420	1.0	0.0030	234	0.1103	C	Yes
43Q3A	514	1.0	0.0041	104.0	0.0000	C	No
43Q10	514	2.4	0.0041	102.0	0.1504	C*	Yes
43Q10A	500	2.4	0.1111	57.3	0.1453	D	Yes
47Q3A	605	1.0	0.1020	23.0	0.1407	D	Yes
47Q10A	605	2.4	0.1400	10.0	0.2203	D	Yes
48Q10A	770	2.4	0.1844	23.4	0.2100	D	No
49Q3	805	1.0	0.2217	14.0	0.2170	D	Yes
49Q10	805	2.4	0.2251	17.3	0.2070	E	Yes
49Q20	805	6.0	0.2252	17.3	0.2410	E	Yes
49Q40A	805	12.7	0.2270	5.00	0.2452	E	Yes
51Q3	942	1.0	NR	NR	NR	NR	NR
53Q3A	1,027	1.0	0.2034	0.00	0.2002	C	No

NR No record obtained.

TABLE 4.11 OVERPRESSURE, SHOT 6 DESERT LANE

Gage	Ground Range	Gage Height	Arrival Time	Maximum Pressure	Time of Maximum Pressure	Positive Phase Duration	Positive Phase Impulse	Wave Form Type	Corr. for γ
	ft	ft	sec	psi	sec	sec	psi-sec		
As-Read									
01B	1,300	0	0.2045	14.1	0.000	0.37	2.54	2	—
01P10A	1,300	10	0.200	10.4	0.000	0.201	1.00	2	No
02B	1,600	0	0.0120	10.0	0.000	0.053	2.11	4	—
02P10A	1,600	10	0.010	12.0	0.070	0.053	2.42	5	Yes
03B	2,000	0	0.000	11.0	0.000	0.470	1.00	0	—
03P10A	2,000	10	0.0000	12.3	0.000	0.400	2.03	0	Yes
A-Sealed to 1 KT Radiological Release at Sea Level									
01B	620	0	0.1045	10.4	0.2703	0.173	1.20	2	—
01P10A	620	4.0	0.1000	22.0	0.2720	0.1020	1.00	2	No
02B	792	0	0.2000	12.0	0.2110	0.2110	1.10	4	—
02P10A	790	4.0	0.2072	10.9	0.2134	0.2110	1.20	0	Yes
03B	941	0	0.4004	12.3	0.4200	0.2200	2.01	0	—
03P10A	941	4.0	0.4007	14.3	0.4200	0.2204	1.10	0	Yes

TABLE 4.12 DYNAMIC PRESSURE, SHOT 6 DESERT LINE

Charge	Ground Range	Charge Height	Arrival Time	Maximum Pressure	Time of Maximum Pressure	Wave Form Type	Corr for a
	ft	ft	sec	psi	sec		
As-Read							
01Q10	1,300	10	0.400	100.0	0.550	C	No
02Q10	1,650	10	NR	NR	NR	NR	NR
03Q10A	2,000	10	0.0006	3.2	0.028	F	Yes
A-Scaled to 1 KT Radiochemical Release at Sea Level							
01Q10	034	4.0	0.1071	127.7	0.2572	C	No
02Q10	792	4.0	NR	NR	NR	NR	NR
03Q10A	961	4.0	0.4067	3.7	0.0320	F	Yes

NR No record obtained.

TABLE 4.13 OVERPRESSURE, SHOT 6 ASPHALT LINE

Charge	Ground Range	Charge Height	Arrival Time	Maximum Pressure	Time of Maximum Pressure	Positive Phase Duration	Positive Phase Impulse	Wave Form Type	Corr. for a
	ft	ft	sec	psi	sec	sec	psi-sec		
As-Read									
04B	1,300	0	0.343	10.1	0.400	0.400	2.71	2	—
04P10A	1,300	10	0.3485	21.0	0.010	0.40	2.10	2	Yes
06BA	1,650	0	0.0000	7.17	0.030	0.043	2.25	4	—
06P10	1,650	10	0.021	7.63	0.045	0.047	2.25	4	Yes
08B	2,000	0	0.7550	4.23	0.01	0.070	1.52	4	—
08P10	2,000	10	0.7575	0.30	0.010	0.070	1.90	4	Yes
A-Scaled to 1 KT Radiochemical Release at Sea Level									
04B	034	0	0.1004	11.7	0.1004	0.2320	1.47	2	—
04P10A	034	4.0	0.1620	25.4	0.2000	0.234	1.72	2	Yes
06BA	792	0	0.3462	0.34	0.2047	0.3033	1.22	4	—
06P10	792	4.0	0.3462	0.07	0.3017	0.3033	1.22	4	Yes
08B	961	0	0.2020	4.01	0.420	0.2004	0.02	4	—
08P10	961	4.0	0.2042	7.42	0.4236	0.2000	1.00	4	Yes

TABLE 4.14 DYNAMIC PRESSURE, SHOT 6 ASPHALT LINE

Charge	Ground Range	Charge Height	Arrival Time	Maximum Pressure	Time of Maximum Pressure	Wave Form Type	Corr for a
	ft	ft	sec	psi	sec		
As-Read							
06Q10	1,300	10	0.352	07.4	0.540	C	Yes
08Q10A	1,650	10	0.532	3.01	0.045	D	Yes
06Q10A	2,000	10	0.7190	4.10	0.043	D	Yes
A-Scaled to 1 KT Radiochemical Release at Sea Level							
06Q10	034	4.0	0.1046	70.4	0.2520	C	Yes
08Q10A	772	4.0	0.2400	5.83	0.2110	D	Yes
06Q10A	961	4.0	0.2032	4.06	0.0040	D	Yes

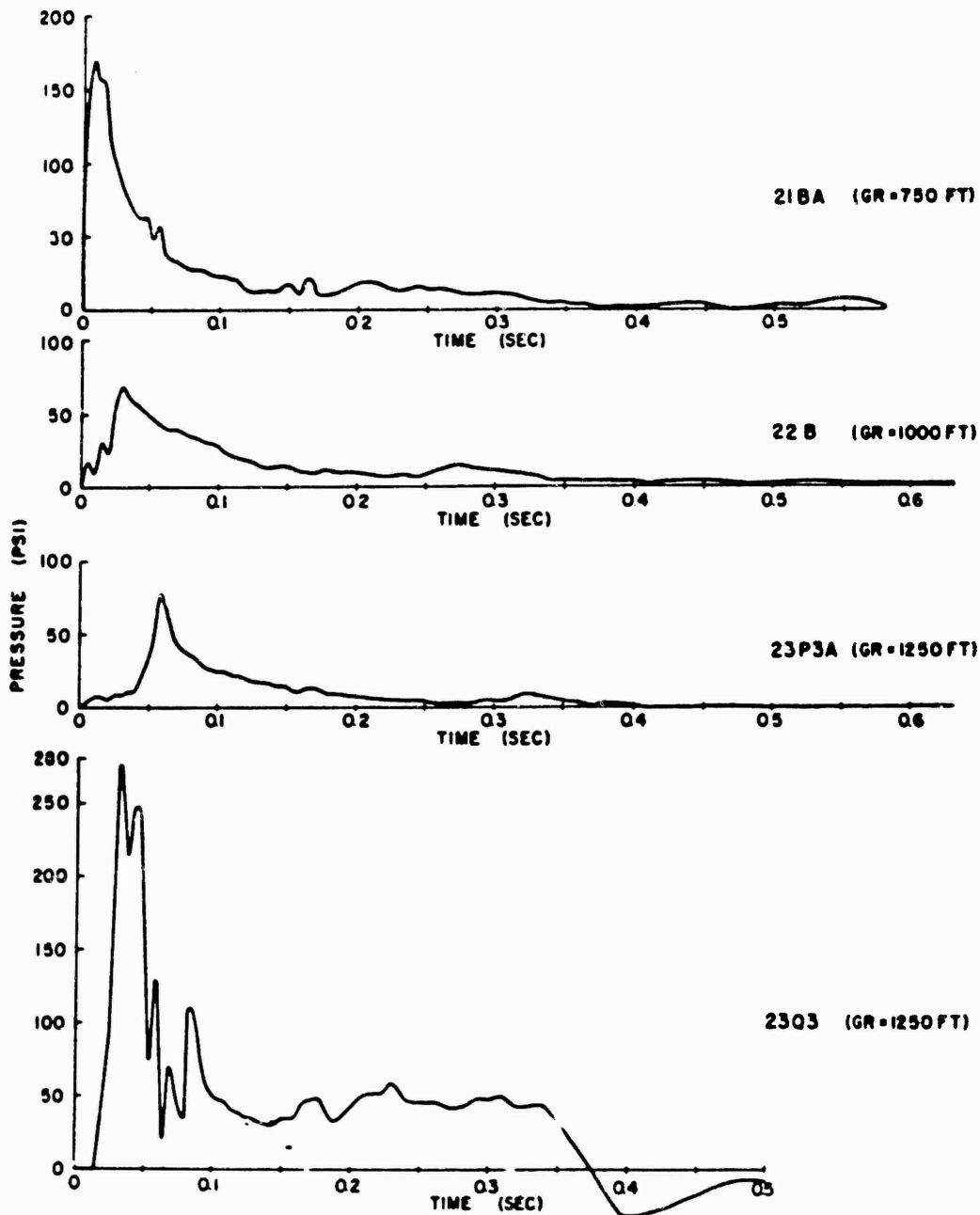


Figure 4.3 Pressure versus time, water line, Shot 12  
(ground range = 750 feet - 1,250 feet).

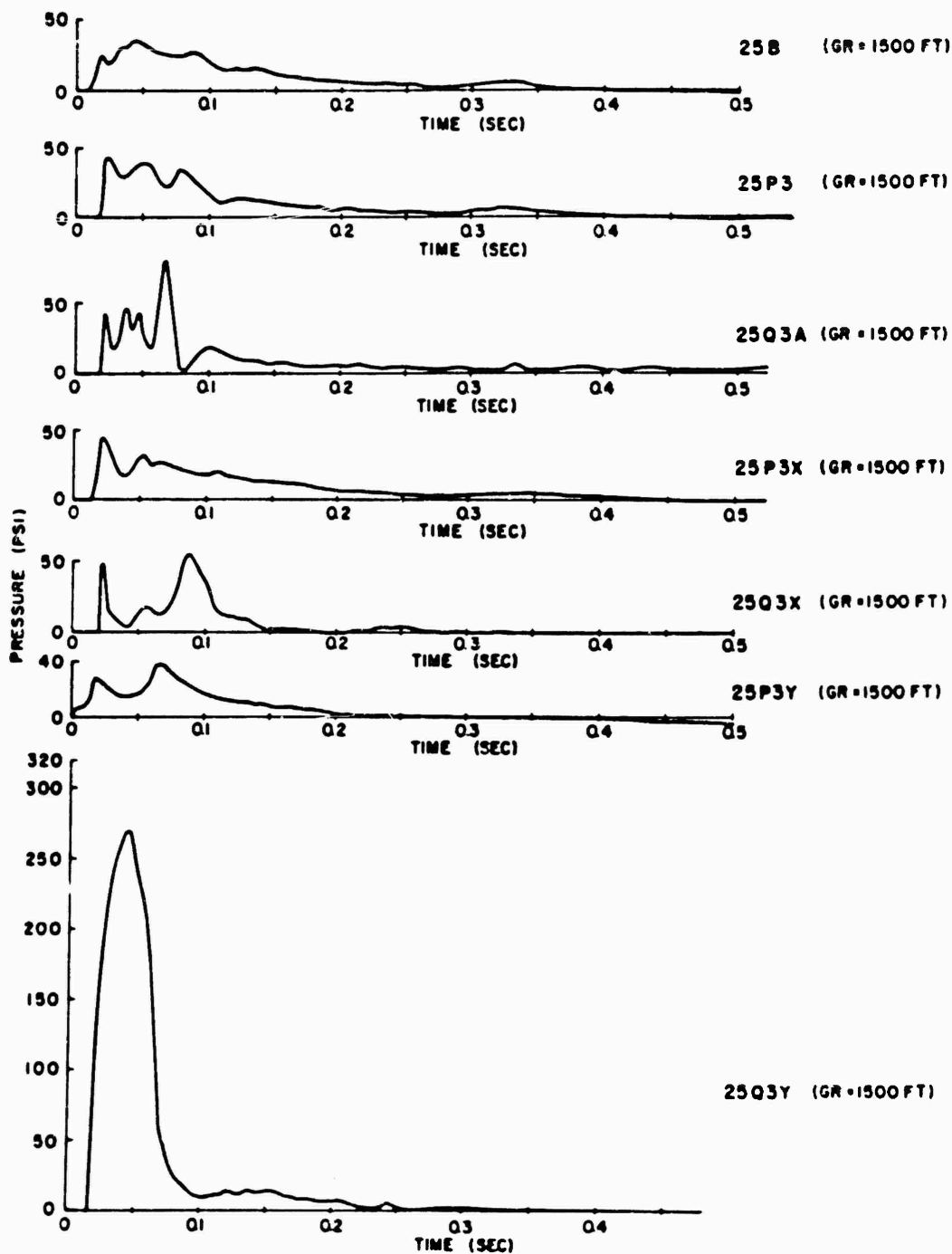


Figure 4.4 Pressure versus time, water line, Shot 12  
(ground range = 1,500 feet).

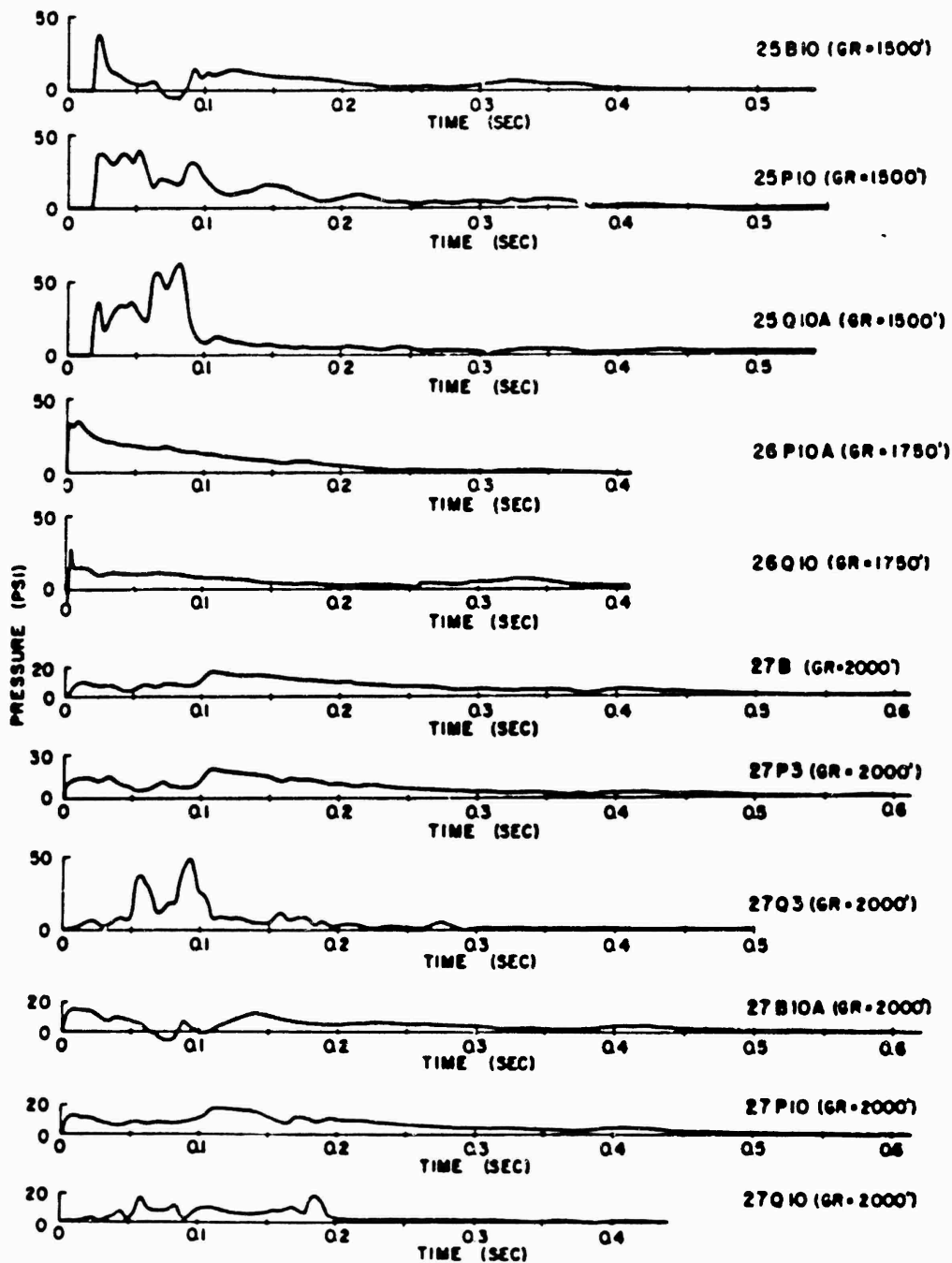


Figure 4.5 Pressure versus time, water line, Shot 12  
(ground range = 1,500 feet-2,000 feet).

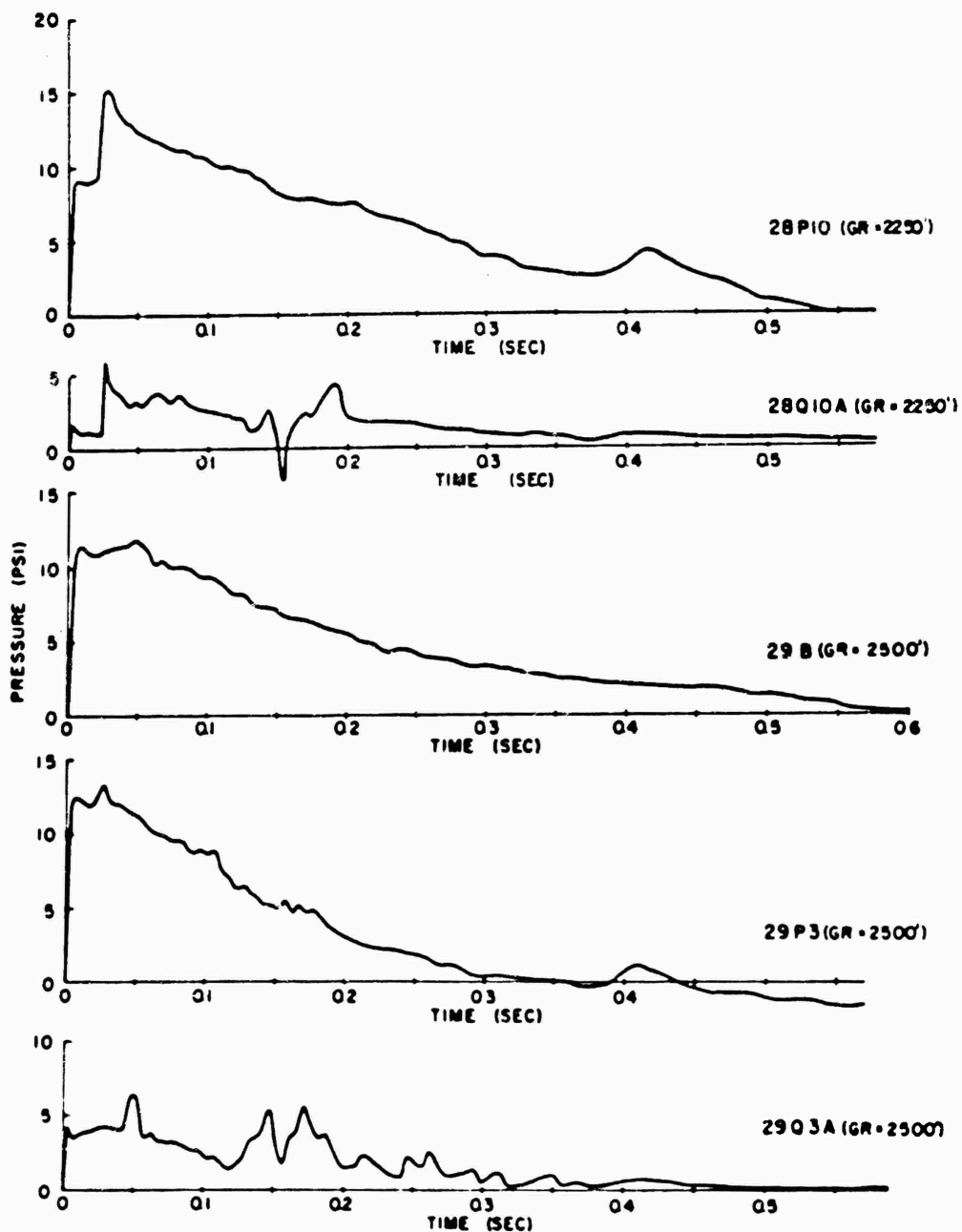


Figure 4.6 Pressure versus time, water line, Shot 12, (ground range = 2,250 feet-2,500 feet).

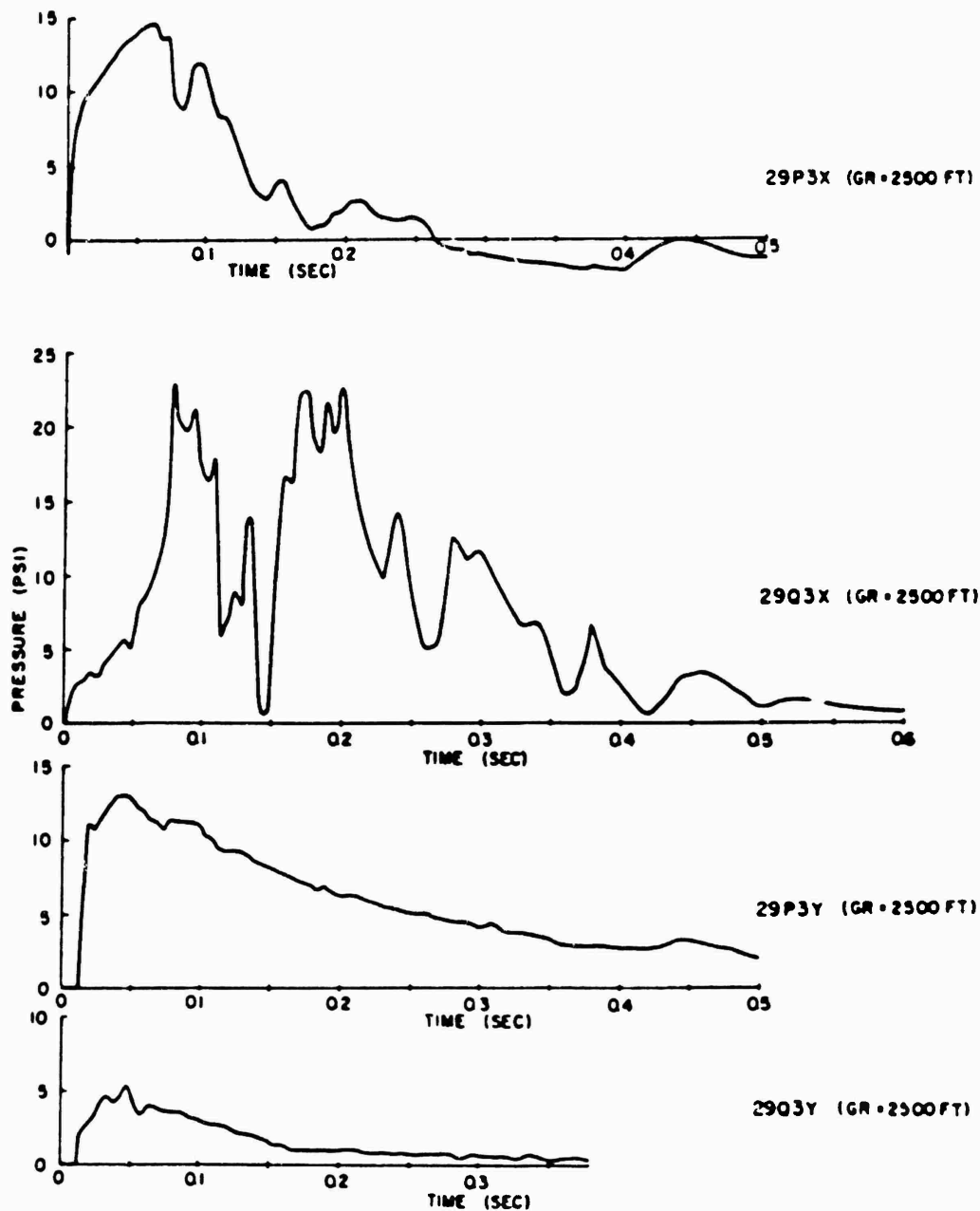


Figure 4.7 Pressure versus time, water line, Shot 12  
(ground range = 2500 feet).

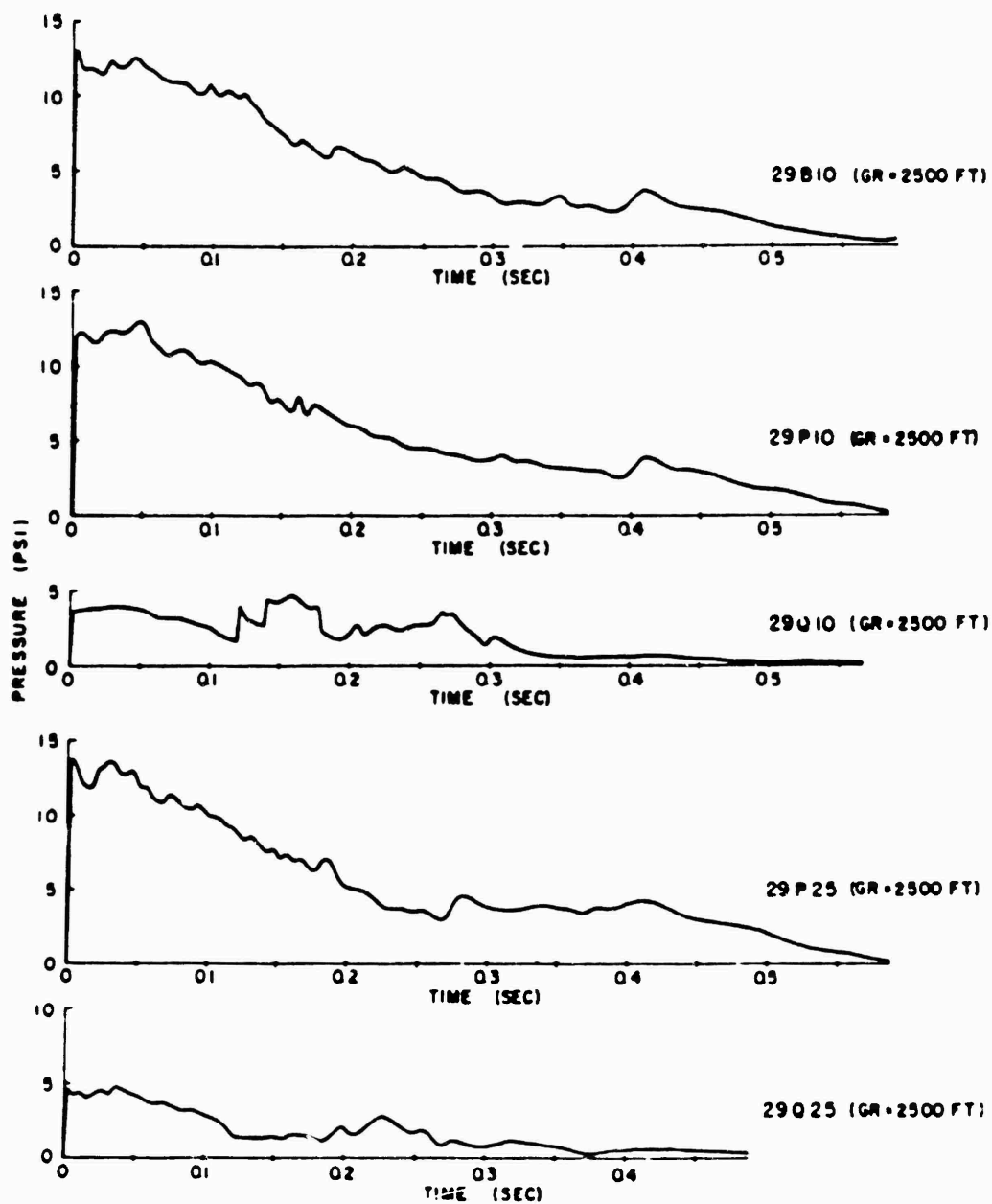


Figure 4.8 Pressure versus time, water line, Shot 12  
(ground range = 2,500 feet).



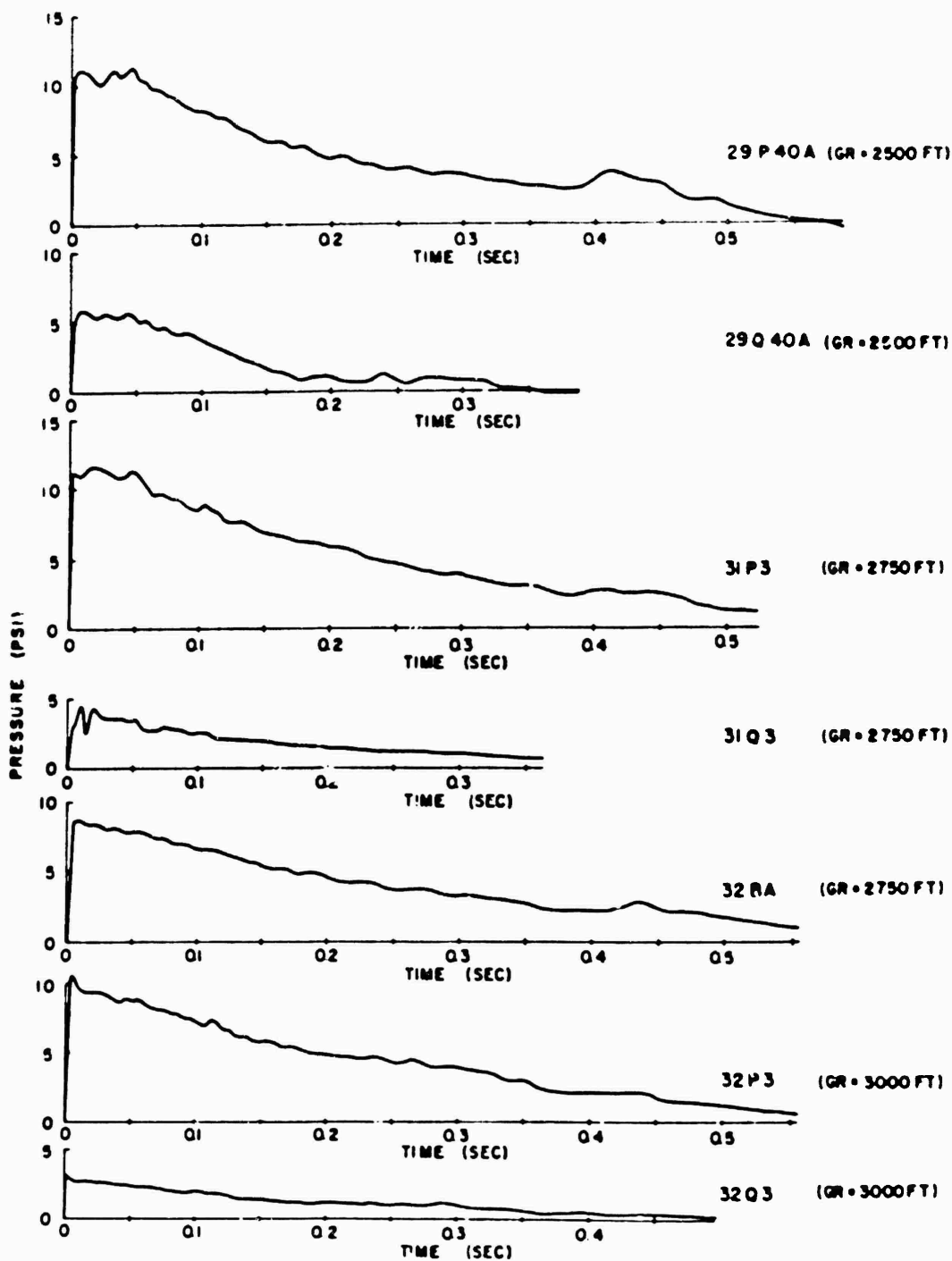


Figure 4.9 Pressure versus time, water line, Shot 12  
(ground range = 2,500 feet-3,000 feet).

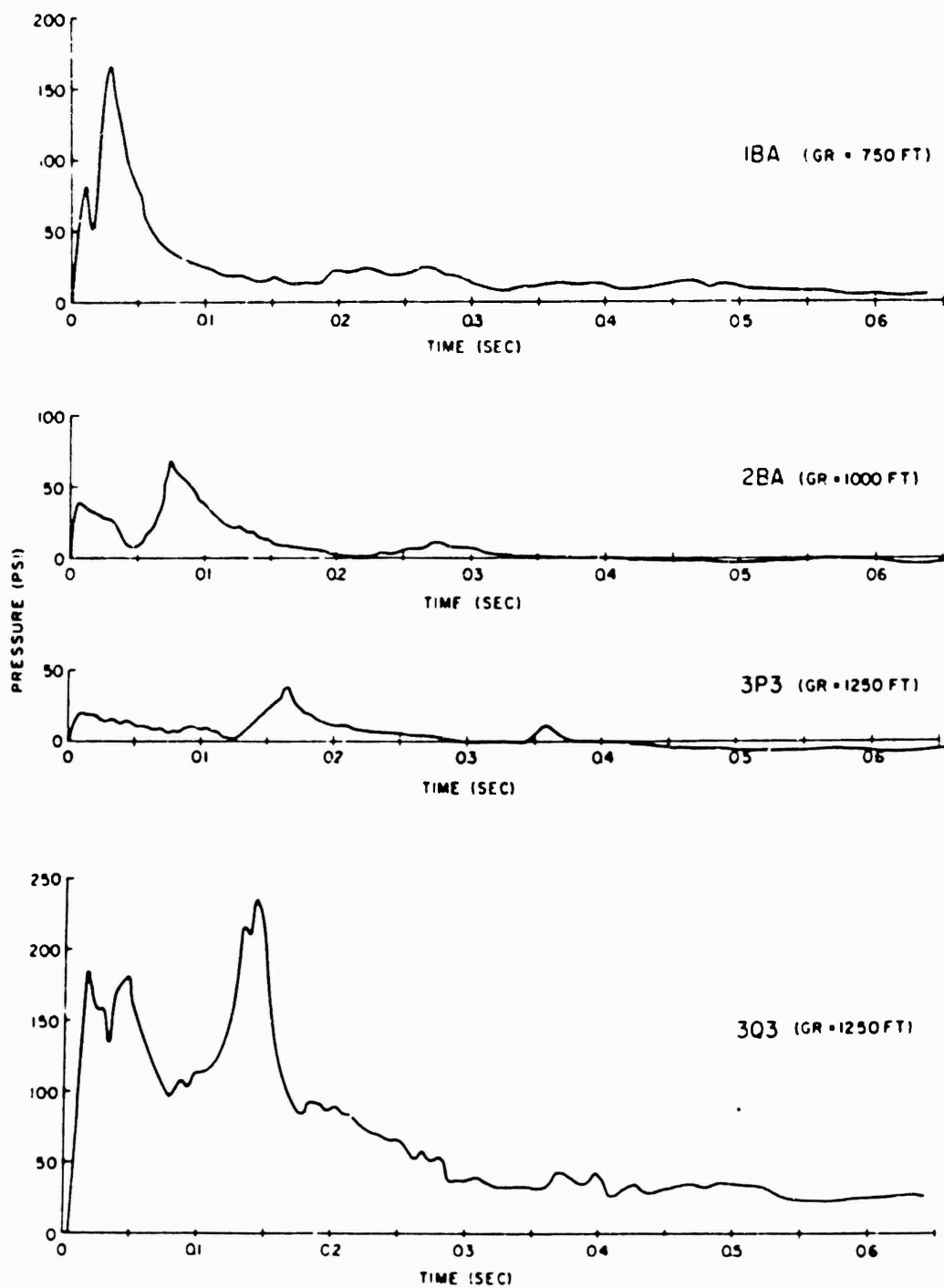


Figure 4.10 Pressure versus time, desert line, Shot 12  
(ground range = 750 feet-1,250 feet).

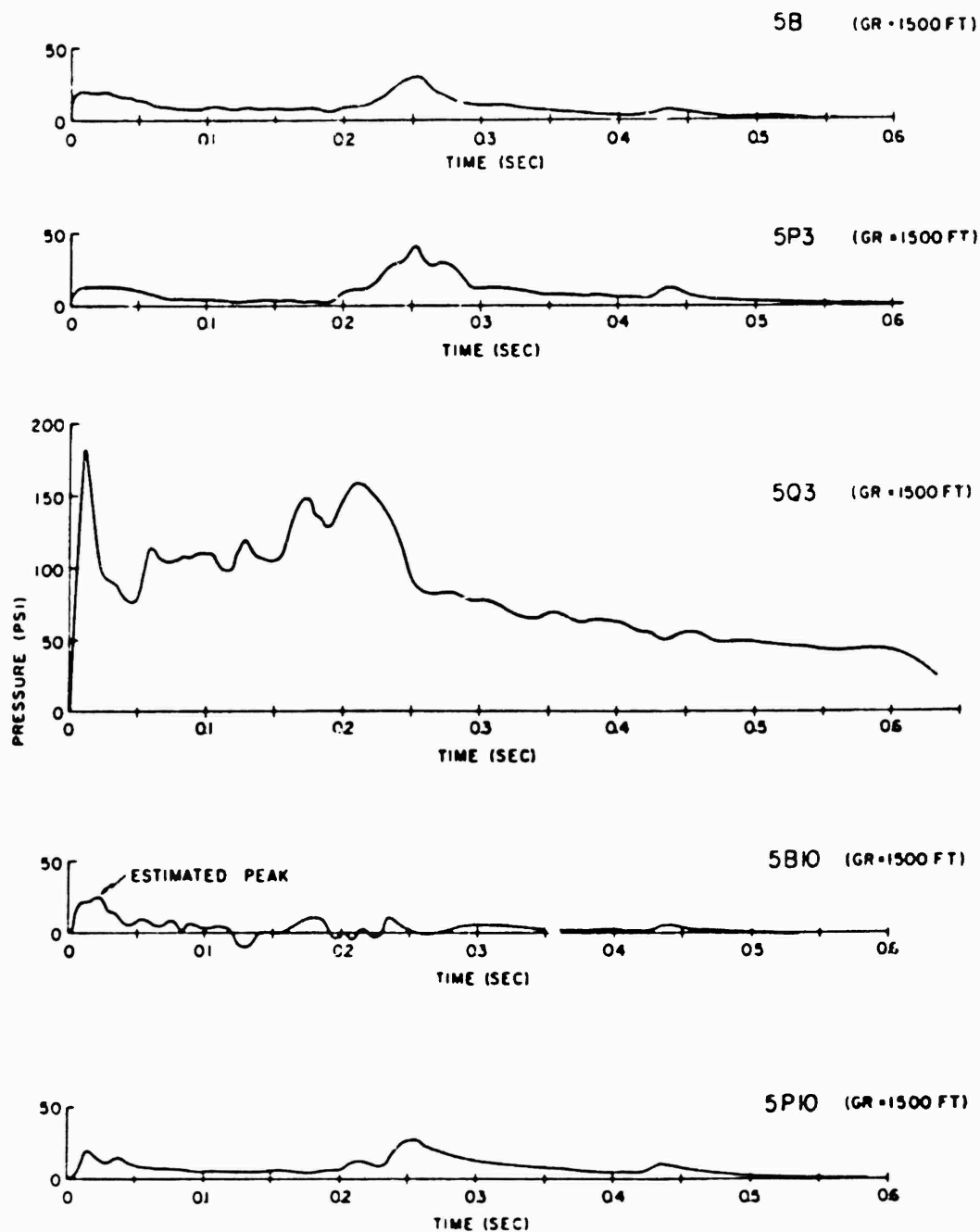


Figure 4.11 Pressure versus time, desert line, Shot 12  
(ground range = 1 500 feet).

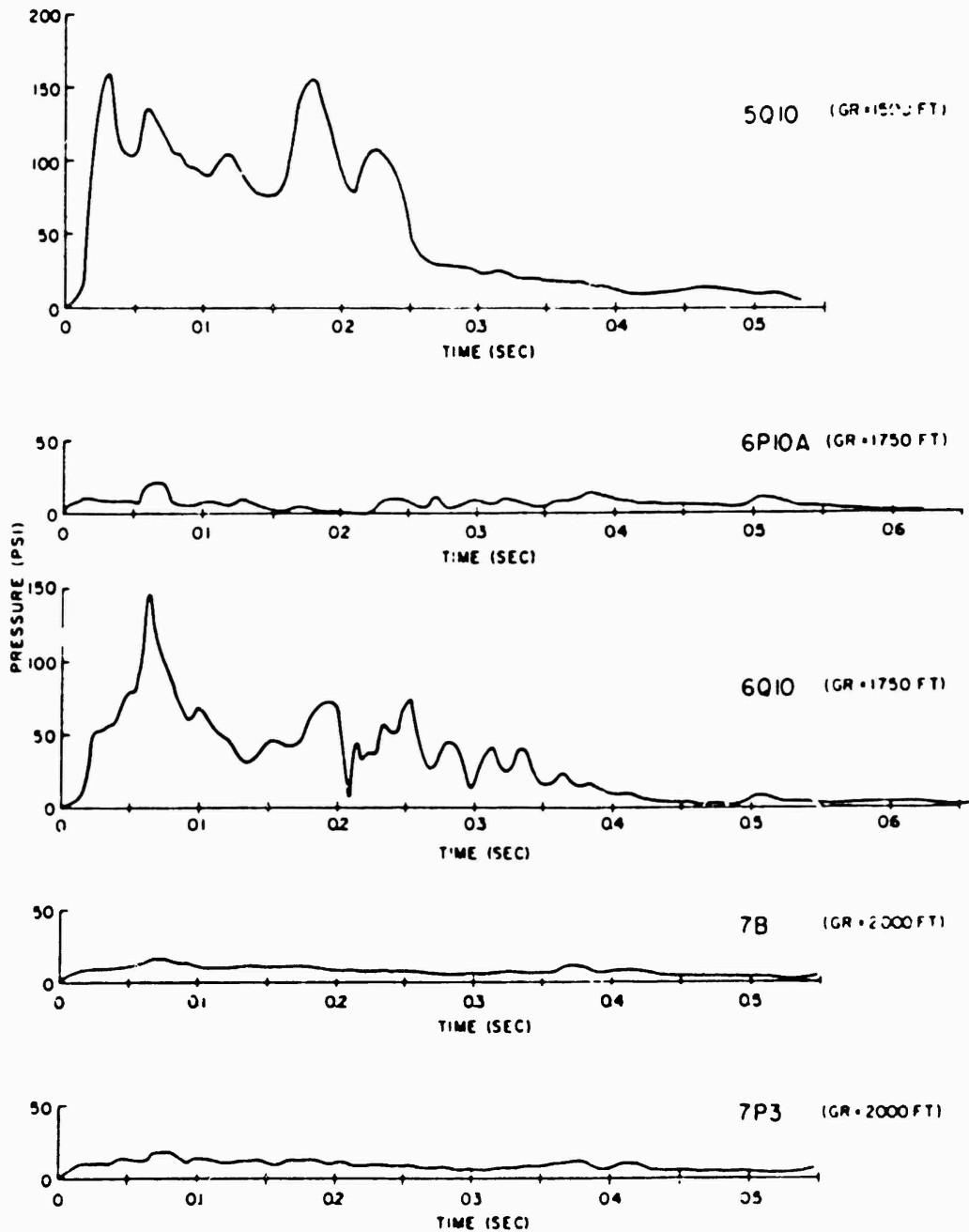


Figure 4.12 Pressure versus time, desert line, Shot 12  
(ground range = 1,500 feet-2,000 feet).

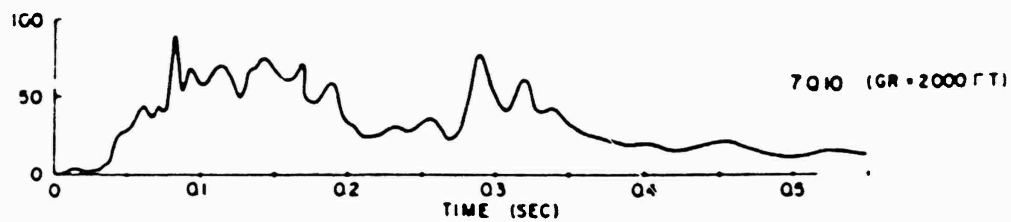
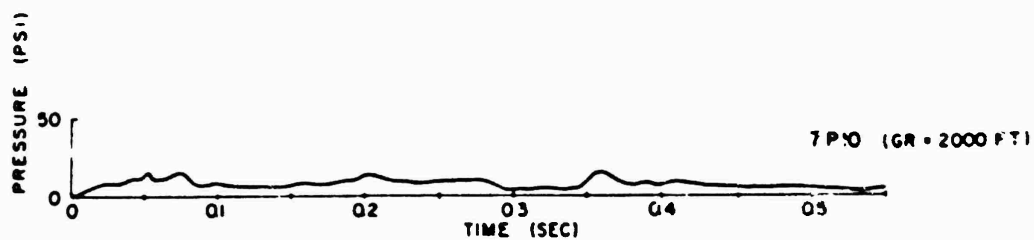
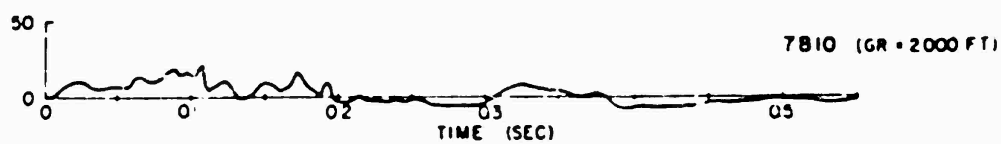
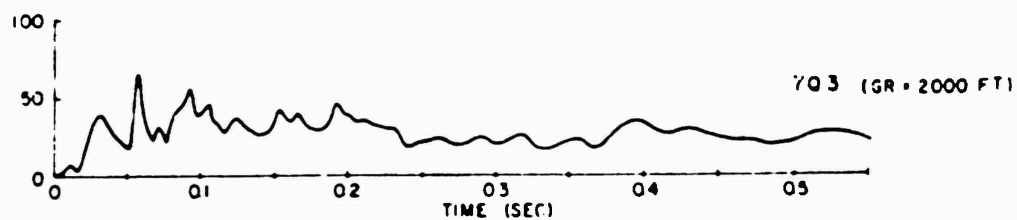


Figure 4.13 Pressure versus time, desert line, Shot 12  
(ground range = 2,000 feet).

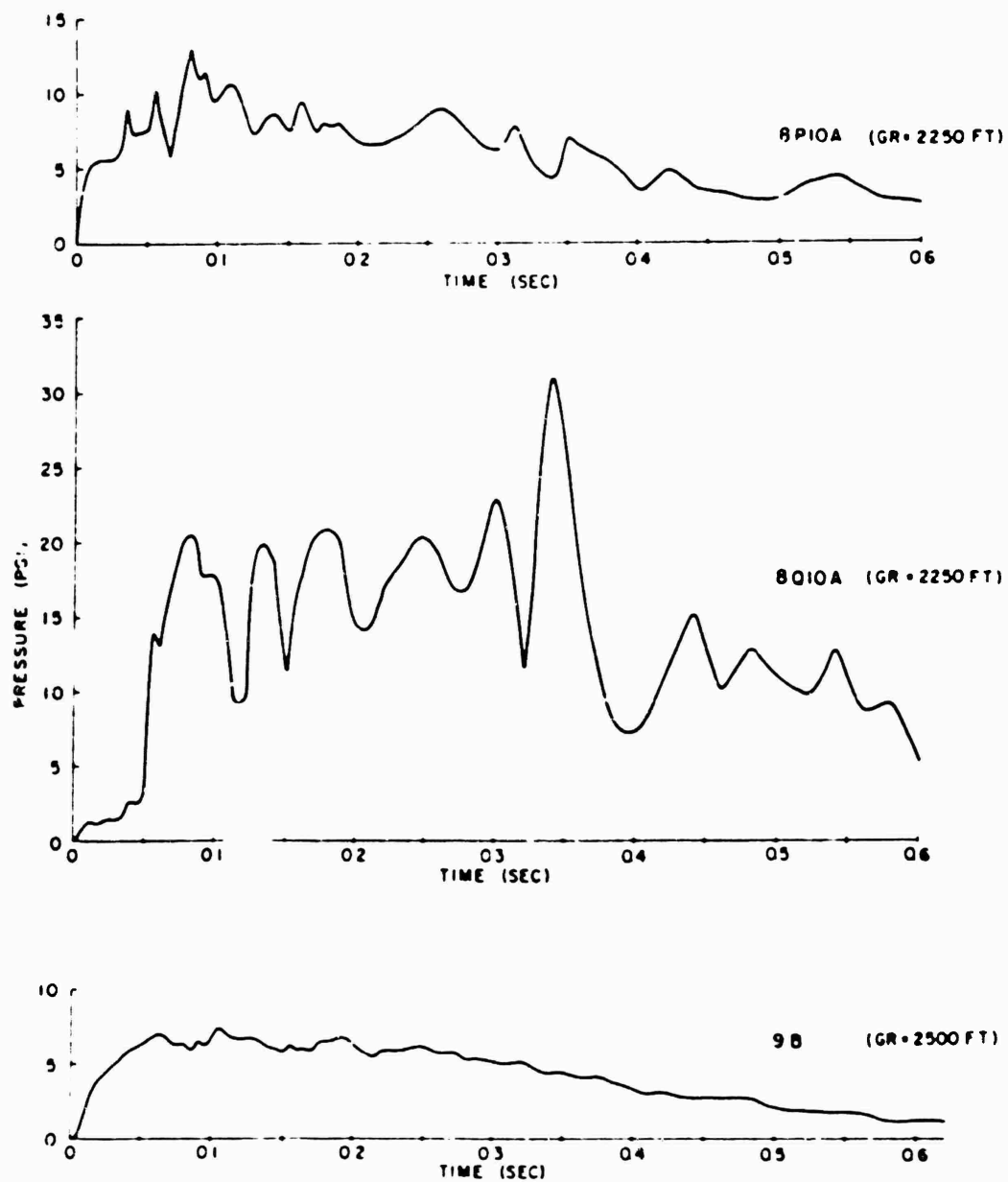


Figure 4.14 Pressure versus time, desert line, Shot 12  
(ground range = 2,250 feet - 2,500 feet).

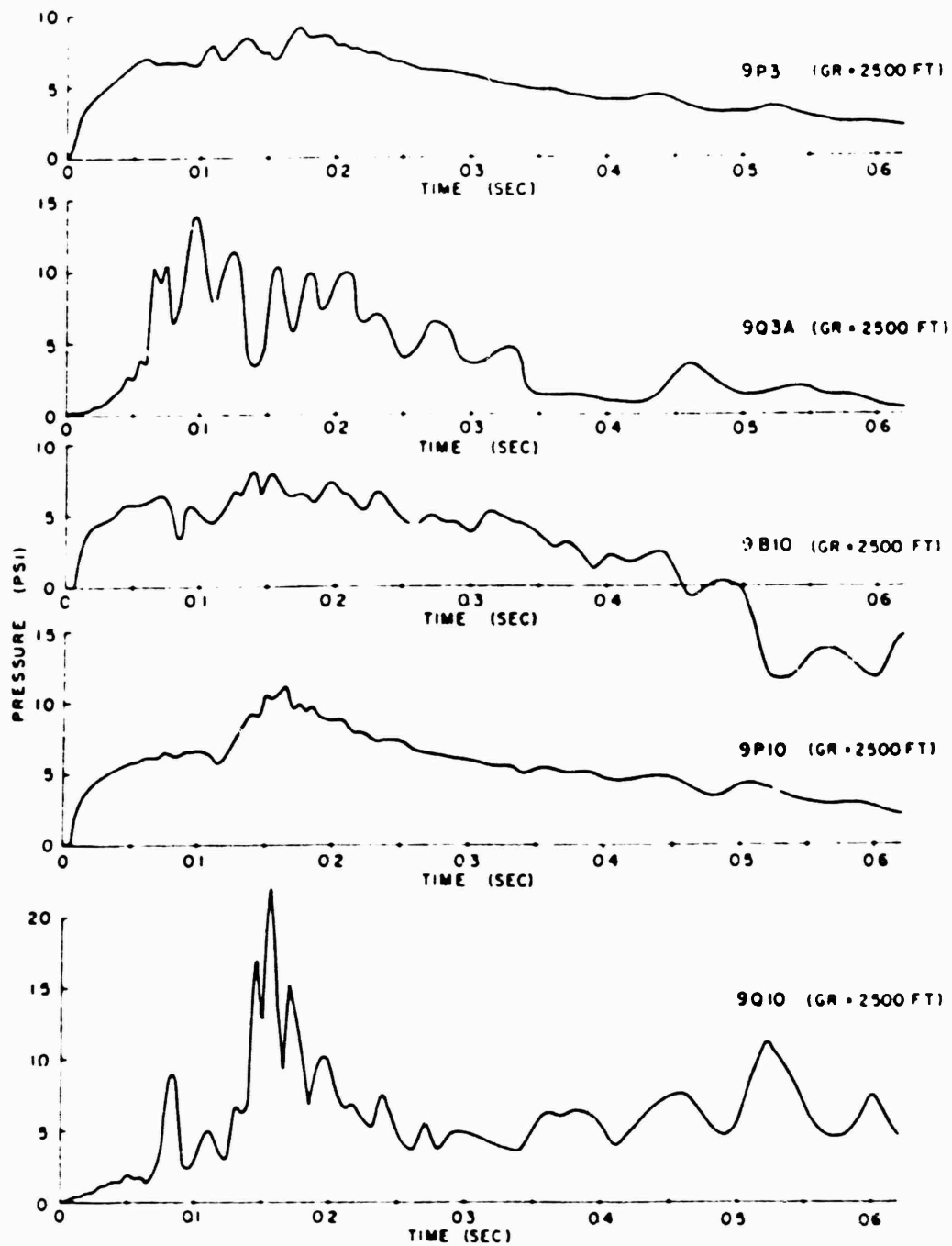


Figure 4.15 Pressure versus time, desert line, Shot 12  
(ground range = 2500 feet).

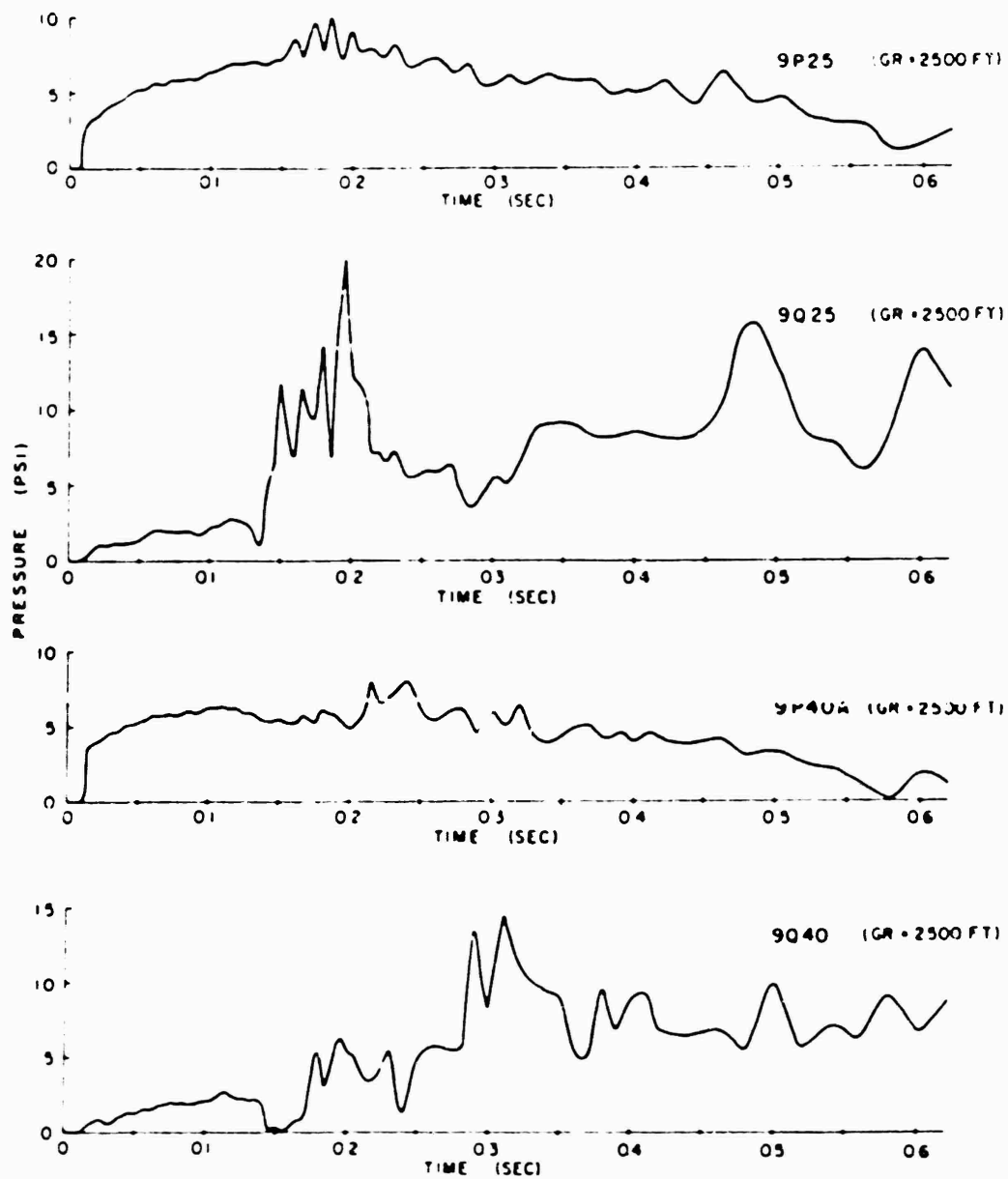


Figure 4 16 Pressure versus time, desert line, Shot 12  
(ground range = 2,500 feet)



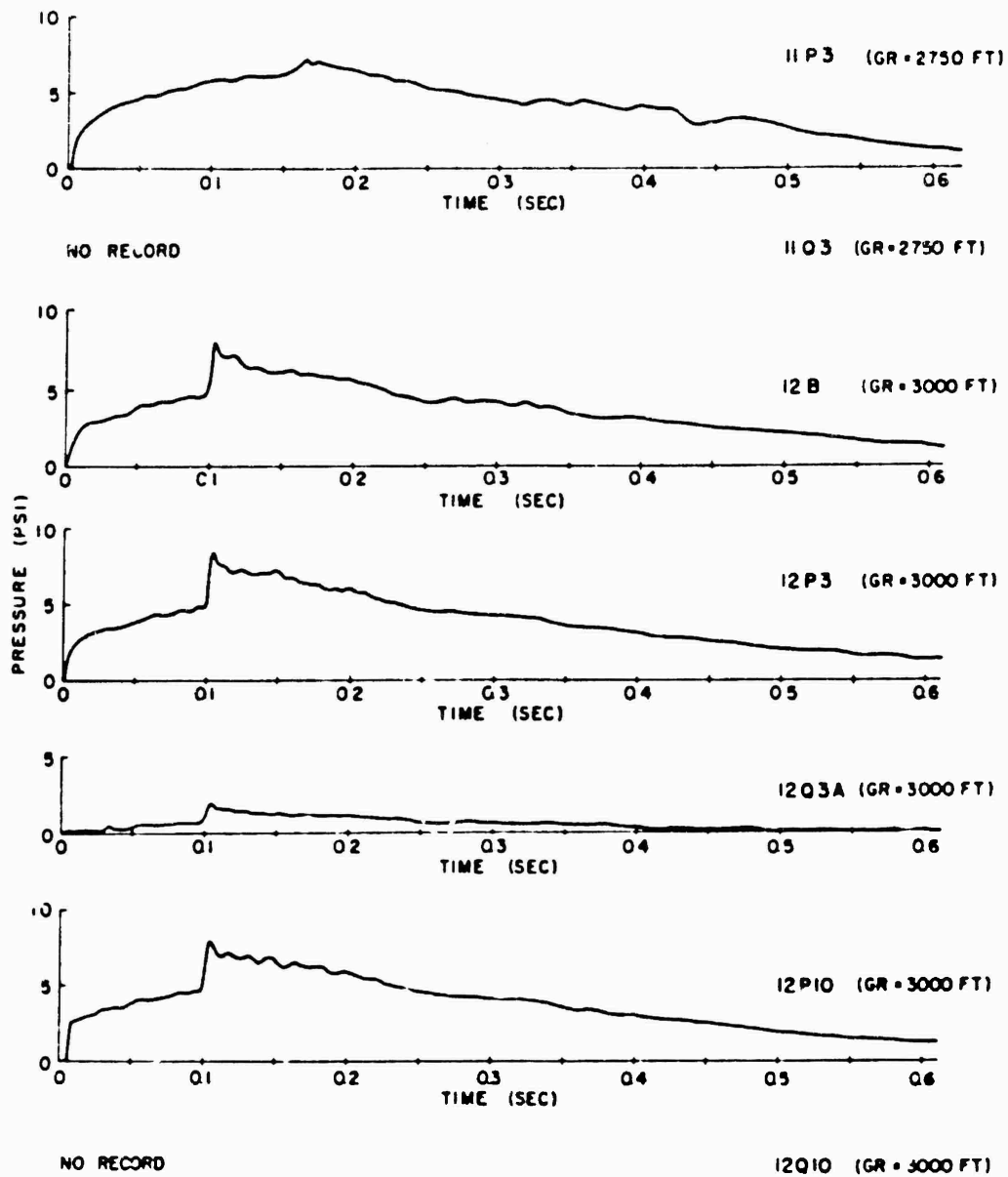


Figure 4.17 Pressure versus time, desert line, Shot 12  
(ground range = 2,750 feet-3,000 feet).

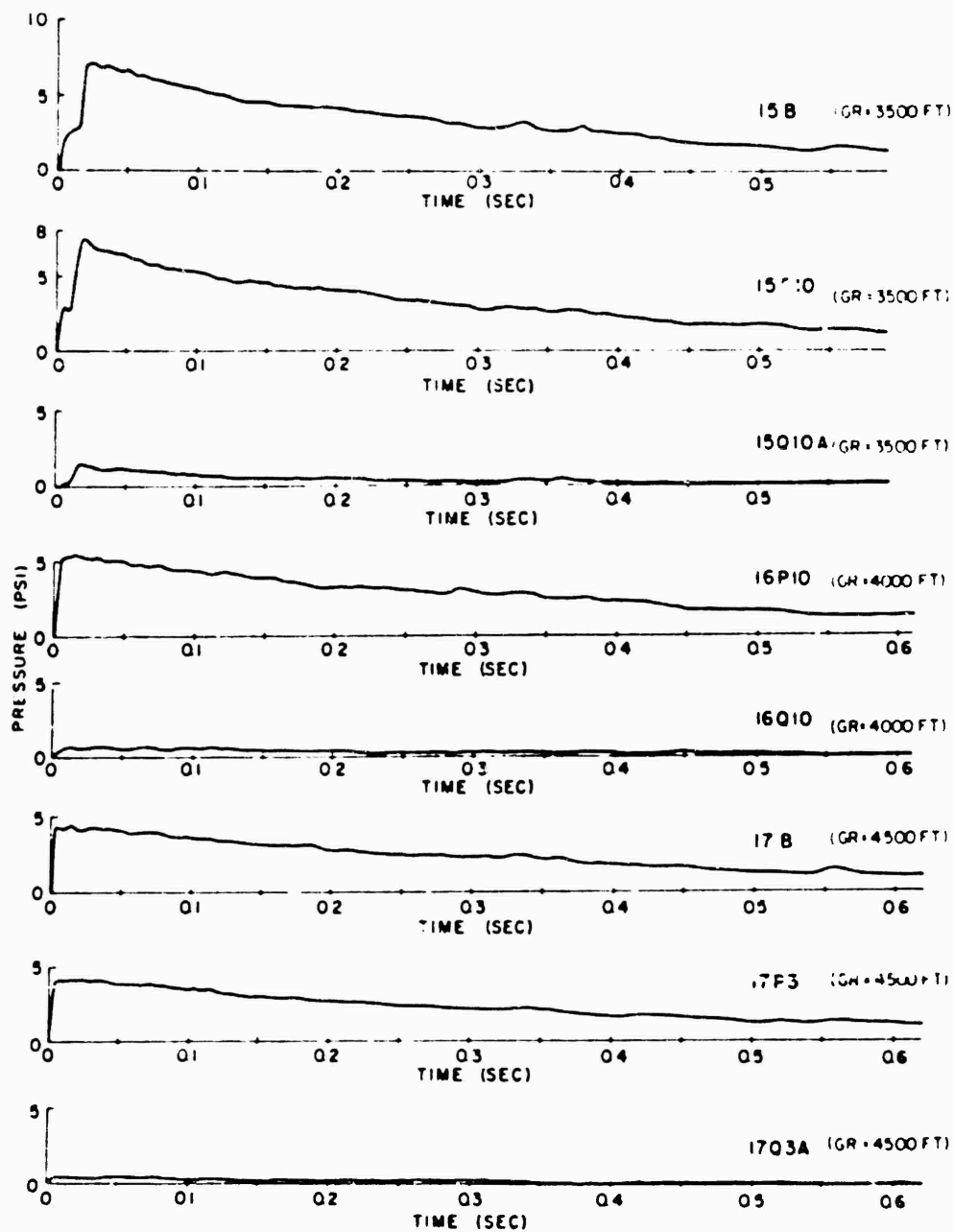


Figure 4.18 Pressure versus time, desert line, Shot 12  
(ground range = 3,500 feet-4,000 feet).

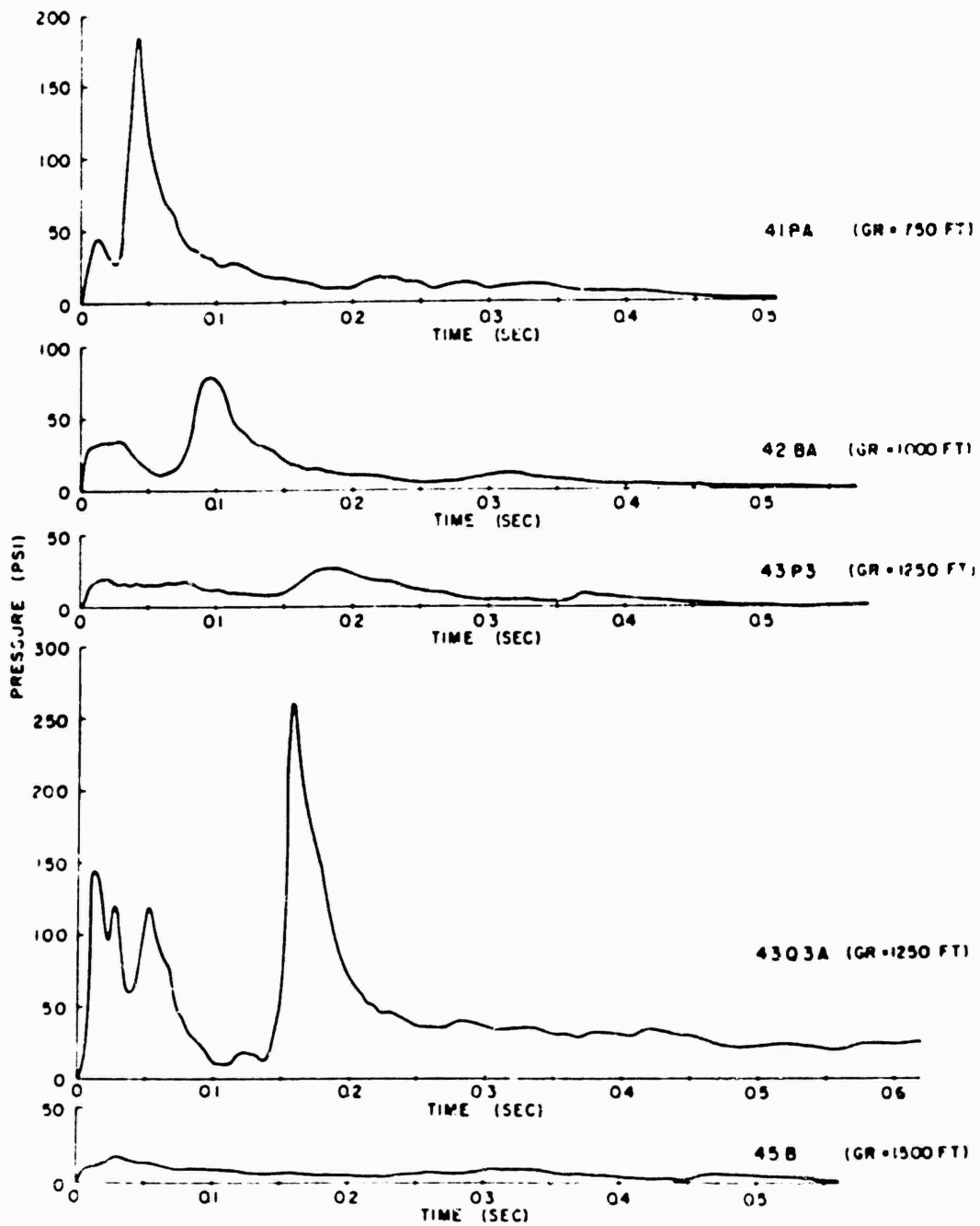


Figure 4.19 Pressure versus time, asphalt line, shot 12  
(ground range = 750 feet-1,500 feet).

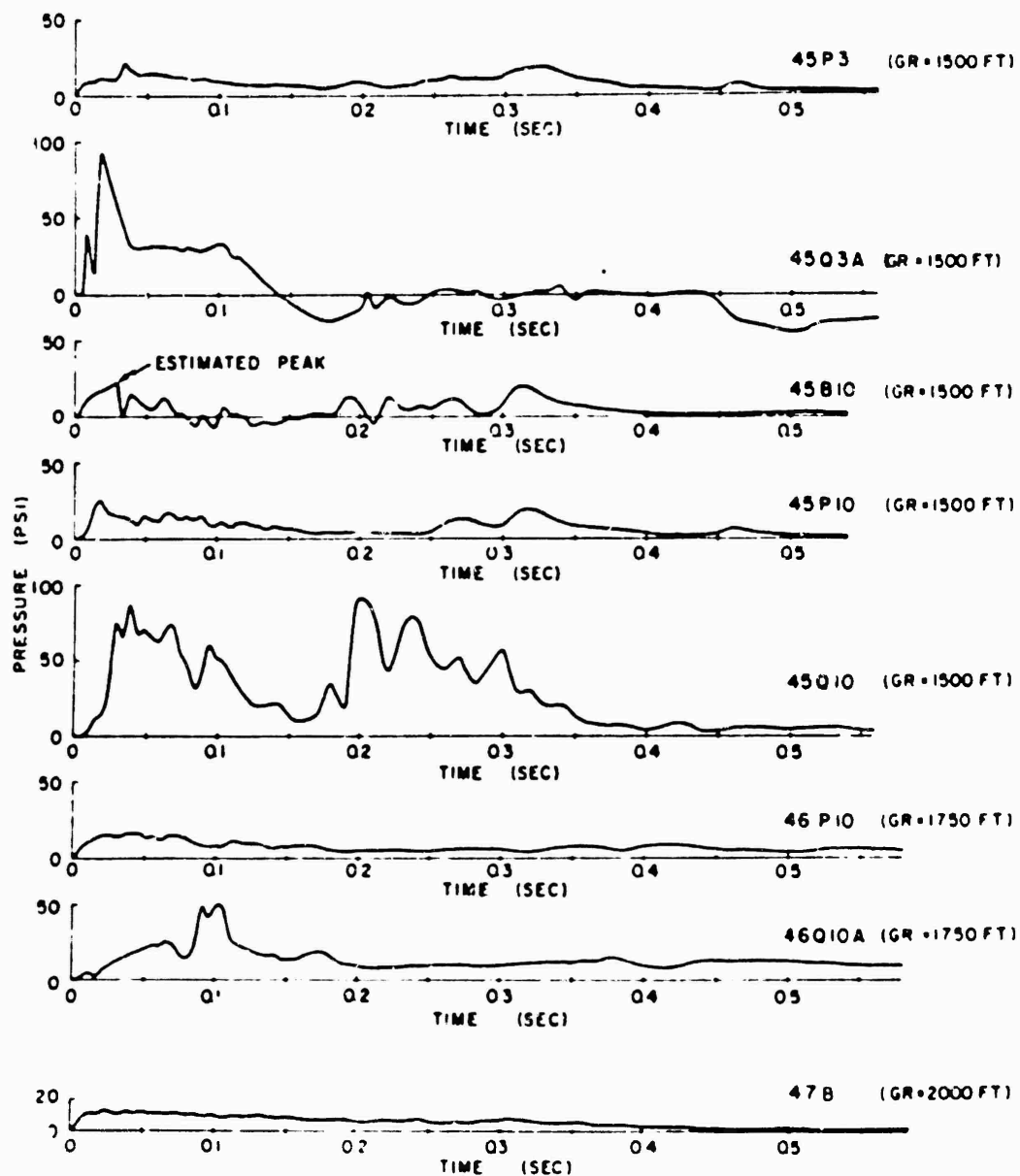


Figure 4.20 Pressure versus time, asphalt line, Shot 12  
(ground range = 1,500 feet-2,000 feet).

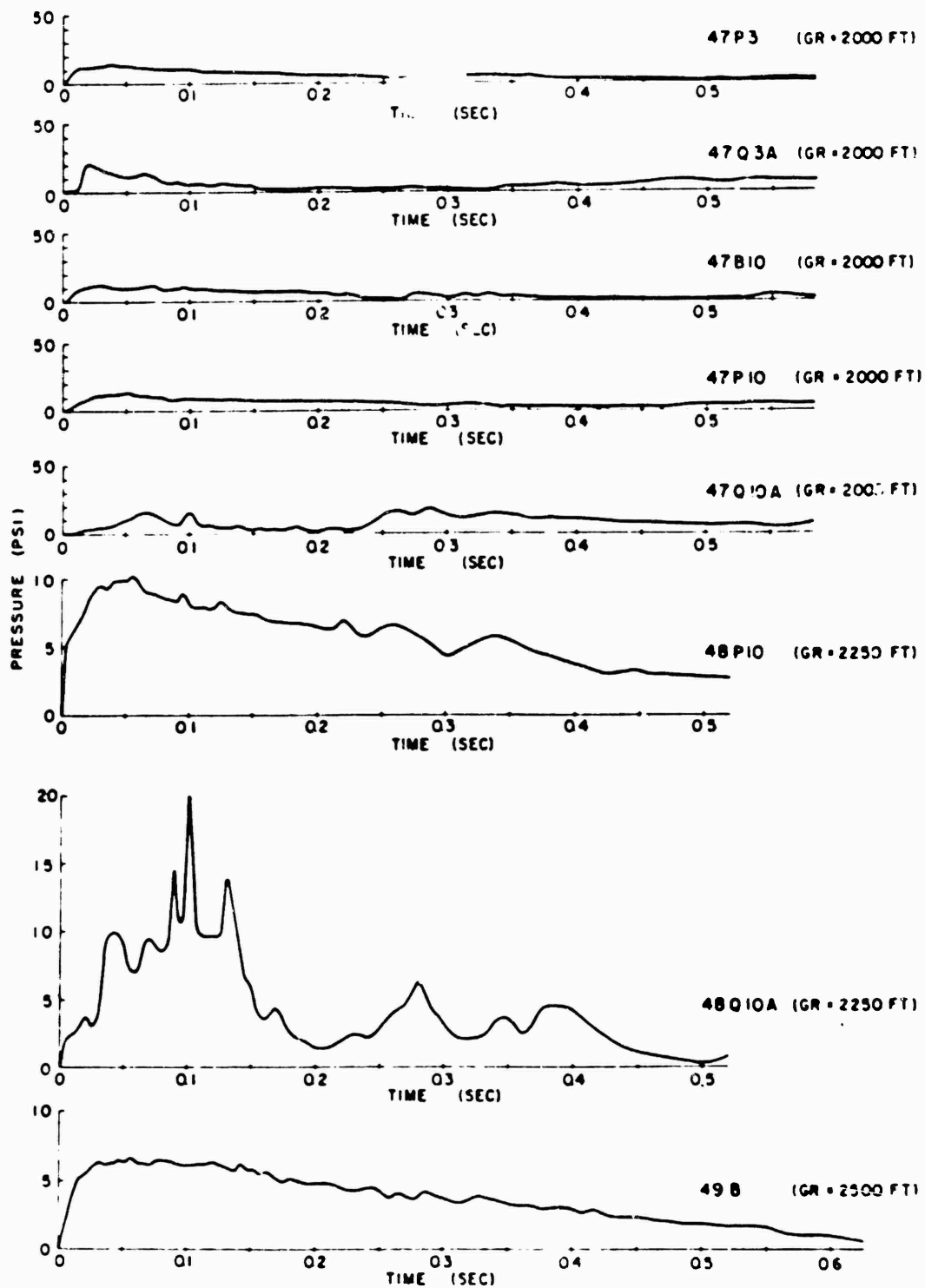


Figure 4.21 Pressure versus time, asphalt line, Shot 12  
(ground range = 2,000 feet - 2,500 feet).

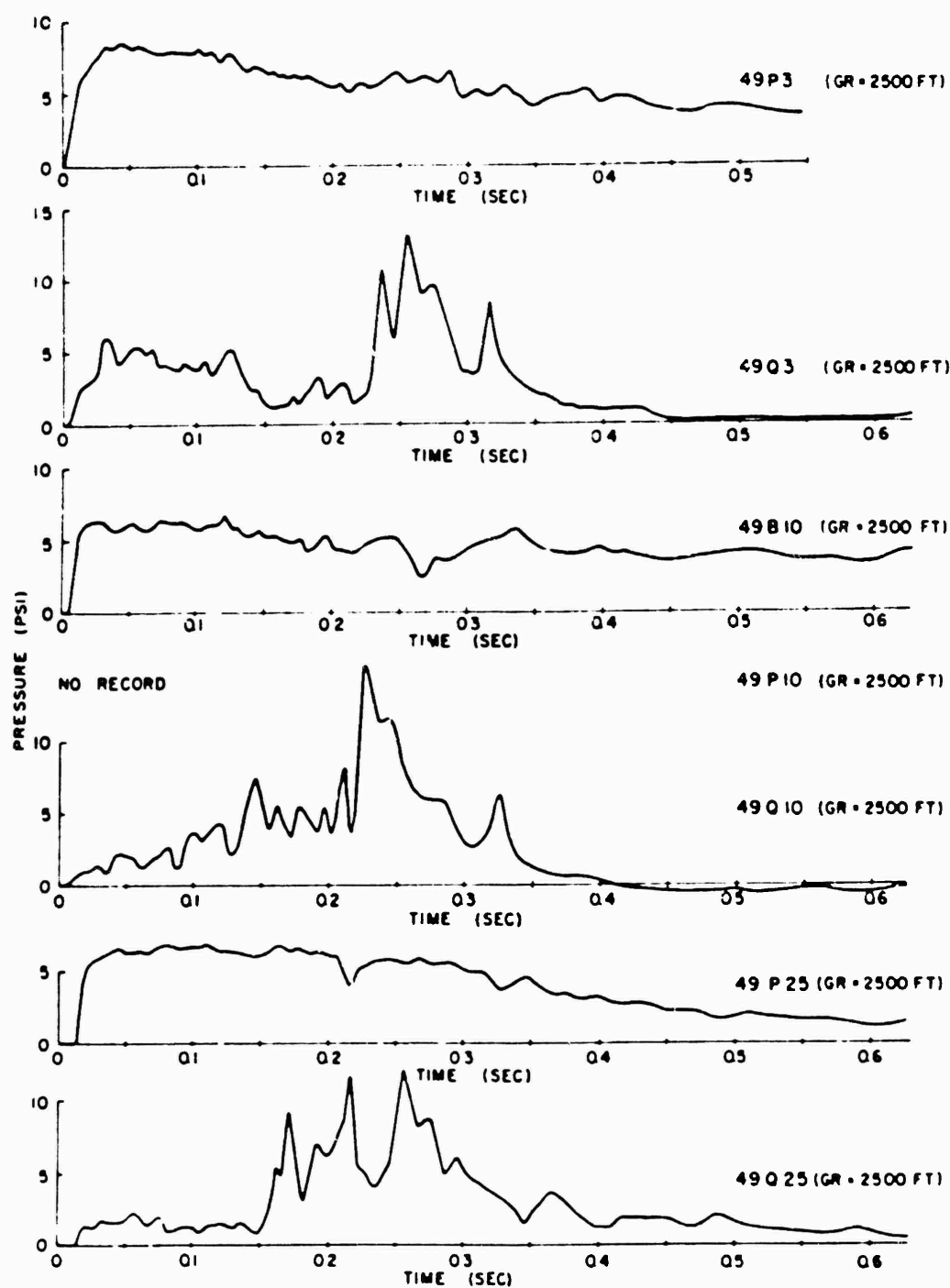


Figure 4.22 Pressure versus time, asphalt line, 8shot 12  
(ground range = 3,500 feet).

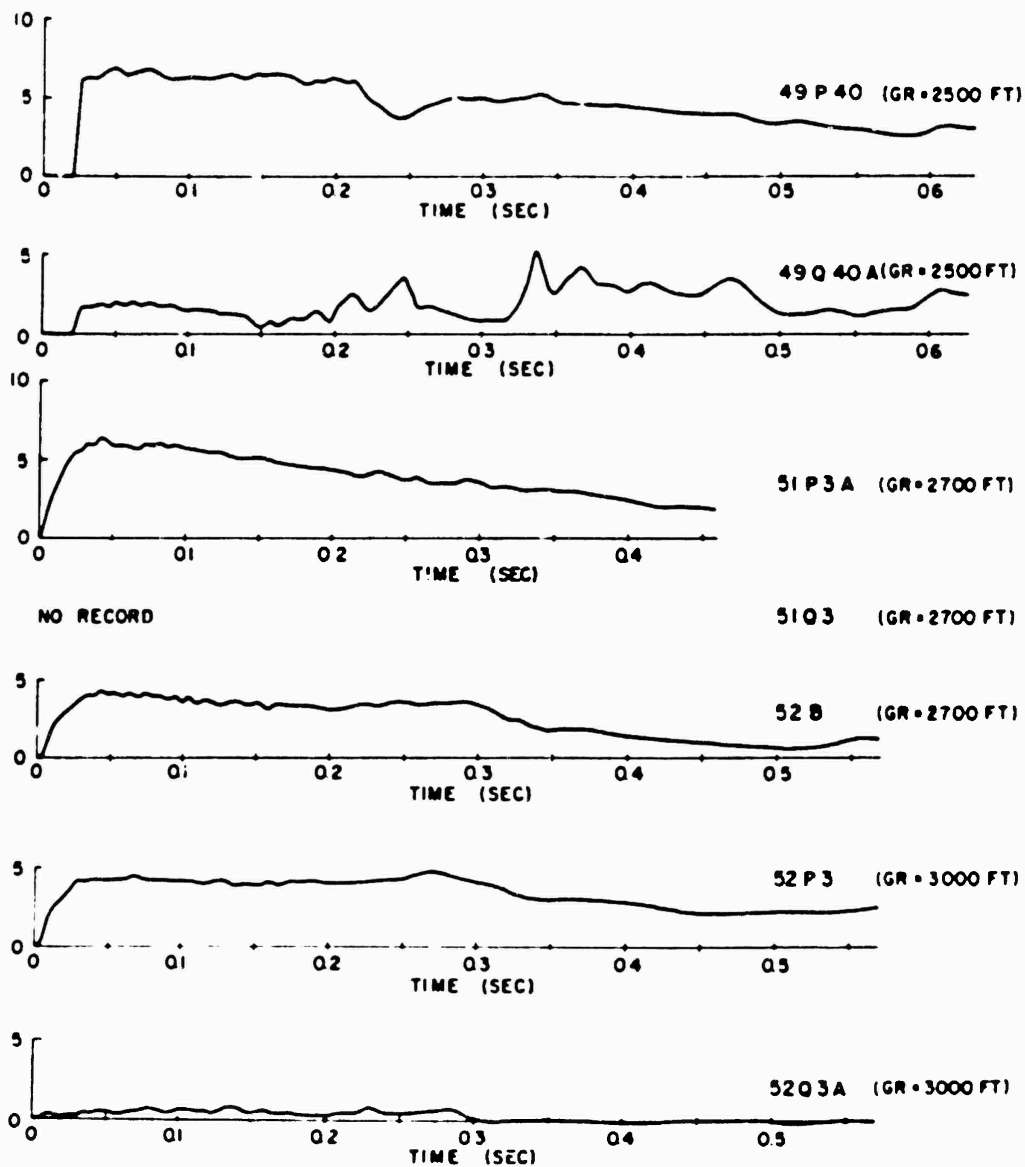


Figure 4.23 Pressure versus time, asphalt line, Shot 12  
(ground range = 2,500 feet-3,000 feet).

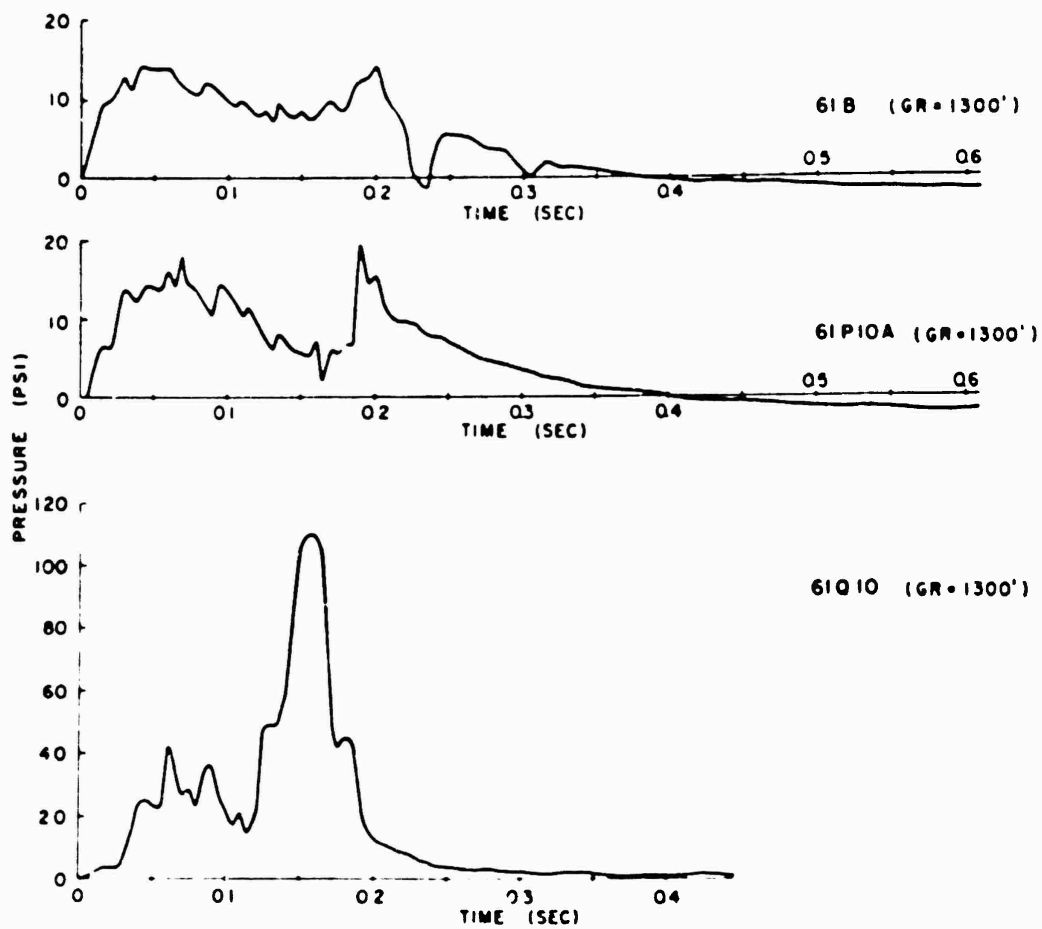


Figure 4.24 Pressure versus time, desert line, Shot 6  
(ground range = 1,300 feet).



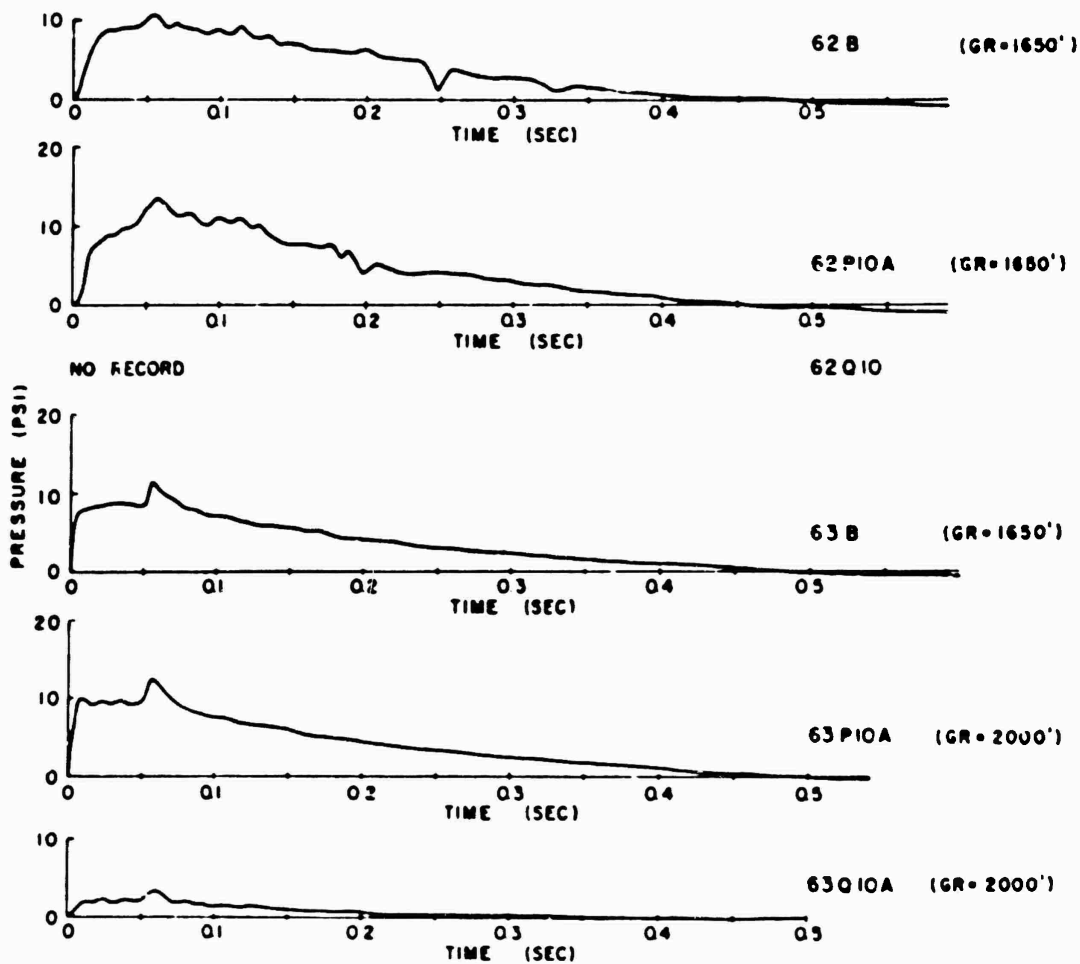


Figure 4.28 Pressure versus time, desert line, Shot 6  
(ground range = 1,650 feet-2,600 feet).

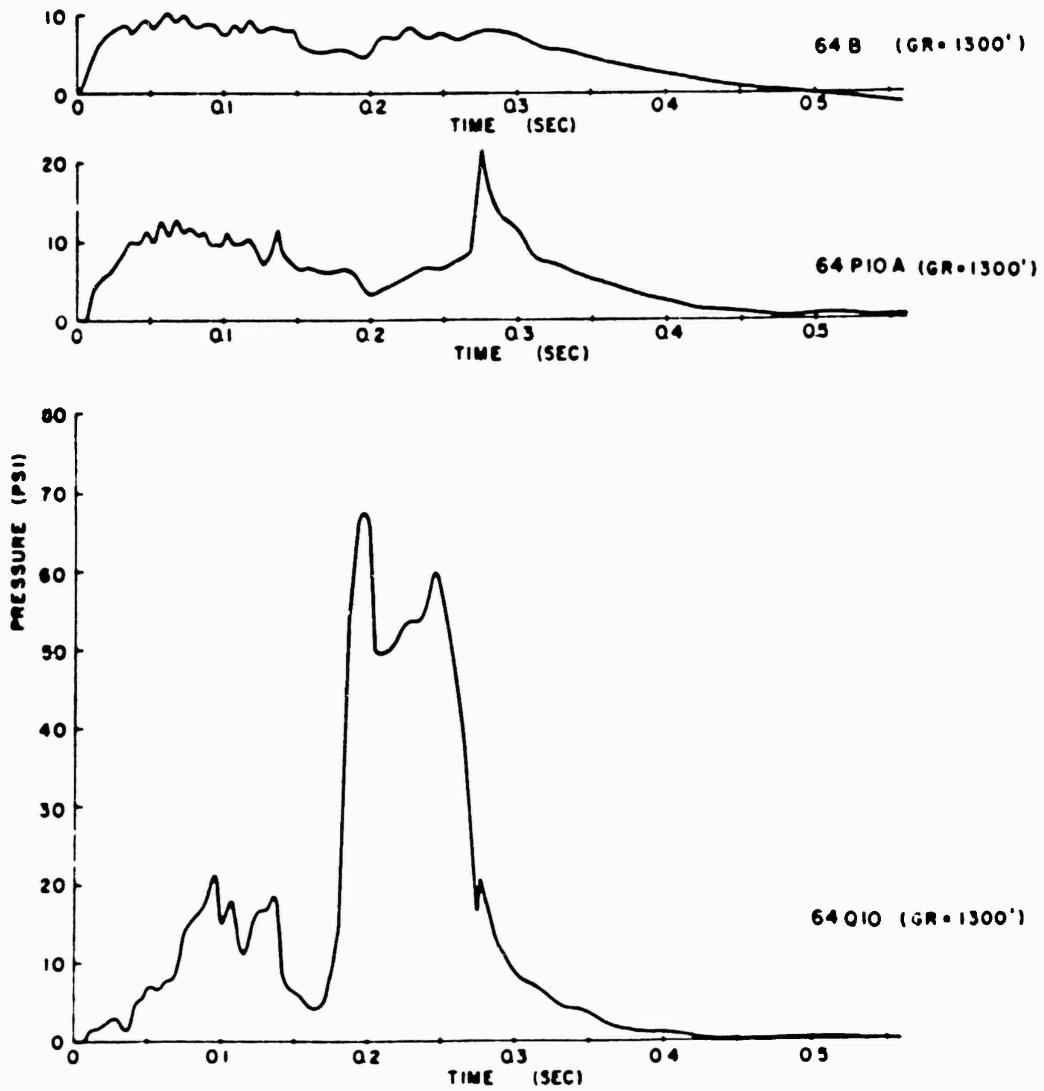


Figure 4.26 Pressure versus time, asphalt line, Shot 6  
(ground range = 1,300 feet)

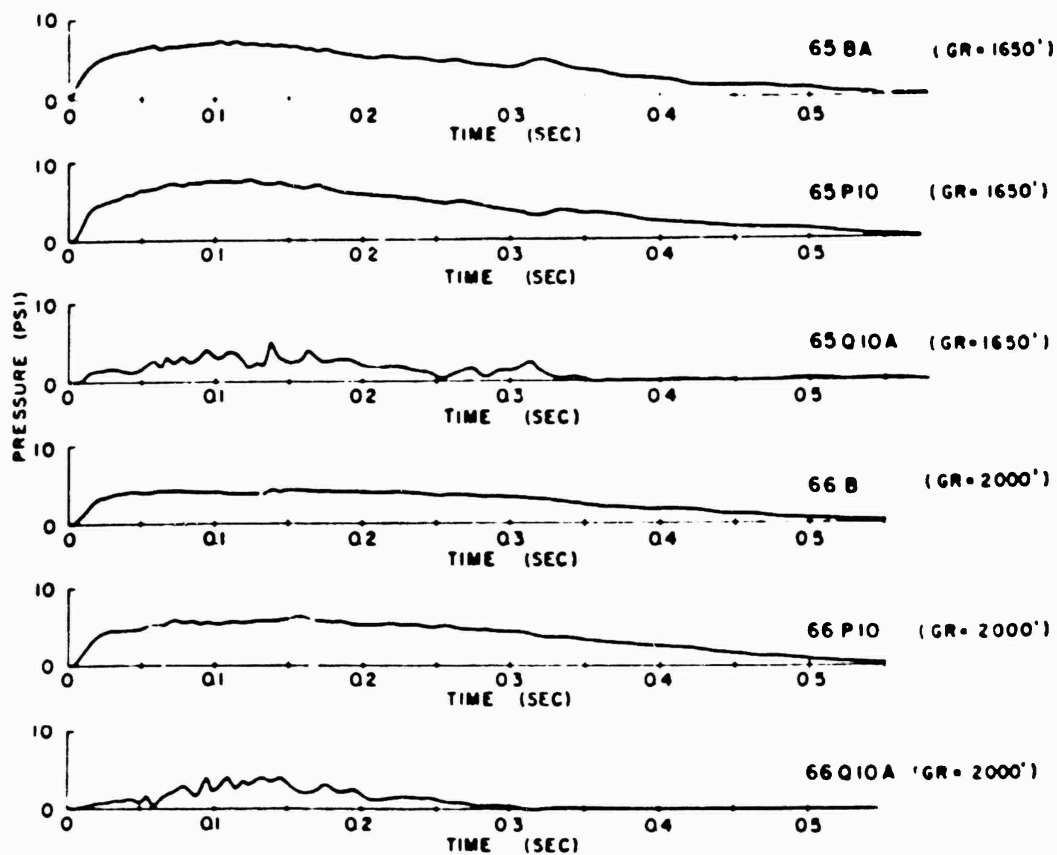


Figure 4.27 Pressure versus time, asphalt line, Shot 6  
(ground range = 1,650 feet-2,000 feet).

ASPHALT

DESERT

WATER

GENERAL

TYPE

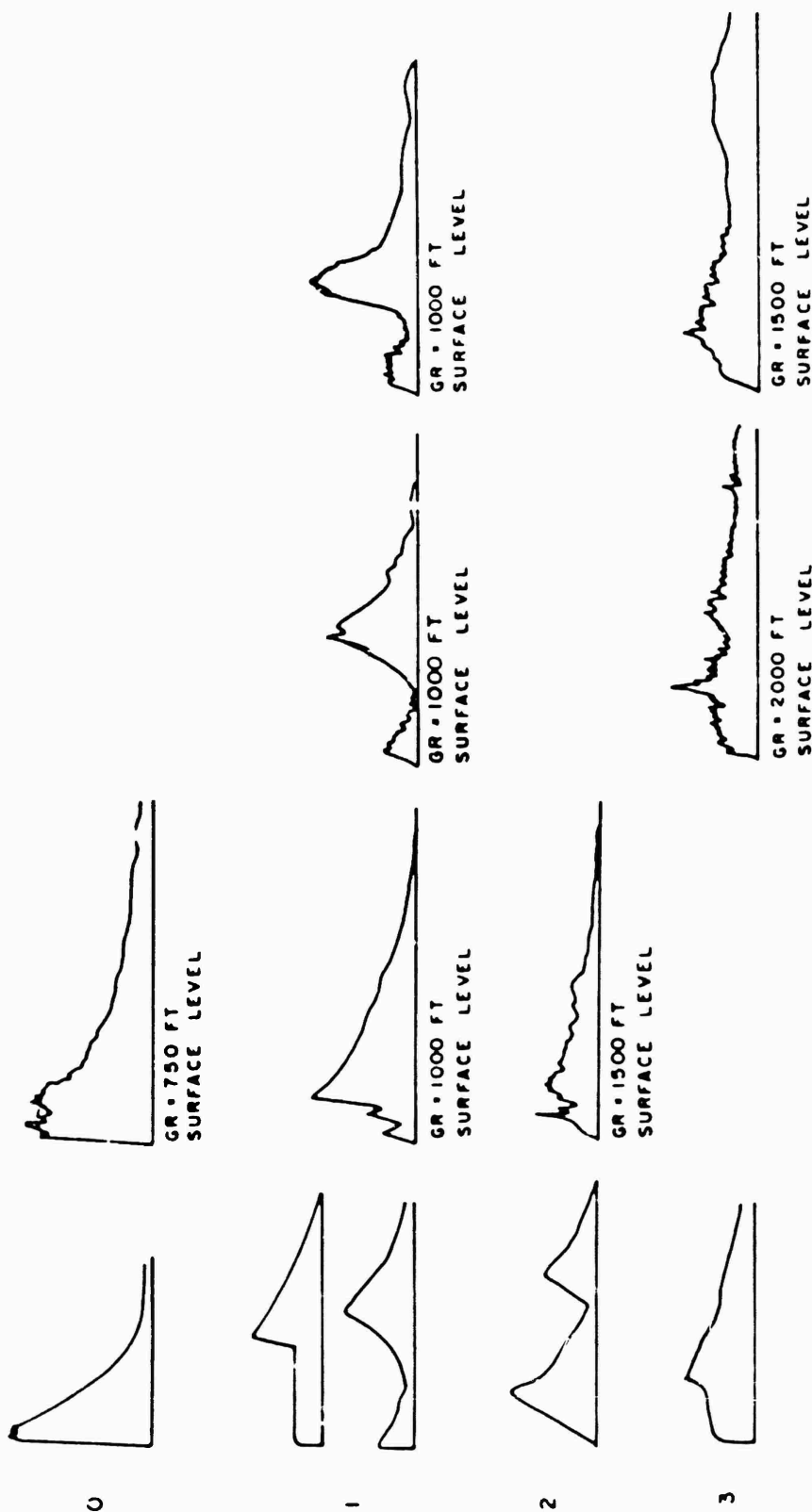


Figure 4.26 Wave forms of overpressure records, Sbot 12, Type 0-3.

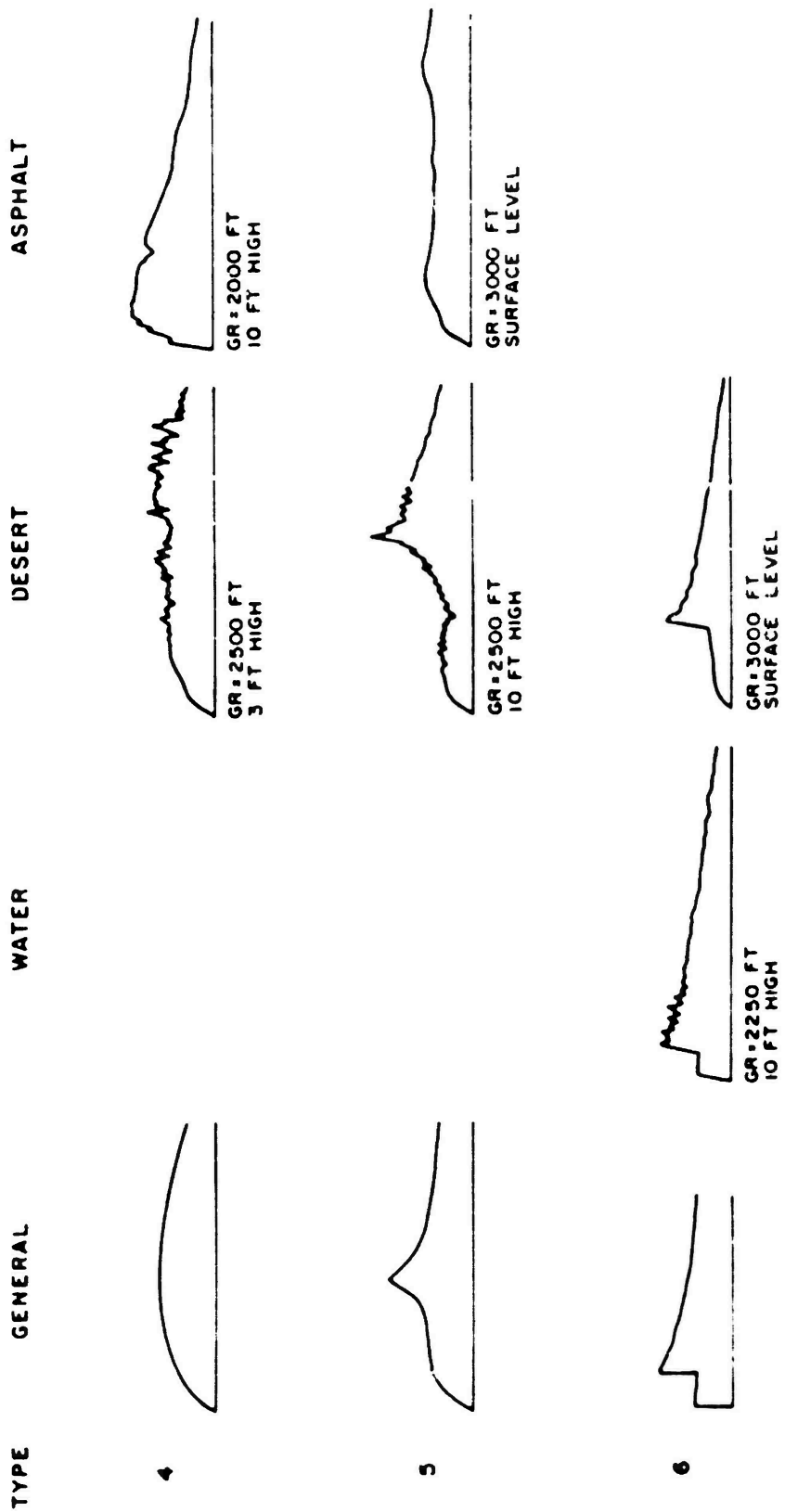


Figure 4.29 Wave forms of overpressure records, Sbox 12, Types 4-6.

CONFIDENTIAL

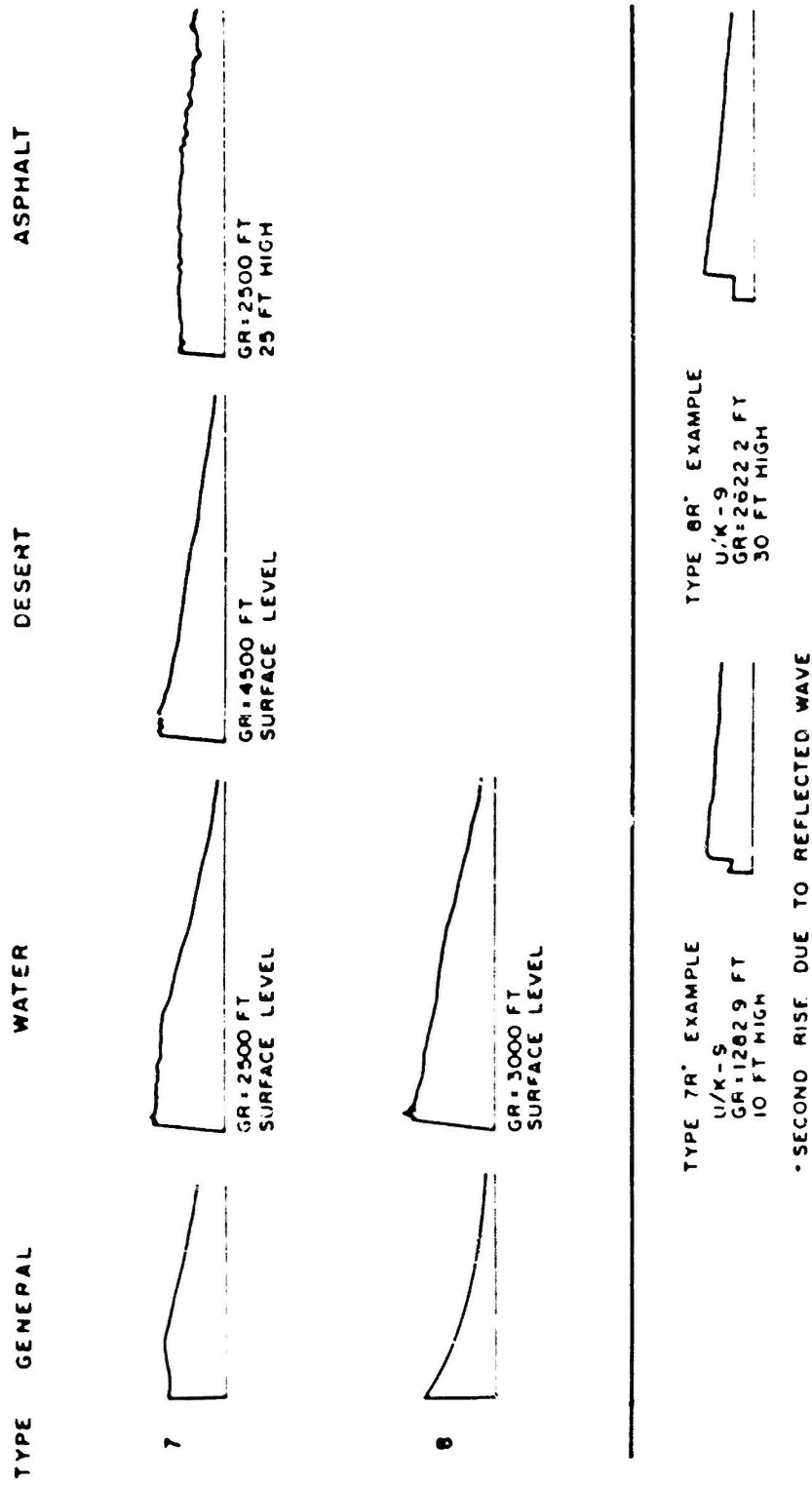


Figure 4.30 Wave forms of overpressure records, 8but 12, Types 7, 8, 7R, and 8R.

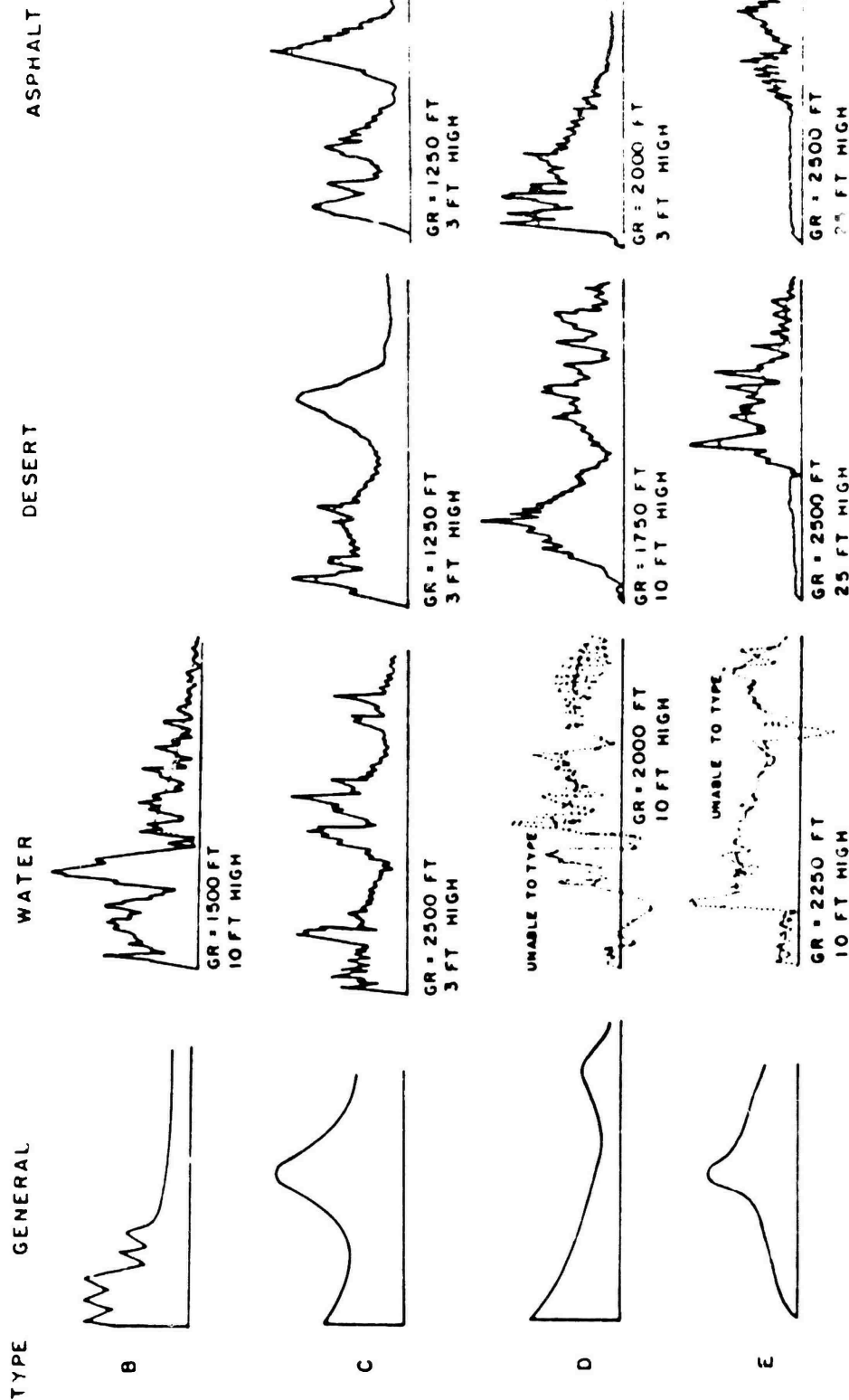


Figure 4.31 Wave forms of dynamic pressure records. Shot 12. Types B-E

CONFIDENTIAL

CONFIDENTIAL

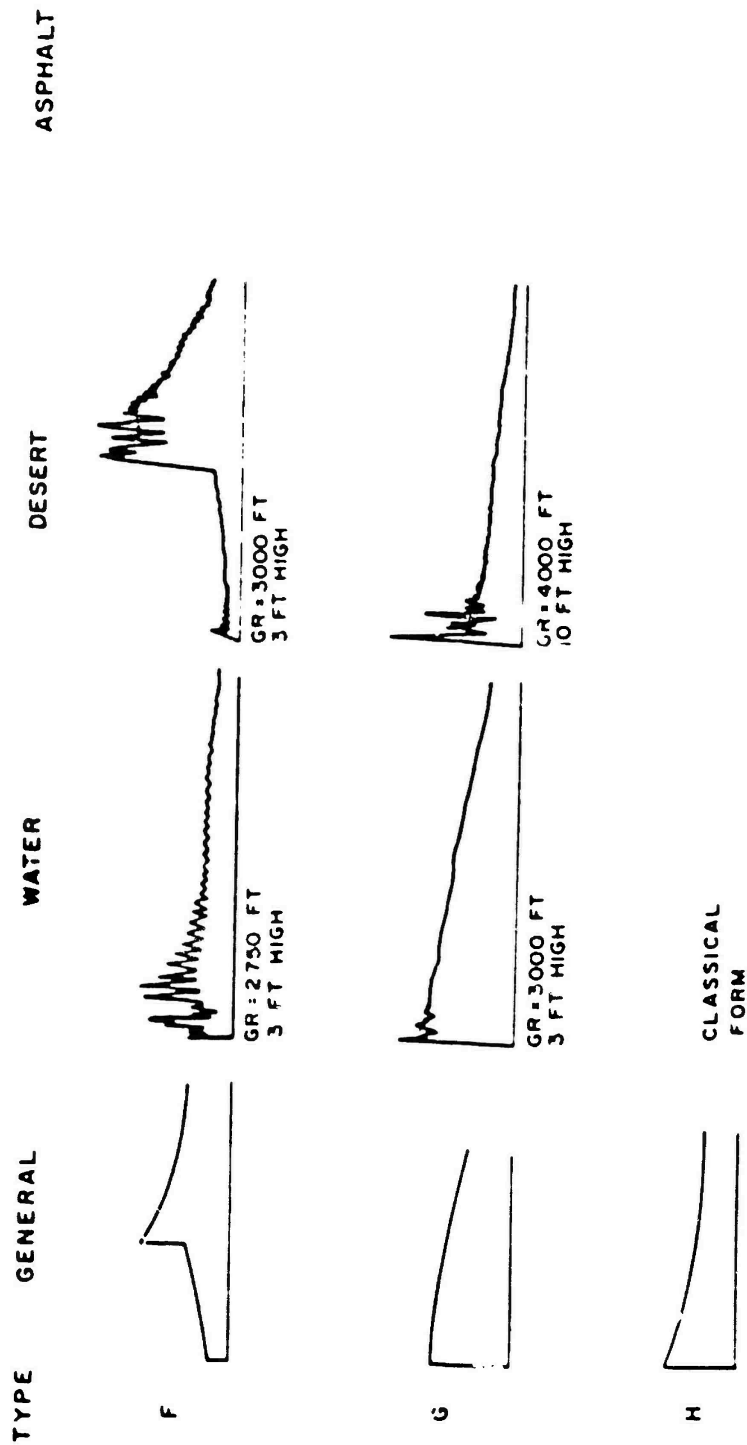
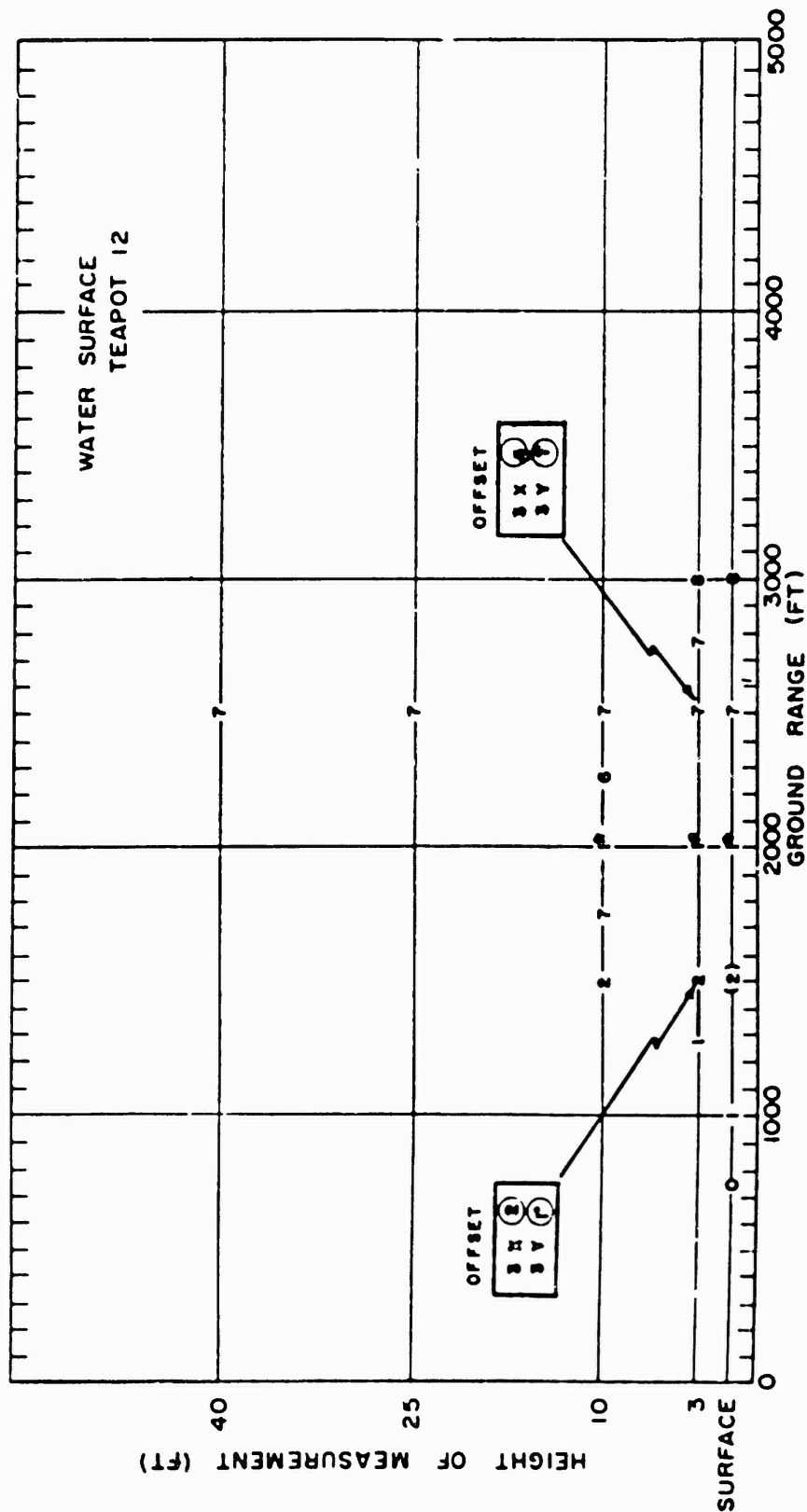


Figure 4.32 Wave forms of dynamic pressure records, Shot 12, Types F-H.





• See discussion in Section 4.5.2.

Figure 4.33 Overpressure wave form type versus ground range and gage height, water line, Shot 12.

CONFIDENTIAL

CONFIDENTIAL

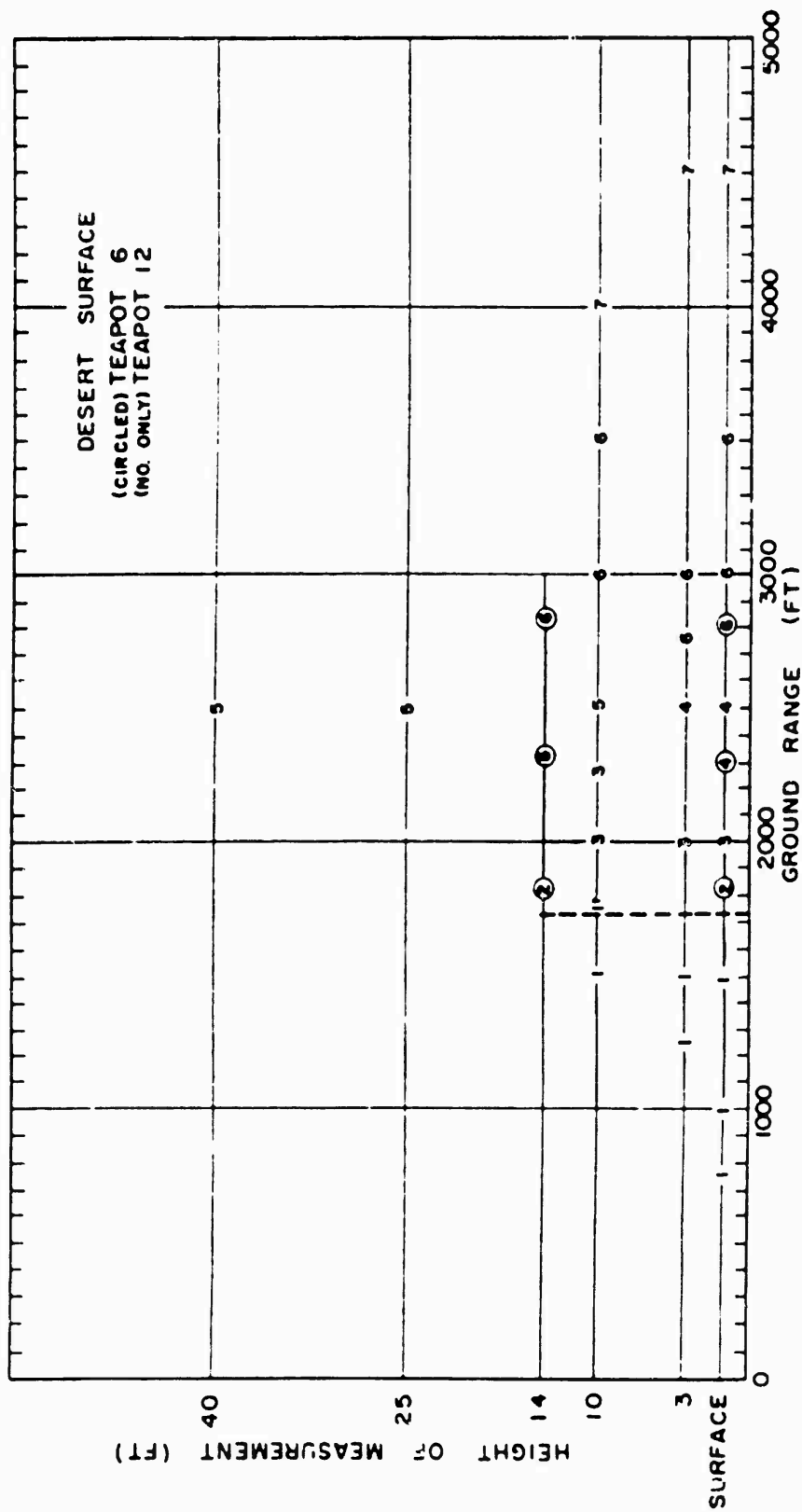


Figure 4.34 Overpressure wave form type versus ground range and gage height, desert line, Shots 6 and 12.

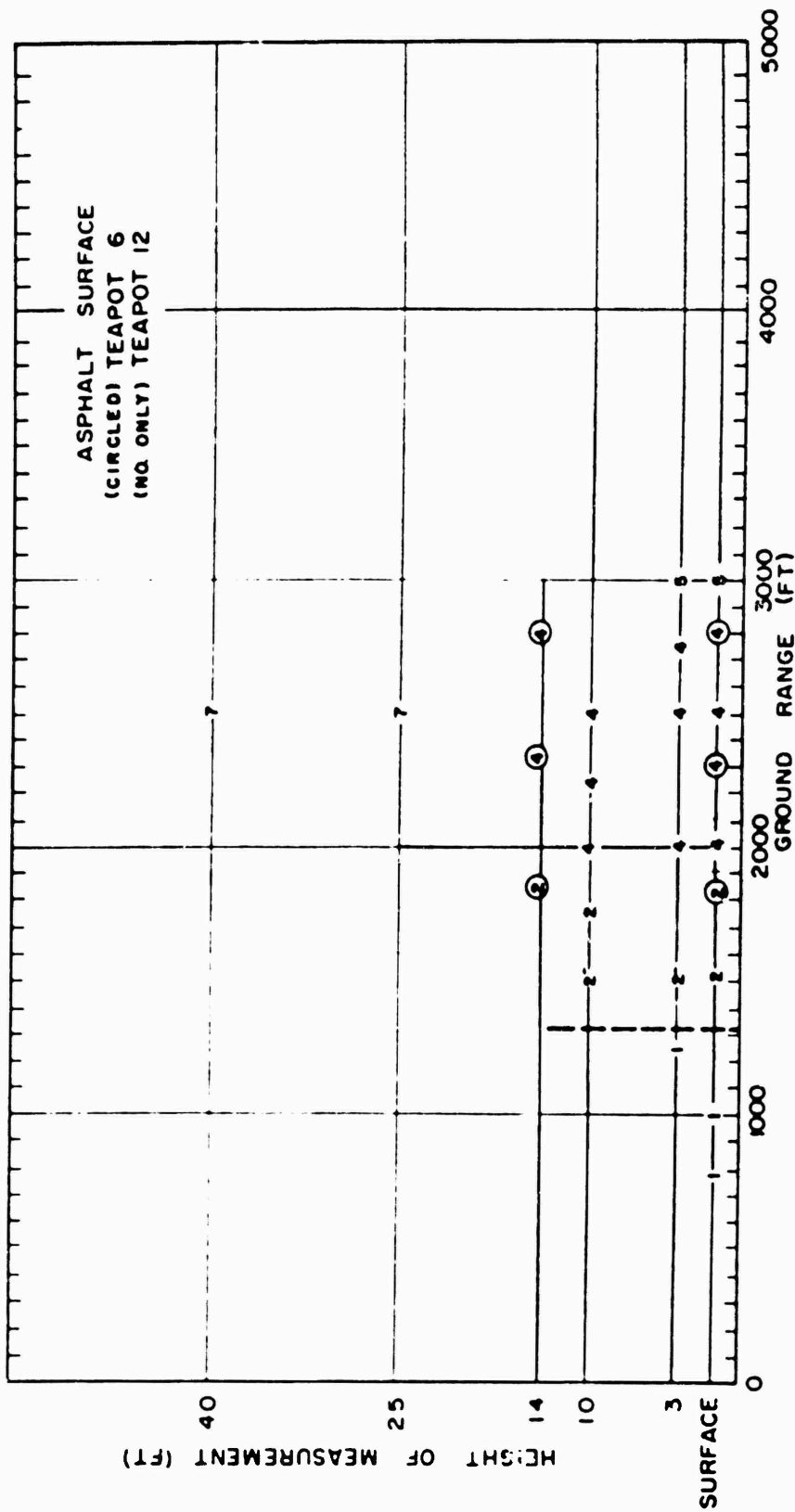


Figure 4.35 Overpressure wave form type versus ground range and gage height, asphalt line, Shots 6 and 12.

CONFIDENTIAL

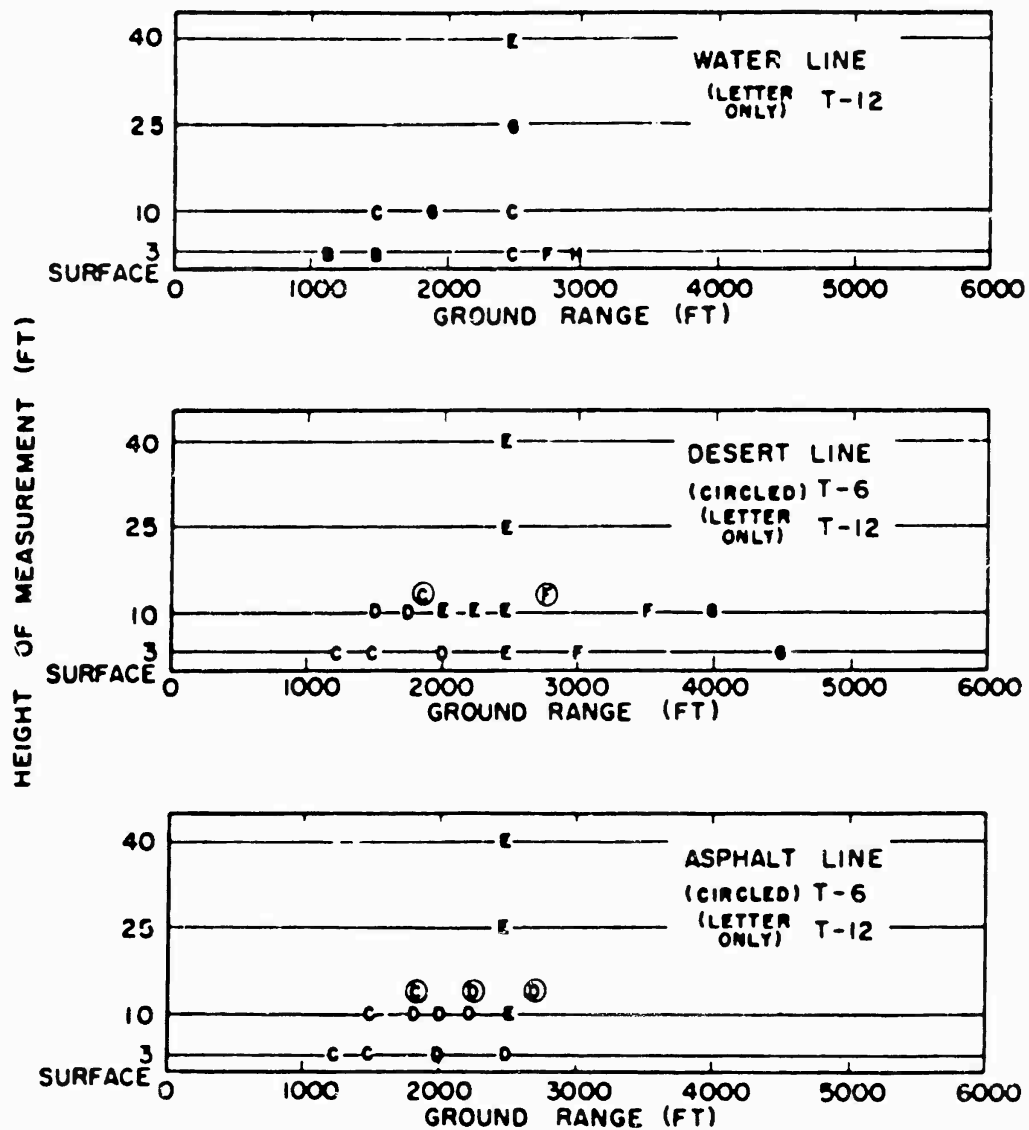


Figure 4.36 Dynamic pressure wave form type versus ground range and gage height, Shots 6 and 12.

## Chapter 5

### DISCUSSION

In this chapter, Operation Teapot Project 1.10 data will be analyzed and discussed under the following main subjects: (1) quantities derived from arrival-time data; (2) air overpressure measurements and their significance; (3) pitot-tube dynamic-pressure measurements; (4) precursor formation and effects; and (5) relations between air-pressure measurements and damage.

The analyses and discussion of Teapot results are supplemented by consideration of wave-front classification. Whenever information from projects other than 1.10 is used, the source will be credited.

#### 5.1 ARRIVAL-TIME DATA

Arrival time of the pressure wave at a static gage is probably the least ambiguous of the quantities measured on Project 1.10. Using these data from Shots 6 and 12, it was possible to obtain several useful derived quantities such as shock velocity and wave-front orientation.

5.1.1 Time of Arrival and Shock Velocity. The arrival-time data obtained from the surface-level static-pressure gages on Shot 12 are summarized in Figure 5.1. The figure illustrates the influence of surface characteristics upon time of arrival: the pressure disturbance (at same ground range) consistently arrives earliest on the asphalt line, next on the desert line, and last on the water line. The data show small differences in arrival times at the closest gage station (750 feet) on each blast line, whereas these differences increase at greater ground ranges. At the farthest instrumented station on all three lines (3000 feet), there is some evidence that the water and desert arrivals are merging, but no such tendency is apparent from the asphalt-line arrival data.

Also included in Figure 5.1 is an ideal curve for surface-level arrival times versus ground range. This curve was calculated as follows. A-scaled ground range for the onset of Mach reflection (113 feet) was calculated from the ideal critical angle (Reference 11), and the ideal arrival time at the corresponding slant range was found from a composite, nuclear, free-air, arrival-time curve.<sup>1</sup> At ground ranges between 113 and 275 feet (overpressures greater or equal to 200 psi) the ideal height of the Mach stem was obtained (Reference 11), and the arrival times at Mach stem height were found from the complete composite free-air curve. The ideal wave was assumed to be perpendicular to the ground surface so that arrival times at ground level would correspond to those just described. At ground ranges beyond 275 feet, the ideal arrival times were computed by referring to the ideal-overpressure-height-of-burst chart (Reference 12) to obtain the curve for ideal pressure versus ground range. Overpressure was converted to shock velocity using Rankine-Hugoniot relations, and arrival times were found by integrating numerically the relation:

---

<sup>1</sup> To be published.

$$t - t_0 = \int_{r_0}^r \frac{dt}{dr} \cdot dr = \int_{r_0}^r \frac{1}{v} \cdot dr \quad (5.1)$$

Where:  $t_0$  = burst time

$r_0$  = initial ground range, i. e. 275 feet (A-scaled)

These results were then transformed to Shot 12 ground-level conditions with the appropriate scaling factors.

Reference to the ideal arrival-time curve of Figure 5.1 indicates that the arrival at the first water line gage (750 feet) was almost ideal, i. e., about 118 msec compared with the 124-msec ideal value. However, at subsequent gage stations on the water line (e. g., 2,000 feet) arrival times 110 msec earlier than the ideal times were observed. Of course, the arrivals measured on the desert and asphalt blast lines deviate more seriously from ideal. There is some indication that the slopes of the curves of Figure 5.1 at long ground ranges approach the slope of the ideal curve; this will be discussed more fully in connection with shock-velocity determinations.

To obtain shock velocity versus ground range, it is necessary to differentiate the time-of-arrival curves of Figure 5.1. This was done using a method originally outlined in Reference 13 and extended in Reference 14. The method consists of calculating two forward and two backward first-order finite differences at the given point with different intervals and then obtaining the "derivatives" by a graphical interpolation. When this is done for Shot 12 data, the curves of Figure 5.2 are obtained. Also included in this figure, for comparison purposes, is the ideal shock-velocity curve from which the ideal time-of-arrival data were derived. Several statements can be made, based upon the results illustrated in Figure 5.2:

1. The asphalt and desert curves, both well above ideal, have the same general form showing asphalt-line shock velocities consistently higher.
2. At 3,000-foot ground range, asphalt and desert line velocities are approximately equal and nearly the same as the ideal velocity.
3. Actually, at ranges beyond 2,300 feet, many of the shock velocities over the desert and asphalt lines appear to be less than ideal. This result is consistent with the depressed peak pressures measured on these same blast lines.
4. The water-line curve, exhibiting a pronounced inflection in the 1,500-foot region, deviates markedly from the ideal curve at the close-in ranges. While the ideal shock velocity at 750 feet would be about 3,300 fps, the water-line data indicate a velocity of about 6,000 fps.
5. The inflection in the water-line curve is followed by velocity data which agree well with desert-line velocities at 2,000 and 2,250 feet. This behavior suggests a feed-in phenomenon or some other unusual condition occurring on the water line (see Section 5.2.2).
6. Finally, reference to Figure 5.2 and the gage records of Chapter 4 points up that agreement of an experimental shock velocity with the ideal is not a sufficient criterion for the existence of undisturbed (ideal) blast waves.

Using the shock-velocity curves of Figure 5.2 and the arrival times of aboveground gages, it is possible to determine the orientation of the wave fronts at several ground ranges for Shot 12.

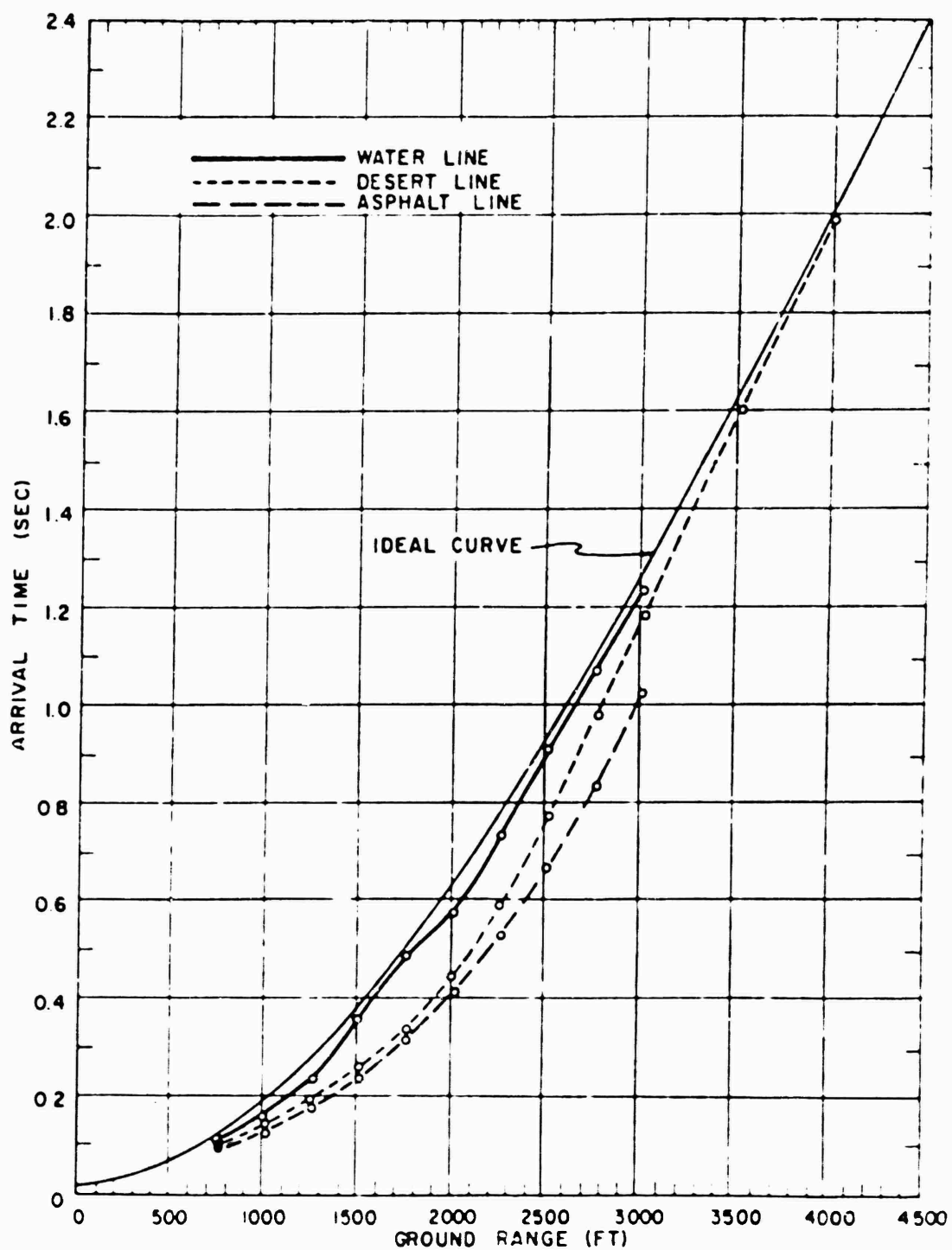


Figure 5.1 Arrival time versus ground range, Shot 12.

**5.1.2 Wave-Front Orientation.** The calculations involved in determining wave-front orientations from arrival-time data can be described as follows:

1. The as-read arrival times for each gage are corrected for differences in actual location of surface and aboveground gages using the horizontal shock velocity (Figure 5.2) at each gage station. This procedure assumes that all portions of the front are moving at the same velocity, an assumption which is verified when aboveground trace velocities are computed.
2. Using the corrected arrival times and the arrival at the surface gage as the station reference, the time interval ( $\Delta t$ ) for each level is determined.
3. The  $\Delta t$  values corresponding to each level are multiplied by the shock velocity to obtain  $\Delta R$ .

The results of these calculations for Shot 12 are shown in Table 5.1 and plotted in Figures 5.3, 5.4, and 5.5, in the order desert, water, asphalt.

The desert-line results (Figure 5.3) present a picture of wave-front orientations similar to those observed on shock photographs. Angles of the wave fronts taken from Naval Ordnance Laboratory (NOL) photographic data (Reference 15) at ground ranges near 1,500 feet and 2,000 feet are shown in the figure, and the agreement is quite good. The small difference in orientation at 1,500 feet may be explained, as noted by NOL, by the wave fronts observed on the photographs often being obscured by dust near the ground surface; thus, since the angle determined by the 3- and 10-foot-level gage arrivals is nearly equal to the NOL wave-front angle, the two methods are essentially equivalent except for regions close to the ground. Figure 5.3 shows how the wave-front orientation changes as the wave travels out to increased ranges. The angle between the front and the ground surface gradually increases so that at 3,500 feet the front is approximately perpendicular to the ground plane. It is interesting that at 2,500 feet (the station with the most aboveground data) the wave-front angle was fairly constant up to 25-foot height.

The water-line wave-front data (Figure 5.4) are quite different from the desert-line results (no comparable water-line photographic data are available). At 1,500-foot ground range, the front orientation indicates a pronounced toe near the ground surface which was running out ahead of the aboveground portion of the wave front. This behavior is not evident on the desert line; on the contrary, there is some indication that the wave front was concave downward (Figure 5.3). The front orientation at the 2,000-foot water line station is not easily explained; the data indicate a complete reversal of behavior between 1,500 and 2,000 feet on this blast line. In a sense, this treatment is merely another way of pointing out the anomalous behavior of the water-line shock velocity in this ground-range interval (see Figure 5.2). Also, the Project 1.11 pitch gage measurement at this 2,000-foot station is consistent with the wave-front orientation: i. e., an initial negative pitch was recorded.

A pressure measurement on a Program 3 structure (3.2a3), also at 2,000 feet on the water line but offset about 80 feet from the Stanford Research Institute (SRI) gage station, yielded a relatively clean shock record arriving about 25 msec after the Project 1.10 arrival time. The Project 1.10 records (25 P3 and 25 P10) definitely could not be classified as clean wave forms. This information, as well as some discussions which follow later in this report, emphasizes the severe differences in blast behavior which may become evident over distances of less than 100 feet on the same blast line.

The wave-front orientation at 2,500 feet over the water line is essentially perpendicular to the ground plane up to a height of 40 feet. Thus, there is some indication that at this range there is less tendency for localized disturbances.

Figure 5.5 (wave-front orientations over the Shot 12 asphalt line) indicates that the angle of the front remains approximately constant out to 2,500-foot range. The compari-



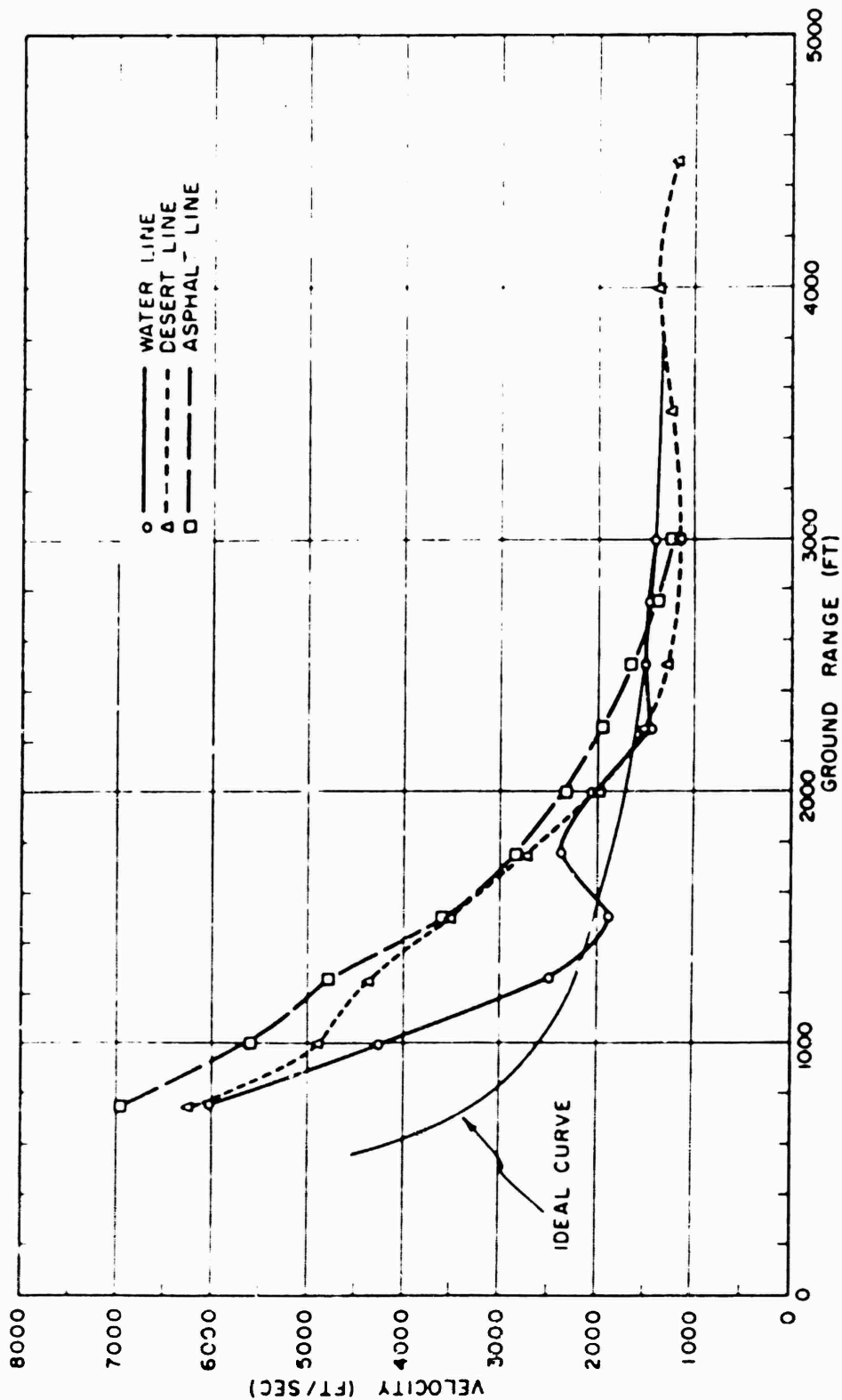


Figure 5.2 Shock velocity versus ground range, Shot 12.

CONFIDENTIAL

son with NOL shock photography (at 1,500 feet) indicates a behavior similar to that observed on the desert line (Figure 5.3). However, unlike the desert case, the orientation at 2,500 feet shows little indication of approaching a perpendicular configuration—more evidence that the deviation of airblast phenomena from ideal over the asphalt surface persisted to larger ground ranges, compared with the results over the water and desert surfaces.

## 5.2 OVERPRESSURE MEASUREMENTS $p$ (pitot)

In previous weapon-effect tests, it has been possible to describe the essential characteristics of most of the overpressure results using a few physical quantities such as peak pressure, positive-phase duration, and positive impulse. The data lent themselves well to such description because, with few exceptions, pressure records were classical in form.

With these data, plots of peak pressure versus ground range, impulse versus ground range, etc., were constructed which became the bases for military planning, damage analysis, and comparisons with other test results.

It scarcely needs stating that the Teapot (specifically Project 110) pressure records are overwhelmingly nonclassical in form. The classical physical quantities seldom have corresponding counterparts on a disturbed (non-classical) airblast record. That is, a quantity such as maximum airblast (static) pressure loses much of its value as a dependable and useful parameter when, for disturbed blast waves, the peak pressure may occur almost any time after blast arrival and the maximum may be associated with either a sharp-peaked or a broad-humped pressure rise. In other words, when dealing with non-classical wave forms it is virtually impossible to select a set of quantities which describe the phenomenon unambiguously and which can be useful in comparisons with more classical results.

The above limitations on conventional airblast parameters do not preclude the need for data to assist damage analysis and military planning. Therefore, a revised method of data presentation is described in the following section to eliminate some of the ambiguities inherent in the usual, unqualified peak-pressure-versus-distance curves.

**5.2.1 Effects of Surface Characteristics.** In Section 4.5.2, it was shown that wave-form development was different over the desert, water, and asphalt surfaces. Figures 5.6, 5.7, and 5.8 are examples of an effort to include the wave-form differences on the conventional peak-pressure-versus-ground-range plot. The various symbols on these plots indicate the maximum overpressure recorded at each ground range, and the numbers inside the symbols designate the wave-form type associated with each record. It should be emphasized that the overpressure data taken from pitot-tube measurements have been corrected for angle of pitch and Mach number.

The Shot 12 water-line maximum-overpressure data shown in Figure 5.6 indicate that aboveground peak pressures were significantly higher than those measured at the ground surface. The decrease of maximum pressure with ground range appears to be smooth, exhibiting none of the inflections or humps which are so often observed on tower shots and are particularly evident near 7- to 8-psi pressures on the desert-line plot of Figure 5.7. This latter figure illustrates clearly that the maximum-pressure behavior over the desert was not as orderly as it was over the water. It is not possible, from the figure, to make a definite statement concerning the relative magnitudes of aboveground and surface-level pressures; however, it is clear that beyond 3,000-foot ground range the peak pressures at all heights are approximately equal. The Teapot Shot 12 asphalt-

TABLE 51 WAVE FRONT ORIENTATION DATA

Gage	Exact Ground Range	Arrival Time	Trace Velocity	Nominal Ground Range	Arrival at Nom Ground Range		$\Delta R$
	feet	sec	ft. sec	feet	sec	sec	feet
Desert Line							
5B	1800.2	0.265	3820	1500	0.2649	0	0
5P3	1497.4	0.265		1500	0.2657	0.0008	2.9
5P10	1497.4	0.268		1500	0.2607	0.0030	13.4
7B	2000.2	0.4525	1990	2000	0.4524	0	0
7P3	1997.4	0.4525		2000	0.4538	0.0014	2.0
7P10	1997.4	0.4588		2000	0.4578	0.0084	10.8
9B	2500.4	0.791	1270	2500	0.7907	0	0
9P3	2497.4	0.790		2500	0.820	0.0012	1.6
9P10	2497.4	0.782		2500	0.7840	0.0023	4.2
9P25	2497.4	0.7998		2500	0.7906	0.0090	12.4
9P40A	2497.4	0.7813		2500	0.7935	0.0120	19.2
12B	2997.4	1.192	1180	3000	1.1943	0	0
12P3	2997.4	1.192		3000	1.1642	0	0
12P10	2997.4	1.184		3000	1.1982	0.0020	2.4
15B	3600.2	1.0118	1240	3600	1.0113	0	0
15P10	3497.4	1.010		3600	1.0121	0.0008	1.0
17B	4499.6	2.3875	1170	4500	2.3878	0	0
17P3	4497.4	2.386		4500	2.3882	0.0004	0.47
Water Line							
25B	1500.2	0.3688	1890	1500	0.3684	0	0
25P3	1497.4	0.372		1800	0.3744	0.0060	18.1
25P10	1497.4	0.376		1800	0.3774	0.0110	29.7
27B	1999.6	0.586	2640	2000	0.5892	0	0
27P3	1997.4	0.5865		2000	0.5876	-0.0014	-2.0
27P19	1997.4	0.5888		2000	0.5876	-0.0014	-2.8
29B	2499.6	0.914	1500	2500	0.9143	0	0
29P3	2497.4	0.913		2500	0.9147	0.0004	0.0
29P10	2497.4	0.913		2500	0.9147	0.0004	0.0
29P25	2497.4	0.913		2500	0.9147	0.0004	0.0
29P40A	2497.4	0.913		2500	0.9147	0.0004	0.0
32BA	3000.2	1.246	1419	3500	1.2459	0	0
32P3	2997.4	1.248		3500	1.2468	0.0009	1.3
Asphalt Line							
45B	1499.0	0.241	3560	1500	0.2411	0	0
45P3	1497.4	0.241		1500	0.2417	0.0006	2.1
45P10	1497.4	0.2443		1500	0.2432	0.0041	14.6
47B	2000.2	0.410	2320	2000	0.4109	0	0
47P3	1997.4	0.410		2000	0.4191	0.0012	2.0
47P10	1997.4	0.421		2000	0.4221	0.0043	9.7
49B	2500.2	0.674	1640	2500	0.6729	0	0
49P3	2497.4	0.674		2500	0.6756	0.0017	2.0
49B10	2500.2	0.679		2500	0.6799	0.0080	8.3
49P25	2497.4	0.688		2500	0.6896	0.0157	26.1
49P40	2497.4	0.698		2500	0.6966	0.0227	37.7
52B	3000.2	1.034	1230	3000	1.0338	0	0
52P3	2997.4	1.032		3000	1.0341	0.0063	6.4

line overpressure data (Figure 5.8) indicate a slight inflection in the surface-level peak-pressure curve near 2,000-foot ground range. Also, in comparison with ground level, there is an indication of a small but consistent increase in peak pressure at the 3-foot level.

The Shot 6 maximum static pressures versus ground range are shown in Figures 5.9 and 5.10. Data (Figure 5.9) from both the desert and asphalt lines, although limited, indicate consistently higher peak pressures at the aboveground (10-foot) levels than at the surface level.

Figure 5.10 shows the comparisons of Shot 6 peak pressures along the two blast lines measured at 10 feet and the surface. The surface-level pressures of Figure 5.10 indicate that the maximum values over the asphalt were greatly depressed; the presentation also indicates that the wave forms along the two blast lines were not significantly different. In Figure 5.10, the close-in (1,300-foot ground range) overpressure records on the two lines compare well in magnitude and form. Also included on this latter Shot 6 figure is an ideal peak-overpressure-versus-ground-range curve; this was obtained from the height-of-burst curves of Reference 12. At both gage heights, the peak pressure at 2,000 feet on the desert line agrees well with the ideal curve; however, the wave-form type (Type 6 in both cases; see Figure 4.29) is not ideal, emphasizing the value of a method which includes wave-form classification as well as pressure magnitude.

The comparisons of Shot 12 peak overpressure measured over the three blast line surfaces are presented in Figures 5.11, 5.12, and 5.13. The surface-level results of Figure 5.11 are comparable in both wave form and magnitude at the 750- and 1,000-foot-ground-range stations, but the pressures are noticeably lower than the ideal curve. It appears that at ground ranges exceeding 1,000 feet the effects of surface characteristics begin to manifest themselves markedly. At specific ground ranges, the curves, in order of decreasing peak pressures, are first ideal, then water, desert, and asphalt. It is interesting to note that at 3,000 feet, even though the water-line record exhibits classical form (i. e., Type 8), the peak pressure observed is slightly less than ideal. However, the desert-line 4,500-foot gage recorded a maximum pressure equal to ideal, although the wave form was not classic.

Figure 5.12 (3-foot-level peak overpressures, Shot 12) indicates that some above-ground water-line pressures were equal to or larger than ideal. The desert and asphalt results show a similar behavior to that evident for the surface-level case (Figure 5.11) where the two curves cross at 2,500 feet and then diverge markedly at 3,000-foot ground range. The asphalt maximum pressures decrease steadily with increased range, whereas the desert results indicate a definite inflection near 2,500 feet.

The curves of Figure 5.13 (10-foot-level) exhibit some of the same characteristics; one important deviation is the severe depression of desert-line pressures at 1,500- and 1,750-foot ground ranges. In addition, on the Shot 12 desert line a nonideal wave form (Type 4) produced a peak pressure (about 7 psi) which agrees well with the ideal curve (Figure 5.13); this same behavior was observed on Shot 6 (see Figure 5.10) at about 13-psi overpressure.

In summary, the following general statements apply to the Project 1.10 maximum-overpressure measurements: (1) peak pressures were depressed most severely on the asphalt line and least on the water line; (2) aboveground maximum pressures were higher than those measured at the ground surface; (3) the familiar inflection observed on the desert-line plot of peak pressure versus ground range is not apparent for water and asphalt results; and (4) maximum overpressures comparable to the predicted ideal pressures are not always associated with classical wave-form records.

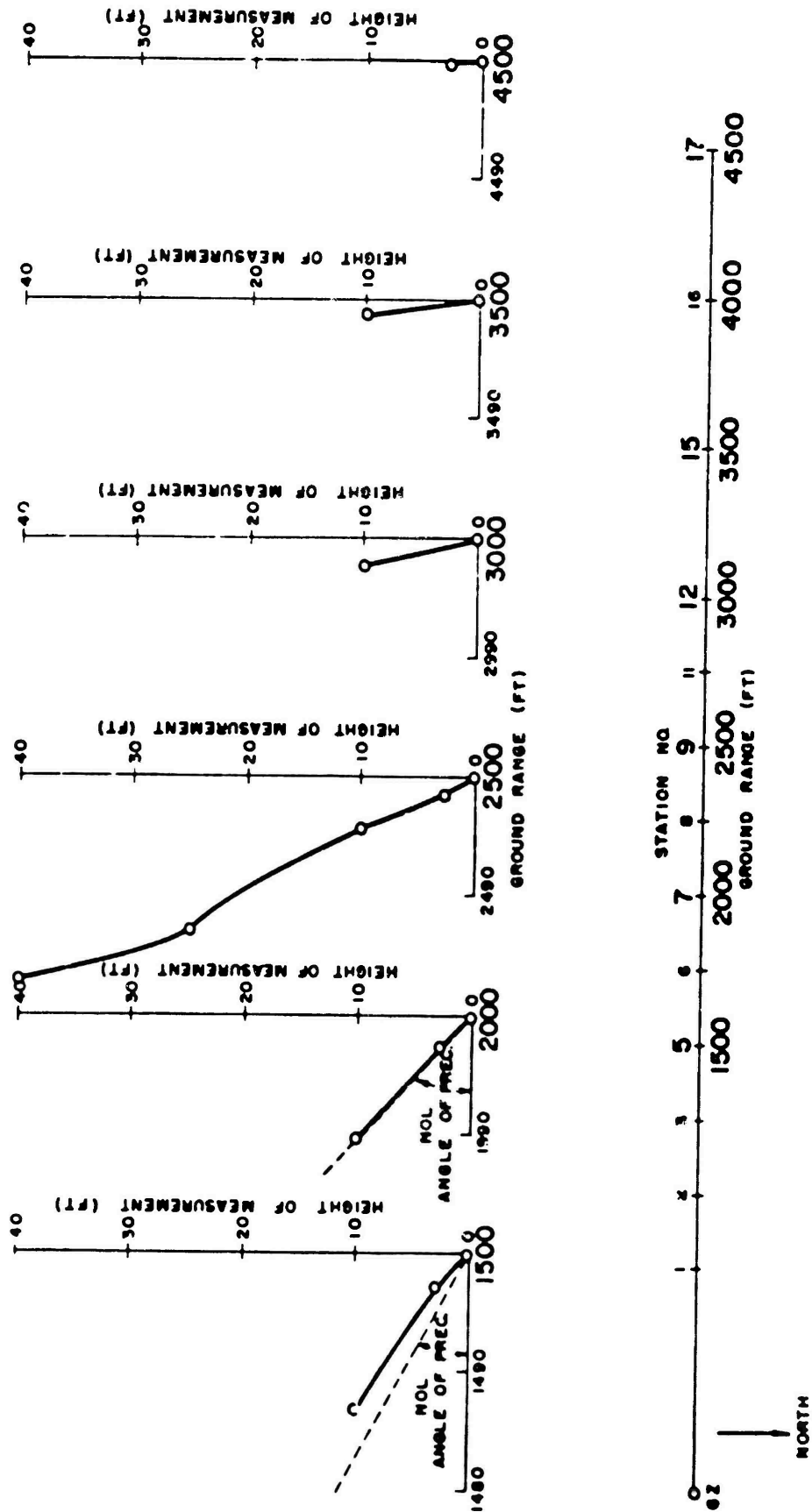


Figure 5.3 Wave front orientations, desert line, Shot 12.

CONFIDENTIAL

**5.2.2 Additional Surface Effects and Cross-Feed.** Additional insight may be gained into the effect of surface characteristics upon Shot 12 overpressure measurements by considering the Ballistics Research Laboratories (BRL) investigation of blast-wave symmetry. For this purpose, BRL installed 36 surface-level, self-recording pressure gages on a 220-degree arc located 2,500 feet from ground zero. The peak pressures recorded on the 2,500-foot gage ring (Reference 12) are shown in Figure 5.14. The figure shows the arcs subtended by the water and asphalt surfaces at 2,500-foot radius and the arcs which the blast wave presumably traveled over a portion of the water and asphalt surfaces near ground zero. Also included are the Project 1.10 electronic-gage peak-pressure measurements at the same ground range and the wave-form classifications to be assigned to each pertinent pressure-time record. Since decisions on wave-form types are usually

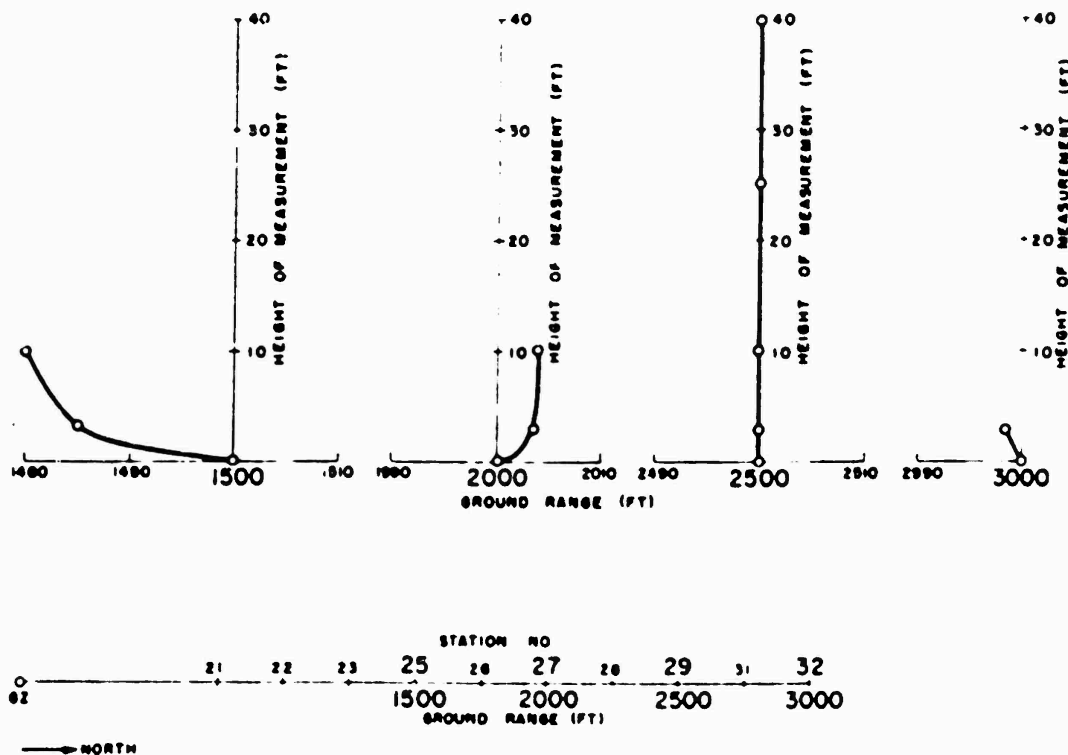


Figure 5.4 Wave front orientations, water line, Shot 12.

guided by the pressure-time results immediately preceding and/or following the record to be classified, the classification task for the BRL arc records was particularly difficult and was done with some loss in accuracy.

The maximum overpressures shown in Figure 5.14 indicate that the BRL and Project 1.10 results, where comparisons are possible, agree quite well; however, the overall picture is confusing. The figure shows a rather orderly behavior across the asphalt surface with the expected depressed peak pressures in evidence; however, the BRL gages at their Stations 27 through 22 indicate an abrupt increase in peak pressure in the desert-asphalt transition sector. Continuing around the gage arc toward the main desert blast line, it is obvious that both the BRL and Project 1.10 pressures are again depressed; in



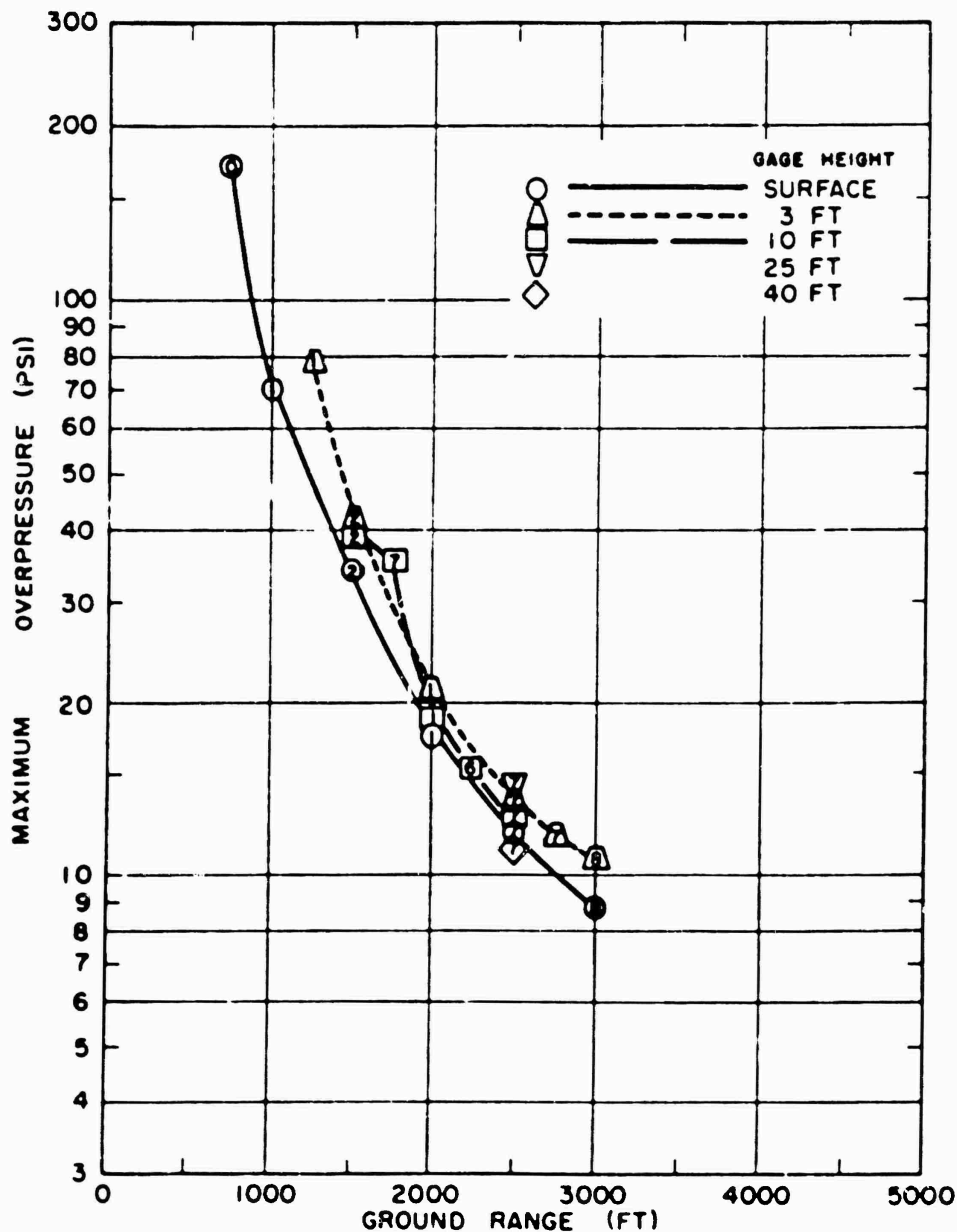


Figure 5.6 Maximum overpressure versus ground range, water line, Shot 12.

fact, peak pressures measured here are not unlike those measured near the center of the asphalt surface. At gage Stations 17 through 12 (BRL), although the results are irregular, there is evidence that maximum pressures were significantly higher in this desert sector. Proceeding around toward the water surface, both BRL and Project 1.10 overpressure data show large variations in magnitude, even from pressure gages located near the water blast line. Referring to wave-form classifications included in Figure 5.14, it is apparent that there is some correlation between the higher peak pressures and the gage records which exhibit more advanced wave forms, i. e., Types 6 and 7. This is thought to be characteristic of the so-called cleaning-up region of the disturbed-blast-wave evolution.



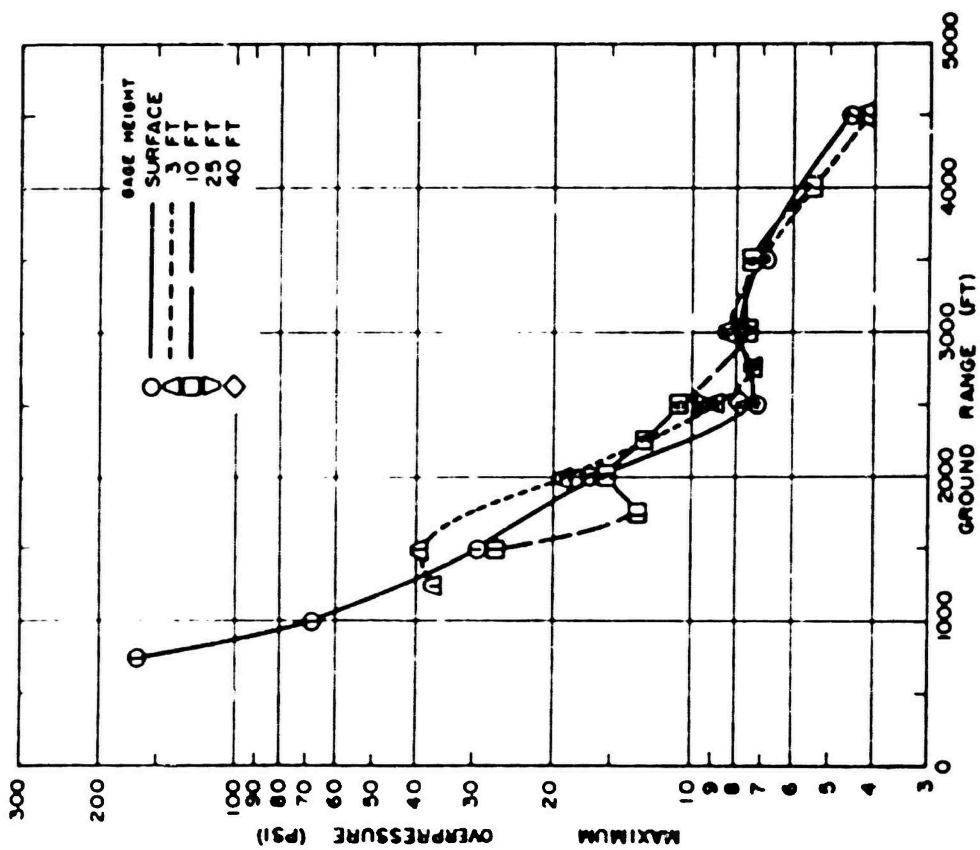


Figure 8.7 Maximum overpressure versus ground range, desert line, Shot 12.

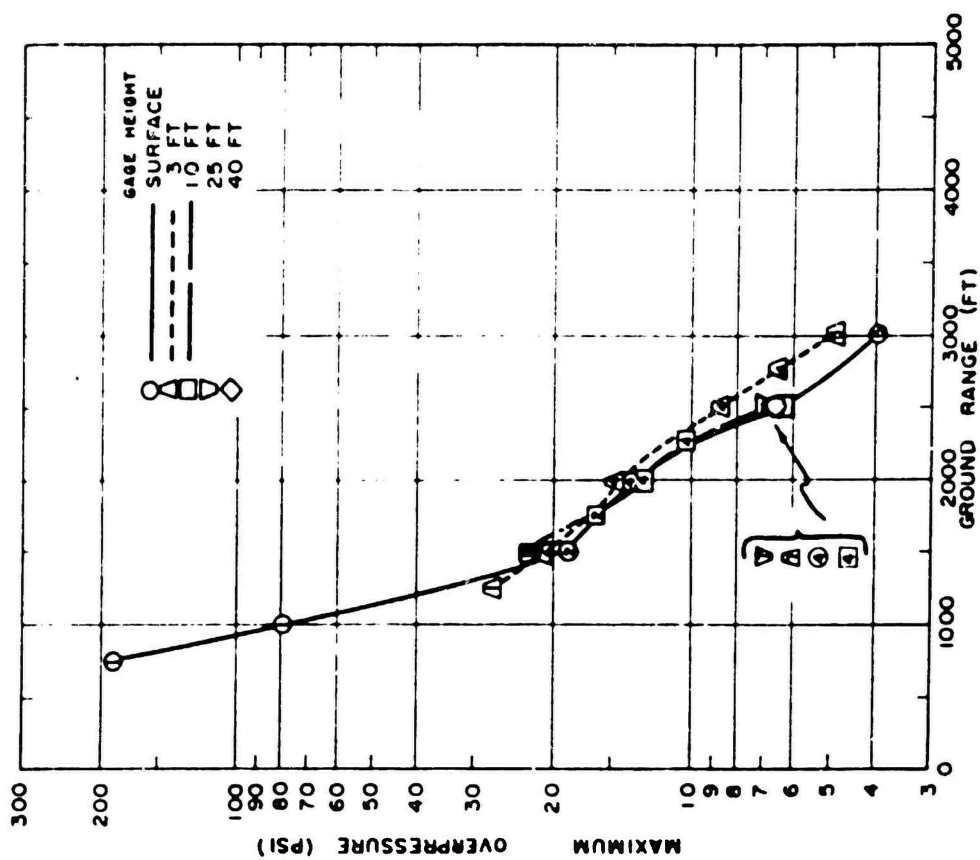


Figure 8.8 Maximum overpressure versus ground range, asphalt line, Shot 12.

DECLASSIFIED

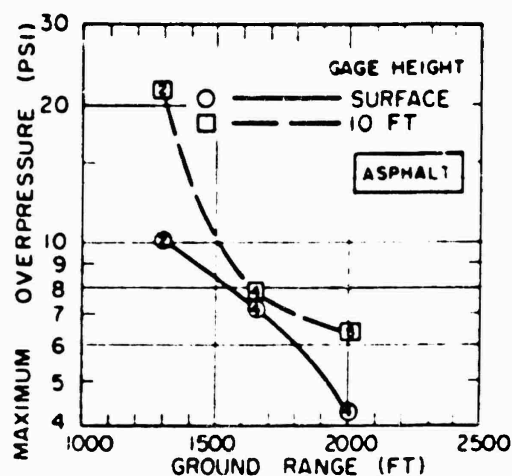
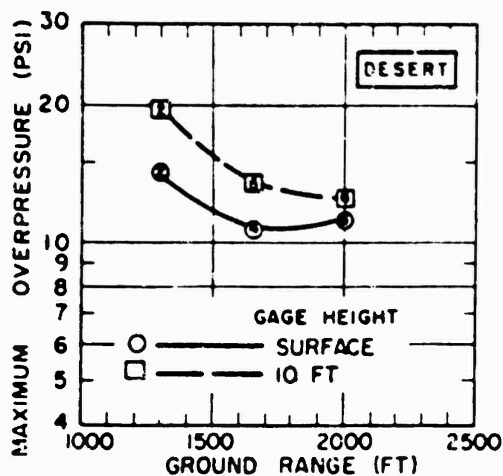


Figure 5.9 Maximum overpressure versus ground range, surface and 10-foot level, Shot 6.

The Shot 12 area map (Figure 5.15) might help to explain the phenomena observed by the BRL instrumentation. This area map shows portions of the Frenchman Flat test area which have undergone stabilization for Teapot and previous operations; also shown on the map, for easy comparison, are the BRL gage-station locations around the instrumented arc. Figures 5.16 and 5.17 are postshot area photographs showing the character and extent of the stabilized areas. It may be more than mere coincidence that most of the BRL gages which recorded the higher peak overpressures were those located near or on a stabilized pad. The obvious conclusion is that abrupt localized changes in the characteristics of the surface over which a blast wave is traveling may have significant effects upon the peak overpressure and time history of a measurement taken in the near vicinity of the altered surface. Nonetheless, it should be emphasized that the symmetry measurements

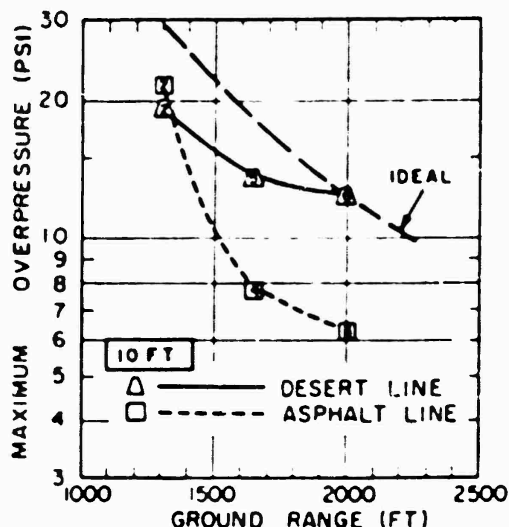
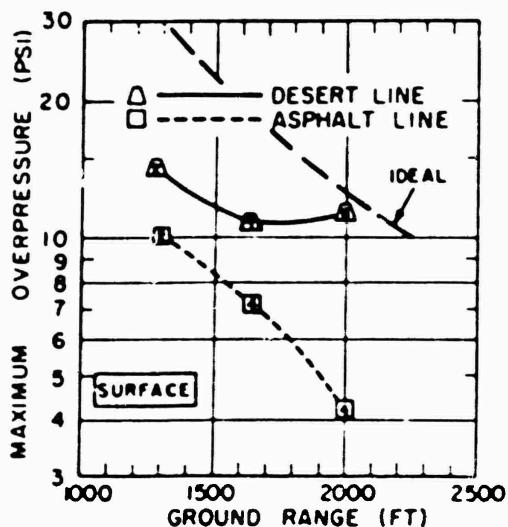


Figure 5.10 Maximum overpressure versus ground range, desert and asphalt, Shot 12.

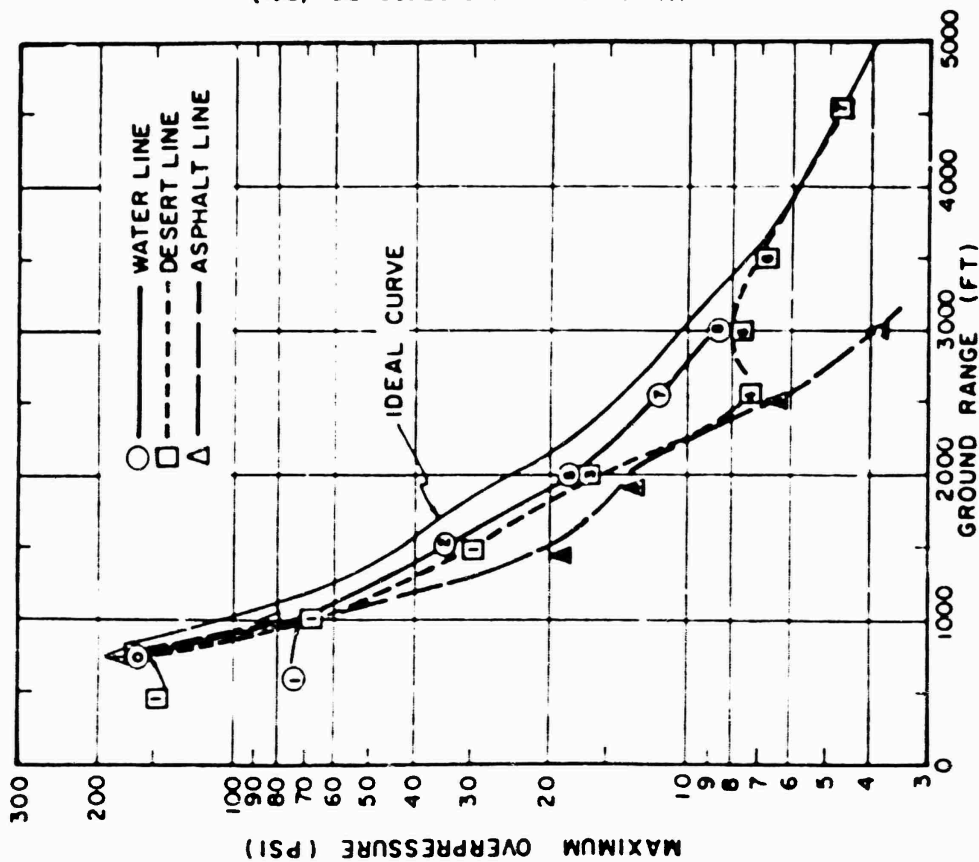


Figure 5.11 Maximum overpressure versus ground range, surface level, Shot 12.

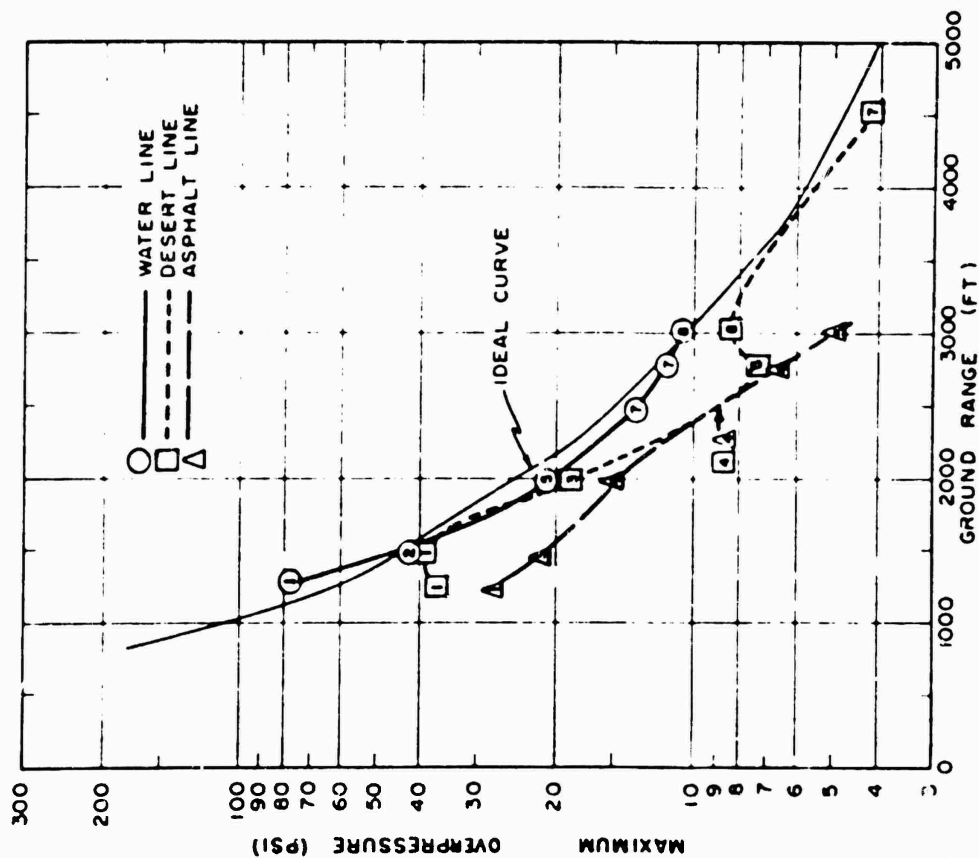


Figure 5.12 Maximum overpressure versus ground range, 3-foot level, Shot 12.

0000000000

taken on only one shot in the test series were available and at a ground range (2,500 feet) where the blast wave disturbances were somewhat spent. Therefore, it is recommended that similar instrumentation be included on future tests, both within and beyond the regions of disturbed blast waves.

The above discussion logically leads to a consideration of the results obtained from the Shot 12 offset gages at 1,500 and 2,500 feet on the water blast line (see Figure 2.4). These gages were installed for the purpose of detecting the possible cross-feed of blast disturbances from the desert area to the water area. One method for analysis of cross-feed effects makes use of the arrival time and position data to compute interval velocities between the desert-water interface and the various gage stations. A summary of these velocities is listed in Table 5.2. The velocities have been determined assuming blast-

TABLE 5.2 CROSS-FEED DATA, SHOT 12

Gage	Surface	Ground Range	Arrival Time	Position	Distance from Edge	Velocity	Wave-From Type
		feet	sec		feet	fps	
21B	Water	750	0.1195	Blast line	400	27,000	0
1B	Desert	750	0.104	Blast line	0*		1
22B	Water	1000	0.1096	Blast line	400	19,500	1
2B	Desert	1000	0.140	Blast line	0*		1
23P3	Water	1250	0.255	Blast line	400	7,850	1
2P3	Desert	1250	0.302	Blast line	0*		1
25P3Y	Water	1500	0.3375	Offset	125	1,350	1
25P3X	Water	1500	0.3715	Offset	225	2,110	2
25P3	Water	1500	0.373	Blast line	400	3,700	2
2P3	Desert	1500	0.365	Blast line	0*		1
27B	Water	2000	0.589	Blast line	400	2,930	1*
7B	Desert	2000	0.4525	Blast line	0*		3
29P3Y	Water	2500	0.914	Offset	150	1,130	7
29P3X	Water	2500	0.903	Offset	270	2,200	4
29P3	Water	2500	0.913	Blast line	400	3,010	7
9P3	Desert	2500	0.700	Blast line	0*		4

\* Blast-wave symmetry assumed

† A hybrid form of Type 1

wave symmetry, so that desert blast-line arrival times are the assumed arrival times at equal radii near the desert-water interface.

If a disturbance traveling over the desert surface is to feed-in energy across the desert-water interface, this energy would be propagated over the water with the local sound velocity. Table 5.2 indicates that Shot 12 times of arrival observed at the first three water-line stations (750- and 1,250-foot ranges) yield propagation velocities too high to be identified with sonic velocity. Therefore, the first disturbances as well as a major portion of the pressure-time history observed at these stations are free of cross-feed effects. However, Table 5.2 shows that at 1,500-foot ground range the offset gage nearest the interface (25P3Y) yields an arrival time which suggests cross-feed of energy at this gage. The other offset gage (25P3X) at this range and the blast-line gage (25P3) show later arrivals; however, it is probable that the cross-feed is manifest at some time following blast arrival on the gage records obtained at these stations.

The foregoing is supported by wave-form observations on the water line (Section 4.5.2); that is, at 1,500 feet the water-line offset gage closest to the desert is a Type 1, similar to the desert blast-line record, whereas the other offset gage trace (25P3X) resembles the measurement obtained on the water line.

Analysis of wave forms at 2,000 feet produces evidence of effect of cross-feed upon

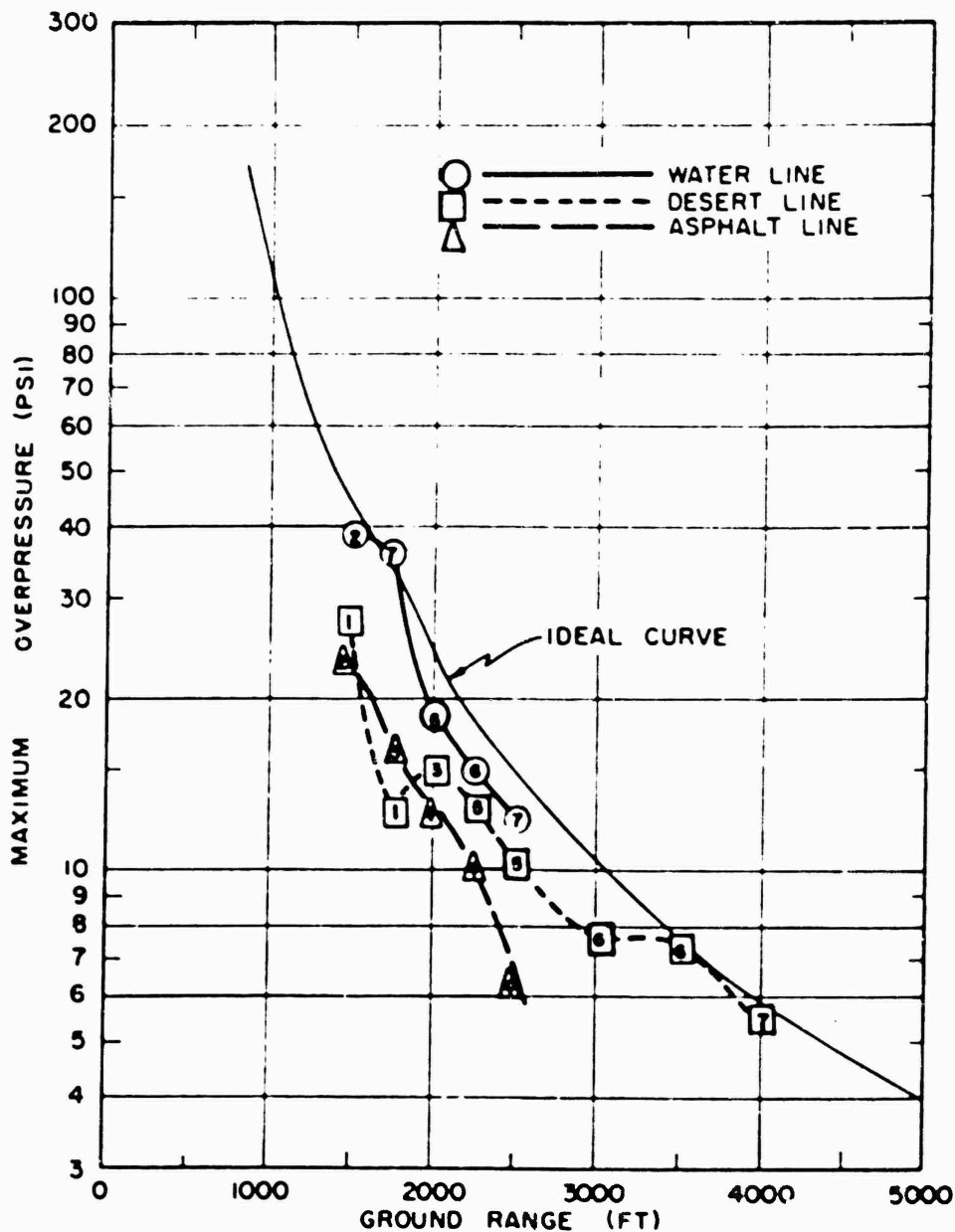


Figure 5.13 Maximum overpressure versus ground range, 10-foot level, Shot 12.

a blast-line gage record obtained over the water on Shot 12. The unsmoothed records (Appendix B) show that the 27B gage record (2,000 feet) is not a true Type 1 form because approximately 100 msec after arrival the pressure-time trace takes on the appearance of the 7B gage record (Type 3) which was recorded at the same ground range over the desert. At 2,500-foot ground range, the interval velocities (Table 5.2) are less than those for comparable gages at 1,500 feet. However, the trend is the same, and although the wave forms do not appear to be completely consistent, the BNL gage arc at this same ground range produced similar wave-form variations over similar gage-station separations.

In conclusion, it can be established with some assurance that the observation over the water line of earlier-than-ideal arrival times and Type 1 wave forms was not due to

cross-feed from the desert surface. Since these observations are identified with the propagation of a precursor wave, it can be stated that a precursor formed over the water on Shot 12 and was observed at the close-in ground ranges.

A postshot view of the water line, looking toward ground zero, is shown in Figure 5.17, while Figure 5.18 is a postshot view of the Shot 12 asphalt line looking south toward ground zero. The highest gage tower, visible just left of center in the photograph, is the Project 1.10 2,500-foot gage station. It appears that the blast wave lifted off chunks of the surface, leaving deep pocks in the asphalt. However, the pocks are not distributed in a random fashion over the line; instead, there is a rather high density out to about 2,000 feet, then a relatively unmarked region out to about 2,800 feet, where a good deal of the asphalt surface is missing.

**5.2.3 Overpressure Decay Behind Shock Front.** An analytical representation of the overpressure profile of the classical shock wave at a given distance from an explosion is provided by:

$$p = p_m (1 - t/\Delta t) e^{-t/\Delta t} \quad (5.2)$$

Where:  $p$  = overpressure at time  $t$

$p_m$  = peak value of the overpressure at  $t = 0$

$t$  = time measured from shock arrival

$\Delta t$  = positive phase duration of the blast wave (Reference 16)

Equation 5.2 is approximately valid for overpressures not exceeding 25 psi. In a theoretical paper on strong-shock spherical blast waves (Reference 17), some relations are derived for the pressure decay behind a spherical shock moving through an ideal gas medium. It shows that for peak pressures above one atmosphere the decay is not a simple exponential, since the early portion of the pressure-time function decays more rapidly than do the later parts. The results of Reference 17 and Equation 5.2 become identical when:

$$\frac{p_o}{p_1} = 0.5 \quad (5.3)$$

Where:  $p_1$  = ambient pressure in front of the shock front

Both of these methods of computation are strictly limited to the case of free-air wave propagation. Thus, any application of the methods to shock phenomena which are influenced by a ground plane (i.e., in regular or Mach reflection regions) necessarily involves an approximation of unknown magnitude. Nevertheless, it seems worthwhile to make some comparisons between theory and experiment using some of the Shot 12 data.

Comparisons of the calculated and measured decay of overpressure versus time on Shot 12 are shown in Figures 5.19 and 5.20. Only those records which appeared reasonably undisturbed were selected for analysis. Figure 5.19 includes all of the Shot 12 water-line records which were analyzed for pressure decay. For the records at 750 (21BA) and 1,750 feet (26P10A), as would be expected on the basis of their high peak pressures, the method of Reference 17 agrees better with the experimental results than does the method

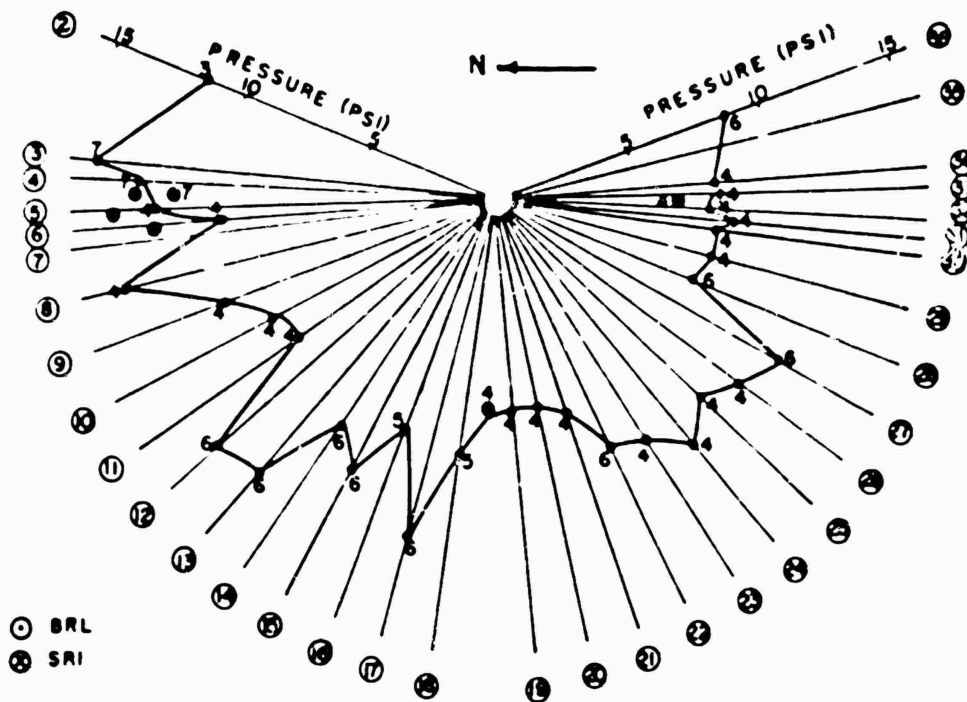


Figure 5.14 Results from BRL measurements on gage-arc, Shot 12.

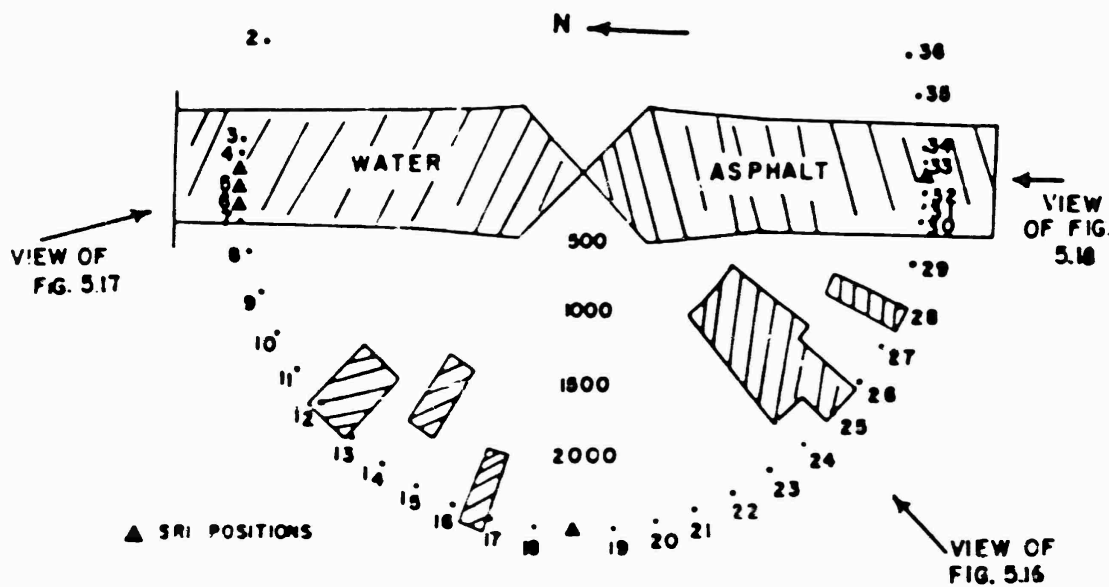


Figure 5.15 Area layout of Shot 12 test area, showing stabilized areas.

of Equation 5.2. At subsequent ground ranges on the water line (2,500 feet and beyond), the differences between the two computation methods appear small; however, if a choice must be made, it seems that the method of Equation 5.2 corresponds best with the experimental data. The gage records at 2,500 (29P3Y and 29P40A) and 2,750 feet (31P3) exhibit a definite nonclassical behavior in the first 100 msec after shock arrival. That is, if the measured peak pressure is taken as the basis for subsequent calculation, there appears to be a pressure hump when comparison is made with computed decay. However, it could equally well be assumed that these records (i. e., 29P3Y, 29P40A, and 31P3) are the result of a rounding-off of the more classical sharp-peaked wave form. If this latter con-

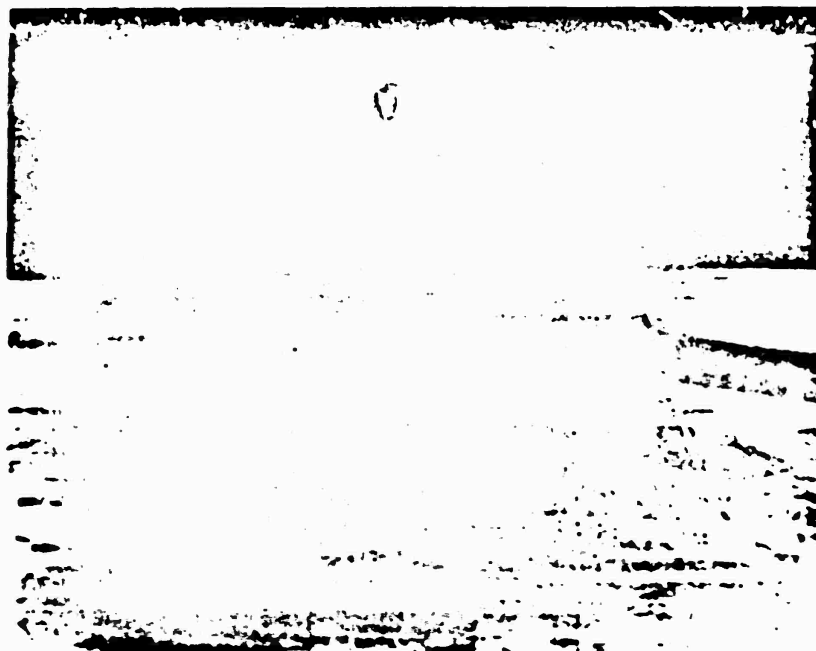


Figure 5.16 Post-Shot 12, desert line, looking northeast toward ground zero.

dition is considered, the decay calculation must be based upon an extrapolated (see Figure 5.19) peak pressure. It is evident from the figure that the decay computed from the extrapolated maximum pressure agrees well with the experimental record beyond about 150 msec.

The Shot 12 desert-line records (Figure 5.20) agree well with both methods of computation of overpressure decay. Since the peak pressures of the records approximately satisfy Equation 5.3 ( $p_m = 6.5$  psi for Shot 12), it is to be expected that the two methods would be equivalent. Figure 5.20 also includes one gage record (49P40) obtained on the asphalt line. Because of the base-line corrections which were necessary for this record, the positive-phase duration is in doubt. For this reason, the Equation 5.2 decay calculation was performed using three possible positive durations; it is obvious from the figure that the gage record does not agree with any of the computed decay curves, indicating that deviations from the classical pressure-time wave form were most complete over the asphalt surface.

The fact that the Reference 17 method of calculating overpressure decay behind the shock front appears to agree best with experiment at high pressures leads to the conclusion





Figure 5.17 Post-Shot 12, water line, looking south toward ground zero.



Figure 5.18 Post-Shot 12, asphalt line, looking north toward ground zero.

that pressure-time records at close-in ground ranges (less than 750 feet) would probably exhibit the peaking effect shown on the 21BA record (Figure 5.19).

**5.2.4 Comparisons with Previous Data.** These comparisons can be made by considering such properties as pressure-time wave form, maximum overpressure versus ground range, impulse, and positive duration. The comparisons are made using, in all cases, the A-scaled data. Of course, only desert-line Teapot data are used.

For A-scaled comparisons, the pertinent shots may be divided into two main A-scaled classifications: (1) shots which have similar A-scaled burst heights, but different yields and (2) shots which have similar yields, but different A-scaled burst heights. The descriptions of these pertinent shots are summarized in Table 5.3. The wave-form comparisons

TABLE 5.3 SHOT DESCRIPTIONS FOR DATA COMPARISONS

Shot	Yield	Height of Burst	A-Scaled Height of Burst	Classification
	kt	feet	feet	
Teapot Shot 6	8.1	500	337	Variable Yield
Upshot-Knothole Shot 10	14.9	834	304	Similar A-scaled Height of Burst
Tumbler Shot 4	19.0	1,040	363	Variable Yield
Upshot-Knothole Shot 11	60.0	1,334	317	Similar A-scaled Height of Burst
Teapot Shot 12	23	400	135	Variable Yield
Upshot-Knothole Shot 1	18.2	300	113	Similar A-scaled Height of Burst
Upshot-Knothole Shot 1	18.2	300	113	Similar Yield
Upshot-Knothole Shot 10	14.9	834	304	Variable A-scaled Height of Burst
Upshot-Knothole Shot 9	26	1,433	764	Similar Yield
Teapot Shot 13	23	400	135	Variable A-scaled Height of Burst

for each pair of shots listed in the table are included in Figures 5.21 through 5.24. Both coordinates of these pressure-time plots have been normalized to 1-kt, sea-level conditions; an attempt is made to compare wave forms from gages at comparable A-scaled ground ranges. Figure 5.21, showing examples of Teapot Shot 6 and Upshot-Knothole Shot 10 wave-form comparisons, indicates that although the maximum pressure measured on the Teapot shot is significantly higher, the wave forms are very similar. The same is true for the Tumbler Shot 4 and Upshot-Knothole Shot 11 results shown in Figure 5.22; it is noteworthy that these latter two shots had widely different yields (3:1). Proceeding to the next set of wave-form comparisons (Teapot Shot 12 and Upshot-Knothole Shot 1) shown in Figure 5.22, it is evident that at the close-in ranges (about 280 and 340 feet, A-scaled) the normalized wave forms from the two shots are similar. However, at about 500 feet (A-scaled) the Teapot record displays a prominent second peak which is absent on the Upshot-Knothole pressure-time result; these results indicate that greater differences in wave form are to be expected for a given change of burst height for heights of burst of the order of 100 feet (A-scaled) than would occur at heights of between 200 and 400 feet. It should also be noted that the Teapot normalized peak pressures are consistently higher, indicating that for detonations that have low A-scaled burst heights, A-scaled peak pressures may depend upon weapon yield.

The Upshot-Knothole Shot 1 and Shot 10 wave-form comparisons are included in Figure 5.23. As summarized in Table 5.3, these shots had similar yields but different A-scaled burst heights. The figures show little similarity in wave forms; specifically,

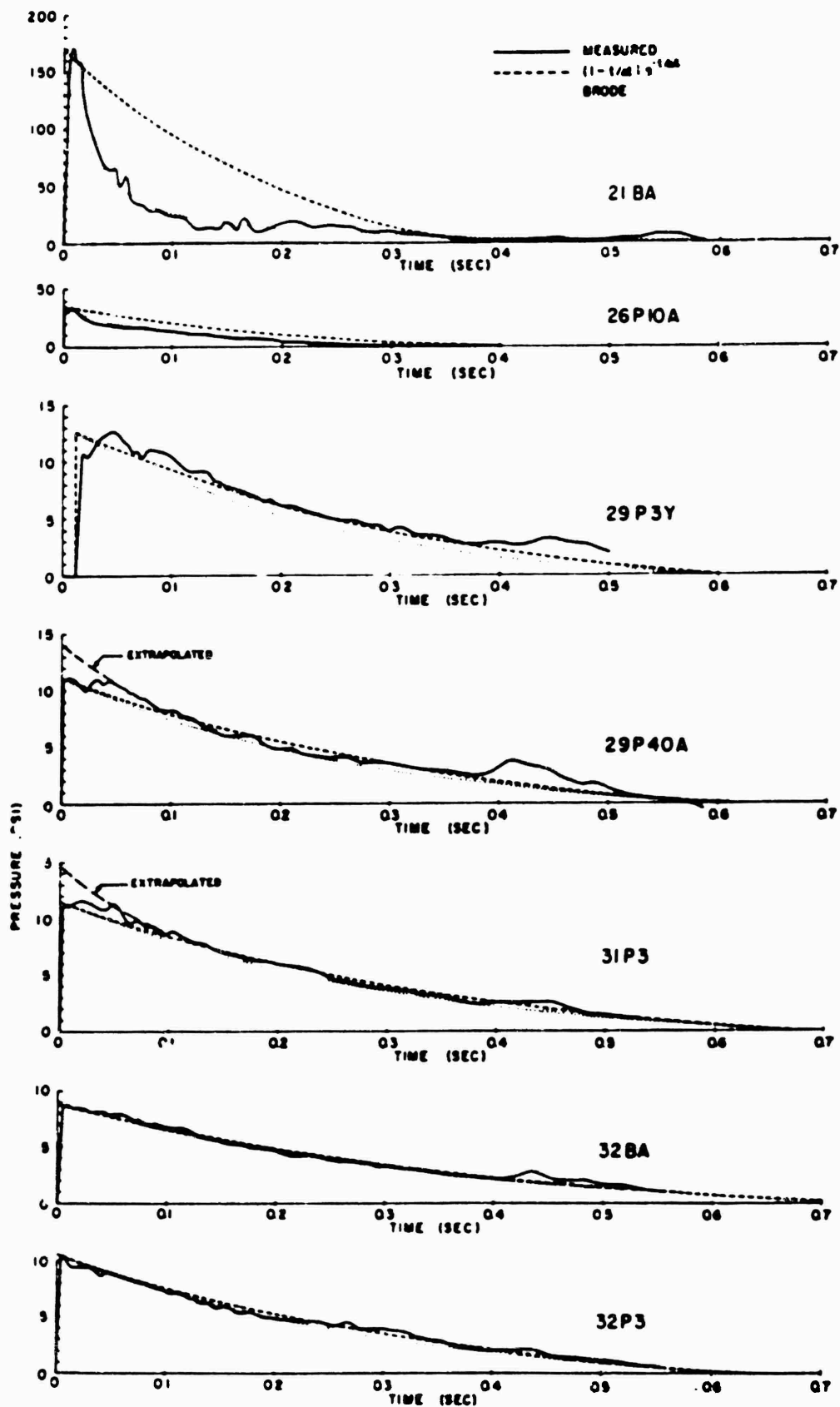


Figure 6.19 Decay of overpressure behind shock front, water line, Shot 12.

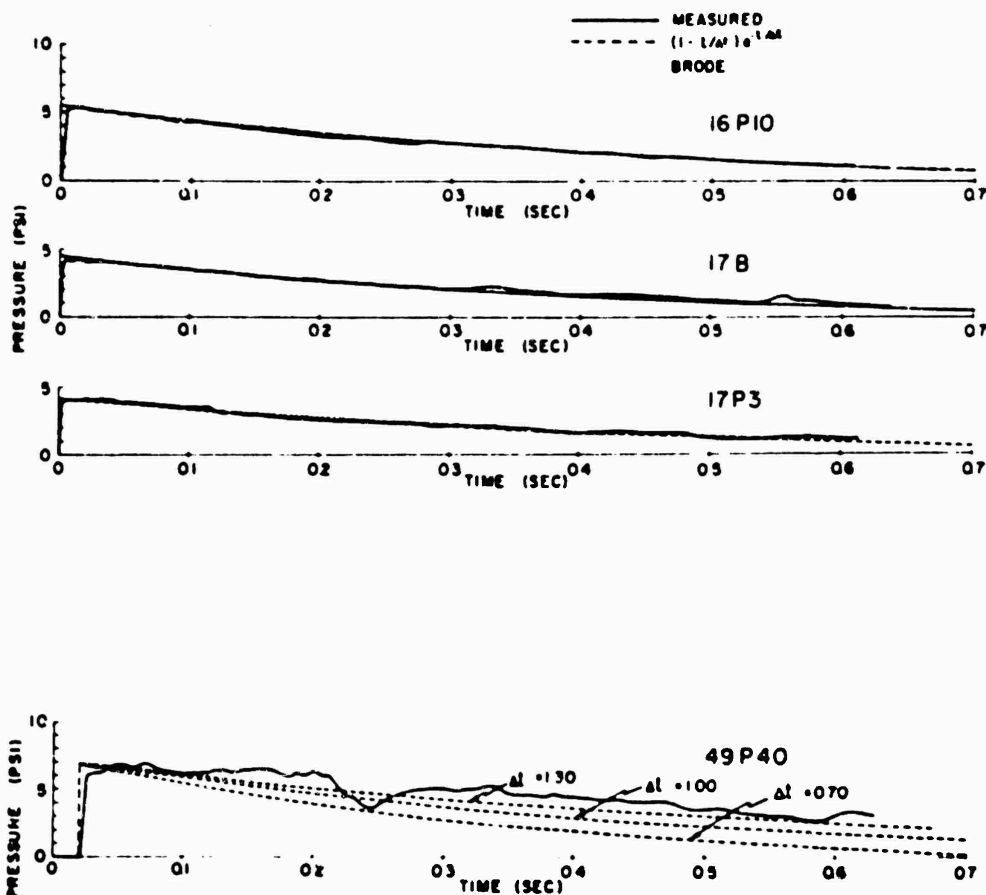


Figure 5.20 Decay of overpressure behind shock front, desert and asphalt lines, Shot 12.

the Shot 1 pressure-time records exhibit shock-like pressure rises, whereas the Shot 10 results show slow-rise, compression-like wave fronts, particularly at the close-in ranges. The last set of wave-form comparisons, shown in Figure 5.24, include Upshot-Knothole Shot 9 and Teapot Shot 12. The A-scaled burst heights for the former were too high for precursor formation (see Table 5.3), which explains the disturbed wave forms observed on the Teapot Shot only. The figures show the extremely poor correspondence between pressure-time wave forms obtained on these shots: the Upshot-Knothole records are consistently classical, while the Teapot results show the influence of disturbing effects out to about 1,100 feet (A-scaled range).

In addition to wave-form comparisons, the Project 1.10 data may be compared with previous results on the basis of peak overpressure versus ground range. This comparison is documented in Figure 5.25, where the A-scaled surface-level peak pressures are plotted against A-scaled ground range. Included on this figure are wave-form classifications, ideal overpressure curve (solid line), and the Teapot Shot 12 curve (dashed line). At A-scaled ranges less than 1,000 feet, peak pressure data are significantly depressed below ideal values; the experimental points appear first to merge with the ideal at about 1,200 feet (A-scaled), which corresponds to 7 or 8 psi (A-scaled). There is a tendency for Tumbler Shot 4 maximum pressures to be notably low at the close-in ranges, a result

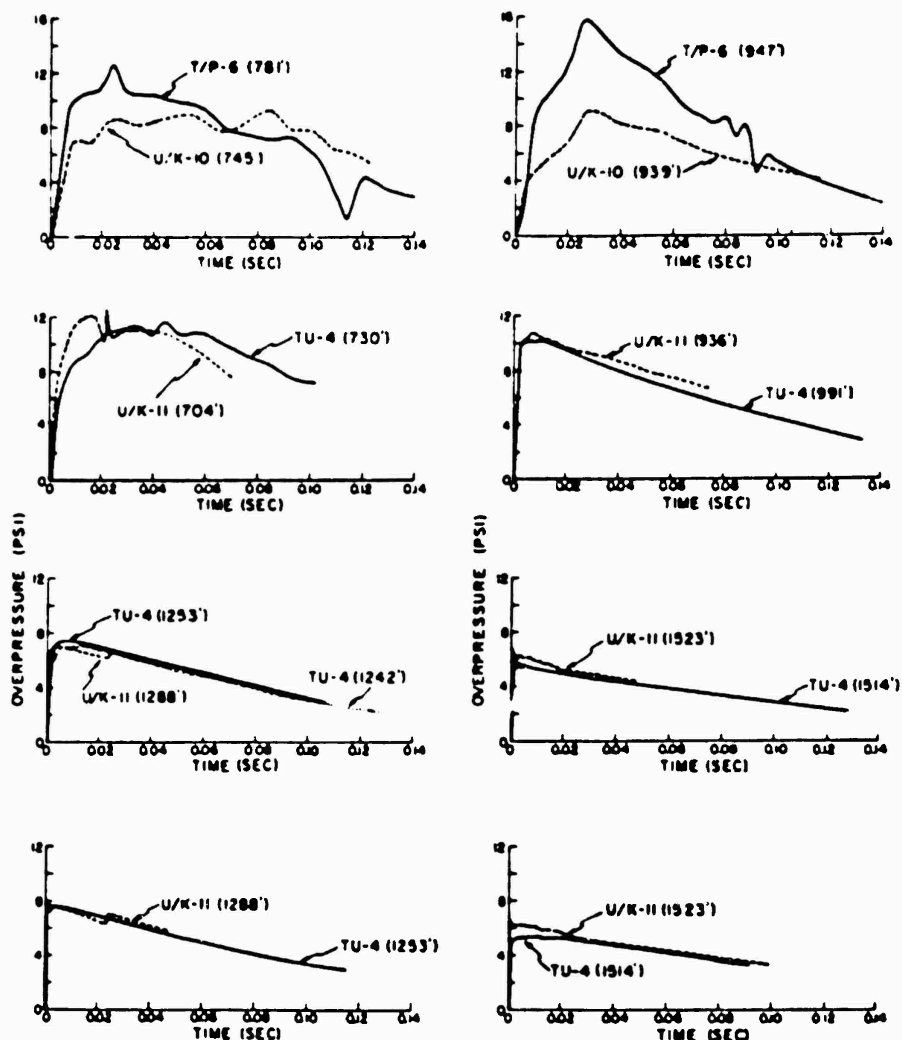


Figure 5.21 Wave form comparisons (A-scaled), Teapot Shot 6, Uphot-Knothole Shot 10, Tumbler Shot 4, Uphot-Knothole Shot 11.

which may be explained by the relatively high A-scaled burst height for this shot.

For Uphot-Knothole, Reference 9 presents a treatment of overpressure positive-phase duration and positive impulse as a function of peak pressure. This report includes composite plots of these quantities using A-scaled results from all nuclear air bursts detonated prior to the fall of 1953; it was possible to draw average smooth curves through the array of data points. These curves are presented in Figures 5.26 and 5.27, where the dashed lines define the  $\pm 15$ -percent deviation from the average curve. Although the data from previous shots scattered a good deal, it was found that about 90 percent of the data points fell within the  $\pm 15$ -percent limits. In addition, it was found that the smoothed curve did not fit data corresponding to pressures higher than about 30 psi (A-scaled). For completeness, Figures 5.26 and 5.27 include all data from Teapot Project 1.10 and only those data from previous shots which correspond to maximum pressures in excess of 30 psi.

The positive-duration-versus-maximum-pressure plot (Figure 5.26) shows that data from Teapot Shots 6 and 12 over all three types of surface agree well with the composite curve; however, at overpressures in excess of 30 psi there is a tendency for the Teapot and previous data to diverge. Data from other shots show a definite trend toward de-

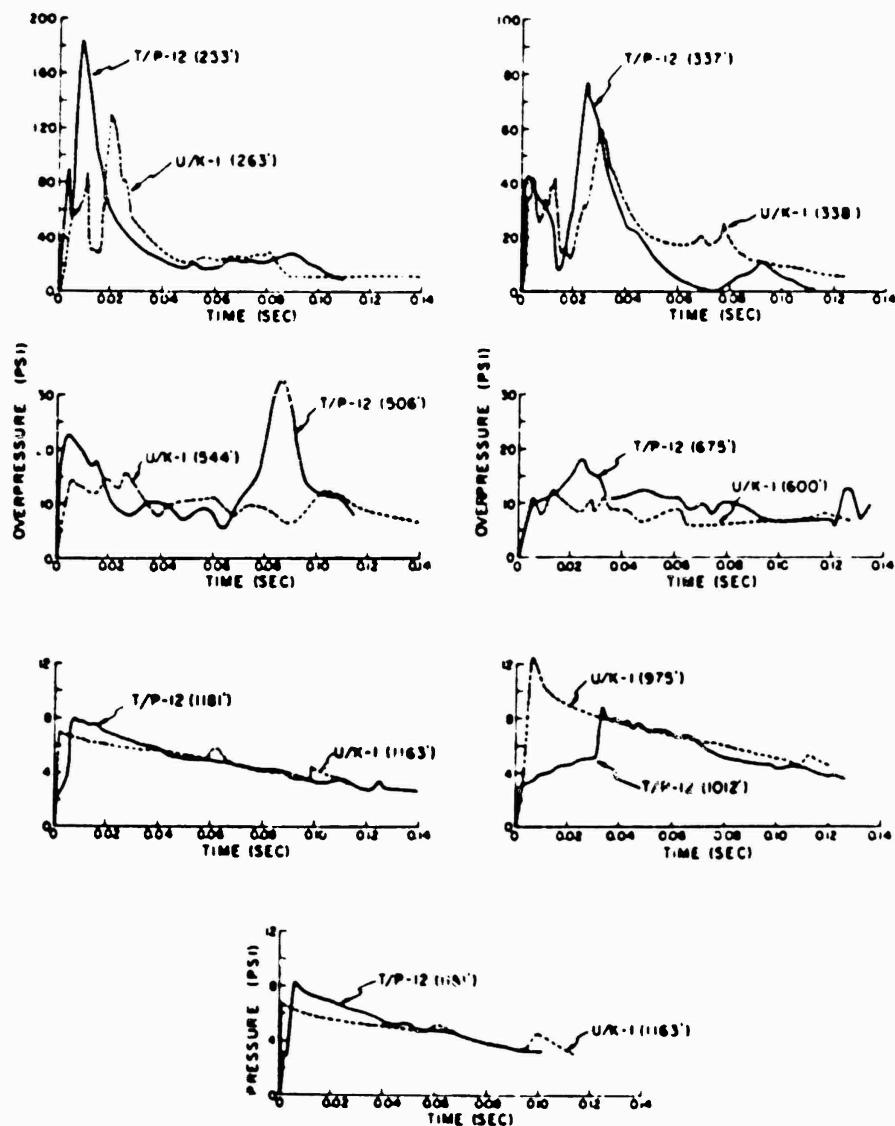


Figure 5.22 Wave form comparisons (A-scaled), Teapot Shot 12, and Upspot-Knothole Shot 1.

creasing duration with increased maximum overpressures in the high-pressure region; on the contrary, the Shot 12 positive durations corresponding to pressures near and above 100 psi (A-scaled) are significantly higher than previous data would predict. It is possible that the very long durations at close-in gage stations are due to some uncompensated instrumental error, e. g., a short time-shift in the zero-signal response characteristics of the gage immediately following shock arrival at the gage. However, it should be noted that the analysis of the free-air case in Reference 17 predicts the observed increase in positive-phase durations at the higher shock strengths.

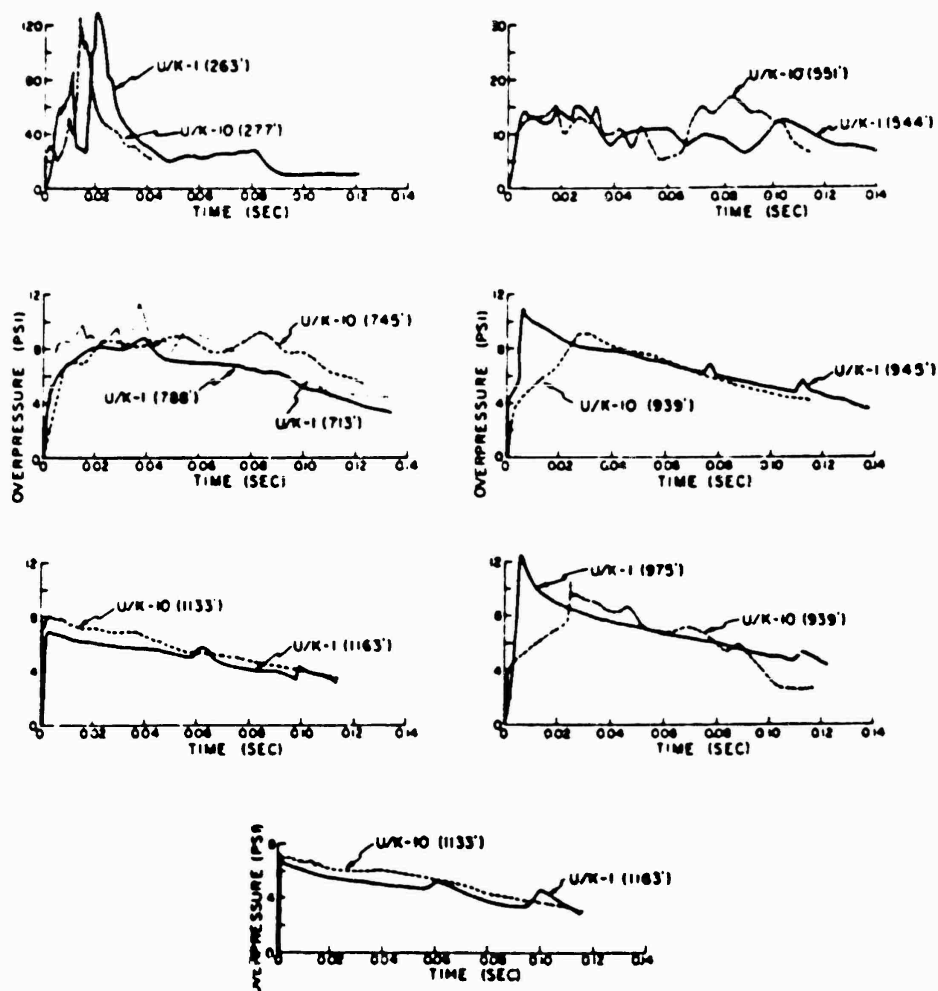


Figure 5.23 Wave form comparisons (A-scaled), Upshot-Knothole Shots 1 and 10.

The positive-impulse data shown in Figure 5.27 are presented in the same manner as were the positive-duration data. Although the Shot 6 asphalt-line impulse data are consistently too high and outside the  $\pm 15$ -percent limits, the Shot 12 data show no definitive effects of surface properties. There appears to be some tendency for the Teapot Project 1.10 impulse data (below 30 psi) to be higher than the composite curve. For A-scaled maximum pressures above 30 psi, the Teapot impulse results do not disagree significantly with previous results; however, at these higher pressures, it appears that the positive impulse is always lower than would be indicated by the extension of the composite curve to pressures above 30 psi. In addition, since positive impulse is obtained by integration of the pressure-time record, it will be less critically influenced by possible short-time instrumental disturbances than will the positive-phase-duration variable.

### 5.3 DYNAMIC PRESSURE MEASUREMENTS $q^*(p_{itot})$

The general method of presentation of the Project 1.10 overpressure data included in the previous section will be applied to the discussion of the  $q^*(p_{itot})$  measurements. First, the effect of surface properties upon the data will be considered, after which com-

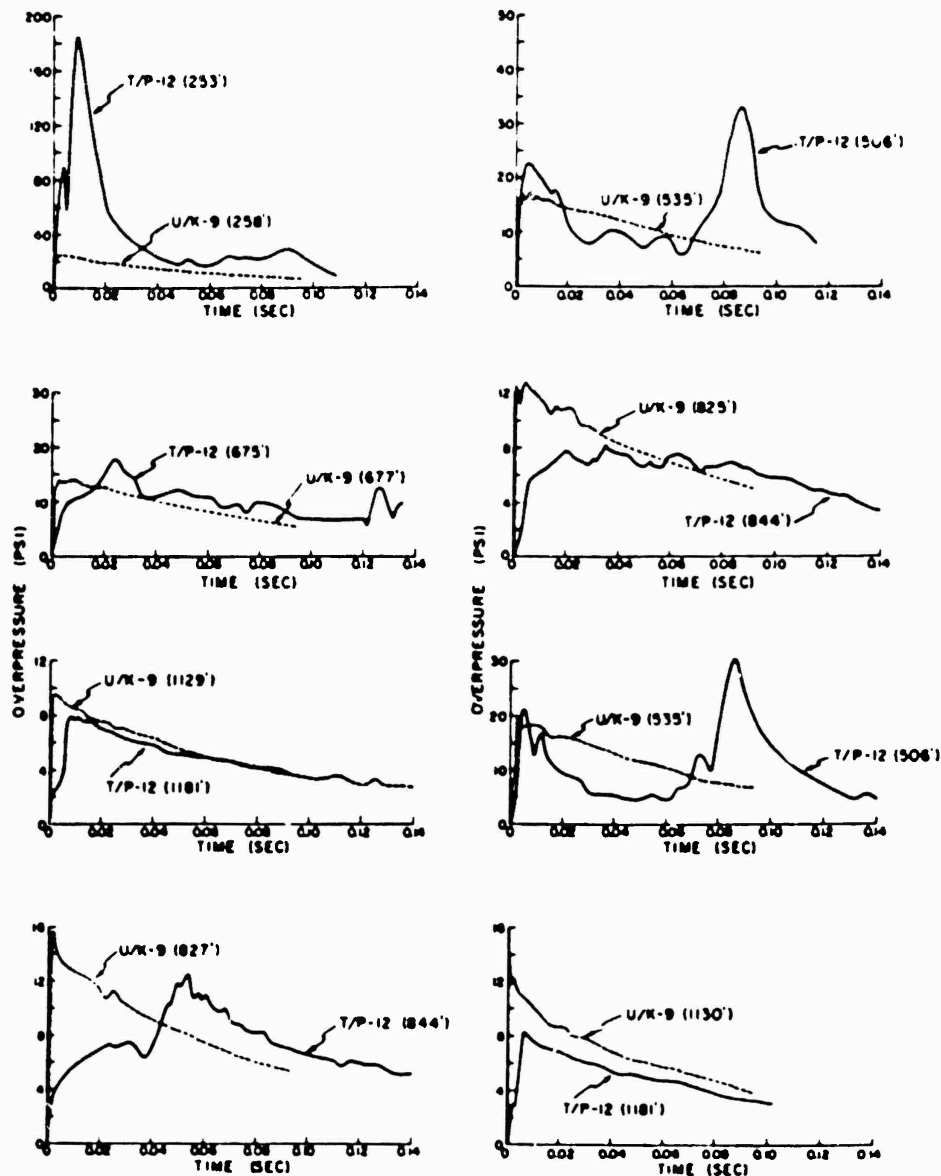


Figure 5.24 Wave form comparisons (A-scaled), Teapot Shot 12 and Upshot-Knothole Shot 9.

parisons will be made with available results from previous shots.

**5.3.1 Effects of Surface Characteristics  $q^*$ (pitot).** The plots of maximum  $q^*$ (pitot) pressure versus ground range for Shot 12 are shown in Figures 5.28, 5.29, and 5.30. The various symbols on these plots indicate the maximum  $q^*$ (pitot) pressure recorded at each ground range, and the letters inside the symbols designate the wave-form type associated with each record; no letter inside a symbol indicates that the wave form does not correspond to any specific classification. Again, the data have been corrected for pitch angle and Mach number.



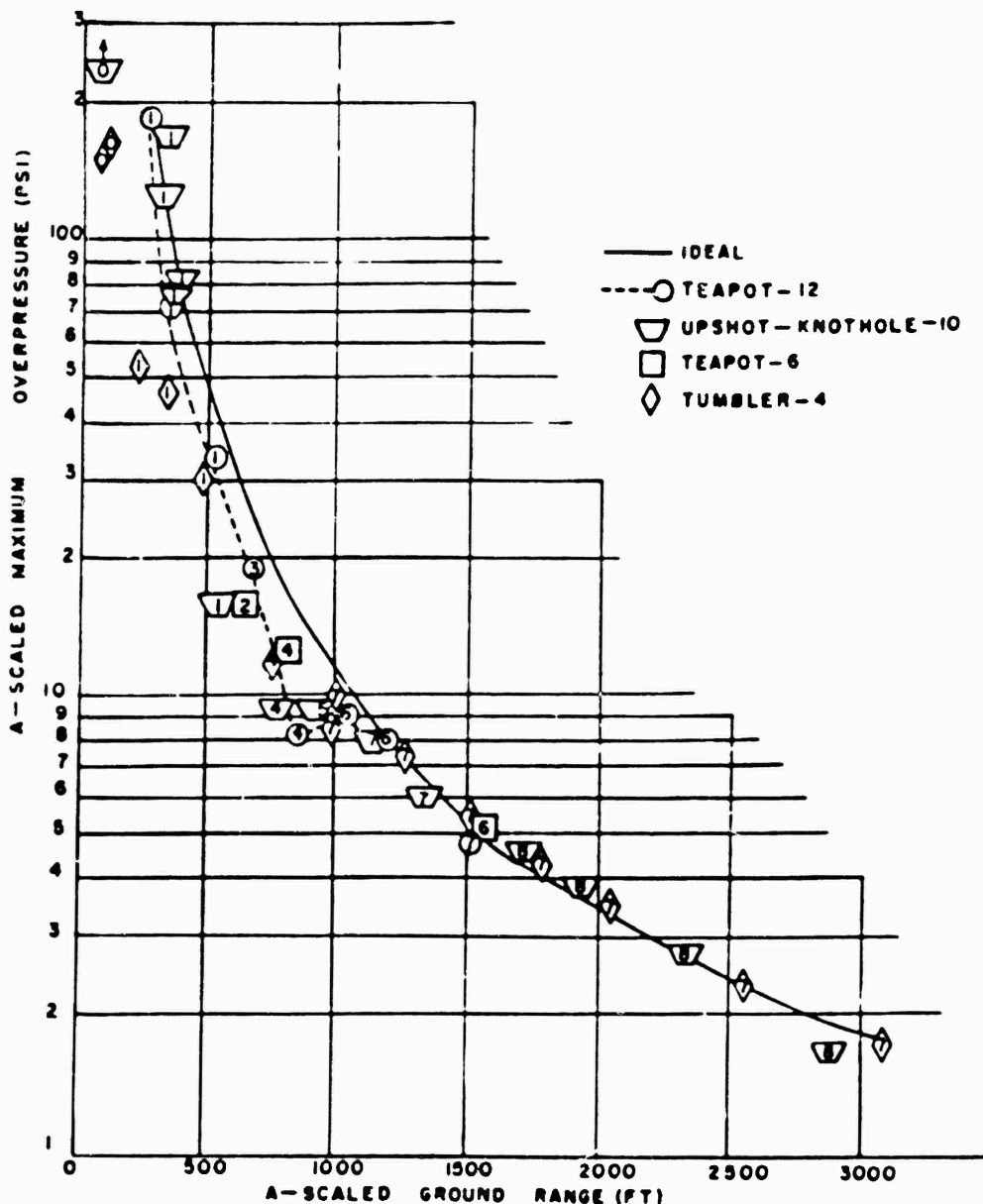


Figure 5.25 A-scaled maximum overpressure, surface level, Teapot Shots 6 and 12, previous shots, desert line.

The Shot 12 data for the water-line maximum  $q^*$ (pitot) pressure shown in Figure 5.28 indicate that 3-foot pressures are significantly higher than those measured at 10 feet; however, because of the steep slope the position of the 3-foot data point at 2,000 feet ground range has a profound influence upon the shape of the curve. The attenuation of peak  $q^*$ (pitot) pressure with distance is quite severe. The curve of Figure 5.28 indicates a drop in pressure from about 300 to 3 psi in a ground range interval of less than 2,000 feet. As stated previously, the water-line  $q^*$ (pitot) records do not lend themselves well to wave-form classification, which accounts for the many blank symbols on Figure 5.28.

The desert-line  $q^*$ (pitot) data of Figure 5.29 show an attenuation of pressure with distance which is similar to that observed over the water line; however, unlike the water line data, the 3-foot maximum pressures over the desert appear to be depressed relative to 10-foot values.

Figure 5.30, showing the  $q^*$ (pitot) results over the asphalt line, is not significantly different in appearance from the plots corresponding to the water and desert lines. There is apparently little difference in the maximum pressures at 3- and 10-foot levels; moreover, the decrease in  $q^*$ (pitot) peak pressure between 2,500-foot ground range (13.1 psi) and 3,000-foot ground range (0.85 psi) is most severe on the asphalt line. It is noted that the single data point at 3,000 feet produces the aforementioned appearance of serious attenuation; however, the fact that the 40-foot-level gage at 2,500 feet recorded a depressed  $q^*$ (pitot) maximum lends some validity to the curves drawn in Figure 5.30. In fact, the obvious consequence of the marked attenuation characteristics (evident in Figures 5.28 through 5.30) is that one or two data points may influence profoundly the character of the best-fit curve drawn through the data. If this danger is kept in mind, the discussion of the composite Shot 12  $q^*$ (pitot) curves can proceed more profitably.

Figure 5.31 is the composite graph of Shot 12, 3-foot  $q^*$ (pitot) maximum pressures over the three blast lines; the figure also includes the ideal-dynamic-pressure-versus-ground-range curve (Reference 12). Primarily, it is obvious that the  $q^*$ (pitot) maxima over the three surfaces agree closely at the first gage station (1,250-foot ground range); also, the pressures recorded are larger than ideal at the same range by about a factor of five. Maximum  $q^*$ (pitot) pressures approach ideal at 2,500-foot ground range on the water line, but on the desert the earliest indication of agreement is at 3,000 feet. The value over the asphalt at 3,000 feet falls appreciably below the ideal; it will be recalled (Figure 5.12) that a severely depressed peak overpressure was also recorded at this range.

The 10-foot level  $q^*$ (pitot) composite for Shot 12, presented in Figure 5.32, indicates that at this gage height the effect of surface properties is more systematic than is the case for the 3-foot measurements. The pressures measured over the desert are highest; at the close-in 10-foot gage station (1,500 feet) the peak pressure is again larger than ideal by a factor of five. Desert-line  $q^*$ (pitot) maxima are close to ideal at ground ranges of 3,500 and 4,000 feet; the same is true for water-line measurements at 2,250 and 2,500 feet. However, in the latter case, the wave forms of the  $q^*$ (pitot)-time records are far from ideal in appearance (see Figure B.3). This suggests, as pointed out in Section 5.2.1 in connection with overpressure data, that it is misleading to label a blast wave ideal on the basis of its maximum pressure only.

The Shot 6 maximum  $q^*$ (pitot) data are presented in Figure 5.33, all obtained from 10-foot-high gages. Because so few measurements were taken on this shot, the usefulness of the data is restricted to supplementing the Shot 12 results. Figure 5.33 shows that at the closest gage station (1,300-foot ground range) the peak  $q^*$ (pitot) pressure was higher over the desert surface; also, the pressure exceeded the ideal value at the same ground range by factors of about four (over asphalt) and six (over desert). The Shot 6  $q^*$ (pitot) data, like those of Shot 12, exhibit severe attenuation of maximum pressure as a function of ground range.

It is possible, with reference to the Shot 12 photographic data reported by NOL (Reference 15), to determine the approximate arrival times at various ranges of what appears to be a dust front. Upon checking some of these dust arrivals against the pressure-time records obtained on Project 1.10, it appears that some measured effects may be attributed to the dust. An example is the 3-foot-level pitot-tube results at 3,000 feet (9P3 and 9Q3 of Figure B.7). The  $q^*$ (pitot) record (9Q3) shows a slow pressure rise fol-

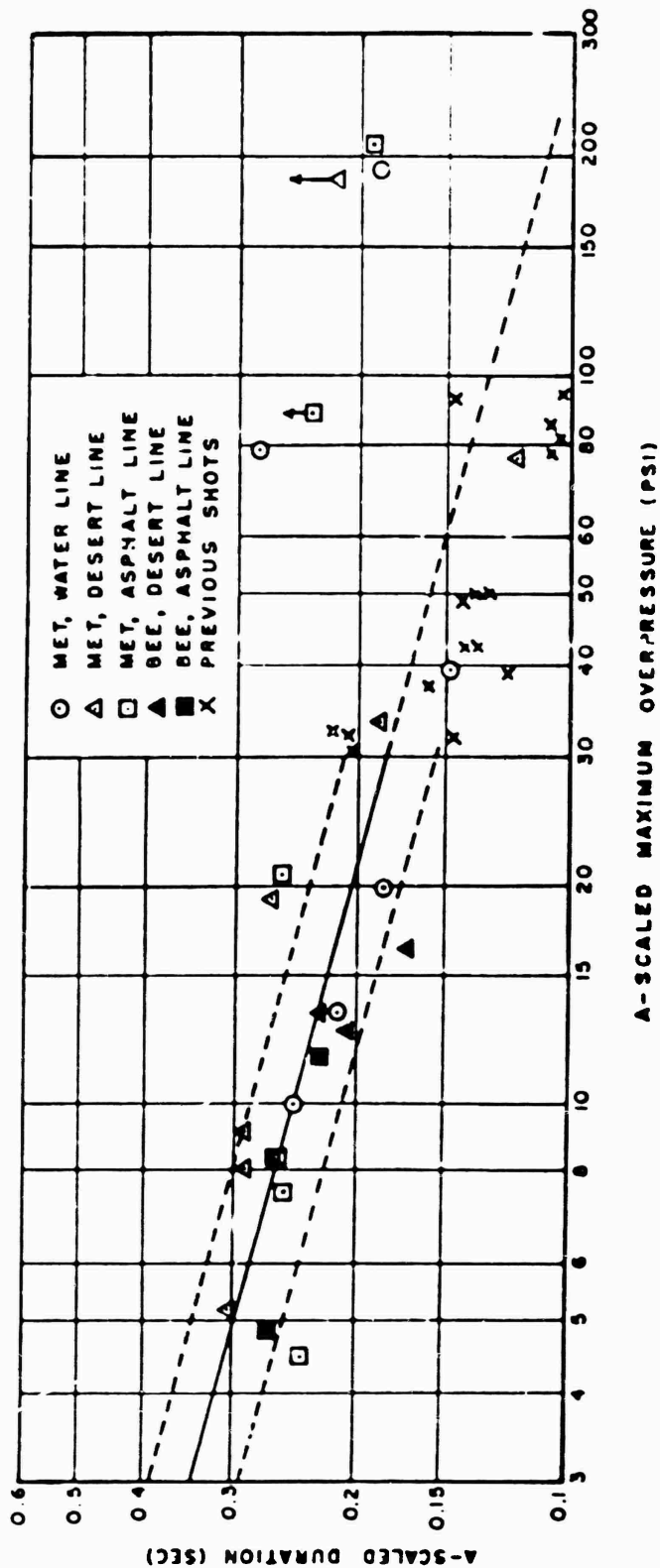


Figure 5.26 A-scaled positive phase duration versus A-scaled maximum overpressure, Teapot Shots 6 and 12, previous shots.

CONFIDENTIAL

lowed (about 30 msec after the initial arrival) by a sharp, high amplitude disturbance. The delay between initial arrival and the high amplitude portion corresponds well to the NOL photographic data for time delay of dust-front arrival at this station. The side-on record (9P3) shows only a rather minor indication of dust arrival at a somewhat later time than observed for the head-on gage. This same behavior is characteristic of several pitot-tube gage stations on the Shot 12 desert line.

**5.3.2  $q^*$ (pitot) Positive Impulse.** It was realized from previous nuclear test series that the drag forces and the damage to certain classes of drag-sensitive targets in the regions of disturbed blast waves did not correlate with the results anticipated from utilization of measured overpressures. The limited pitot-tube dynamic-pressure measurements available indicated, in general, that in the disturbed region,  $q^*$ (pitot) pressure is substantially higher than would be calculated using classical relationships and the measured overpressures. It is well-known that one of the most prominent characteristics of precursor blast waves, manifest in both dynamic pressure and overpressure measurements, is the marked increase in positive duration and impulse in the region of severe disturbance. Since damage to drag targets is of great interest, it was thought expedient to investigate the impulse associated with the  $q^*$ (pitot) measurement of Project 1.10.

For this investigation, rather than attempt to obtain the total positive impulse, it was decided that a more useful purpose would be served if the impulse-versus-time function were determined for each  $q^*$ (pitot) measurement. The results of these successive integrations are summarized in Figures 5.34 through 5.38. Some general statements can be made on the basis of these figures:

1. On Shot 12, out to 2,500-foot ground range; the 3-foot-level results show that the effects of the asphalt and water lines are comparable, while the desert  $q^*$ (pitot) impulse reaches values as much as ten times larger than those indicated on the other blast lines (Figures 5.34 and 5.35).
2. At the 10-foot height, the impulse in order of decreasing value is desert-asphalt-water; the impulse magnitudes over the desert surface are usually three or four times larger than those measured over the asphalt or water surfaces.
3. Only at 3,000-foot ground range (see Figure 5.37), where the  $q^*$ (pitot) impulse maximum is about one percent of the largest value measured, do the water-line data exceed those over the desert and asphalt.
4. The one Shot 6 comparison (see Figure 5.38) indicates that the impulse-time curves for the two blast lines are of the same form, with the desert-line values consistently higher.

It is believed that the very high  $q^*$ (pitot) impulse values measured over the desert surface are caused by the presence of an excessive amount of particulate matter carried along by the pressure wave. It is further believed that this particulate matter affects the pitot-tube gage as would an additional pressure. In regard to using  $q^*$ (pitot) impulse for damage correlation, some information is supplied by reference to the Teapot report on drag-target investigations (Reference 18). To summarize, those results indicated similar damage to drag targets on both the water and desert lines of Shot 12, but a slightly more severe damage level on the asphalt line. The fact that the  $q^*$ (pitot) impulse curves of Figures 5.34 and 5.35 would not have predicted this general result suggests the possibility that the factors affecting the  $q$ -impulse measurements are not the same as those which significantly influence damage to drag-sensitive targets.

**5.3.3 Comparisons with Previous Data.** Unlike the situation with regard to overpressure measurements, there are only a few  $q^*$ (pitot) results from previous shots which

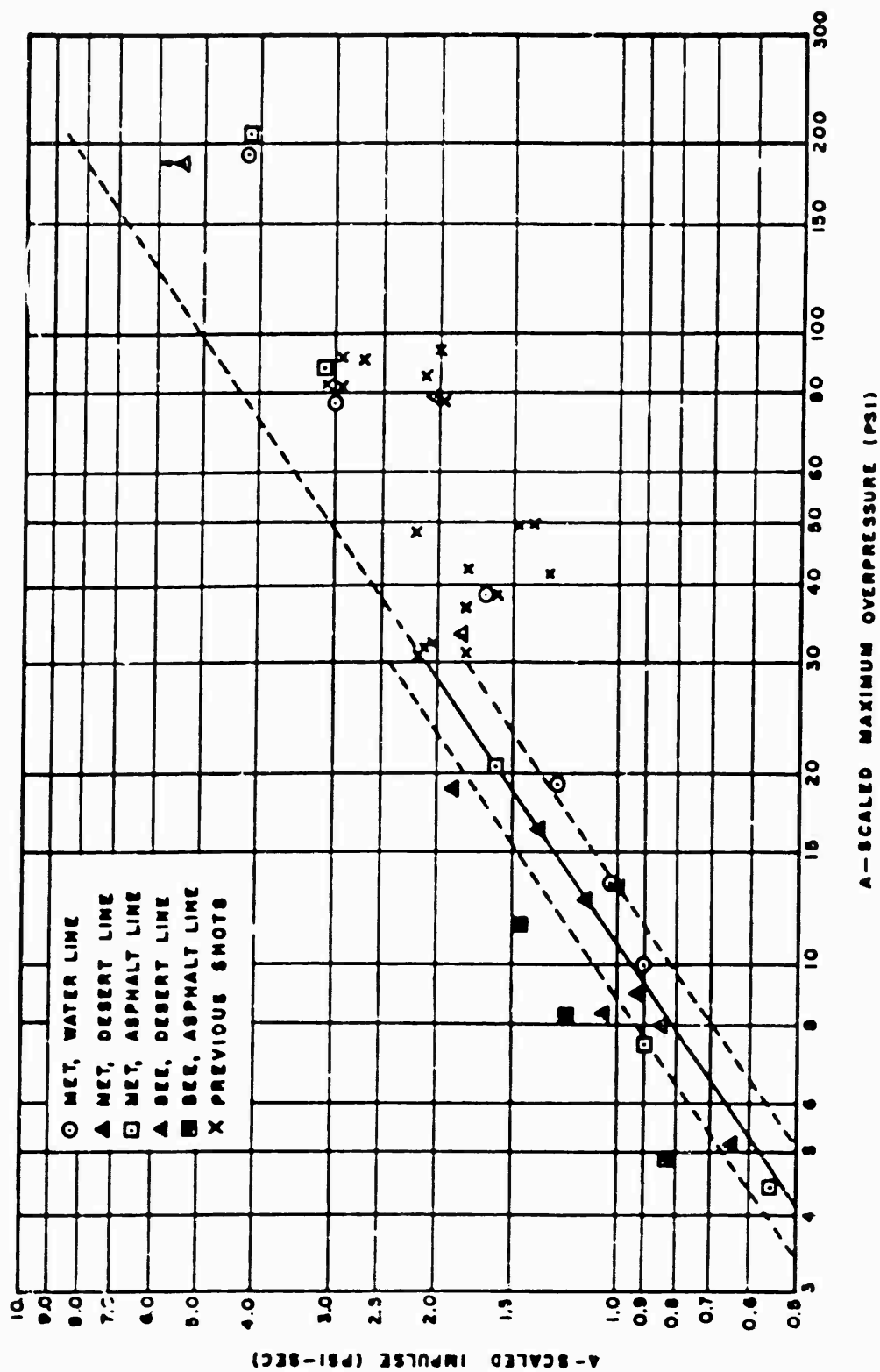


Figure 8.27 A-scaled positive impulse versus A-scaled maximum overpressure, Testshot 8 and 12, previous shots.

CONFIDENTIAL

can be compared with Project 1.10 desert-line data. The plot of maximum  $q^*$ (pitot) pressure versus ground range (A-scaled) is shown in Figure 5.39. Included are wave-form classifications (where possible), the ideal  $q^*$ (pitot) curve (solid line), and (for Shot 12) the 10-foot-level desert-line data and curve (dashed line). Also shown in Figure 5.39 are the available  $q^*$ (pitot) pressure data (corrected for Mach number) from previous shots; namely, Upshot-Knothole Shots 10 and 11. The Upshot-Knothole Shot 10 data at A-scaled ground ranges less than 1,000 feet are probably low (note arrows on symbols) due to suspected gage overload (Reference 6). The remaining Upshot-Knothole data, the Shot 11 result near 800-foot range and the Shot 10 result near 1,500 feet, are in agreement with the ideal values at these A-scaled ranges. Finally, it is apparent that, at A-scaled ground ranges less than 1,000 feet, the Teapot Shot 12  $q^*$ (pitot) maximum pressures over the desert are much greater than have been measured on any previous shots.

#### 5.4 PRECURSOR PHENOMENA

The most significant airblast results of Operation Teapot, and more specifically, Project 1.10, were obtained where airblast behavior departed from ideal. Such departures have been attributed to surface and/or thermal effects on blast and may be classified as precursor phenomena.

5.4.1 Background. Since it was not possible to study the blast characteristics of nuclear explosions without the effects of accompanying thermal radiation on the surface, there were no means before Teapot of experimentally separating the mechanical and thermal effects on blast. High-explosive tests, which have negligible accompanying thermal radiation, showed minor blast effects due to differences in surface mechanical reflection properties and surface dust. Surface nuclear explosions, where geometry limits the thermal radiation incident on the blast surface, gave results similar to TNT tests. In any case, the extreme deviations from ideal blast phenomena which were observed on several low-burst-height nuclear detonations are far greater than the perturbations observed for scaled TNT tests or for surface nuclear tests over the same kinds of surfaces. It therefore appears safe to assume that thermal radiation is the principal cause of blast wave departures from ideal. Of course, the properties of the surface, including dust, can have a profound influence upon the degree to which the thermal radiation affects blast.

It has been customary to use the term precursor to describe the blast conditions representative of low bursts where the thermal effects on blast are of major importance. It must be noted that the disturbing effects on blast can be significant without the actual generation of a precursor wave, or outside the range of the precursor region. The term precursor is used frequently in a general sense to describe the whole region where the thermal effects on blast cause significant departures from the ideal case. In some circumstances the term nonideal is used to describe this behavior.

Anomalous blast behavior was observed on most nuclear test series prior to Teapot. The role of thermal effects on blast was first clearly delineated on Tumbler-Snapper, where the precursor phenomenon was identified. Subsequent re-examination of Buster and Greenhouse blast measurements confirmed precursor existence and showed similar thermal perturbations on blast. It remained for the Upshot-Knothole test series to investigate the effects of such nonideal blast waves on targets and to study further the associated basic-blast phenomena. Much additional valuable information was obtained during Upshot-Knothole which led to qualitative explanations of the thermal effects on blast waves; however, it was the objective of the Teapot series to put this thermal phenomenon

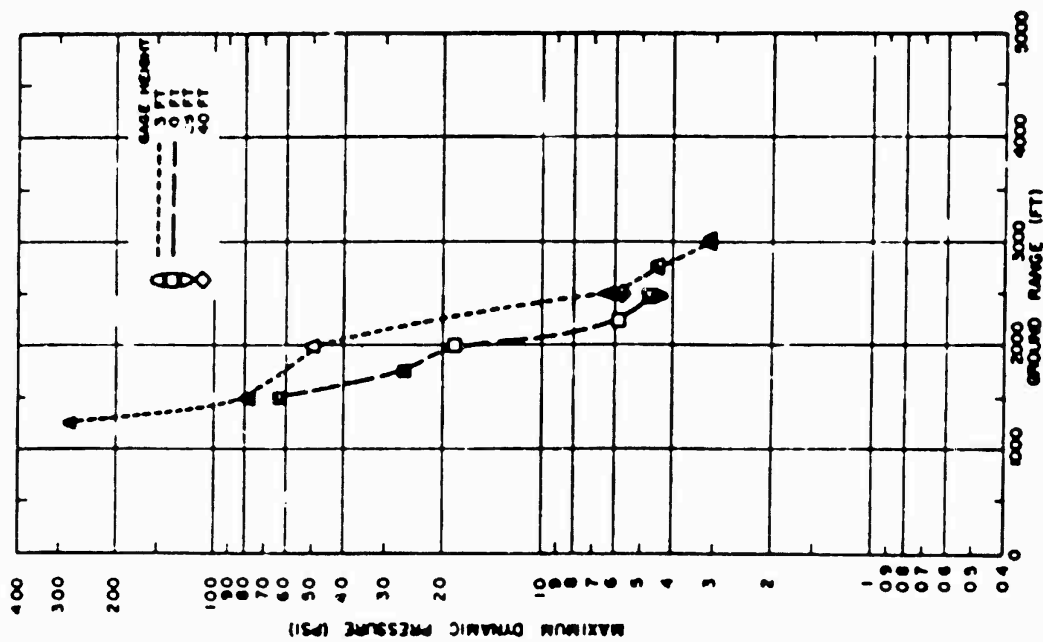


Figure 5.28 Maximum  $q^*$  (pitot) pressure versus ground range, water line, Shot 12.

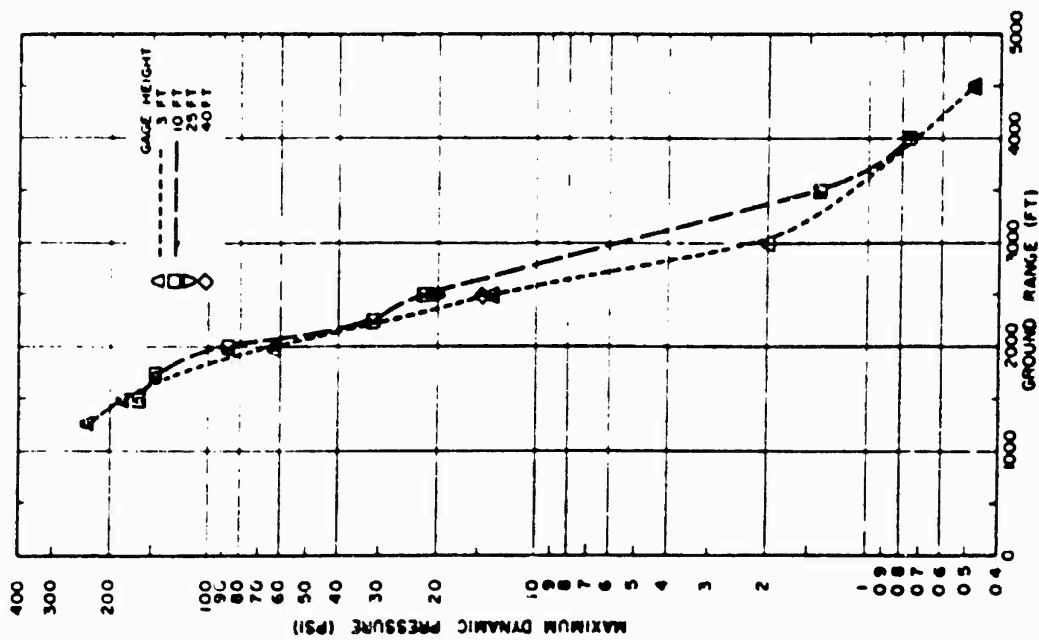


Figure 5.29 Maximum  $q^*$  (pitot) pressure versus ground range, desert line, Shot 12.

on a firmer quantitative basis and to aid in the prediction of the blast behavior of nuclear weapons (at low burst heights) over surfaces other than those characteristic of desert areas.

The blast disturbances observed on previous test series have been explained in part, qualitatively, by the hypothesis that the thermal radiation creates a heated layer of air adjacent to the ground surface prior to shock arrival at the point of observation. Analytical considerations and some supporting shock-tube experiments indicate that a conventional shock wave is markedly influenced by passage into a region having a nonuniform temperature or, more particularly, a nonuniform sonic velocity.

To date there has been no adequate description of the effective mechanism of heat transfer responsible for the generation of the assumed thermal layer. Experimental measurements on previous nuclear tests and additional measurements on Teapot were designed for the purpose of investigating the properties of the thermal layer prior to shock arrival. Such measurements were only moderately successful; general instrumentation problems, plus turbulence and atmospheric instability effects characteristic of the heated region being investigated, have reduced the value of these measurements in a quantitative sense. Therefore, although measurements have proven the existence of a preshock thermal disturbance near the ground, details concerning temperatures, temperature gradients, and height of effective layer at shock arrival have been inconclusive.

**5.4.2 Measured and Computed Preshock Temperature.** A sizable fraction of the total energy released from a nuclear detonation is emitted in the form of thermal radiation. Large amounts of thermal radiation are incident upon the ground before shock arrival, and thus, the existence of a near-surface thermal layer appears to be a sound assumption. Actual measurements of preshock air temperatures (Project 8.4) and preshock sonic velocities (Project 1.5) on Teapot Shot 12 appear to be incompatible; in addition, neither set of these data appears to describe adequately the preshock thermal picture in an understandable manner.

If a near-surface thermal layer is assumed prior to shock arrival, it is possible to set up analytical relationships which can be used to deduce the general characteristic of the thermal layer from the observed blast behavior. Temperatures computed in this manner are, at best, gross averages and apply only to conditions which exist just prior to shock arrival at the range in question. The relationships based upon blast parameters can be divided into three main classifications: (1) those using shock wave equations, measured initial overpressures, and some average wave-front orientation angle (called pressure calculation); (2) those using the assumption that wave propagation velocity equals the sonic velocity characteristic of the medium (called sonic calculation); and (3) those using only angles of shock-wave-front orientation (called angle-of-front calculation). These three methods of approach will be discussed in order.

**Pressure Calculation.** With a shock front moving through a medium of constant  $\gamma$  (ratio of specific heats), analysis yields:

$$\frac{P_2}{P_1} = \frac{2\gamma}{\gamma + 1} \left[ \left( \frac{v \sin \theta}{C_1} \right)^2 - 1 \right] \quad (5.4)$$



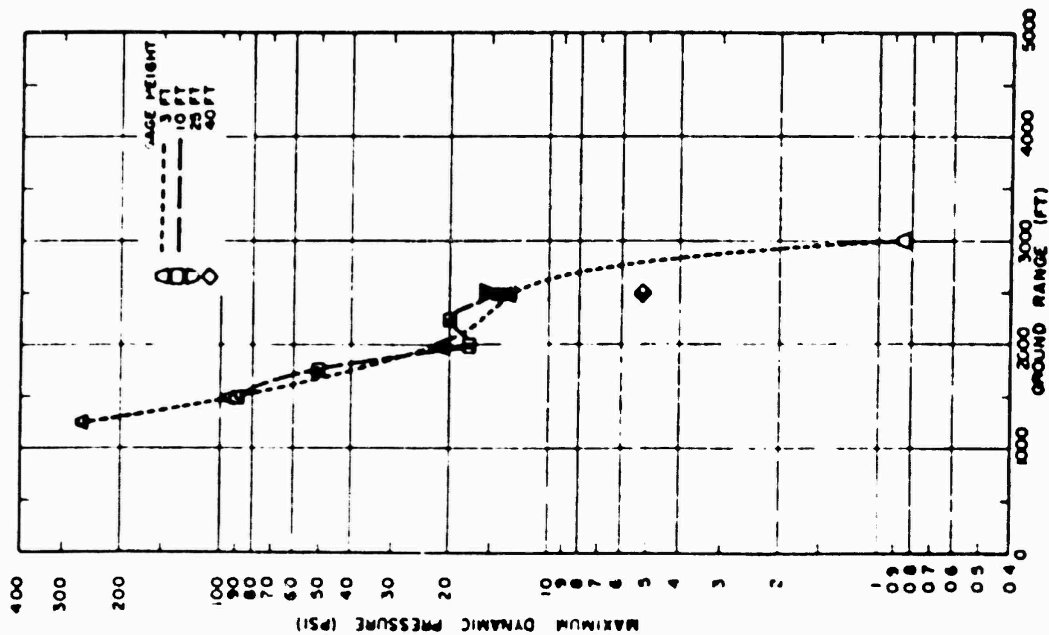


Figure 5.30 Maximum  $q^*$  (pitot) pressure versus ground range, asphalt line, Shot 12.

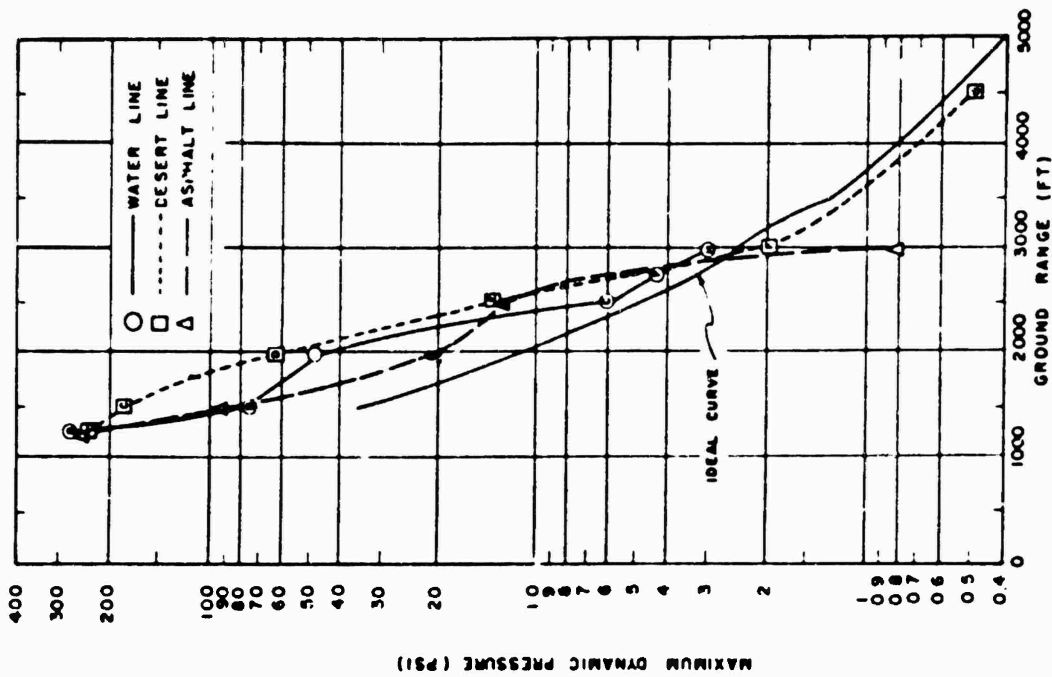


Figure 5.31 Maximum  $q^*$  (pitot) pressure versus ground range, 3-foot level, Shot 12.

Where:  $p_2$  = initial overpressure behind the shock front

$v$  = horizontal trace velocity of the front

$\theta$  = acute angle which the shock front makes with the ground surface

$C_1$  = sonic velocity and pressure of the medium just ahead of the shock front  
(see Figure 5.40)

$p_1$  = sonic velocity and pressure of the medium just ahead of the shock front  
(see Figure 5.40)

From the measured overpressures and the photographic data (Reference 15) showing the orientations of the shock fronts, Equation 5.4 may be used to compute  $C_1$ . Then the preshock temperature  $T_1$  is related to  $C_1$  by:

$$\left(\frac{C_1}{C}\right)^2 = \frac{T_1}{T} \quad (5.5)$$

Where:  $C$  = sonic velocity corresponding to ambient atmospheric conditions

$T$  = absolute temperature corresponding to ambient atmospheric conditions

This method may be extended somewhat to incorporate the assumption that at the ground plane the flow must be parallel to the surface, i. e.  $\theta = 90^\circ$ . Then, for surface-level temperature calculations, Equation 5.4 reduces to:

$$\frac{p_2}{p_1} = \frac{2\gamma}{\gamma + 1} \left[ \left(\frac{v}{C_1}\right)^2 - 1 \right] \quad (5.6)$$

If an error analysis is made on Equation 5.4, it is concluded that for overpressures up to about 30 psi, errors in the computed  $C_1$  are not very sensitive to errors in  $p_2$ ; however, errors in the computed  $p_2$  are quite sensitive to errors in  $C$ ,  $v$ , and  $\theta$ , if  $\theta$  is small.

**Sonic Calculation.** This method is based upon the existence of a compression-type acoustic wave. If this condition is fulfilled, the propagation velocity of the initial disturbance (pressure) equals the sonic velocity of the medium, and Equation 5.5 is immediately applicable for the temperature calculation. Hence:

$$\left(\frac{v \sin \theta}{C}\right)^2 = \frac{T_1}{T} \quad (5.7)$$

$$\left(\frac{v}{C}\right)^2 = \frac{T_1}{T} \quad (5.8)$$

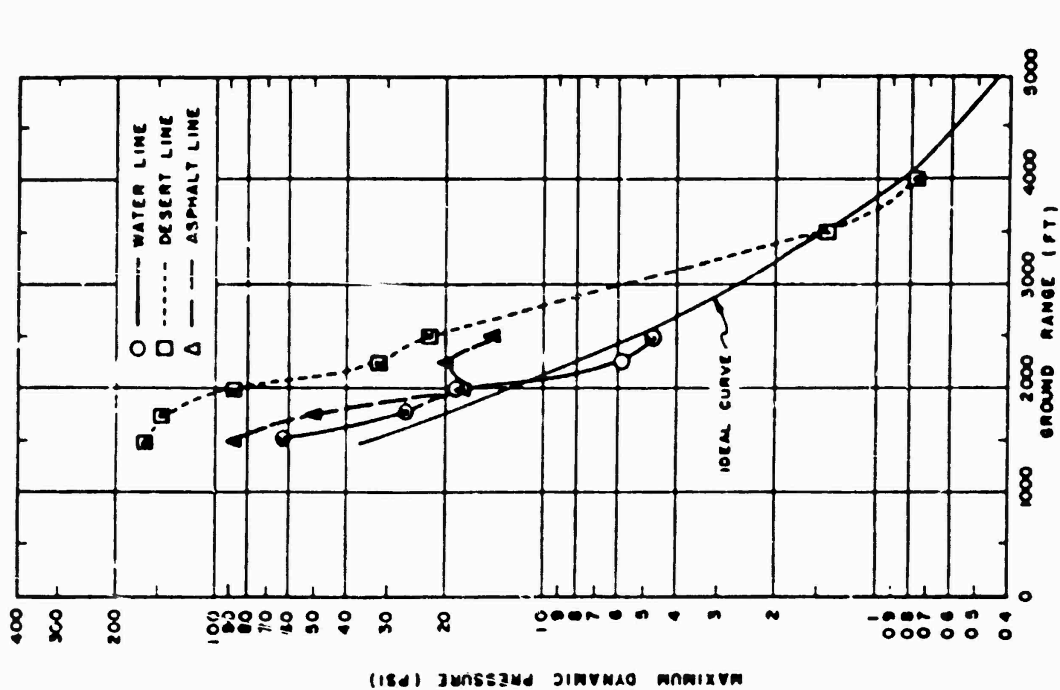


Figure 5.32 Maximum  $q^*$  (pitot) pressure versus ground range, 10-ft level, Shot 12.

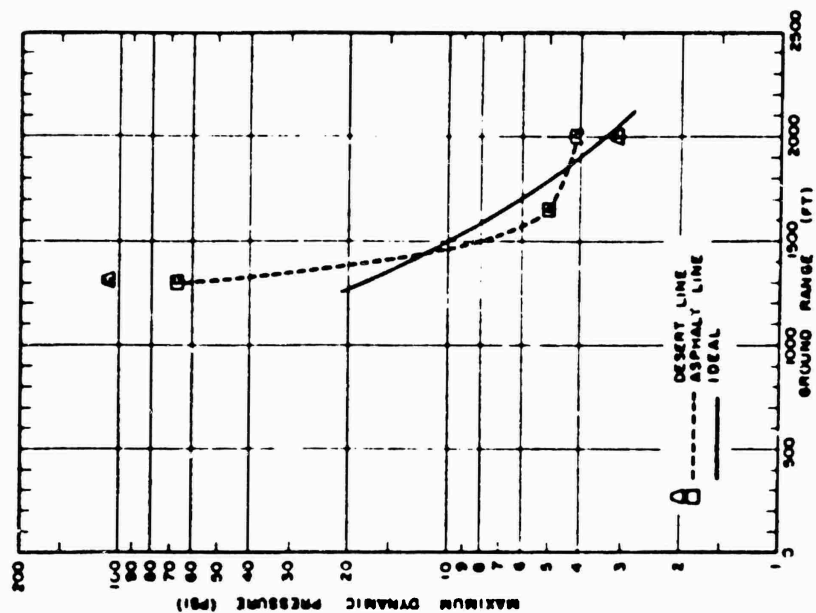


Figure 5.33 Maximum  $q^*$  (pitot) pressure versus ground range, Shot 6.

This calculation (which assumes the wave propagation velocity to be the same as the sonic velocity) if applied erroneously to a shock wave would yield temperatures much larger than those computed from the pressure-calculation or angle-of-front methods.

**Angle of Front.** The assumptions inherent in this method of temperature computations are, in the shock wave region: (1)  $\gamma$  is constant; (2) the precursor front is a shock front which obeys Rankine-Hugoniot relations; (3) the peak pressure is everywhere constant along the shock front; and (4) the precursor front moves along with constant shape; i. e., every part of the front moves at the same horizontal velocity. On the basis of application of the method to a compressional wave front (the acoustic case), only assumptions (1) and (4) are necessary. Referring to Figure 5.41, Equation 5.4 can be written for conditions at the two points of interest in the shock region.

Region A:

$$\frac{p_A}{p_1} = \frac{2\gamma_A}{\gamma_A + 1} \left[ \left( \frac{v_A}{C_A} \right)^2 - 1 \right] \quad (5.9)$$

Region B:

$$\frac{p_B}{p_1} = \frac{2\gamma_B}{\gamma_B + 1} \left[ \left( \frac{v_B}{C_B} \right)^2 - 1 \right] \quad (5.10)$$

Where:  $C_A, C_B$  = sonic velocities ahead of the shock at points A and B.

If  $\gamma_A = \gamma_B$  and  $p_A = p_B$  (see assumptions above), then:

$$\frac{v_A}{C_A} = \frac{v_B}{C_B} \quad (5.11)$$

And, if all points on the wave travel forward at the same horizontal velocity  $v$  then:

$$v = \frac{v_A}{\sin \theta_A} = \frac{v_B}{\sin \theta_B} \quad (5.12)$$

Equations 5.9 and 5.10 reduce to:

$$\frac{C_A}{\sin \theta_A} = \frac{C_B}{\sin \theta_B} \quad C_B = \frac{\sin \theta_B}{\sin \theta_A} C_A \quad (5.13)$$

If it is assumed that close to the ground surface and within the thermal layer the shock front is perpendicular to the ground plane (Figure 5.41), then (Reference 7):

$$\frac{v}{\sin \phi} = v_1 \quad \frac{v}{v_1} = \frac{C}{C_1} = \sin \phi \quad (5.14)$$

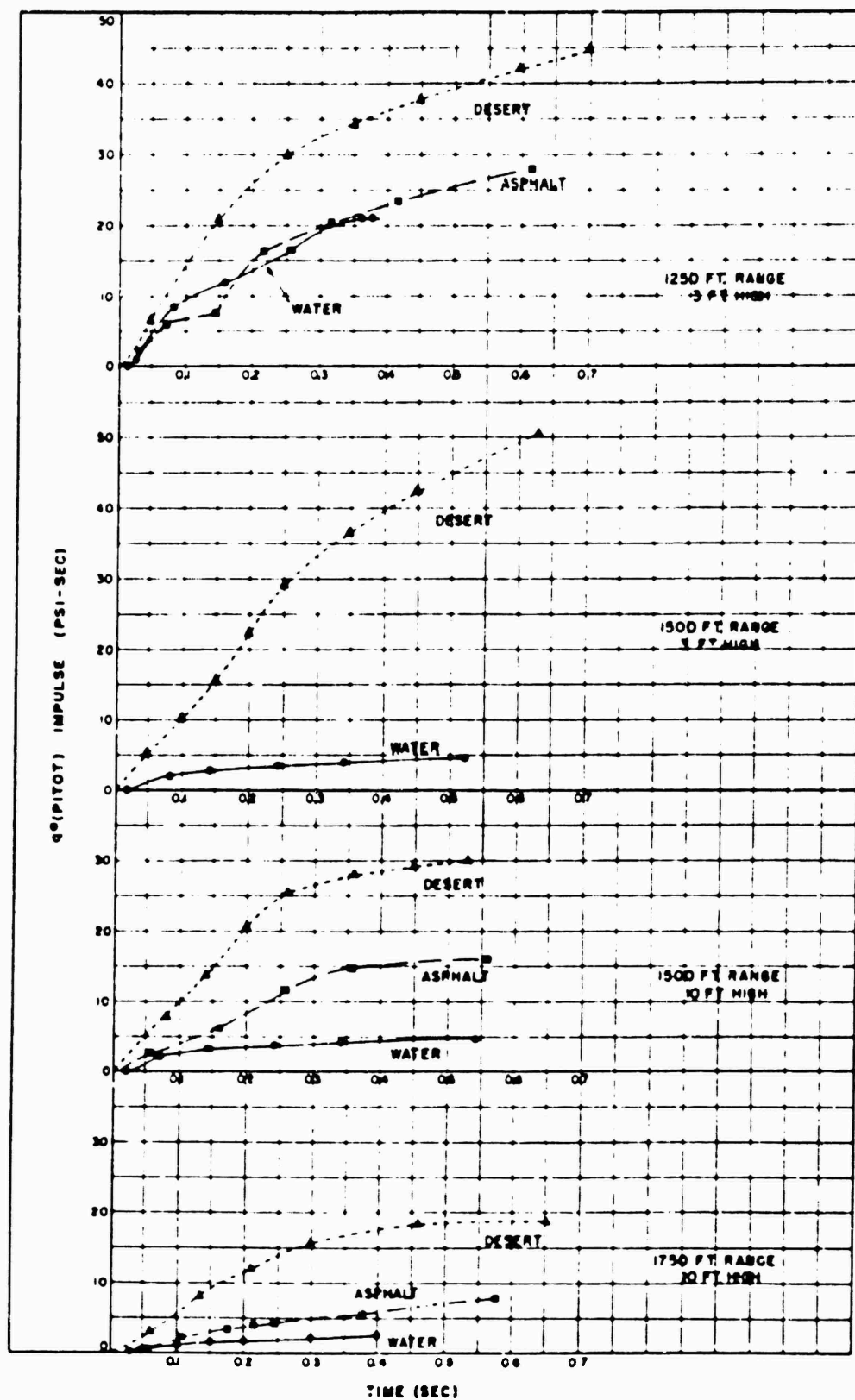


Figure 5.34  $q^*(\text{pitot})$  impulse versus time, 1,250 feet–1,500 feet–1,750 feet, Shot 12.

This last equation was used when, on the streak photographs, a portion of the precursor wave front was obscured by dust near the ground surface. It is obvious that Equation 5.14 will yield higher preshock sonic velocities (and temperatures) than will Equation 5.13. Equation 5.13 applies if the wave is continuously a shock front from A to B or (directly from Equation 5.7) a compression wave from A to B. If the wave front is a compression wave near the ground and a shock wave at higher elevations, as is sometimes the case, Equation 5.13 is in error. If the shock wave merges sharply with the compression wave at E, then the propagation velocity  $v_E^+$  slightly above E (in the shock region) will be greater than the propagation velocity  $v_E^-$  slightly below E (in compression region) due to the overpressure; i.e.:

$$[v_E^- - C_E] < v_E^+ \quad (5.15)$$

If the horizontal propagation velocity remains a constant on both sides of E (which it obviously must) then the wave front must contain a cusp, since:

$$v = \frac{v_E^-}{\sin \theta_E^-} = \frac{v_E^+}{\sin \theta_E^+} \quad (5.16)$$

And hence, using Equation 5.15:

$$\theta_E^- < \theta_E^+ \quad (5.17)$$

In the compression region of Figure 5.41:

$$v = \frac{v_D}{\sin \theta_D} = \frac{v_E^-}{\sin \theta_E^-} = \frac{C_D}{\sin \theta_D} = \frac{C_E}{\sin \theta_E^-} \quad (5.18)$$

In the shock region from Equation 5.13:

$$\frac{C_A}{\sin \theta_A} = \frac{C_B}{\sin \theta_B} = \frac{C_E}{\sin \theta_E^+} \quad (5.19)$$

And hence from Equation 5.17:

$$\left[ \frac{C_A}{\sin \theta_A} = \frac{C_E}{\sin \theta_E^+} \right] < \left[ \frac{C_E}{\sin \theta_E^-} = \frac{C_D}{\sin \theta_D} \right] \quad (5.20)$$

Or:

$$\frac{C_A}{\sin \theta_A} \sin \theta_D < C_D \quad (5.21)$$

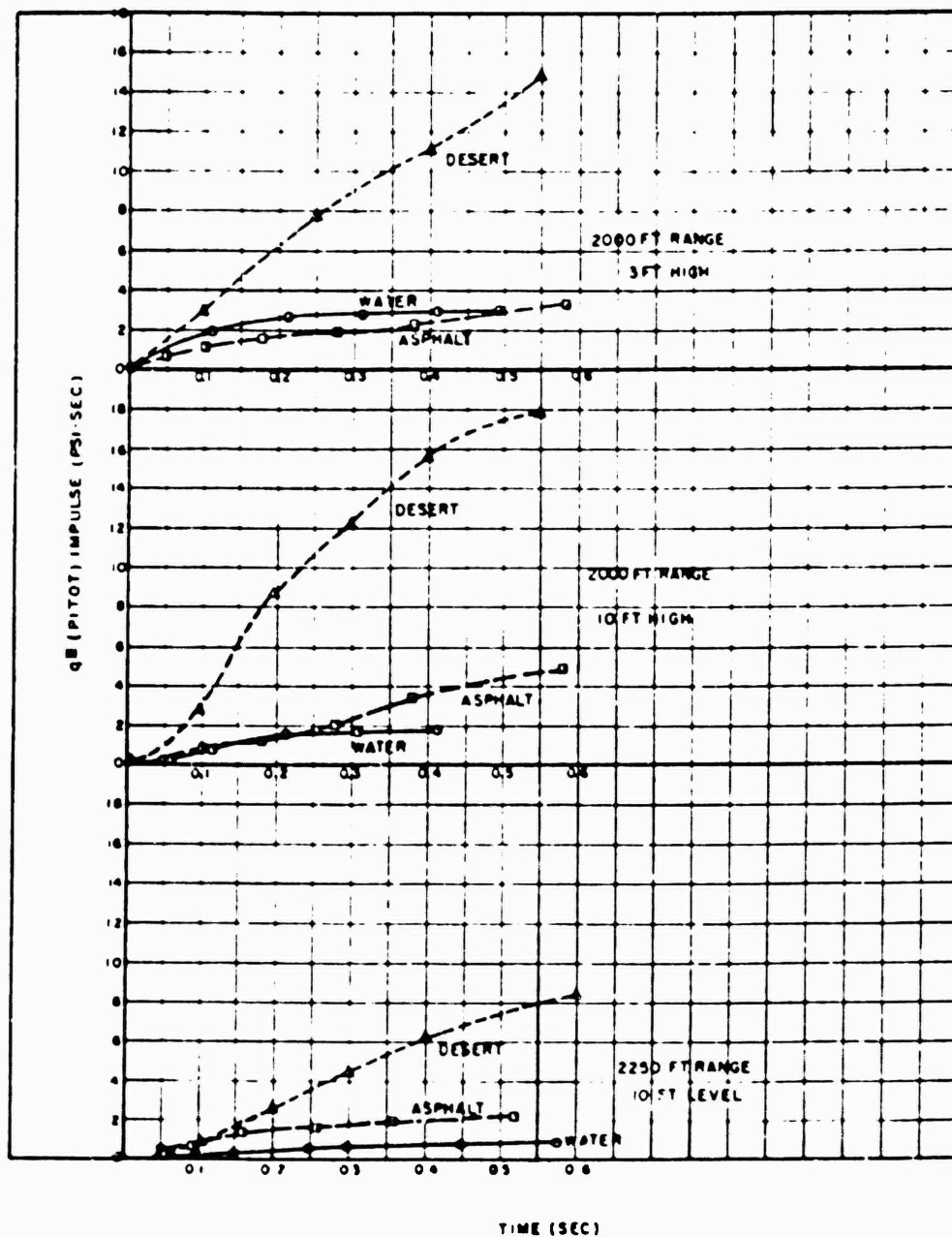


Figure 5.35  $q^*(\text{pitot})$  impulse versus time, 2,000 feet–2,250 feet—Shot 12.

Thus the computed sonic velocity using Equation 5.13 will be less than the actual sonic velocity whenever point A is in a shock region and point D is in a compression region. This error is proportional to the over-velocity caused by peak overpressure and hence the inequality of Equation 5.21 increases with overpressure.

Now that the main elements and limitations of the three methods have been established, the temperature calculations from Shot 12 data may be analyzed critically. Tables 5.3, 5.4, and 5.5 present the results of the computed temperatures along the three Shot 12 blast lines. In each table, the source of data for the temperature calculation is given in the appropriate column heading. In Tables 5.3 and 5.4, the column headed Equation 5.4 contains several temperature values in parentheses—it was sometimes difficult to choose a single unambiguous maximum pressure associated with the precursor wave. Occasionally, therefore, computations were carried out using the two most likely choices. The last column of each table lists what is considered as the best value of computed temperature; this choice is based upon the types of pressure-time record observed at each station; i.e., a shock-type pressure rise would suggest that the best temperature calculation is either the pressure method or the angle-of-front method, whereas a compression-type pressure-time history points to the sonic method. Naturally, the so-called transition form of record presents a problem; however, since it was stressed that the angle-of-front method was equally applicable to the shock or compression cases, it would seem that these angle-of-front temperature calculations, where available, should influence the best value choice in a transition region. In the tables, the best values in parentheses are based upon rather weak assumptions and are included only as approximate temperatures.

Figure 5.42 presents the best-value near-surface temperatures plotted against ground range for the three blast lines of Shot 12. Although the data are meager and of questionable accuracy, some general statements can be made:

1. Near-surface preshock temperatures at ground ranges between about 650 and 1,000 feet are comparable over the asphalt and desert lines.
2. The greatest discrepancy of computed preshock temperature over the desert and asphalt surfaces occurs at 1,500-foot ground range.
3. At 1,500-foot ground range, computed preshock temperature over the water surface is not significantly less than the desert-line surface temperature; however, at 2,500 feet, the value over water is severely depressed with relation to the desert data.

It may be significant that the surface preshock temperatures at close-in stations over the desert all bunch around values in the 1,500°C-region. Reference to the data handbooks (Reference 19) shows that many of the common desert-soil constituents (e.g., silicon oxide, alumina silicate, etc) possess melting temperatures in the range 1,500–2,000°C. This suggests that the chemical composition of the surface material might influence the maximum temperature rise prior to shock arrival.

One additional piece of evidence pertinent to the analysis may be obtained from a theoretical calculation of the preshock surface temperature on the desert line. The maximum temperature rise of the air at grade level during Tumbler has been shown to be correlated with the total thermal energy delivered normal to the surface divided by the square root of the time to the second thermal maximum i.e.,  $Q_n + \sqrt{t_m}$  (Reference 20). Since shock arrival does not appear to correspond to the time at which the surface temperature is at maximum, the above temperatures must be corrected by the method outlined in Reference 21, Pages 16–18.

Since thermal-yield measurements were not a primary measurement on Shot 12, thermal yield and time of the second thermal maximum were determined from Reference 22. Thermal yield may be calculated as an air burst (8.5 kt) or, since the maximum



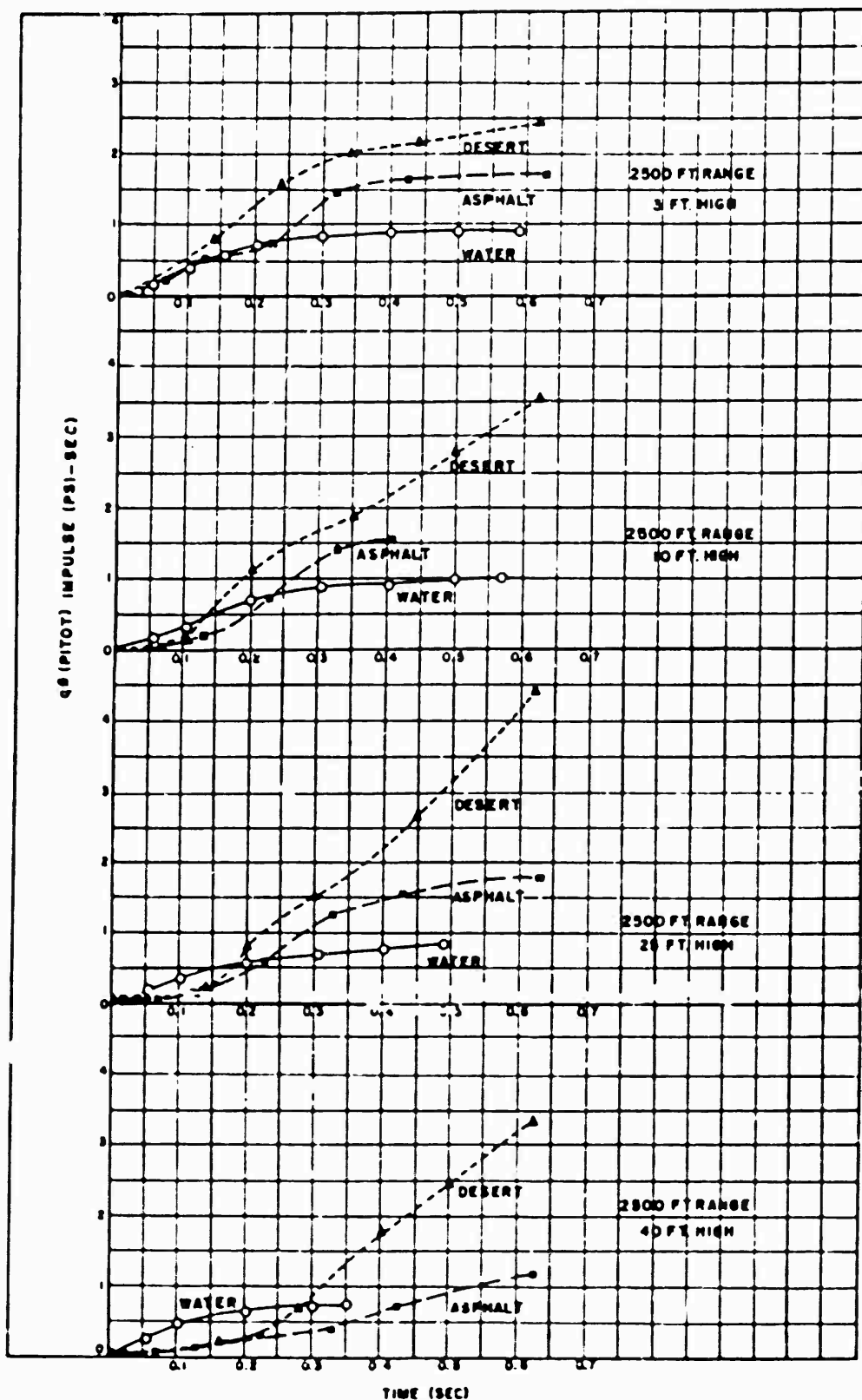


Figure 5.36  $q^*(\text{pitot})$  impulse versus time, 2,500 feet, Shot 12.

fireball radius exceeded the height of burst, by the method of Reference 22, Page 47, (6.5 kt).

Temperatures corresponding to both these yields were computed as follows:

$Q_n + \sqrt{t_m}$  was found for each station, assuming the cosine law to hold. The maximum temperature rise was found from Figure 8 of Reference 20. From Figure 5 of Reference 21, the ratio of time of maximum temperature rise to time of thermal maximum was

TABLE 8-4 DESERT-LINE COMPUTED TEMPERATURES FOR SHOT 13

Ground Range	Arrival Time	Height	Computation Methods					Type of wave	Best Value
			Eqn. 8-4	Eqn. 8-12	Eqn. 8-12	Eqn. 5-8	Eqn. 5-7		
			SRI Data	NOL Data	SRI Data	SRI Data	SRI Data		
feet	sec	feet	°C	°C	°C	°C	°C		
650		0		1,180					1,180
750	0.104	0		1,365		8,700		Shock	1,365
950		0		1,811					1,811
1,000	0.140	0		1,441		8,300		Shock	1,441
1,300		0		1,084					
1,370		3	180*			4,100		Shock	(180)
1,500	0.265	0	540	971	590	2,600	1,540	Shock	540-890
		3	430				1,000	Shock	430
		10	17				315	Trans.	17-315
1,700		0		763					
1,780		10				1,430	(440)†	Trans.	(< 440)
2,000	0.453	0	72	225	135	810	250	Trans.	135-250
		3	17				185	Trans.	17-185
		10	22				73	Trans.	22-73
2,250		10				260	(50)†	Trans.	(50)
2,500	0.760	0	-30(-60)		-10	90	27	Comp.	27-90
		3	0(-50)				25	Comp.	25
		10	-10(-60)				30	Trans.	< 30
		25	-5(-60)				35	Trans.	< 35
		60	60(5)				98	Trans.	< 98
2,800	1.192	0	22		60	60	45	Comp.	45
		3	17				60	Shock	17
		10	-30				-10	Shock	-30
3,000	1.612	0	30		30	60	70	Shock	20-30
		10	20					Shock	20
4,000		0				101		Shock	
4,500		0	-10		20	41	35	Shock	20
		3	-10					Shock	

\* Used NOL wave front angle data.

† Used same wave front angle as observed at nearest gage station.

found to equal 2.4.<sup>1</sup> Using the observed time of arrival, the ratio of time of arrival to time of maximum temperature was computed. Then using Figure 3 of Reference 21, the temperature ratios may be found and the temperature at shock arrival computed. These results are shown in the table below. Temperatures at stations closer than 2,000 feet are not tabulated due to the tenuous nature of the calculation in these regions. Note that the values in the table are larger than those given by the shock-wave calculation.

<sup>1</sup> Operation Tumbler data yield  $\alpha / \sqrt{KSC} \leq 33$ . Estimated values are  $\alpha = 0.7$ ,

$\epsilon = 0.5$  so that  $\epsilon \sqrt{t_m} / \sqrt{KSC} \leq 10$ .

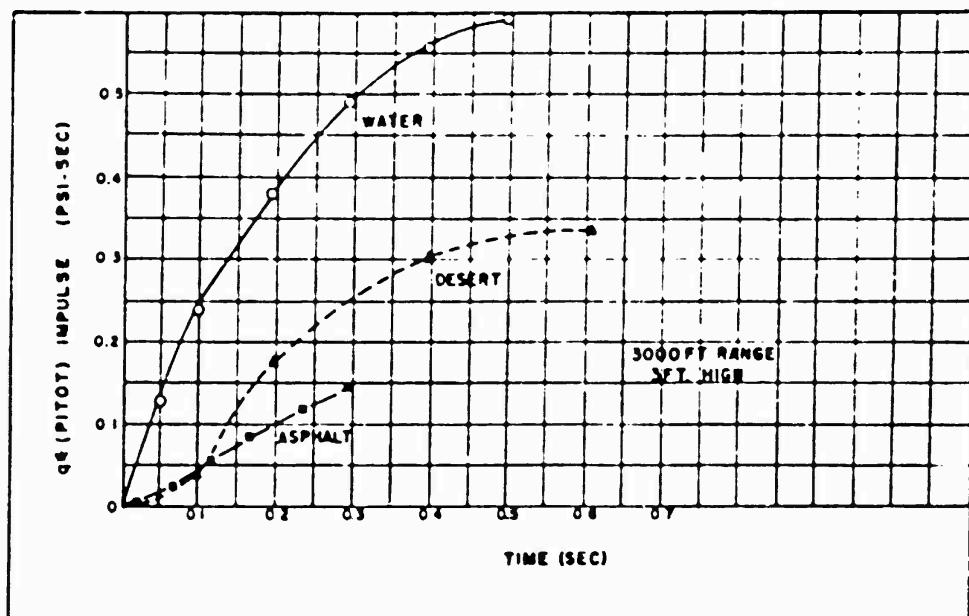


Figure 5.37  $q^*(\text{pitot})$  impulse versus time, 3,000 feet, Shot 12.

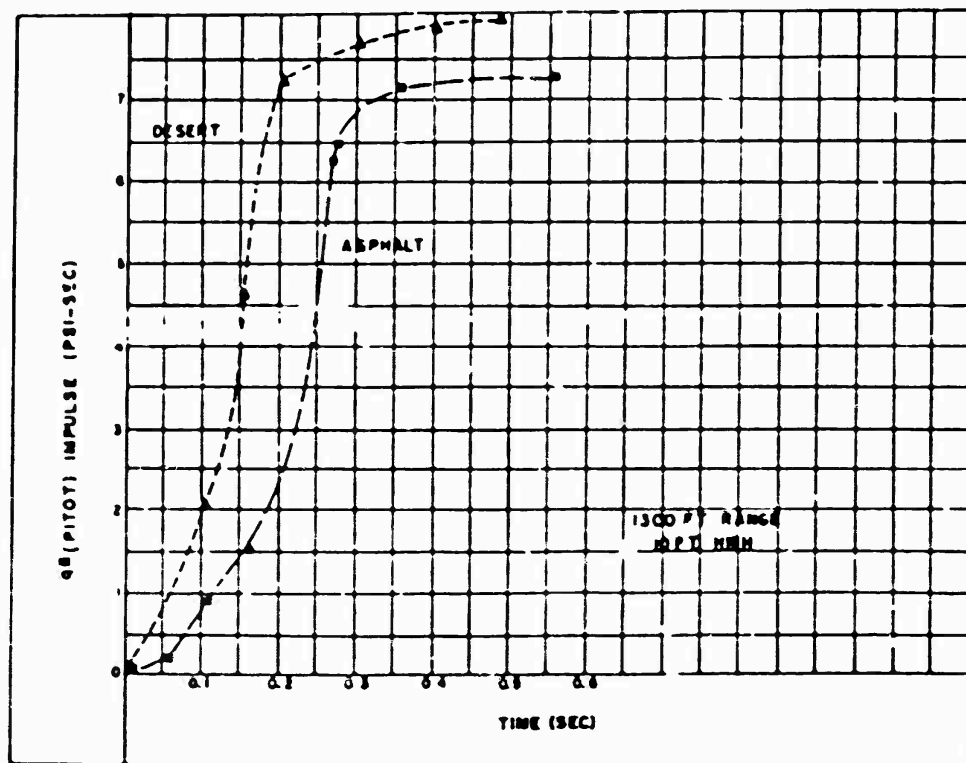


Figure 5.38  $q^*(\text{pitot})$  impulse versus time, 1,300 feet, Shot 6.

Ground Range	Surface Temperature, Desert Line	
	Thermal Yield 8.5 kt	Thermal Yield 6.5 kt
feet	°C	°C
2,000	1,300	825
2,500	445	200
3,000	100	75
4,000	40	30

Since the computed temperature is determined on the basis of conditions obtaining at shock arrival, it is obvious that the computations over the different blast lines, although they refer to the same ground range, correspond to different absolute times. Therefore, a legitimate criticism of the Figure 5.42 presentation of temperatures is that at the same ground range, temperatures over as well as under are determined at times significantly earlier than those computed over the desert. So, to complete the analysis, Figure 5.43 presents the computed temperatures as a function of arrival time for Shot 12. This presentation indicates a rather consistent behavior over the three blast-line surfaces—it is possible to draw a single average curve which agrees well with the derived temperature data. The general form of this curve is a flat maximum out to about 0.2 second, followed by a sharp drop in temperature to about 0.5 second, and then a slower decline out to approximately ambient values at 1.6 second. It is noteworthy that on the time plot of Figure 5.43 the asphalt data near 2,000°C and the water temperature near 400°C appear quite compatible with the remaining results—only at later arrival times do the water line preshock temperatures fall well below the average curve.

To conclude, it can be stated that a careful analysis of airblast data will yield some useful information concerning preshock temperatures near the ground surface. It would be desirable in future operations to obtain more complete data from which to compute wave-front orientations, in addition to the more conventional pressure-time documentation.

**5.4.3 Precursor Development.** Although much attention has been directed toward the study of the precursor wave, its formation and development, the origin and mechanisms responsible for this phenomenon have not been clearly explained. Some questions which are as yet unanswered are: Can the heated-layer theory predict the formation and development of the precursor wave from a particular weapon detonated over a particular surface? Does the heated layer concept exclude the existence of a so-called thermal-shock wave? What is the origin of the precursor wave? How do precursor phenomena scale? Are there meaningful correlations in the detailed results obtained on precursor-producing nuclear weapon tests? These questions will be considered briefly in the discussion which follows.

Considering first the nuclear explosion as a source of thermal radiation, it is pertinent to investigate the dynamic effects produced in a medium as a result of heat release in the medium (Reference 23). (Reference 24 deals with the problem of pressure waves generated by addition of heat in a gaseous medium and obtains the exact solution of an idealized problem in which a finite amount of heat is released uniformly at a section of a tube with a given rate; from this solution, strength of the

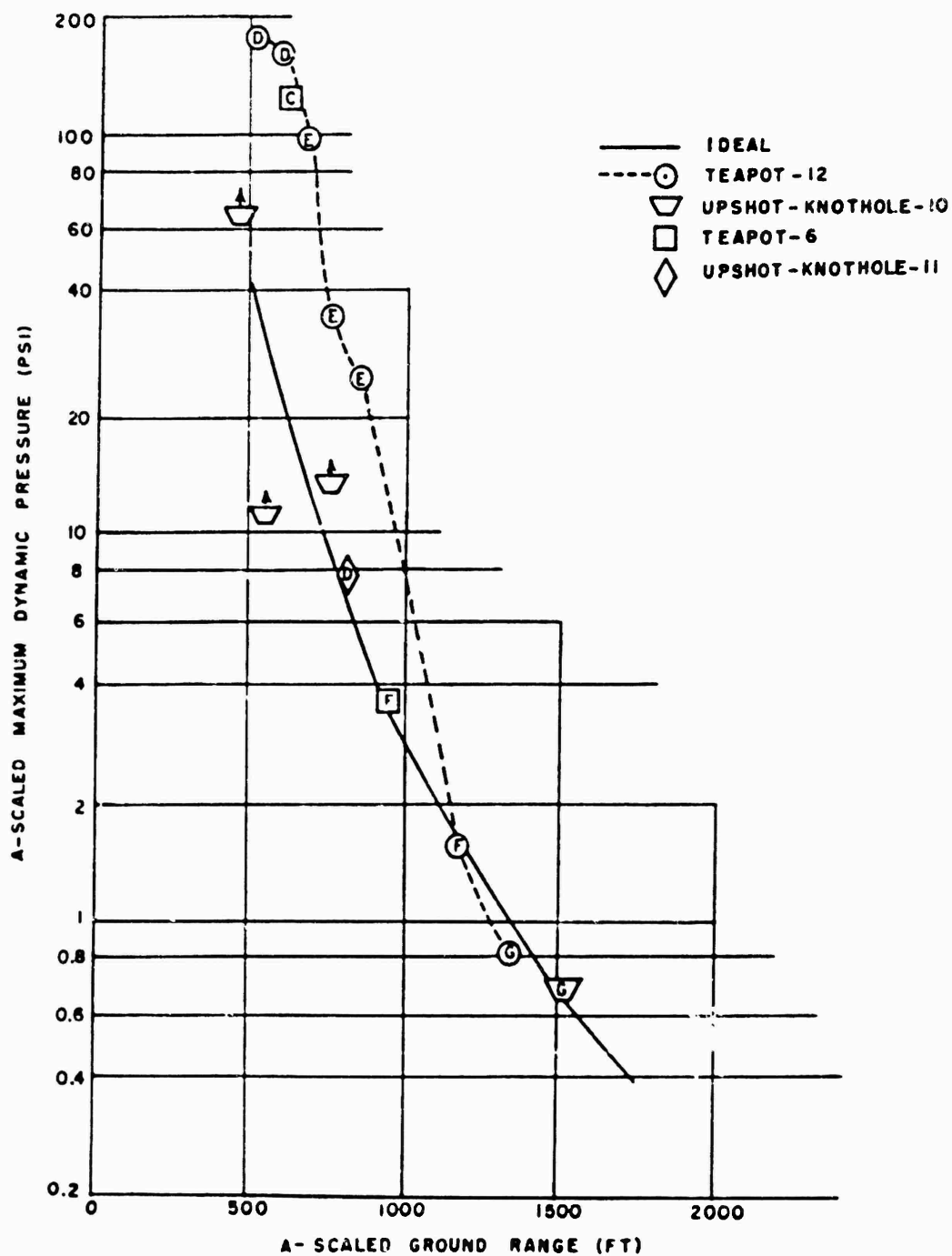


Figure 5.39 A-scaled maximum  $q^*$  (pilot) pressure, 10-foot level, Teapot Shots 6 and 12, previous shots.

shock generated is computed. The basic mechanism by which pressure waves are produced by heat addition is that when heat is added to a volume of gas, the density of the gas is in general reduced. This causes an expansion of the volume occupied by the heated gas, which expansion produces the pressure waves.

In seeking the exact solution to the two-dimensional problem, Reference 24 characterizes the undisturbed medium by two thermodynamic parameters, the pressure  $p$  and temperature  $T$ . Since the velocity of sound  $a$  in the undisturbed medium is uniquely related to the temperature  $T$ ,  $p$  and  $a$  may be used as the two parameters characterizing the undisturbed medium. The strength of the shock wave can be described in terms of the pressure ratio  $p_2/p_1$  across the shock, where  $p_2$  is the pressure immediately behind the shock. It is clear that, in general, the strength of the shock depends upon the rate of heat release per unit area  $S$ , the state of the undisturbed medium being characterized by  $p$  and  $a$  as well as by the time  $t$ . That is:

$$\frac{p_2}{p_1} = F(S, a, p, t) \quad (5.22)$$

The viscous and heat-conductive effects have been neglected in Equation 5.22. Because of dimensional considerations it is necessary to write the above relation as:

$$\frac{p_2}{p_1} = F_1\left(\frac{S}{ap}\right) \quad (5.23)$$

That is, the shock strength must be independent of the explicit time  $t$ , which is actually a direct consequence of the fact that there is neither a characteristic time nor a relevant characteristic length in the problem. The derivation yields:

$$\frac{S}{ap} = \frac{2}{\gamma - 1} \frac{p_2}{p_1} \left( \frac{p_2}{p_1} - 1 \right) \left[ \left( \frac{\gamma + 1}{2\gamma} \right) \frac{p_2}{p_1} + \frac{\gamma - 1}{2\gamma} \right]^{-1} \quad (5.24)$$

The tabulation below lists values of  $S/ap$  computed for selected  $p_2/p_1$  ratios. Also, shown in the tabulation are the corresponding pressures  $p = p_1 + p_2$  and  $S$  quantities; the latter are determined on the basis of  $a = 1,100$  fps and  $p_1 = 14.7$  psi. The heat delivery rate for substantial pressures is not extraordinarily large when compared with thermal energies delivered by nuclear explosions.

$p_2/p_1$	$S/ap$	$p$	$S$
		psi	cal/cm <sup>2</sup> sec
2	7.3	14.7	42
4	31.8	44	180
6	65.2	74	370
8	105.7	103	600
10	152.5	132	870

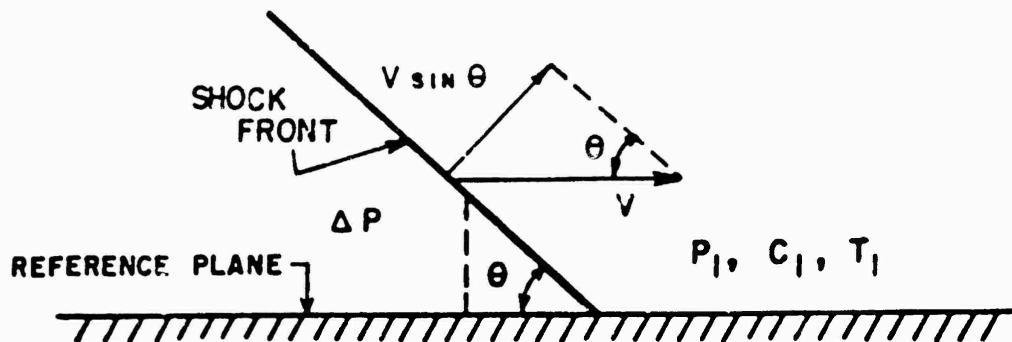


Figure 5.40 Shock front diagram for pressure calculation of preshock temperature.

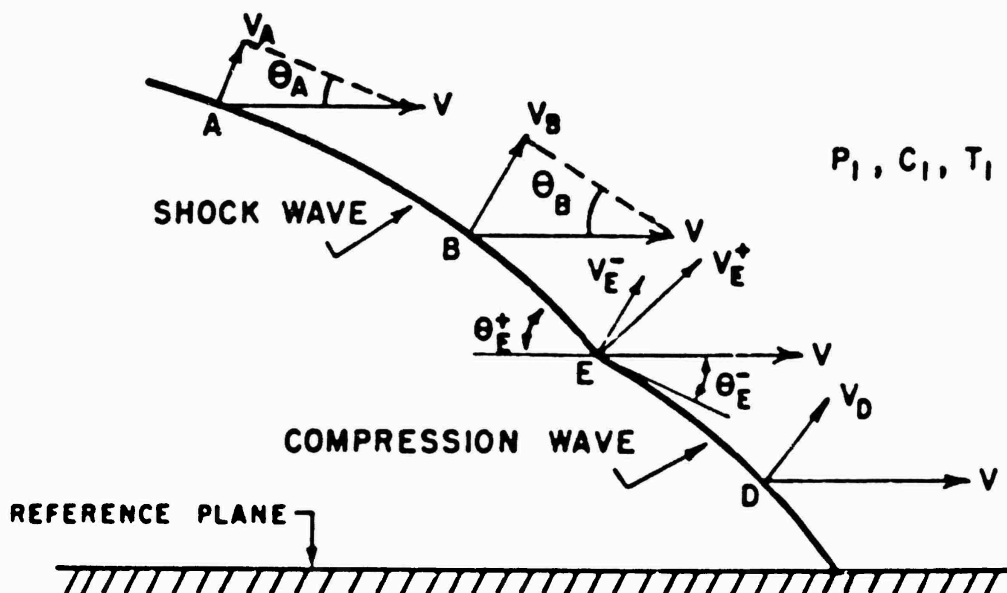


Figure 5.41 Wave front diagram for angle-of-front calculation of preshock temperature.

With this analysis in mind, it is possible to hypothesize concerning the observed propagation velocities of precursor-forming shots. Consider the four ground-range regions shown on Figure 5.44. In each region it is postulated that the velocity of the initial disturbance is governed by different conditions. Now suppose that a pressure wave may be created by addition of heat to the air near the ground (as described in Reference 24) and that there is a threshold criterion which is related to the delivery of thermal energy to the ground. Then, by virtue of the inverse square law for radiation and the time dependency of radiant flux, the threshold will be surpassed at different ground ranges at various times. That is, time of arrival and a velocity can be assigned to the threshold condition and hence to the generated pressure wave. The velocity of this thermal pres-

TABLE 5.6 ASPHALT-LINE COMPUTED TEMPERATURES FOR SHOT 12

Ground Range	Arrival Time	Height	Computation Methods					Type of Wave	Heat Value
			Eqn. 5.4	Eqn. 5.13	Eqn. 5.12	Eqn. 5.8	Eqn. 5.7		
			SRI Data	NOL Data	SRI Data	SRI Data	SRI Data		
feet	sec	feet	°C	°C	°C	°C	°C		
550		0		1,843					1,843
750	0.093	0		1,537		10,500		Shock	1,537
850		0		1,498					1,498
1,000	0.134	0		1,843		6,930		Shock	1,843
1,200		0		1,498					
1,250		0	120*			4,900		Shock	(230)
1,600	0.341	0	1,150	1,306	1,500	3,650	3,230	Trans.	1,150 - 2,230
		3	569				1,130	Shock	569
		10	- 130				100	Shock	
1,700		0		933					
1,750	0.234	0				1,550	(640)†	Trans.	(< 640)
2,000	0.418	0	108		75	950	395	Trans.	108 - 395
		3	95				370	Trans.	95 - 370
		10	45				235	Trans.	45 - 235
2,250		10				600	(94)†	Trans.	(< 94)
2,500	0.674	0	-10 (-30)		60	350	55	Comp.	55
		3	0 (-25)				75	Comp.	75
		10	-50 (-65)				5	Comp.	5
		25	(-25)				25	Trans.	- 25 - 25
		60	45				175	Shock	45
2,750		0				300	(35)†	Comp.	(35)
3,000	1.054	0	30		30	100	75	Comp.	30 - 70
		3	15					Comp.	

\* Used NOL wave front angle data.

† Used same wave front angle as observed at nearest gage station.

sure wave,  $v_d$ , as a function of ground range will be markedly influenced by the choice of the threshold criterion. However, the mechanism by which the thermal flux is related to the pressure wave is of no matter; all that is necessary is to postulate the existence of such a phenomenon.

Referring to Figure 5.44 and Region I, suppose the velocity of the incident wave along the ground (or that of a Mach shock),  $v_i$ , is initially greater than  $v_d$ . This condition will undoubtedly be satisfied at some weapon burst height, since  $v_i \rightarrow \infty$  at ground zero ( $G = 0$ ) and there is some time lag before an appreciable amount of thermal energy is delivered to the medium near ground zero. If  $v_i > v_d$  at  $G = 0$ , then the incident wave will outrun the thermal disturbance until the arrival times are equal; hence in Region I,



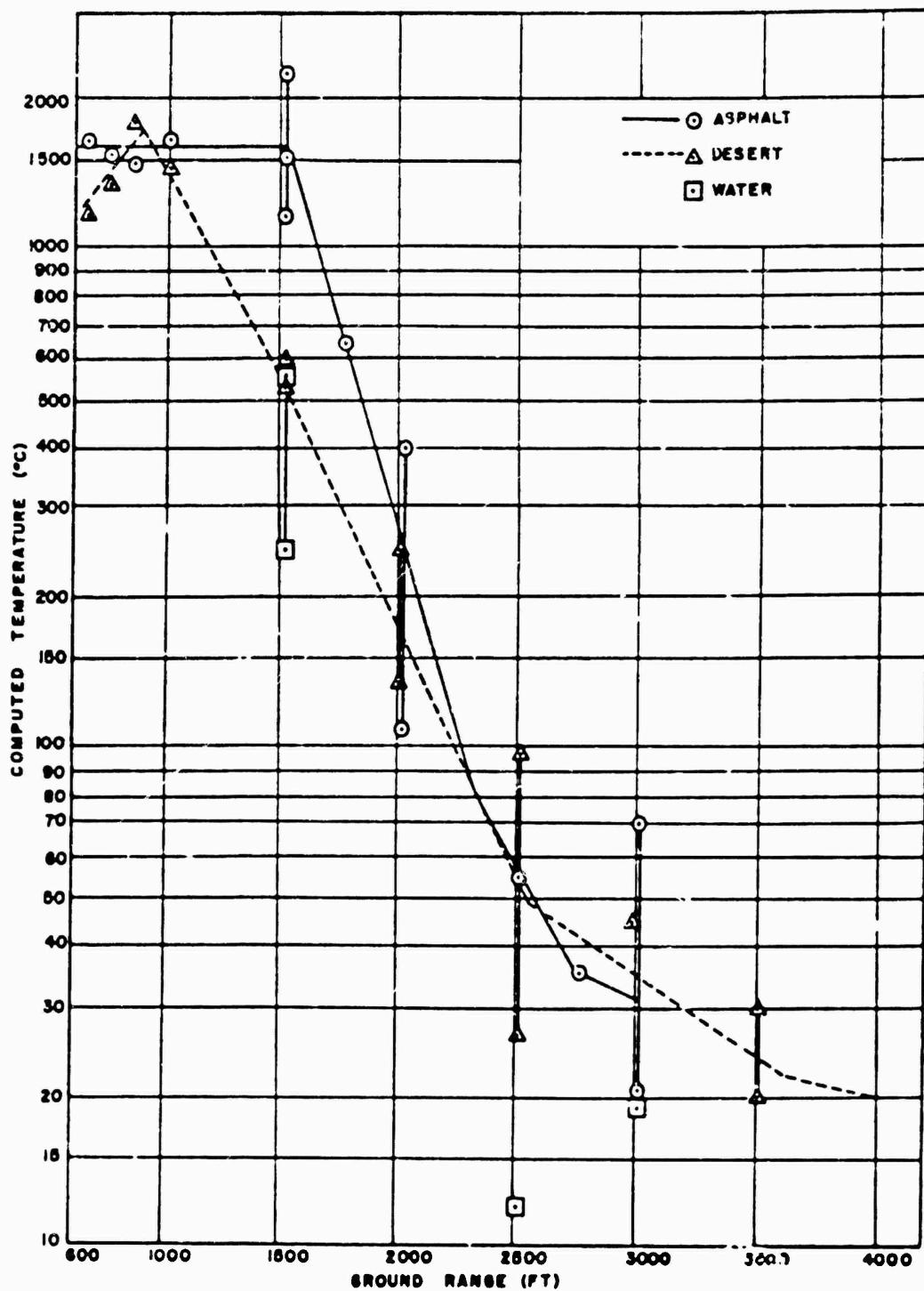


Figure 5.42 Computed preshock temperature versus ground range, Shot 12.

$v = v_1$ . For the thermal disturbance to catch up,  $v_1$  must drop below  $v_d$  at some range. The existence of Region II depends on a subtle relationship between yield, height-of-burst, surface properties, and the mechanism of the generation of the thermal pressure wave. For instance, if the height-of-burst is too high,  $v_1$  may never become less than  $v_d$  and a thermal pressure wave would not be observed in Region II.

In Region II (Figure 5.44),  $v_d > v_1$  (Incident or Mach stem velocity, as the case may be) and  $v = v_d$ . Also, in this region the thermal pressure wave is a shock wave; however, the pressure-time records now show a precursor because the disturbance is traveling faster than the horizontal component of the incident wave velocity. The precursor wave-front angle or angles adjust themselves to maintain the proper geometrical relationships between local sonic and wave velocities. The apparent discontinuity in the velocity curve at the range separating Regions I and II may be resolved by showing a hypothetical arrival-time-distance plot over the same region. Figure 5.45 indicates how reasonable arrival-time data could result in very abrupt velocity variations.

Returning to Figure 5.44, it is apparent that in Region II the sonic velocity ahead of the wave is increasing steadily as more heat is added to the medium. When  $v = C$ , the wave spills out in the usual manner under these conditions, and the shock front degenerates into a compression wave. The toe of the compression wave (near ground surface) now propagates with sonic velocity (Region III) until the compression wave inevitably shocks up and  $v > C$  due to overpressure (Region IV). The tabulation below summarizes the four regions of interest:

Region	Wave Forms	Propagation Velocity	Precursor
I	shock-type	High ( $v \gg C_1$ )	No
II	shock-type	High	Yes
III	compression-type	$v = C_1$	Yes
IV	shock-type	$v = f(p)$	No

Now that the hypothesis has explained some of the details of the precursor velocity picture, it would be profitable to attempt to determine how the phenomena may scale, i.e., to determine if the data from various tests fall into any consistent pattern or system.

**5.4.4 Precursor Arrival-Time and Velocity Characteristics.** If arrival-time data are plotted versus slant range on logarithmic coordinates, as in Figures 5.46 and 5.47, some details of behavior are revealed which are not apparent in Figure 5.1. The precursor arrival data were taken from Project 1.10 pressure-time results and the NOL photography near the ground surface. The incident wave and ideal arrival curves were constructed as previously explained. Evident in Figures 5.46 and 5.47 is the fact that the initial slope, corresponding to the incident wave arrivals, is only slightly less than  $5/2$  whereas the precursor data indicate a consistent  $3/2$  slope in the initial portions. Although Teapot Shot 12 data are not sufficient close to the point of precursor formation to justify extrapolation of arrival times in this direction, critical examination of other precursor-forming shots, particularly Tumbler Shot 4, Upshot-Knothole Shot 10 and Buster Shot Charlie, confirm the fact that initial  $3/2$  slope is indeed quite consistent.

The intersection of the precursor curves with the incident gives a good indication

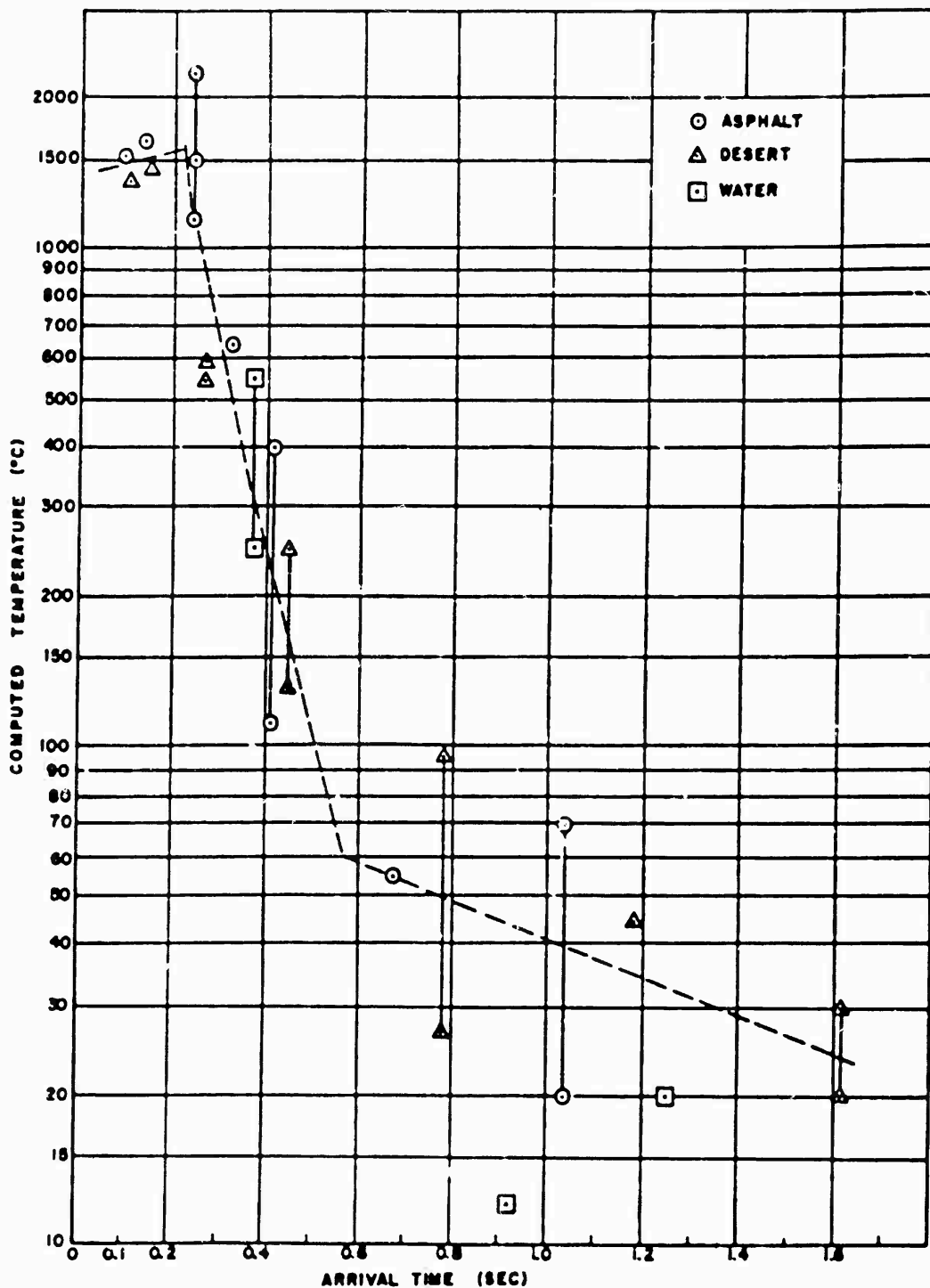


Figure 5.43 Computed preshock temperature versus arrival time, Shot 12.

of the time (or ground range) at which the precursor forms over each of the surfaces considered. In Figure 5.43, the curve corresponding to the water-line data exhibits the same 3/2 slope as observed for the desert and asphalt data; however, the water curve intersects the incident-wave curve latest (at about 710-foot ground range), and it seems to begin to deviate from the 3/2 slope near 1,000-foot range. This result would indicate that, although the effect was short-lived, a true precursor wave was formed over the water line on Teapot Shot 12. The desert and asphalt curves appear to persist along a 3/2 slope out to about 1,500-foot range.

Figure 5.47 shows only one Teapot Shot 6 curve (for asphalt) corresponding to the region of precursor formation. This is explained by reference to the Shot 6 area layout (Figure 2.1), which indicates that ground zero was located so that about 500 feet of asphalt surface was interposed between the shot tower and the desert line. Thus, the Shot 6 precursor formation picture may be considered only on the basis of an asphalt surface. It is further indicated in Figure 5.47 that the differences in surface characteristics (desert versus asphalt) become manifest over ground range distances of the order of 150 feet, e.g., the asphalt pad ends at 500 feet, and the first significant differences in times of arrival are observed at about 650 feet. The reverse situation existed on Teapot Shots 1 and 9 where about 520 feet of nonasphalted area was interposed between ground zero and the asphalt pad of the asphalt line. Initial precursor formation on these lines followed desert behavior until the asphalt pad was engulfed. Since Shot 1 arrival-time data indicate that a precursor did not form over the desert at this height of burst, the asphalt-line precursor over-velocity is more suppressed than on Shot 9, where a precursor did form over the interposed desert. These conclusions are consistent with the results described in Section 5.2.2 which dealt with the effects of localized changes in surface properties.

The similarity of the arrival-time-slant-range curves (Figures 5.46 and 5.47) suggests that a generalized relationship exists of the form:

$$t = BK R^{3/2} f(K) \quad (5.25)$$

Where:  $t$  = the arrival time (A-scaled)

$R$  = the slant range (A-scaled)

$B$  = constant dependent on height of burst and/or yield,

$K$  = a surface constant which depends on the surface characteristics, but should not change with distance over the surface

The velocity of propagation in the horizontal plane, i.e., the precursor velocity (A-scaled), is:

$$V_p = \frac{R}{G} \frac{dR}{dt} = \frac{2}{3} \frac{R^{1/2}}{BK(f + Rf')} \quad (5.26)$$

Where:  $G$  = ground range

' = differentiation with respect to  $R$ .

Multiplying each side of Equation 5.26 by  $t$  from Equation 5.25, the constants  $B$  and  $K$  are eliminated:

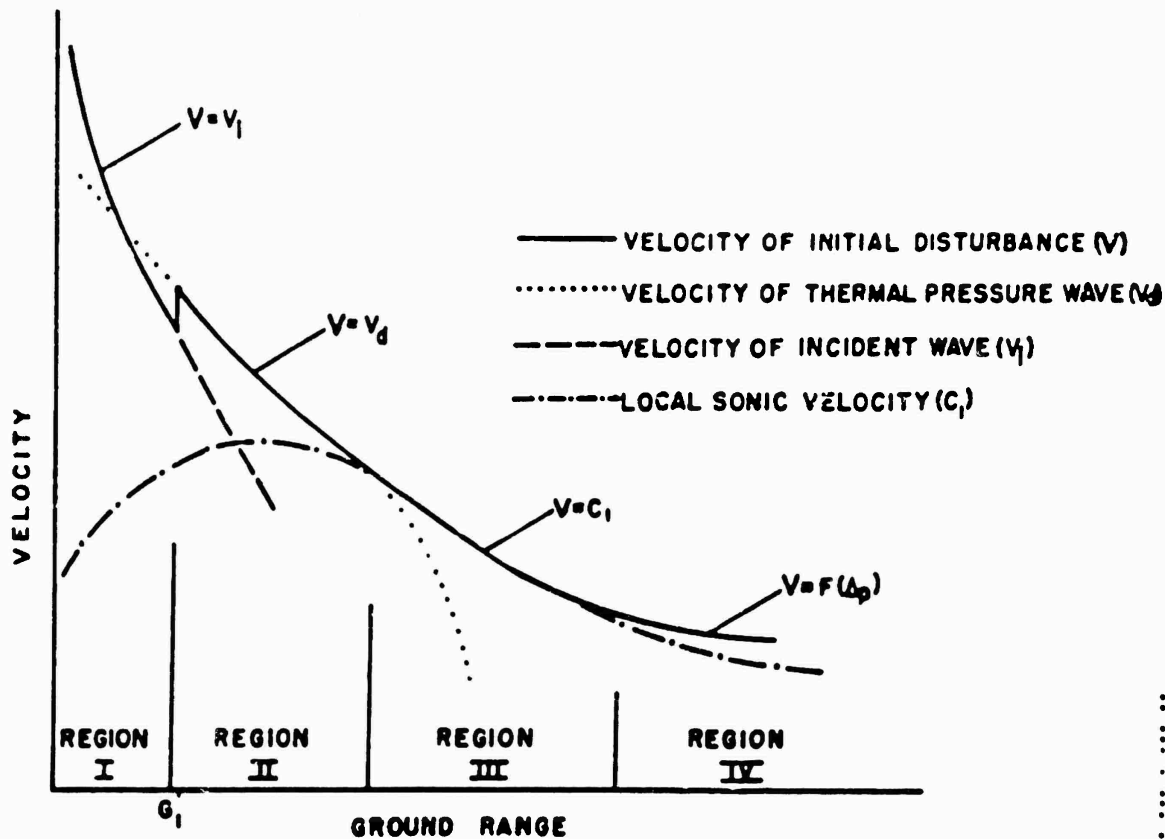


Figure 5.44 Schematic diagram of propagation velocity versus ground range.

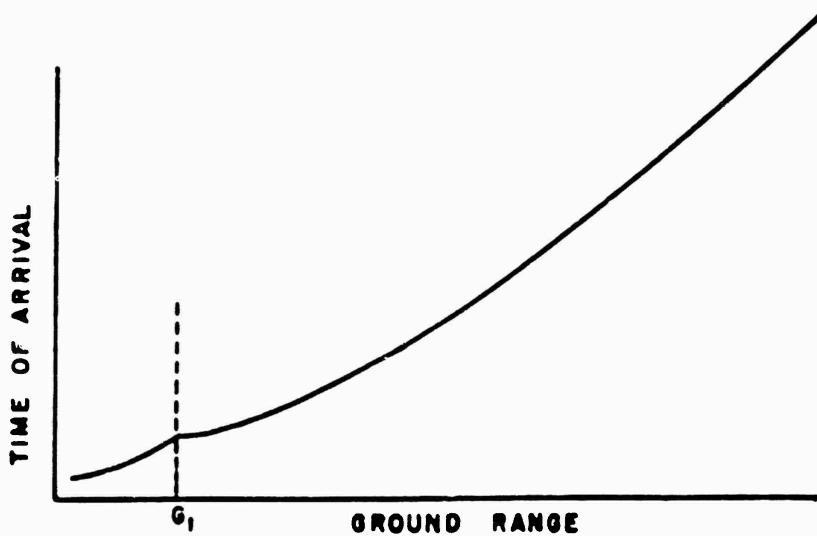


Figure 5.45 Schematic diagram of arrival time versus ground range in region of rapidly changing velocity.

$$\frac{V_x t G}{R^2} = \frac{2}{3} \frac{f}{(f + Rf')} - \frac{2J(R)}{3}$$

Where:  $J(R)$  = a new function of slant range.

Note the left side of Equation 5.27 is independent of scale factors.

Figure 5.48 is a plot of the quantity  $V_x t G/R^2$  versus  $R$  for Teapot Shot 12; Figure 5.49 a plot for Upshot-Knothole Shots 1 and 10. For these shots, definitive time-of-arrival data are available from which accurate velocities could be determined. Reference to Figures 5.48 and 5.49 indicates that the points fall close to a single curve, as well predicted by the foregoing analysis. Decidedly different surface properties are represented in the data of Figure 5.49; Teapot Shot 12 asphalt and desert data are included, as well as data from a shot detonated over the Yucca Flat area (Upshot-Knothole Shot 1). The consistency of the velocity-distance pattern in these figures illustrates the validity of a surface-constant concept. In summary, it appears that although the surface constants of the surfaces considered here are different, the differences do not seem large.

Since Project 1.10 pressure-time data from Teapot Shot 6 are not sufficiently extensive for determination of the shock-velocity-versus-distance function, it is necessary to look elsewhere for time-of-arrival data. The NOL photographic data yield precursor arrival times over both the desert and asphalt surfaces of Shot 6. Using these data, a best-fit arrival-time curve is drawn through the points, and shock velocities are then determined employing the difference method (Reference 14) previously described (Section 5.1.1). Figure 5.50 shows Shot 6 data plotted on the same coordinates as Figure 5.48; also included on the Shot 6 plot is the curve from Figure 5.48. Even though large apparent variations in instantaneous velocity result from reduction of the photometric data, the general trends are consistent.

If the foregoing figures and analyses can be considered representative of what occurs on a precursor-forming shot, it can be concluded that pressure-time measurements on Teapot Shots 6 and 12 were not obtained at close enough range to detect the formation of the precursor wave. Based upon the formation hypothesis offered here, it is expected that if gages were installed in the region of regular reflection, the gage records would register Type 0 (classic) wave forms followed by Types 1, 2, etc., as the precursor forms and develops. It is believed that this behavior was observed on the Tumbler Shot 4 close-in pressure-time results. The NOL gage (Reference 25) closest to ground zero (Station 7-200 at 230-foot ground range) on this precursor-forming shot registered an arrival time and pressure-time history which indicated that the measurement was obtained just prior to the formation of the precursor wave. At the next gage stations (Station 7-201, about 35 feet from Station 7-200), the record was a definite Type 1 wave form with the characteristic double peak.

## 5.5 MEASUREMENTS ON BEAM DEVICE

The beam devices, described in Section 2.5.2 were used for another project on Upshot-Knothole and were included as part of the instrumentation of Teapot Shot 12 as a convenience in connection with Project 1.10. They were designed to yield preliminary information on the behavior of structural beams when subjected to the airblast loading. The two beams were placed at nominal ground ranges of 2,000 and 2,500 feet on the desert line, so as to be in the region of nonclassical blast waves. In the following sec-

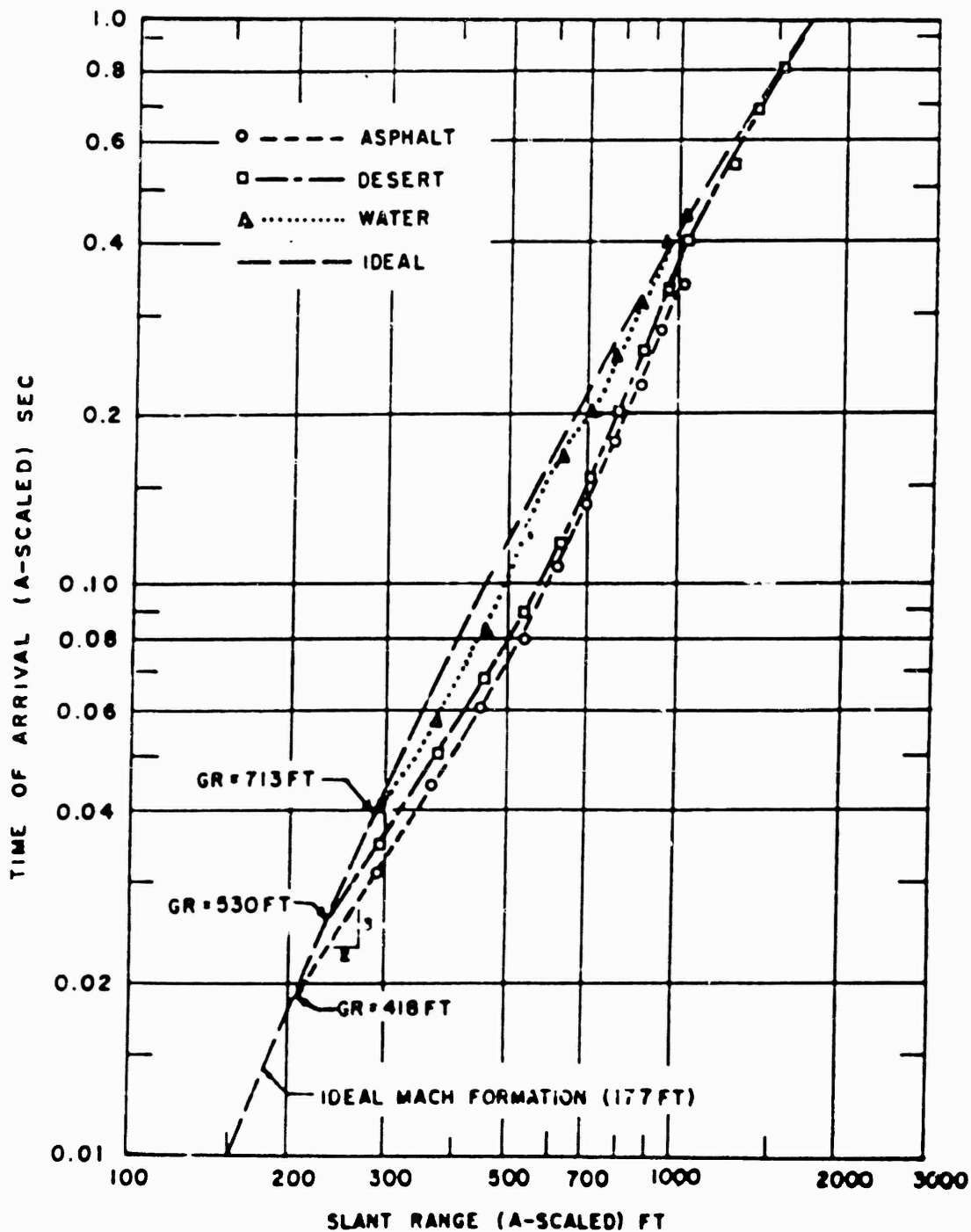


Figure 5.46 A-scaled time of arrival versus slant range, Teapot Shot 12.

tions, after a discussion of the background pertinent to these data, the beam results will be analyzed.

**5.5.1 Background and Definitions.** Fundamentally, so long as flow remains non-rotational, an incompressible fluid moving past a submerged body will impart no motion (i.e., force) to the body, for the resultant of the pressure distribution over the surface of any body in potential flow can never have a component in the direction of flow. Since the equations describing such motion involve only those forces caused by fluid pressure, the motion actually encountered in the case of immersed bodies is evidently due either directly or indirectly to the influence of fluid viscosity.

For flow velocities significantly less than sonic, the actual force imposed upon an immersed body will depend only upon the Reynolds number characterizing the flow and upon the geometrical form and orientation of the body. Dimensional analysis of the several variables involved will lead to the following expression for the resultant force:

$$F = \Phi \left( \frac{uL}{\eta}, \text{form} \right) L^2 \rho u^2 \quad (5.28)$$

Where:  $u$  = velocity

$L$  = length

$\eta$  = kinematic viscosity

$\rho$  = density

The basic drag relationship is generally written in the more convenient form:

$$F = \Phi(R_e, \text{form}) A \frac{\rho u^2}{2} = C_d \frac{A \rho u^2}{2} \quad (5.29)$$

Where:  $A$  = the projected area of the body on a plane normal to the direction of motion

The term  $C_d$  is a variable coefficient of drag:

$$C_d = \Phi(R_e, \text{form}) \frac{2F}{A \rho u^2} \quad (5.30)$$

Where  $\frac{\rho u^2}{2}$  = the expression defining dynamic pressure.

The viscous action of flow may produce three essentially different types of drag force. At very low Reynolds numbers, inertial effects are secondary to those of viscous stress, the latter then extending a great distance into the surrounding flow; this is known as deformation drag. At much higher Reynolds numbers the region in which appreciable deformation occurs is limited to a thin fluid layer surrounding the body, the resulting shear then producing what is called surface drag. Finally, if the form of the body is such that separation occurs, the low intensity of pressure in the wake leads to a force on the immersed body; since the magnitude of this force varies with the shape of the body, it is customarily termed form drag. Under higher-velocity flow conditions



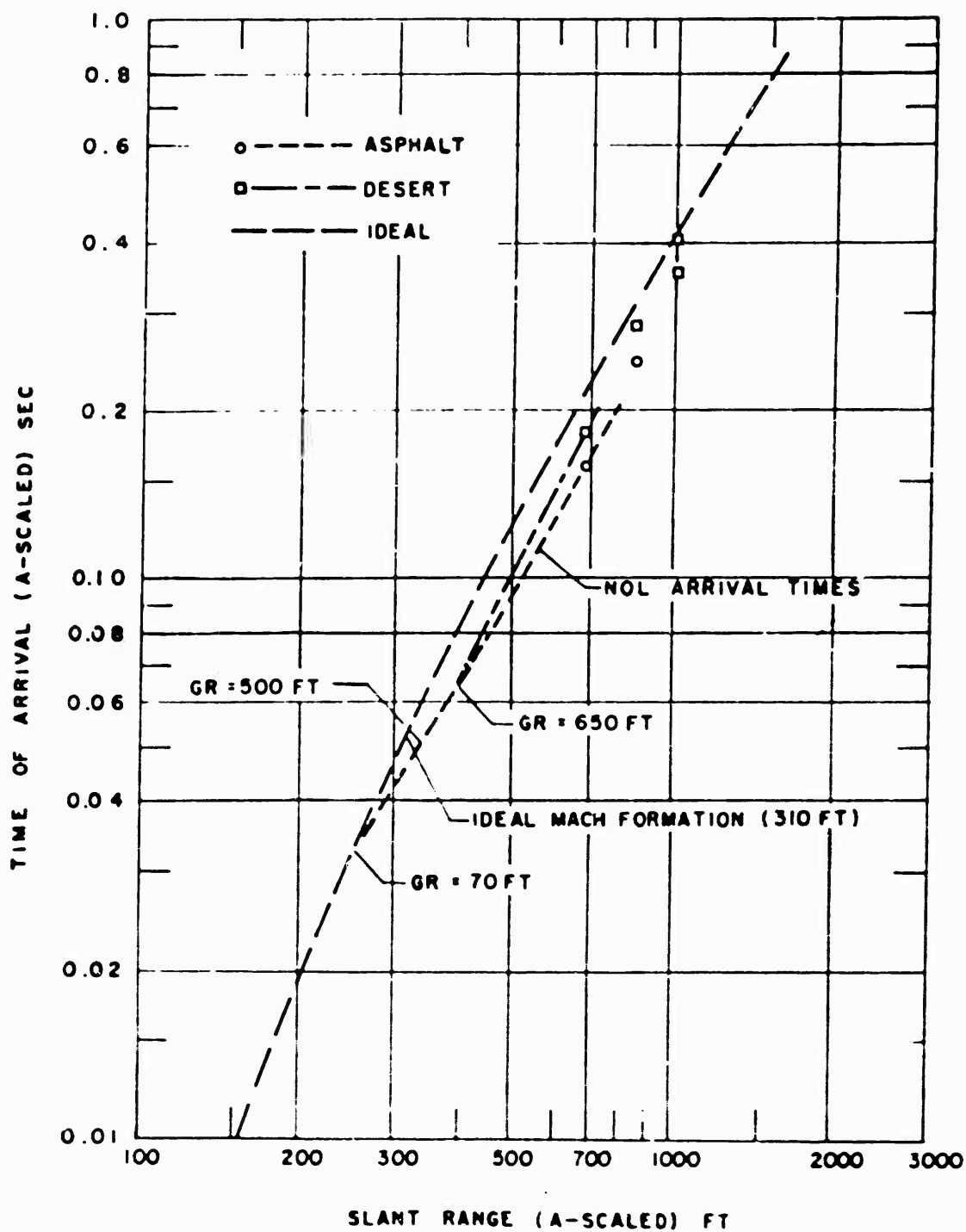


Figure 5.47 A-scaled time of arrival versus slant range, Teapot Shot 6.

(i.e., flow velocities approaching the velocity of sound in the medium), the incompressible flow approximations and use of Reynolds number for establishing dynamic similarity are no longer valid. The two significant dimensionless parameters for compressible flow are the ratio of specific heats and the Mach number  $M$ . At high velocities, the drag is primarily a function of Mach number, so that Equation 5.30 would read:

$$C_d = \psi(M) \quad (\text{form}) \quad \frac{\rho V^2}{4\pi a^2} \quad (5.31)$$

Only in the most elementary cases of deformation drag has it been possible to determine  $C_d$  analytically for certain basic body forms. Cases of motion involving separation have been attacked from various standpoints, but without much success. Quantitative study of drag has, therefore, remained largely experimental. The magnitude of the force on a given body form is usually determined experimentally as a function of Reynolds or Mach number, either in the wind tunnel or the towing tank.

As far as the Project 1.10 beam device field experiment is concerned, there is practically no known previous experimental evidence with which to compare the data. The only wind-tunnel work done on H-beams has been in connection with bridge-design studies. For these purposes, the measurements of drag force are confined to maximum wind pressure of about 50 psi and peak wind velocities of 100 miles per hour. For comparison, the Project 1.10 beam at 2,590-foot ground range (9F3) experienced a maximum pressure of about 1,500 psf (10 psi) and peak wind velocities probably in excess of 500 miles per hour. In addition, it is undoubtedly true that an unknown portion of the pressure on the beam was due primarily to the presence of particulate matter (e.g., water vapor, dust, etc.) suspended in the air stream. These considerations, therefore, lead to the rather convincing fact that the wind tunnel work on H-beams is not pertinent to the problem at hand.

Furthermore, in an analytical sense, the possible presence of particulate matter in the air stream introduces a fundamental anomaly, the significance of which has as yet not been adequately explained. That is, the reliability of Equations 5.30 and 5.31 may be questioned, because it is likely that the determination of drag coefficient as a function of Reynolds and/or Mach number is no longer valid when particulate matter is present. It is probable that it would be necessary to introduce new variables to account for particle size, particle density, and the aerodynamic properties of the suspended particles. Such an effort, although pertinent to all the drag measurements of Teapot, is beyond the scope of this report.

**5.5.2 Beam-Device Results.** The strain-gage records obtained from the two-beam devices are shown in Figure 5.52.

Due to the method of field calibration of these devices, the coordinates appearing on the figure require some explanation. The calibration of the beam was performed in the field as follows. First, the strain gage was mounted on the beam midway between the end supports. Then, using a calibrated hydraulic jack, known loads were applied near the center of the beam span. While these loads were being applied, the strain gage response was noted and the calibration of the beam-gage system completed.

However, it is at once apparent that the method of load application for calibration does not correspond to the loading expected from airblast. For the latter case, the load would necessarily be distributed more or less uniformly over the entire beam length. Simple analysis reveals the relation:

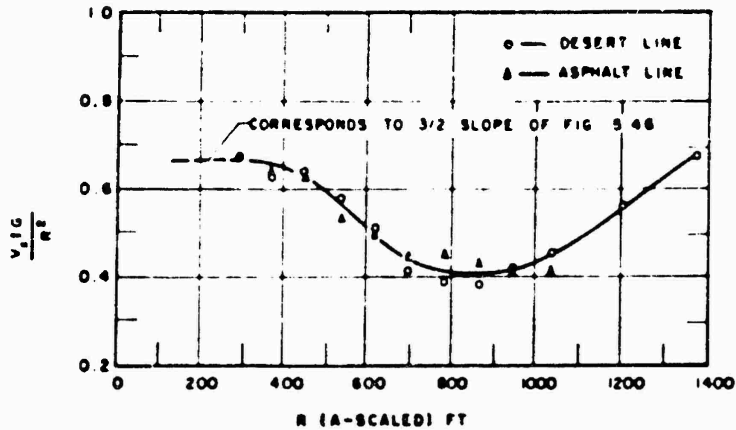


Figure 5.48 A-scaled ( $V_x t G / R^2$ ) versus slant range, Teapot Shot 12.

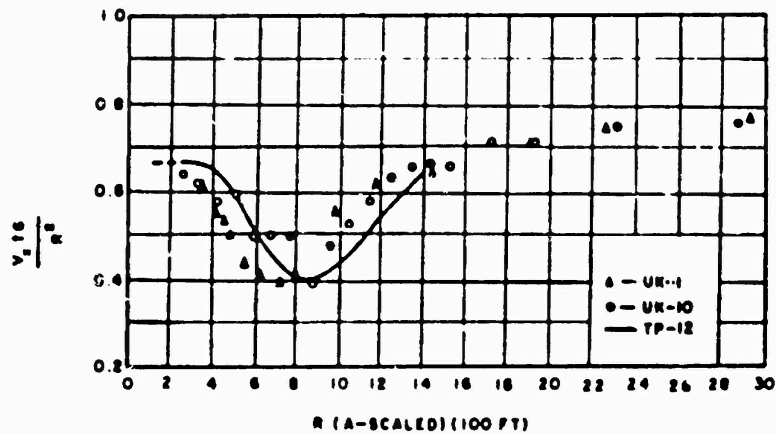


Figure 5.49 A-scaled ( $V_x t G / R^2$ ) versus slant range, Upshot-Knothole Shots 1 and 10 compared with Teapot Shot 12.

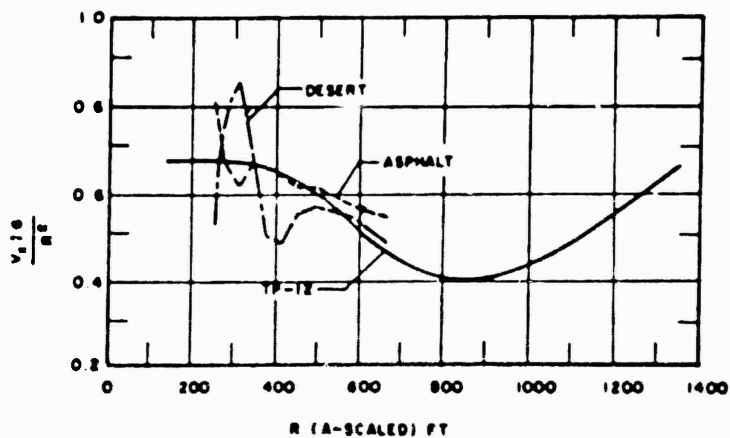


Figure 5.50 A-scaled ( $V_x t G / R^2$ ) versus slant range, Teapot Shot 6 compared with Teapot Shot 12.

$$w = \frac{2P}{L}$$

Where  $w$  = distributed load per unit length

$P$  = the calibrating load (applied near center of span)

$L$  = the length of the beam span.

Applying the above relation to the results of Figure 5.51, it is possible to compute the drag force per unit area; the right hand coordinate shown in the figure presents this drag force calibration for the two-beam devices used. The necessity for presentation of two 7F3 records is caused by some confusion due to a base-line shift for this record. The two records represent the extremes of placement of the base line. Data reduction was terminated when the difference in reduced force exceeded 2 : 1.

TABLE 5.6 WATER LINE COMPUTED TEMPERATURES FOR SHOT 12

Ground Range	Arrival Time	Height	Computation Methods					Type of Wave	Best Value
			Eqn. 5.4	Eqn. 5.13	Eqn. 5.12	Eqn. 5.8	Eqn. 5.1		
			SRI Data	NOL Data	SRI Data	SRI Data	SRI Data		
feet	sec	feet	°C	°C	°C	°C	°C		
750	0.119	0				8.000		Shock	
1,000	0.170	0				3.850		Shock	
1,250		3				1,300		Trans	1,200
1,500	0.247	6	250		< - 270†	550	< - 270†	Trans	250 - 550
		8	- 156				50	Shock	
		10	- 78				330	Shock	
1,750		0				1,050		Shock	
2,000	0.589	0	— *		— *	700	— *	Shock	
		3	35				600	Shock	35
		10	35				700	Shock	35
2,250		10				250		Shock	
2,500	0.814	0	- 10		12	250	150	Shock	12
		3	20				240	Shock	20
		10	25				250	Shock	25
		25	10				250	Shock	10
		40	25				250	Shock	35
2,750		0				250		Shock	
3,000	1.246	0	- 15		20	200	110	Shock	20
		3	- 25				110	Shock	

\* Indeterminant computation — due to angle larger than 90° near ground surface

† This excessive negative temperature due to angle at surface being smaller than aboveground wave front angle, i.e.,  $\theta' = 59^\circ$

‡ No data available

Since the drag force per unit area (versus time) is known and measurements near the beams of  $q$  (pitot) dynamic pressure (versus time) are available, application of Equation 5.30 leads to determination of a drag coefficient  $C_D$  as a function of time. These results are presented in Figure 5.52; it should be emphasized that smoothed  $q^*$  (pitot) records were used for the drag-coefficient calculations. Referring to the figure, several general characteristics are evident:

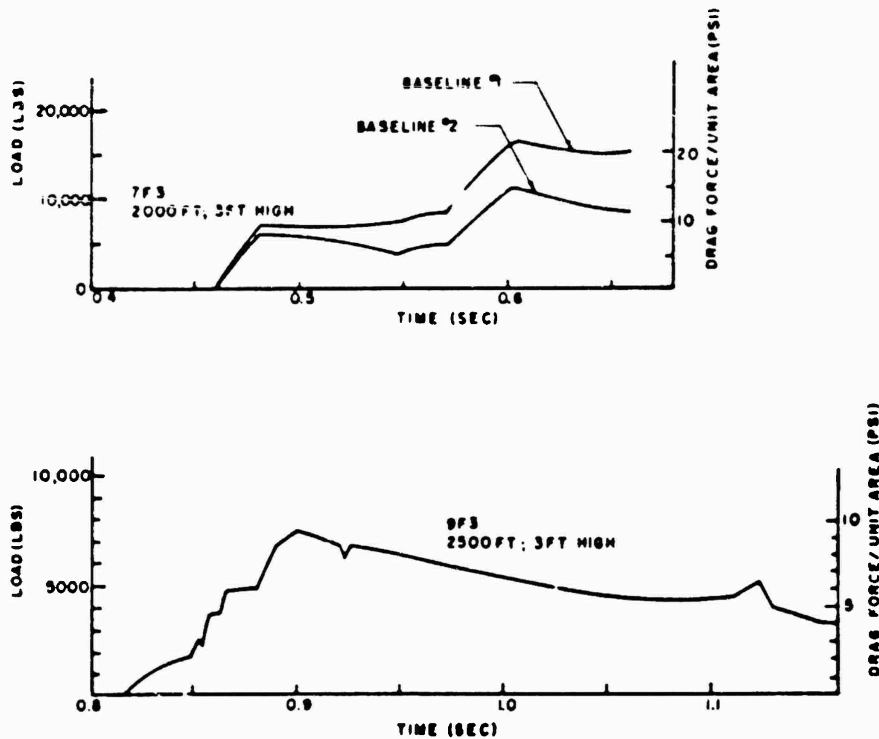


Figure 5.51 Records of force versus time from H-beam devices, Shot 12.

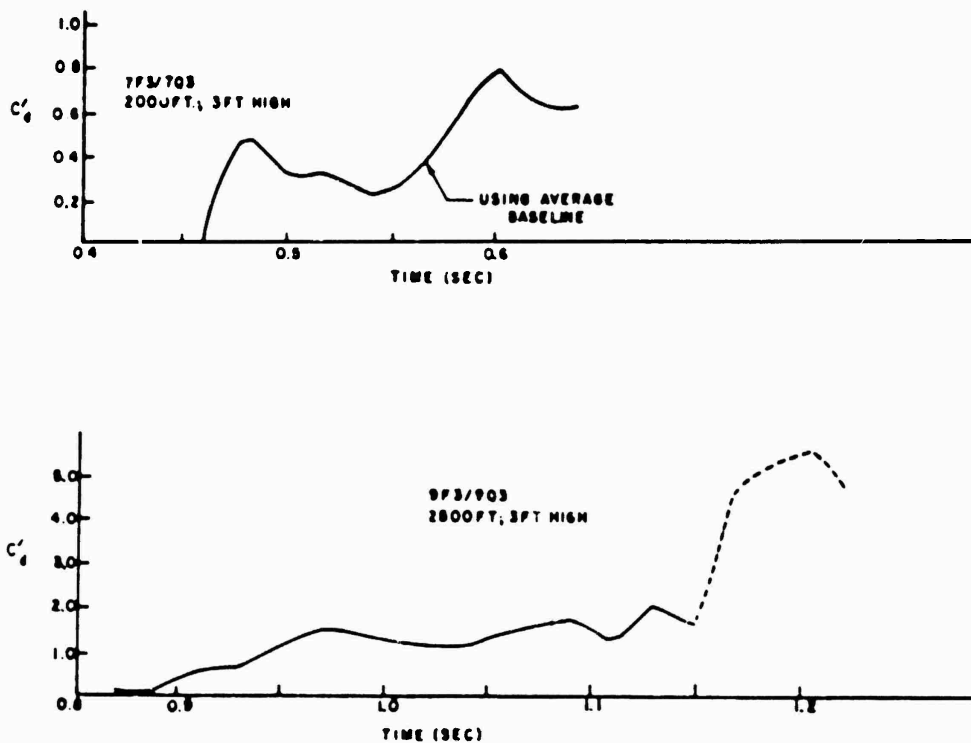


Figure 5.52 Computed drag coefficient versus time for H-beam devices, Shot 12.

1. The computed drag coefficient for a single beam may vary markedly with time (see 7F3/7Q3 trace, Figure 5.22).

2. The results at 2,000-foot ground range show a rather sharp initial rise of drag coefficient, as opposed to the long, slow increase associated with the 2,500-foot measurement.

3. Although it is not possible to compare the computed coefficients at the two stations, at comparable times the average (over the first 100 msec) drag coefficient appears to be significantly larger for the beam at 2,500 feet.

4. The very sudden increase in coefficient near 1.1 second on the 9F3/9Q3 record, Figure 5.52, is the result of a sharp decrease in the  $q^*$  (pitot) pressure at this time; the strain-gage record (Figure 5.51) indicates no corresponding decrease in drag force near 1.1 second.

Since the drag coefficients referred to above have been determined from combining two separate measurements (i.e., drag force and  $q^*$  (pitot) pressure and since no information is available concerning the effects of particulate matter upon each measurement, it is not possible to explain or evaluate the observations included in Figures 5.51 and 5.52. At present, these data represent an initial attempt to determine experimentally the drag force on an H-beam subjected to nonclassical airblast pressure loading. It is probable that when the effects of disturbed blast waves and particulate matter upon drag force and  $q$  (pitot) measurements become better known, the Project 1.10 beam data will be of more-significant value.

## Chapter 6

# CONCLUSIONS and RECOMMENDATIONS

### 6.1 CONCLUSIONS

**6.1.1 Instrumentation Performance.** For Teapot Project 1.10, full length records were obtained on 96 percent of the gage channels (this was not true of previous shots when measurements were made in the precursor region). This excellent performance was largely the result of well-designed instrument towers and mounts. The towers were entirely undamaged on both Shots 6 and 12, and damage to the mounts was limited to the tearing off of the gage baffles on three gages. Such failures as occurred (4 percent) were caused by electrical rather than mechanical damage.

The interpretation of the pitot-tube overpressure and dynamic pressure measurements is hampered by lack of calibration data under shock-wave flow conditions and also by inadequate knowledge of effect of particulate matter upon the measurement. Corrections for pitch, yaw, and Mach number should be available for transonic and supersonic flows.

From the available data obtained from the aboveground baffle-mounted overpressure gages and nearby pitot-tube static pressure gages, it is apparent that the two gage configurations are not equivalent in regions of high pressure and/or disturbed blast waves. In regions of supersonic flow, the above ground baffle-mounted gages are probably not desirable.

**6.1.2 Wave-Form Classification.** With a few exceptions (viz., the water line) it is possible to group the Project 1.10 pressure-time results into two sets of wave-form classification: one system for overpressure (Types 0 through 8) and another for  $q^*$ (pitot) dynamic pressure measurements (Types B through H). As expected, wave-form behavior as a function of ground range is sensitive to the characteristics of the blast-line surface.

For Shot 12, the overpressure wave forms over the water line at least partially traverse two wave-form cycles, while the wave forms over the asphalt surface do not attain classical form (Type 8) even at the last gage station (3,000 feet) on the blast line. However, on the desert line the classical form is observed at 4,500 feet. Although the non-classical behavior persists to longer ranges over the asphalt, the precursor as a distinctly separate wave (Type 1) is observed at longer ranges over the desert. The same general remarks hold for the dynamic-pressure  $q$ (pitot) wave-form classifications.

When the wave-form classification is incorporated into the presentation of peak-pressure-versus-ground range, it becomes evident that it is possible for an ideal peak pressure measurement to be identified with a disturbed (non-ideal) wave form. Consequently, introducing both variables (wave form and peak pressure) into the analysis helps to reduce the ambiguities associated with comparing results from different nuclear tests.

**6.1.3 Shock Velocity and Computed Preshock Temperature.** Considering the horizontal-trace velocity of the shock front as determined from gage-arrival times over

the various surfaces instrumented on Shots 6 and 12, the velocities over the asphalt and desert surfaces are well above ideal, particularly at close-in (less than 1,500 feet) ground ranges. Even over the water surface, shock velocities determined near 1,000-foot ground range are well above ideal values.

From a comprehensive review of the various methods of computing preshock temperature using shock parameters, it is evident that this computation is definitive only when sufficient wave-front orientation and pressure-time data are available. In any case, careful analysis is necessary in the calculation and naturally, the computed temperature yields only some average value at the time of shock arrival. This is a poor substitute for the more desirable direct-temperature-versus-time (i.e., from detonation time) measurement.

**6.1.4 Surface Effects.** The limited wave-front orientation data which could be derived from the Shot 12 results indicate that deviations of airblast phenomena from ideal over the asphalt surface persisted to greater ground range when compared with results over the desert and water surfaces. In general, the wave-front orientations determined from arrival-time data agree very well with the NOL shock photography data.

To summarize, the peak overpressures measured on Shots 6 and 12 were depressed most severely over the asphalt surface and least over the water; in addition, aboveground maximum pressures were generally higher than those measured at ground surface, a result also observed on Shot 10 of Upshot-Knothole.

The Project 1.10 dynamic-pressure  $q(\text{pitot})$  results indicate a severe attenuation of peak pressure with distance for all surfaces. Also, the influence of surface characteristics appears least pronounced at the closest gage station (750 feet) on Shot 12.

From the Shot 12 results obtained on the BRL gage arc (2,500 feet), abrupt localized changes in the characteristics of a surface over which a disturbed blast wave is traveling may have significant effects upon peak pressure and/or wave form in the near vicinity of the surface discontinuity. Data from the offset gages on the water line reveal that precursor characteristics observed on the close-in water-line gage records are not due to cross-feed of energy from the desert surface.

**6.1.5 Precursor Phenomena.** When compared with the results from previous precursor-forming nuclear shots, Shots 6 and 12 display similar behavior: nonclassic wave forms, depressed peak overpressure above 7-8 psi, and close-in dynamic  $q(\text{pitot})$  peak pressures which are several times ideal.

Consideration of the Shot 12 water-line wave-form development, shock velocities, measured pressure-time data, and offset-gage data shows that a precursor formed over the water evidently shortly before the pressure wave reached the first gage (750 feet) and continued to evolve normally out to about 1,500 foot ground range. Gage records at subsequent ground ranges indicate what appears to be a complex competition between normal precursor behavior on the one hand and energy feed-in from the adjacent desert areas on the other.

Basically, the precursor wave over the asphalt line was not much different from that over the desert—the only distinction being that the disturbance appeared more extended over the asphalt.

Analysis of the results of Shots 6 and 12, coupled with the related theoretical approach by Chu, has created renewed interest in the concept of a shock wave produced by high-flux thermal input. Some confidence in the concept is generated by the success of a semi-empirical analysis of data obtained from precursor-forming nuclear explosions.

Using the Project 1.10 data and some curve-fitting procedures, it is possible to



compute the surface constants which apply to the desert and asphalt surfaces. The Shot 6 (T-7 area, Yucca Flat) and Shot 12 (Frenchman Flat) desert-surface constants deviate by only 3 percent, and the asphalt-surface constants differ, at most, by 12 percent from that of the desert.

**6.1.6 Correlation with Damage.** Analysis of the forces acting on the two H-beam devices instrumented on Shot 12 yields only very tentative conclusions. Although it was possible, using the  $q^*(\text{pitot})$ -time results, to determine the computed drag coefficient versus-time for the two beams, there is no pertinent theoretical or experimental data for such devices with which to compare the field results. Also, it is believed that the presence of particulate matter in the blast wave has a profound (but unknown) effect upon the drag (and drag coefficient) of such structural elements.

## 6.2 RECOMMENDATIONS

There appears to be a need for a change in the procedure used for measuring dynamic pressure, particularly in stream flows exceeding Mach 1.0. Impact pressure (total head) should be measured using a carefully designed supersonic tube, whereas the corresponding overpressure measurement should be obtained from a separate ground-level gage. In fact, there is need for a comprehensive investigation of instrumentation to determine what is most useful for measuring airblast parameters in regions of high pressure and high flow velocities. Also, future instrument design must consider effects of suspended particulate matter upon the measurement.

The scheme of wave-form classification and the idea of including considerations of wave-form information in the analysis of peak pressures should be retained and extended to other blast parameters. It is believed that more useful and understandable presentations would result from this method of analysis.

To confirm the conclusion about the influence of localized surface discontinuities upon blast parameters (Section 6.1.4), future nuclear tests should include careful and detailed measurements over areas which include such surface discontinuities.

Since there is some evidence that Shot 12 was not instrumented closely enough to ground zero to detect precursor formation, it would be wise in future tests to obtain at least time-of-arrival measurements at closer stations.

On future tests, in addition to the conventional pressure-time measurements some close-in measurements should be made which are specifically designed to detect and delineate the thermal shock wave, if it exists.

It is evident that more work, both in theory and laboratory testing, is needed in the field of airblast drag forces on structural elements before available (or future) field results can be made understandable.

## REFERENCES

1. Porzel and Reines; "Height of Burst for Atomic Bombs"; LA-743R, Series B, August 3, 1949; Los Alamos Scientific Laboratory, Los Alamos, New Mexico; Circulation limited; Secret Restricted Data.
2. Gilbert, H. K., and Wilson, R. Q.; "Final Report, Operation Buster"; WT-412, July 1952; Armed Forces Special Weapons Project; Secret Restricted Data.
3. Salmon, V.; "Air Pressure versus Time"; Project 1 2, Operation Tumbler, WT-512, February 1952; Stanford Research Institute, Menlo Park, California. Secret Restricted Data.
4. Swift, L. M., and Sachs, D. C.; "Air Pressure versus Time"; Project 1.1b, Operation Upshot-Knothole, WT-711; Stanford Research Institute, Menlo Park, California; Secret Restricted Data.
5. Shreve, J. D. Jr.; "Air Shock Pressure versus Time for a Tower Shot"; Project 1.1c-1, Operation Upshot-Knothole, WT-712; Sandia Corporation, Albuquerque, New Mexico; Secret Restricted Data.
6. Broyles, Carter D.; "Dynamic Pressure versus Time and Supporting Air Blast Measurements"; Project 1.1d, Operation Upshot-Knothole, WT-714; Sandia Corporation, Albuquerque, New Mexico; Secret Restricted Data.
7. Morris, W. E., et al; "Air Blast Measurements"; Project 1.1a-1.2, Operation Upshot-Knothole, WT-710; Naval Ordnance Laboratory, Silver Spring, Maryland; Secret Restricted Data.
8. Cook, T. B. Jr., and Kammermeyer, K.; "Sandia Laboratory Shock-Gage Evaluation Tests"; Tumbler-Snapper Report WT-505, October 1952; Confidential.
9. "Summary Report of the Technical Director"; Operation Upshot-Knothole, WT-782; Armed Forces Special Weapons Project; Secret Restricted Data.
10. Pearson, A. O., and Brown, H. A.; "Calibration of a Combined Pitot-Static Tube and Vane-Type Flow Angularity Indicator at Transonic Speeds and at Large Angles of Attack or Yaw"; NACA RM L52F24, September 1952; Langley Aeronautical Laboratory; Unclassified.
11. Kelso, J., and Hesse; "Mach Shock Formation From a Nuclear Detonation"; AFSWP-510, March 10, 1955; Secret Restricted Data.
12. "Summary Report of the Technical Director"; Operation Teapot, WT-1153; Armed Forces Special Weapons Project; Secret Restricted Data.
13. Kauffman, W. F., and Shinbrot, M.; "A Method for Differentiation of Experimental Data"; J. Aero. Sci. 20, 428-430, June 1953; Unclassified.
14. Wang, Chi-Teh, and DeSanto, D. F.; "Differentiation of Experimental Data by Means of Higher Order Finite-Difference Formulae"; J. Aero. Sci. 20, 792-793, Sept. 1953; Unclassified.

15. Moulton, J. F.; "Shock Photography Measurements"; Project 1.2, Operation Teapot, WT-1102; Naval Ordnance Laboratory, Silver Spring, Maryland; Secret Restricted Data.
16. "Effects of Atomic Weapons"; Revised, September 1950; Los Alamos Scientific Laboratory, Los Alamos, New Mexico; Unclassified.
17. Brode, H. L.; "Numerical Solution of Spherical Blast Waves"; J. App. Phys. 26, 766, June 1955; Unclassified.
18. Bryant, E. J.; "Response of Drag Type Equipment Targets in the Precursor Zone"; Operation Teapot, WT-1123; Secret Restricted Data.
19. "Handbook of Chemistry and Physics"; Chemical Rubber Publishing Company, 38th Edition, 1954; Unclassified.
20. Sauer, F. M.; "The Preshock Sound Velocity Field Over Inorganic and Organic Surfaces"; USDA, AFSWP-420, December 1954; Secret.
21. Sauer, F. M.; "Corrective Heating of Air Above an Inorganic Surface Heated by Radiation from a Nuclear Weapon"; USDA, AFSWP-862, November 1955; Confidential.
22. "Capabilities of Atomic Weapons"; Department of the Army Manual TM 23-200, July 1955, Revised Edition; Secret Restricted Data.
23. Porzel, F.; Armour Research Foundation, private communication.
24. Chu, Boa-Teh; "Pressure Waves Generated by Addition of Heat in a Gaseous Medium"; Johns Hopkins University, NACA TN 3411, June 1955; Unclassified.
25. Aronson, C. J., et al; "Free-Air and Ground Level Pressure Measurements"; Project 1.3 and 1.5, Operation Tumbler, WT-514; Naval Ordnance Laboratory, Silver Spring, Maryland; Secret Restricted Data.

## Appendix A

### ACCELERATION RESPONSE OF WIANCKO PRESSURE GAGES

It has been generally assumed that the Wiancko balanced-reluctance pressure gage has a negligible response to acceleration forces because of the two-coil, rocking-armature design. Figure A.1 shows that acceleration forces tend to move the armature similarly with respect to both coils, whereas pressure applied to the sensing element moves it in opposite direction from each coil. Thus, acceleration forces tend to maintain the balanced conditions, producing no electrical output. Measurements of this acceleration response show maximum responses of the order of 0.0005 psi/g for a 30-psi gage (0.0016 percent FS/G); Sandia Corporation tests show similar results (Reference 8).

The above measurements do not necessarily indicate the true performance. A change in the geometry of the transducer may produce no unbalance while the gage is balanced, but may seriously affect its response, in this case, to pressure. A force which moves the armature away from the coils, for instance, may drastically affect its sensitivity. Thus, if transient accelerations are applied while a steady pressure is simultaneously applied, a pronounced acceleration may result.

Tests were made on a small number of Wiancko pressure gages to determine their acceleration sensitivity under load. Each gage was provided with a check valve at its inlet, so that pressure could be applied and maintained after removal of the hose connection. The gages were mounted on a Schenitz spin table in several orientations, with slip-ring connections to a normal demodulation circuit. The effect of spin-table speed (radial acceleration) up to 90 g was then observed. Figure A.2 shows the results on a typical 30-psi gage.

In this figure, the percentage error (of the reading, not of full scale) caused by various values of acceleration when the gage is deflected to one-third, two-thirds, and full range is shown for various orientations of the acceleration force. These results are typical of all gage ranges, but there is a considerable variation between gages. Higher-range gages (100 and 300 psi) show much smaller errors (25 to 30 percent as great), and 10-psi gages show slightly larger errors.

Note that transverse acceleration in the tangential direction tends to cause comparable errors to acceleration in the opening-closing direction—a somewhat unexpected result. It will be observed that proportional error is generally greater when the pressure is less than full scale, but is by no means constant in terms of full-scale reading. At zero pressure, no measurable deflection was observed up to 90 g except for longitudinal acceleration, where 90 g produced a deflection equivalent to about 0.04 psi.

The results of these tests intimate that some of the hash observed in pressure-time measurements after shock wave arrival may be caused by acceleration of the mounts.

In general, there is no way to check this possibility, but one approach appears profitable. In the pitot-tube gage, two Wiancko pressure transducers are mounted a few inches apart. These gages are mounted similarly with regard to transverse accelerations. Any response to transverse or vertical acceleration of the mount should be in the same direction on the two gages. A check of the records may then show relatively high-frequency disturbances which if due to acceleration should be in phase on the two records. No such results have been observed (see Section 2.5.5), which indicates that the high-frequency hash is probably not due to the acceleration of the gage mounts.

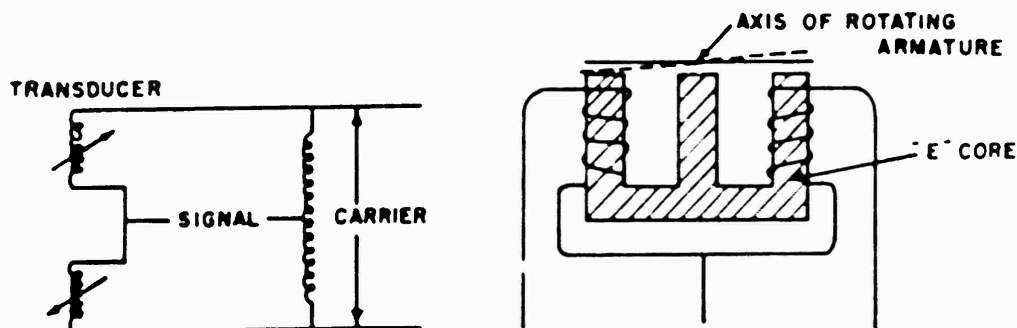


Figure A.1 Schematic diagram of Wiancko pressure transducer system.

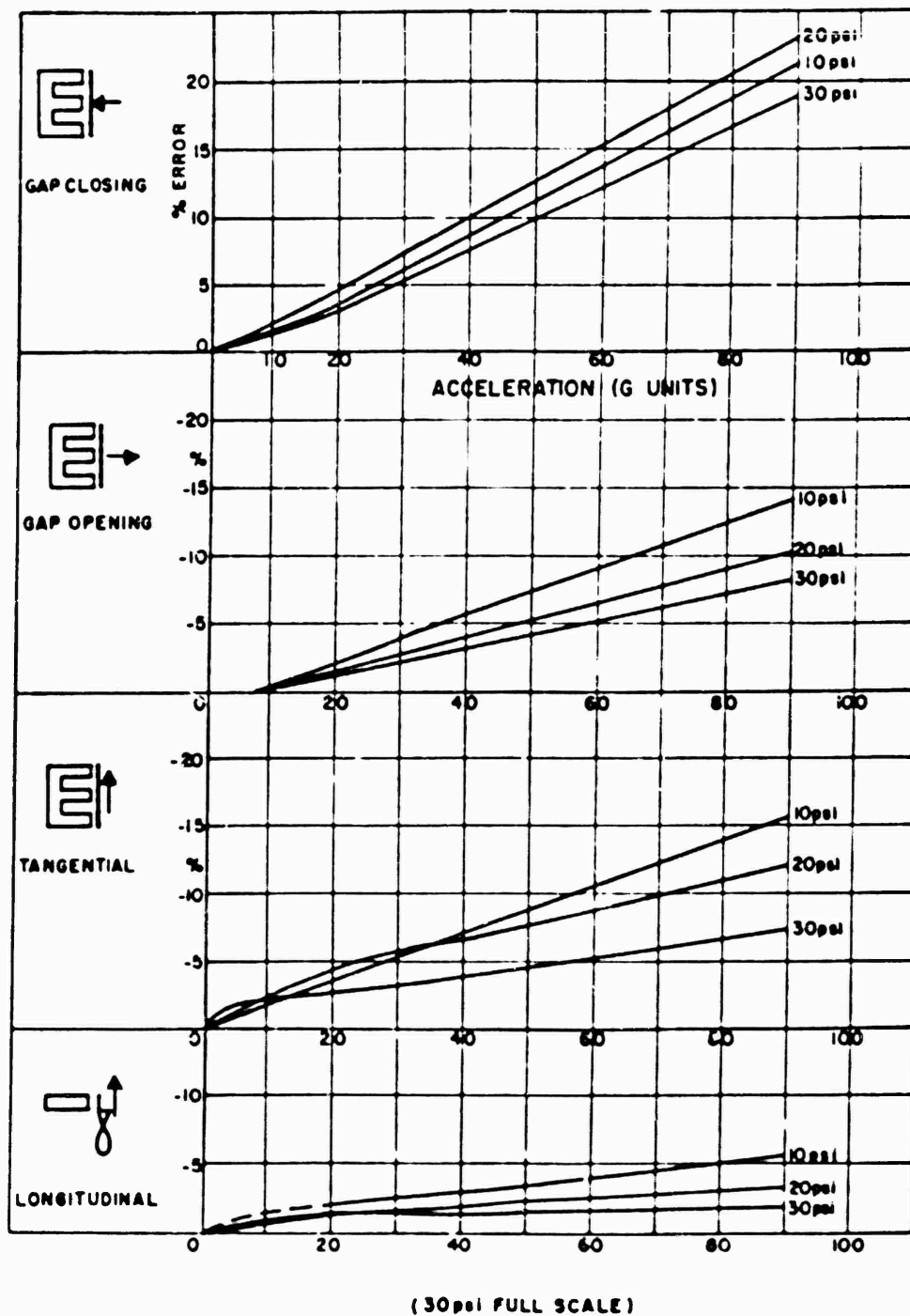


Figure A.2 Effects of acceleration; Wiancho gage.

## Appendix B

### GAGE RECORDS

Reductions of tracings of the significant portion of all usable gage records comprise this Appendix. Features such as lengths of positive phase and secondary shock do not appear in these reductions. These aspects of the pressure-time functions, where pertinent, are documented in the tables.

The records are arranged first by shot (Shot 12 precedes Shot 6), then by blast line (water, desert, asphalt), then by ground range for each vertical level (surface level first). Auxiliary records (offset gages, etc.) are introduced into the main sequence following the primary gage record.

Each record is provided with suitable time and pressure coordinates. The time indicated refers to zero time of the shot. The dotted curves document the manner in which the records were smoothed before corrections for pitch and/or Mach number were applied.

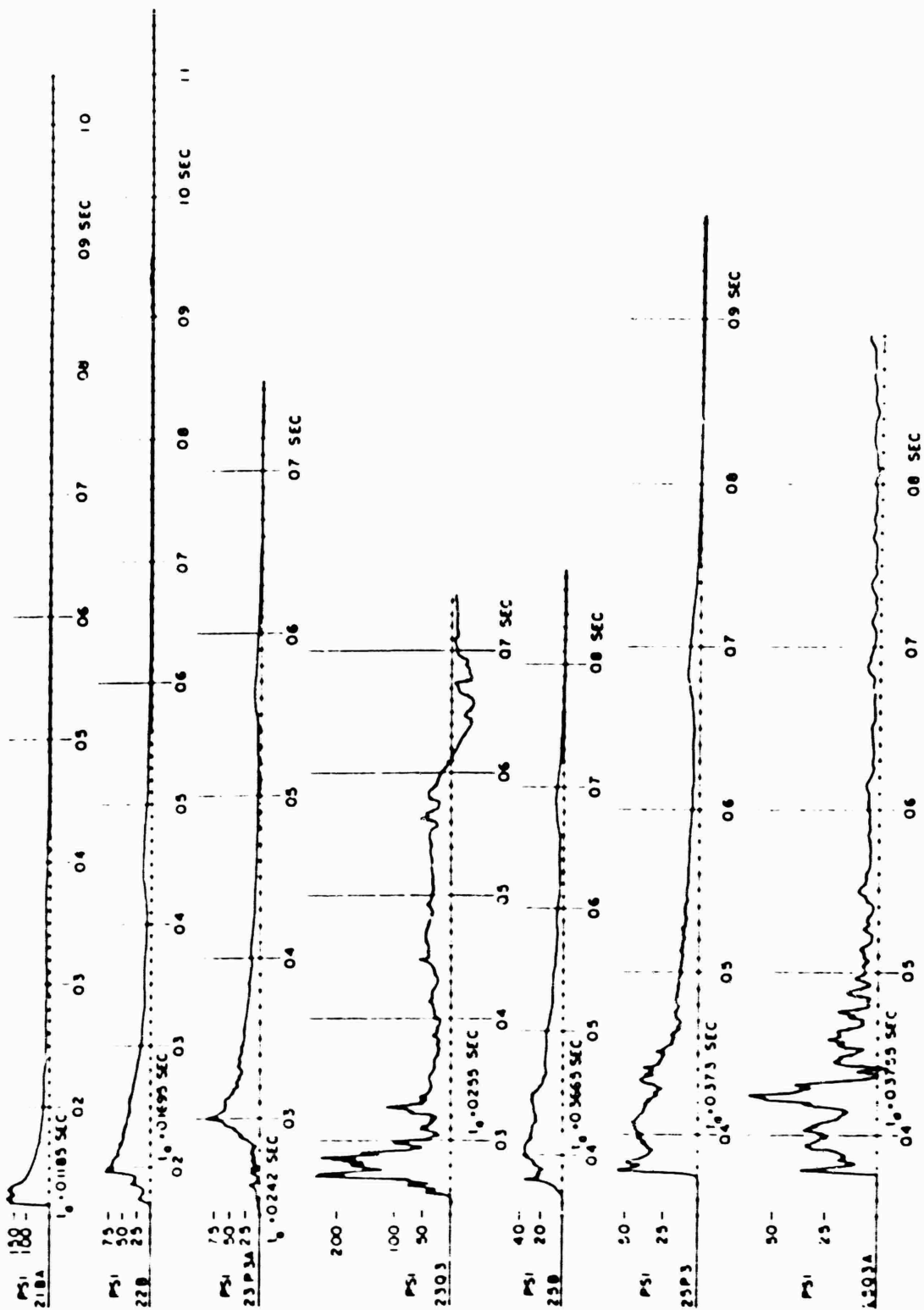


Figure B.1 Original records, Shot 12, water line, 750 feet - 1,500 feet.

CONFIDENTIAL

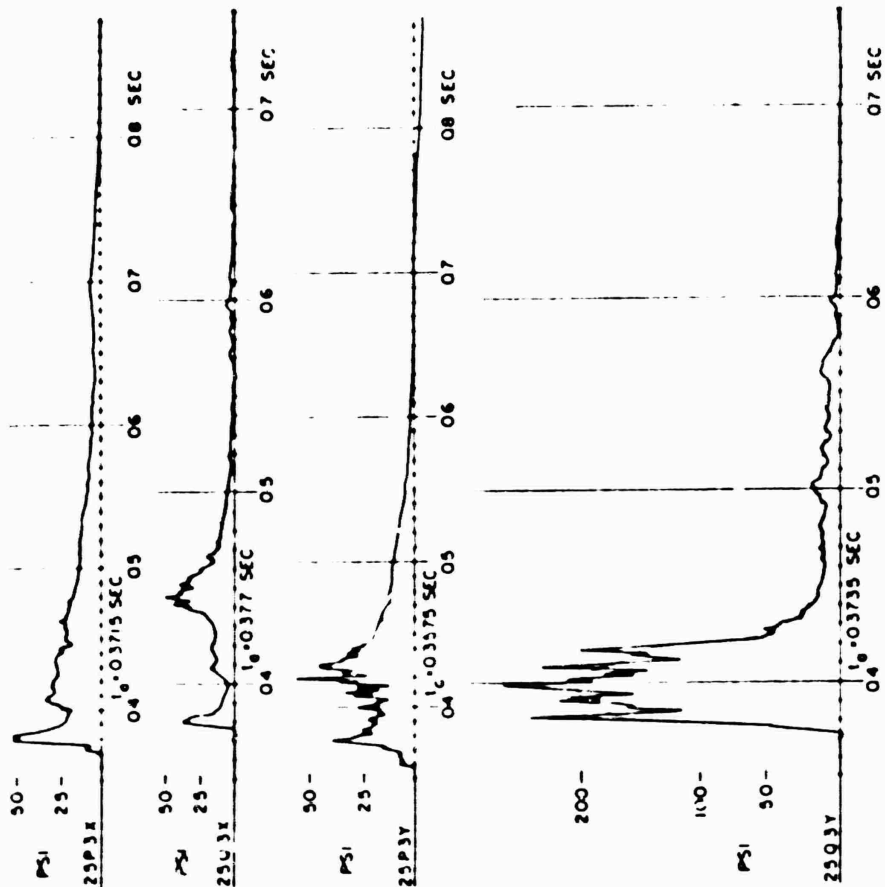


Figure B.1 Continued.



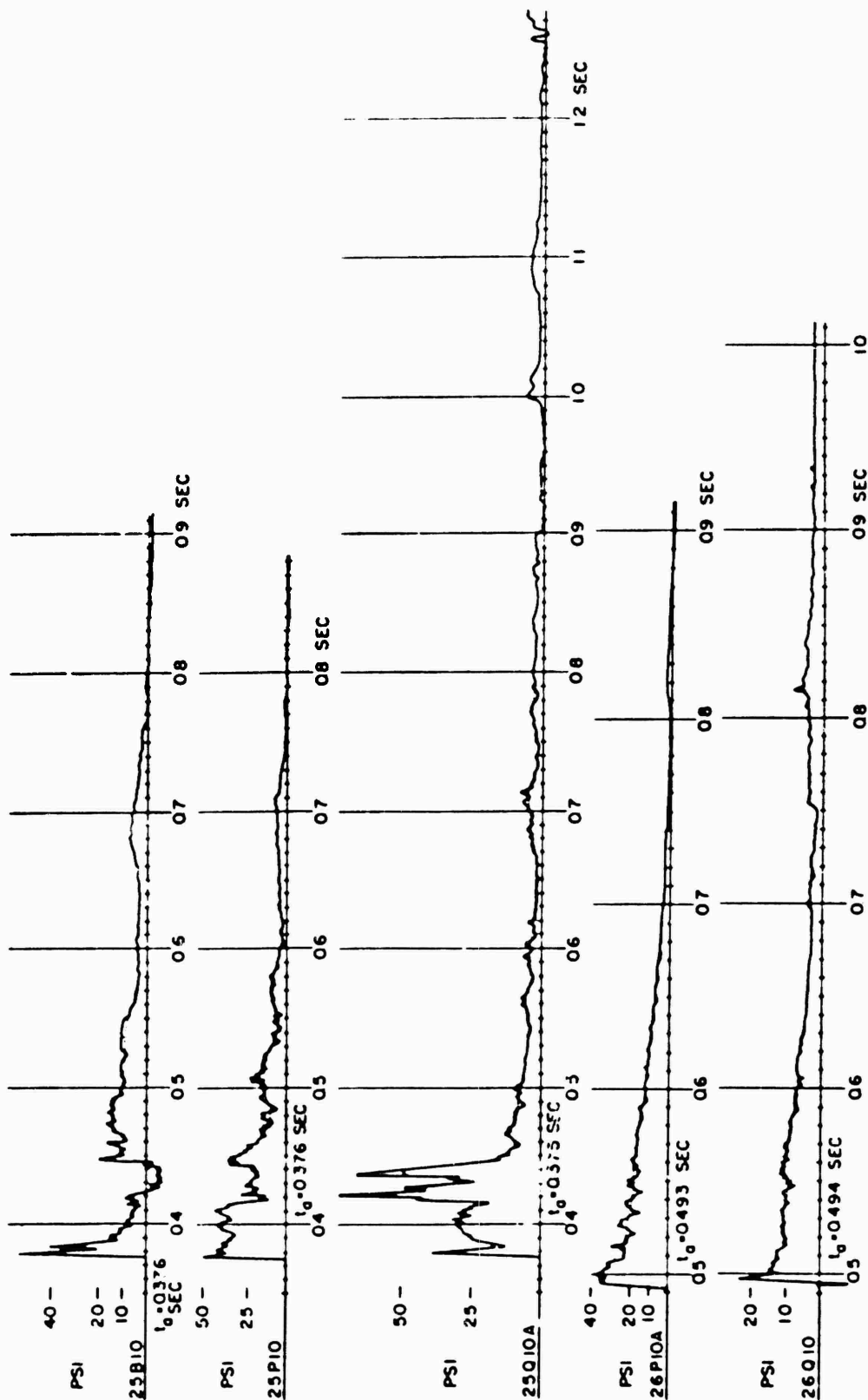


Figure B.2 Original records, Shot 12, water line, 1,500 feet—2,000 feet.

CONFIDENTIAL

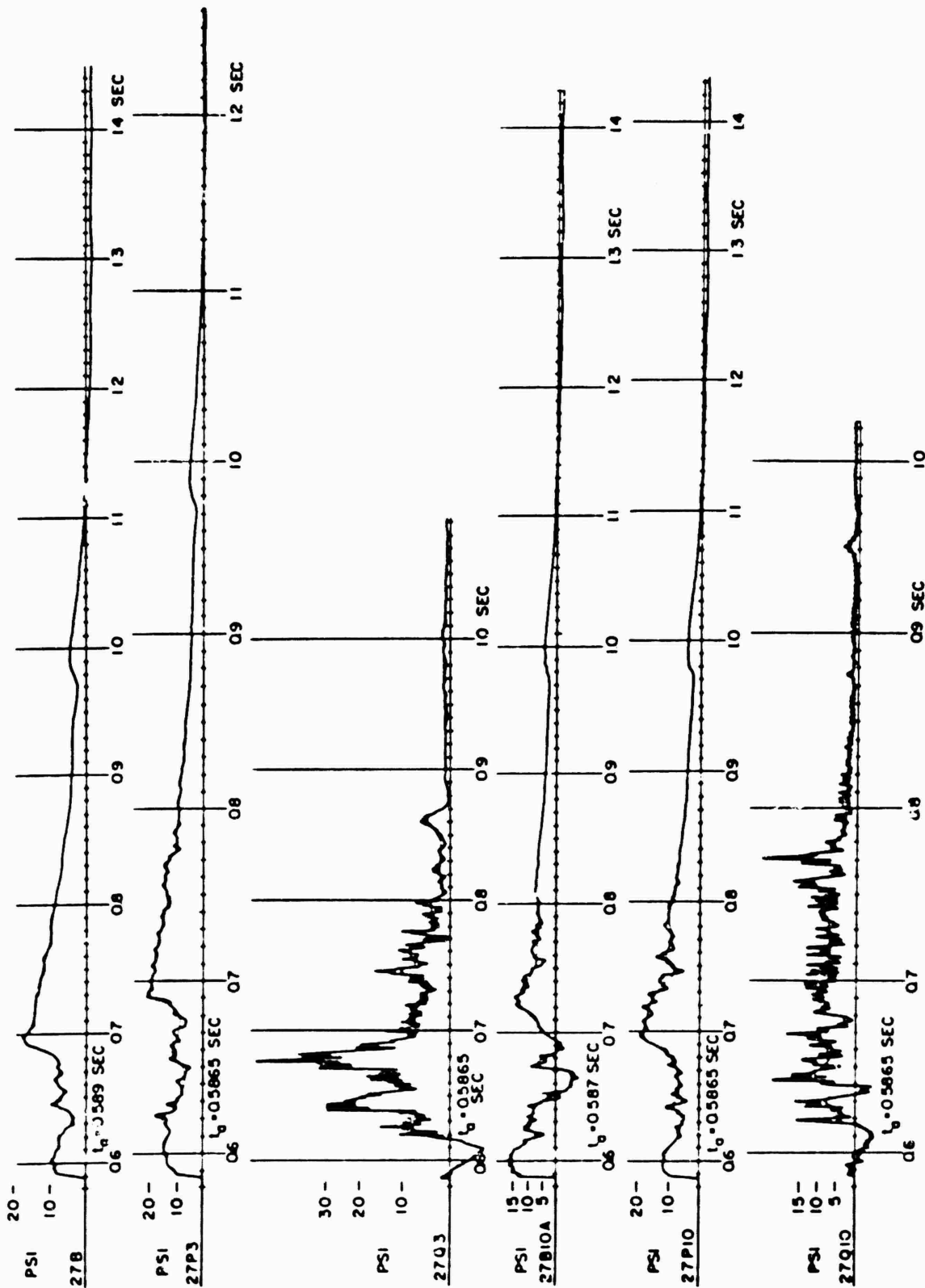


Figure B.2 Continued.

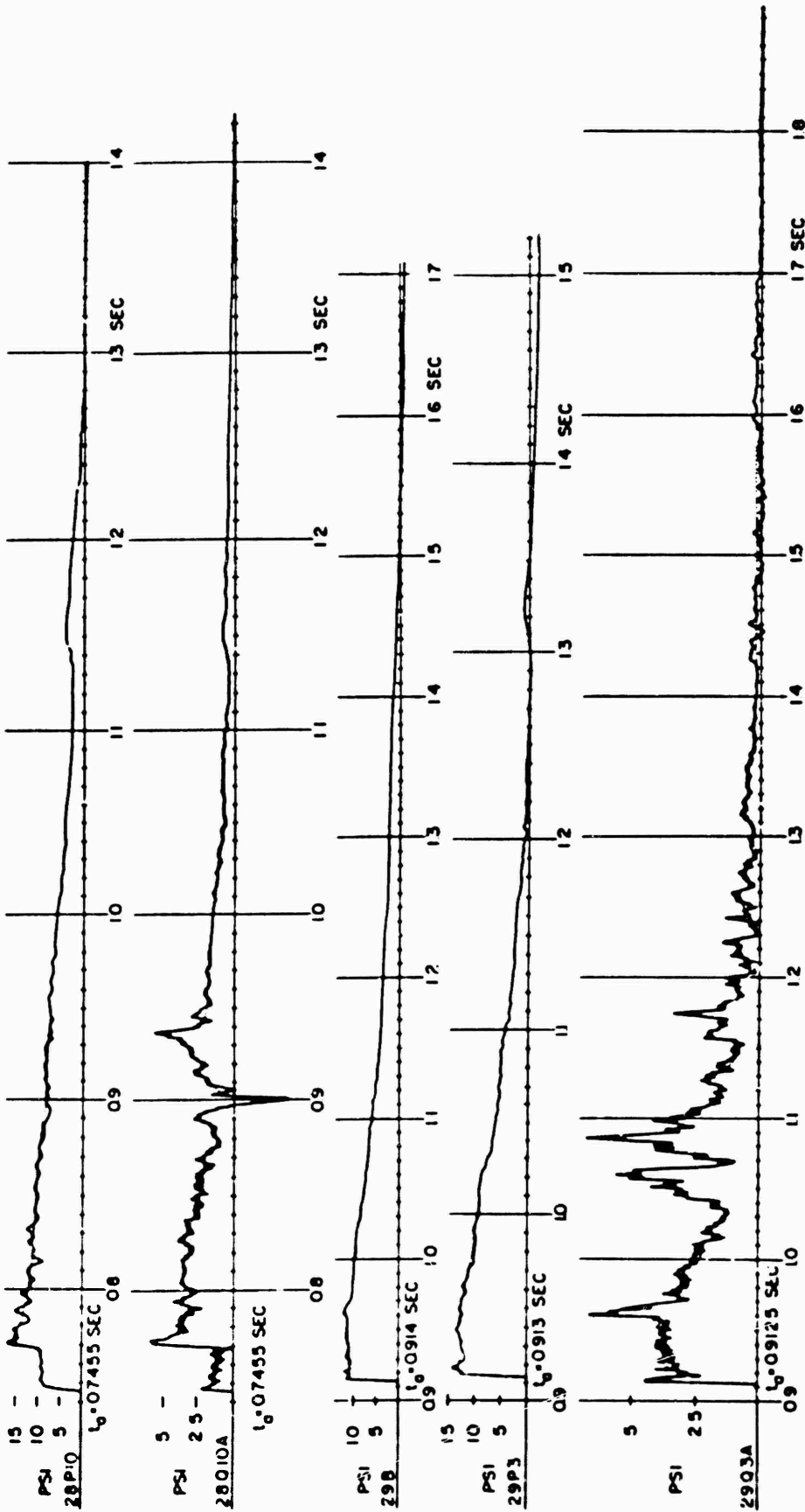


Figure B.3 Original records, Shot 12, water line, 2,000 feet - 2,500 feet.

CONFIDENTIAL

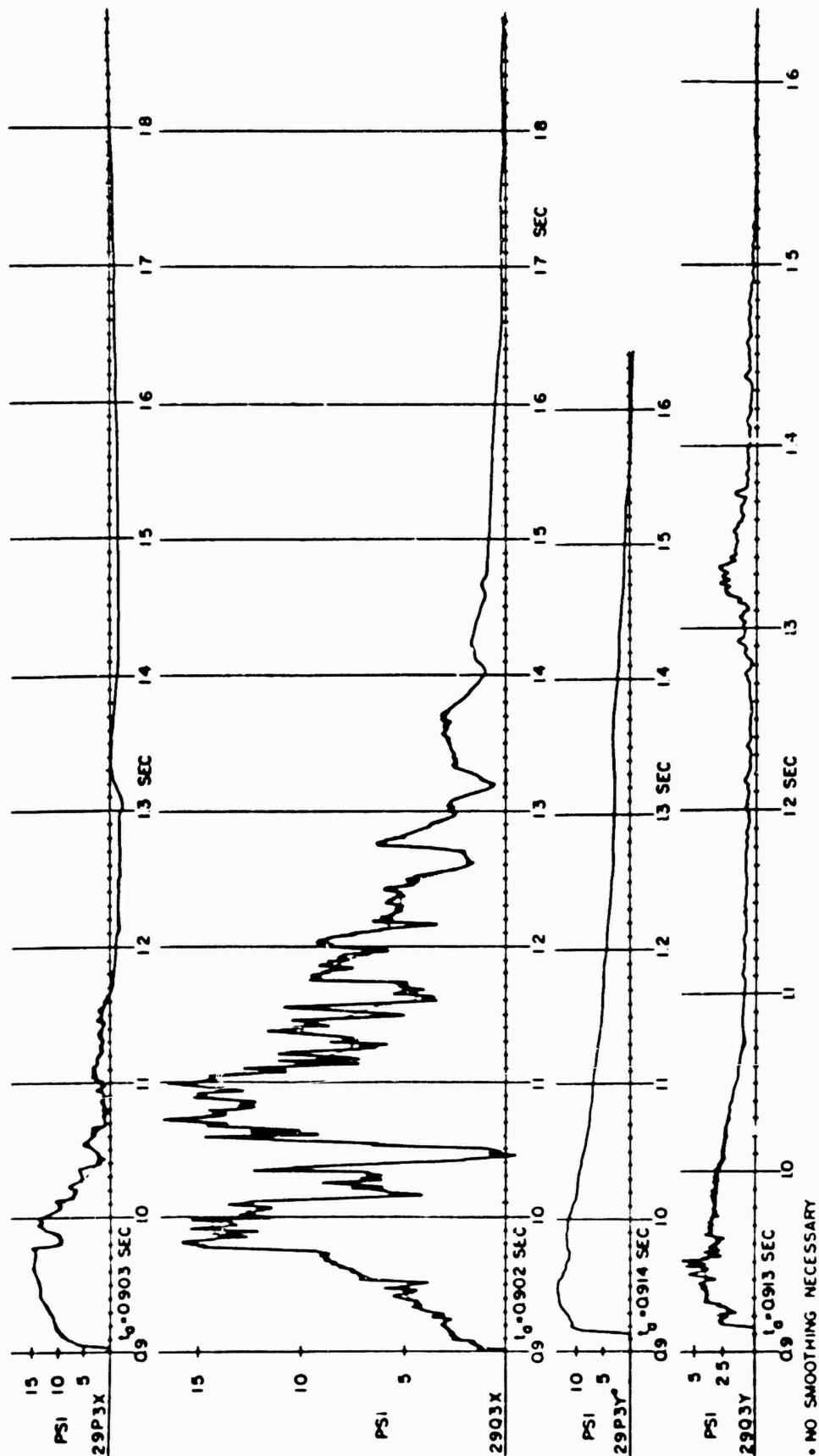


Figure B.3 Continued.

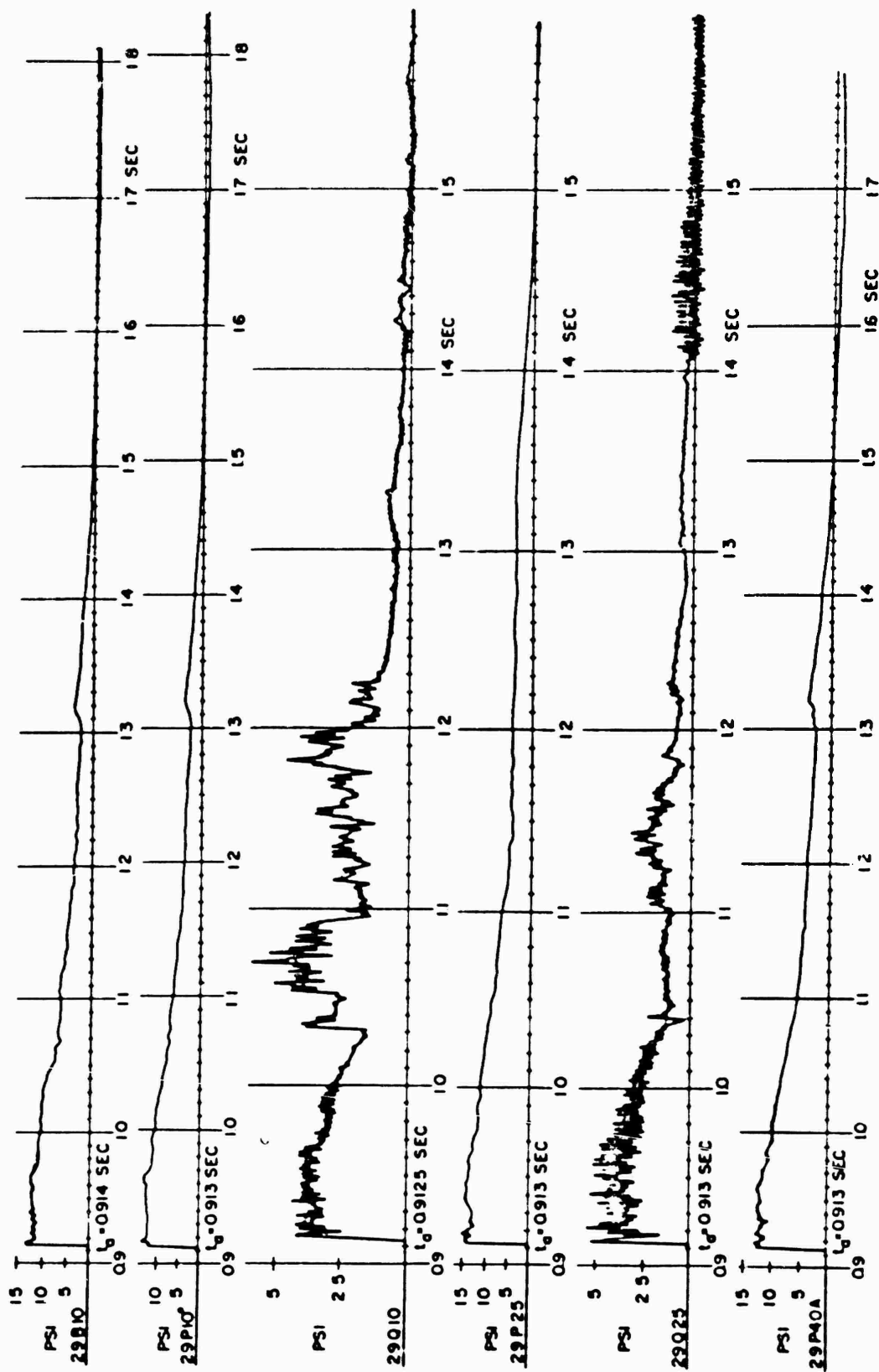


Figure B.4 Original records, Shot 12, water line, 2,500 feet - 3,000 feet.

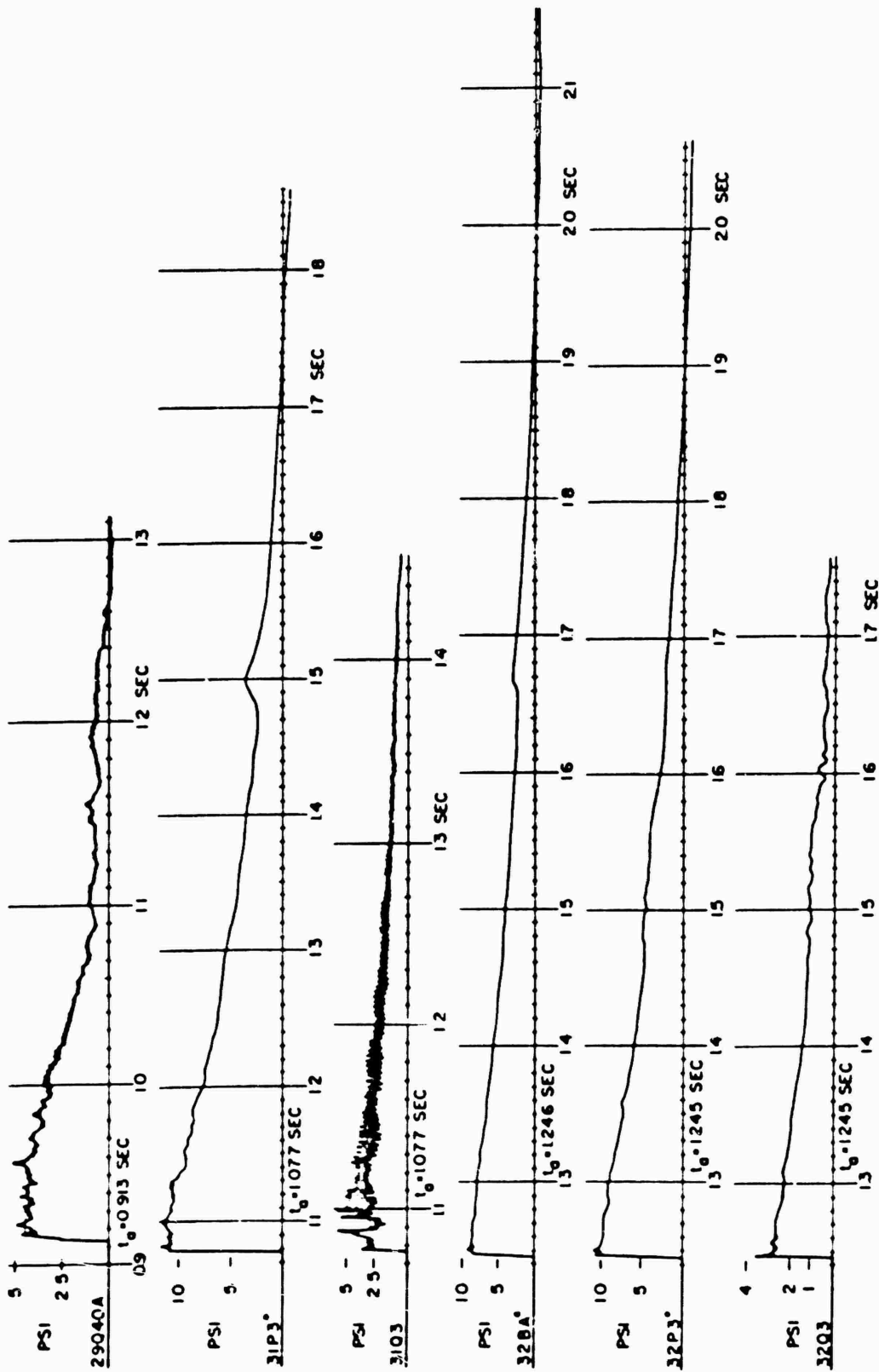


Figure B.4 Continued.

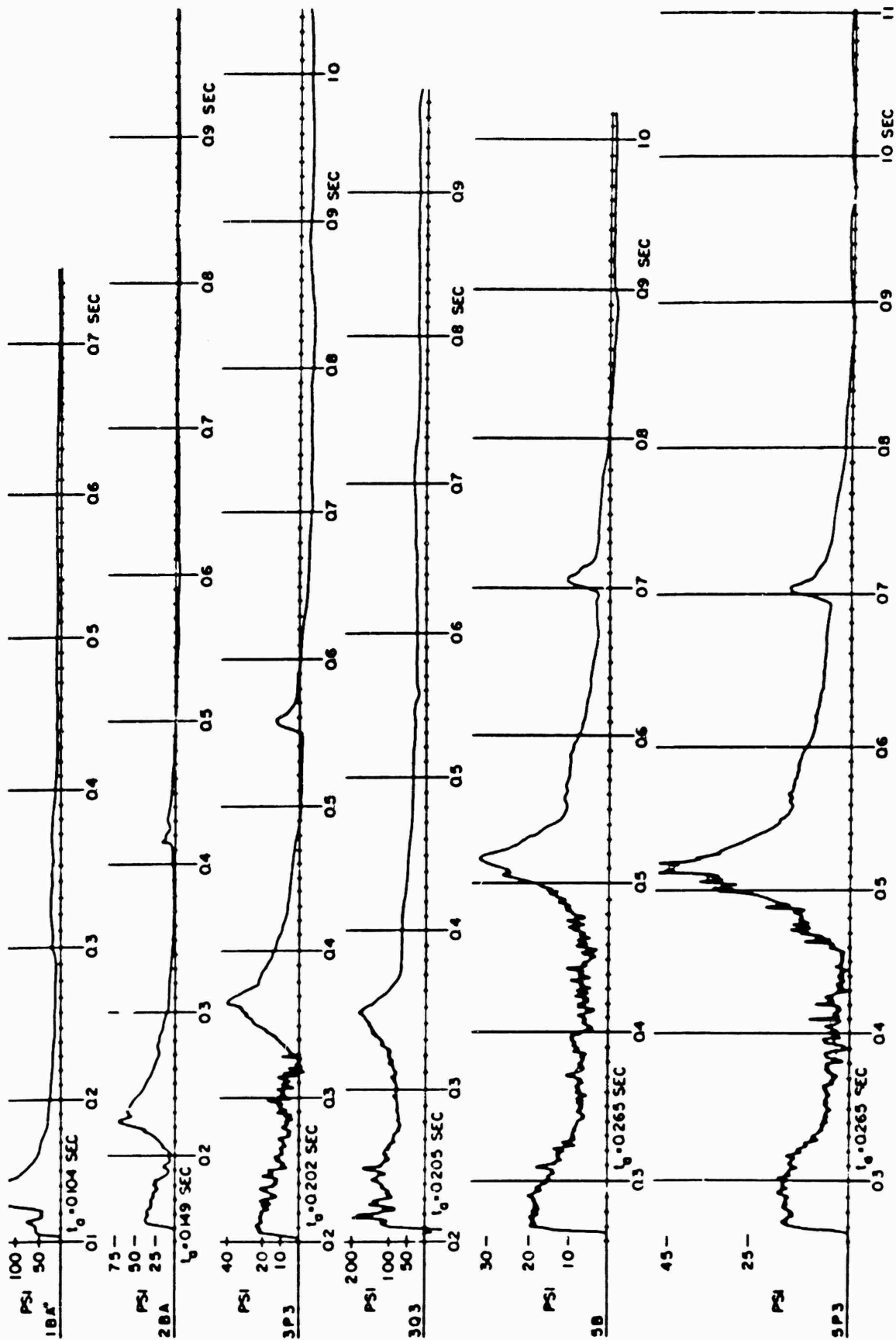
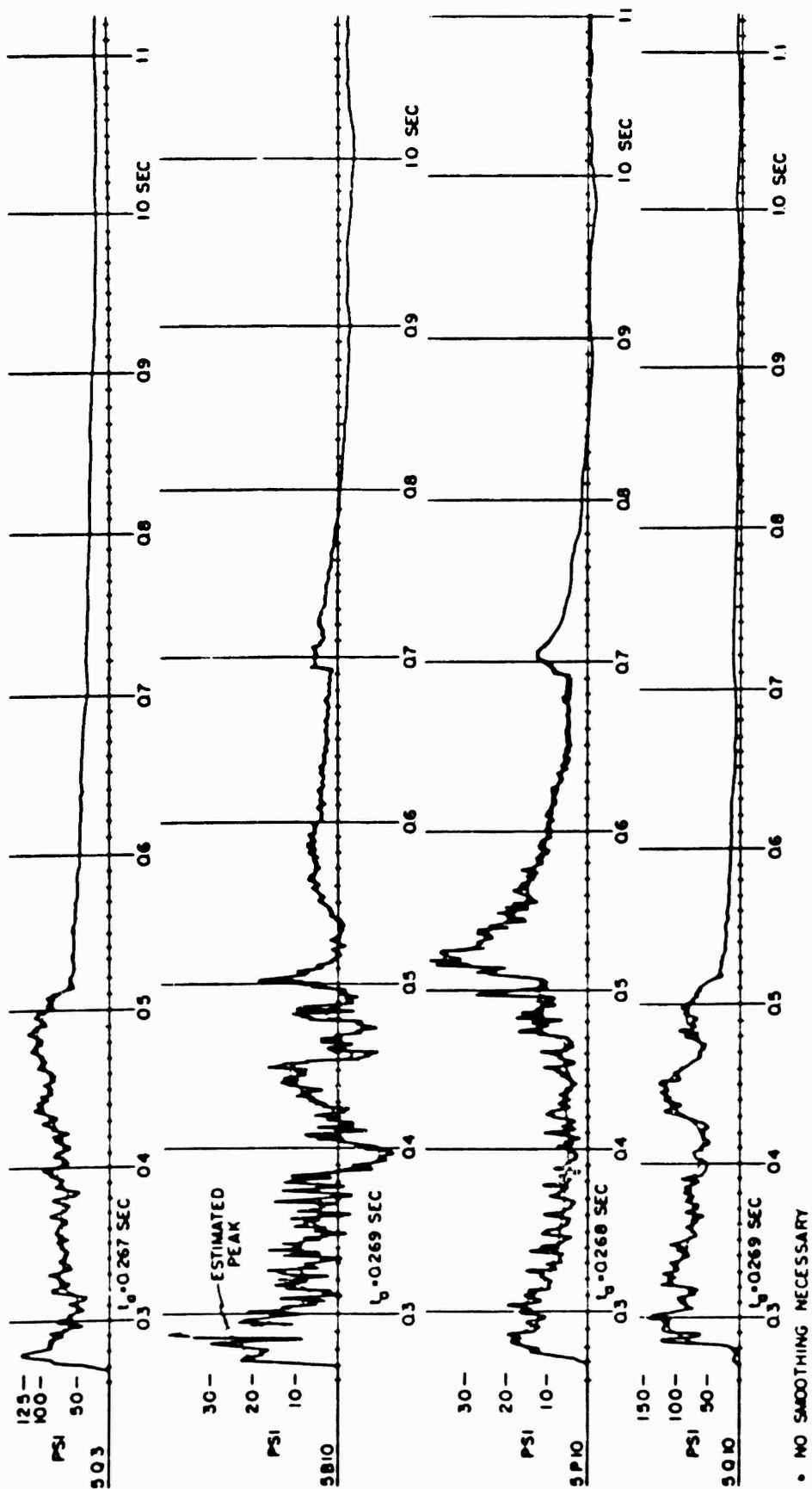


Figure B.3: Original records: Shot 12, desert line, 750 feet - 1,500 feet.

CONFIDENTIAL



• NO SMOOTHING NECESSARY

Figure B.5 Continued.



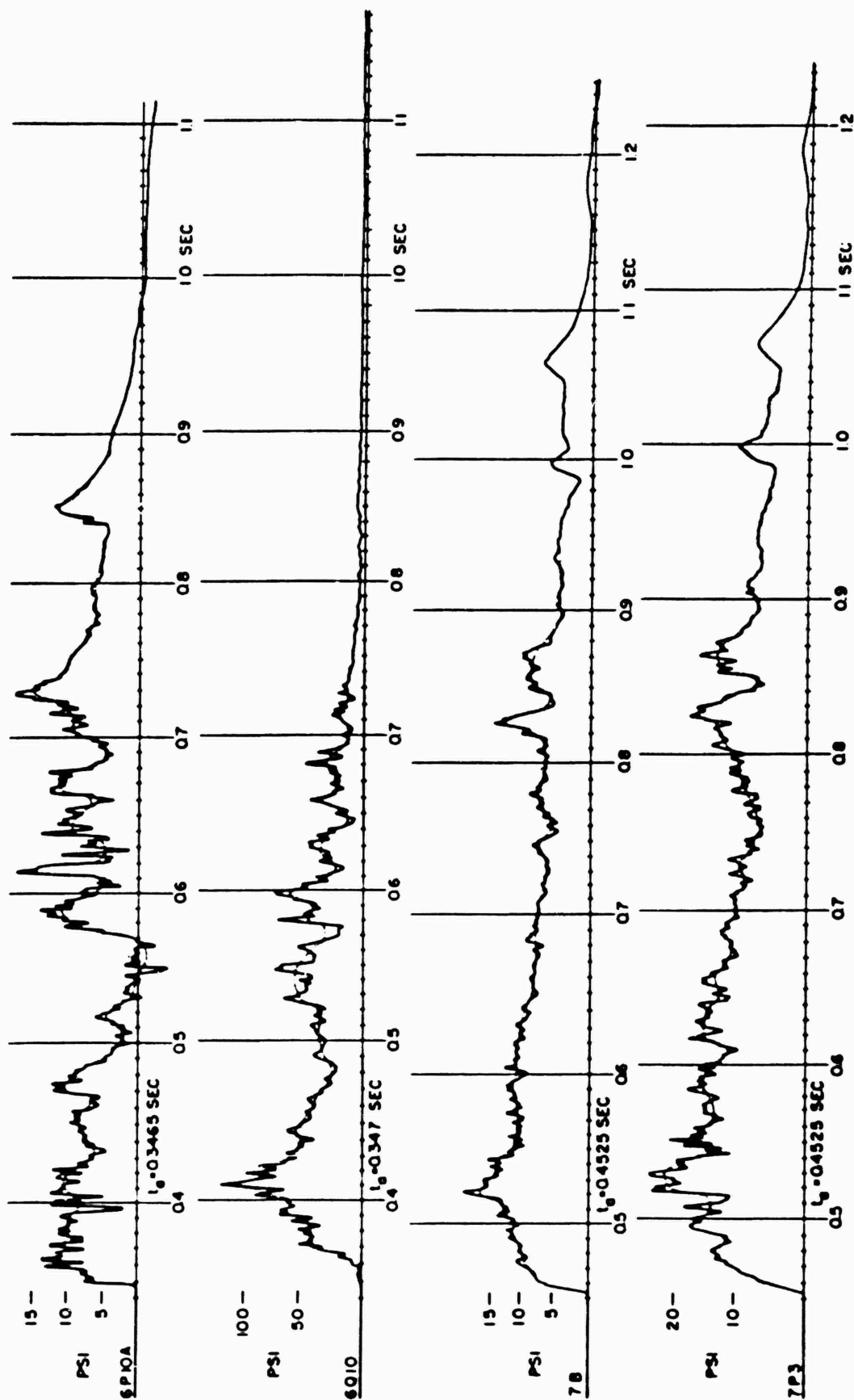


Figure B.6 Original records, desert line, 1,750 feet - 2,000 feet.

DECLASSIFIED

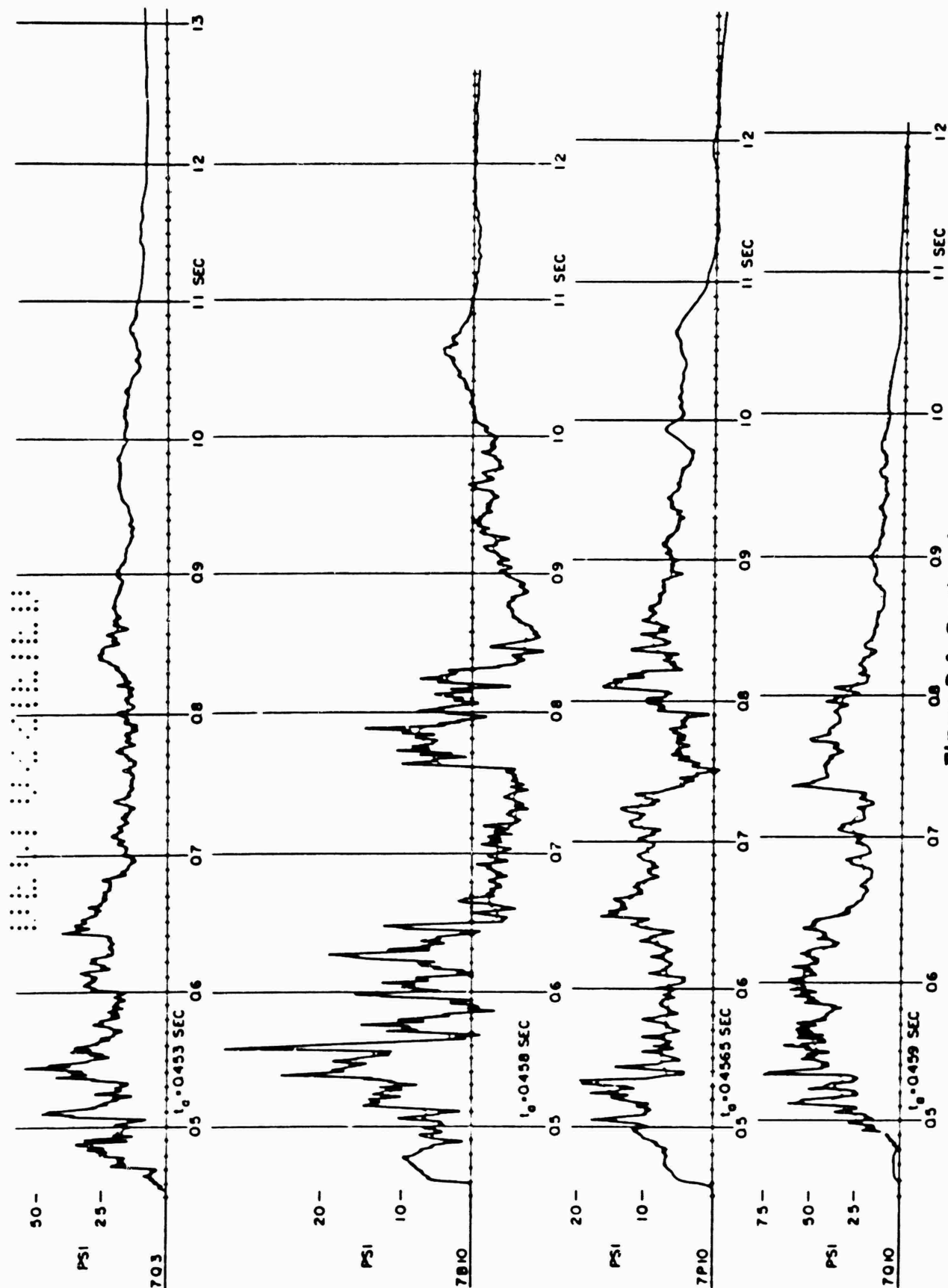


Figure B.6 Continued.

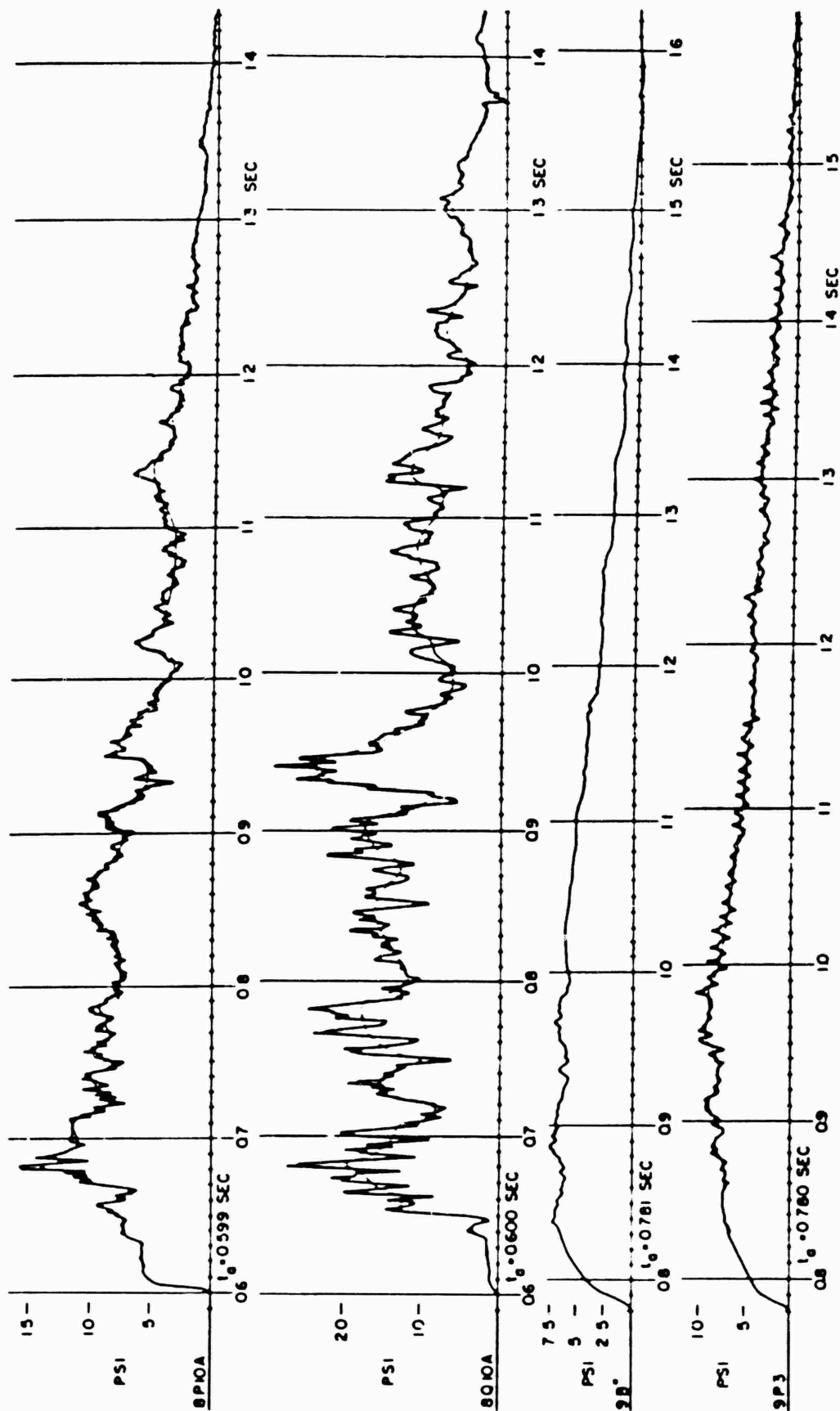


Figure B.7 Original records, Shot 12, desert line, 2,250 feet - 2,750 feet.

0001030700

CONFIDENTIAL

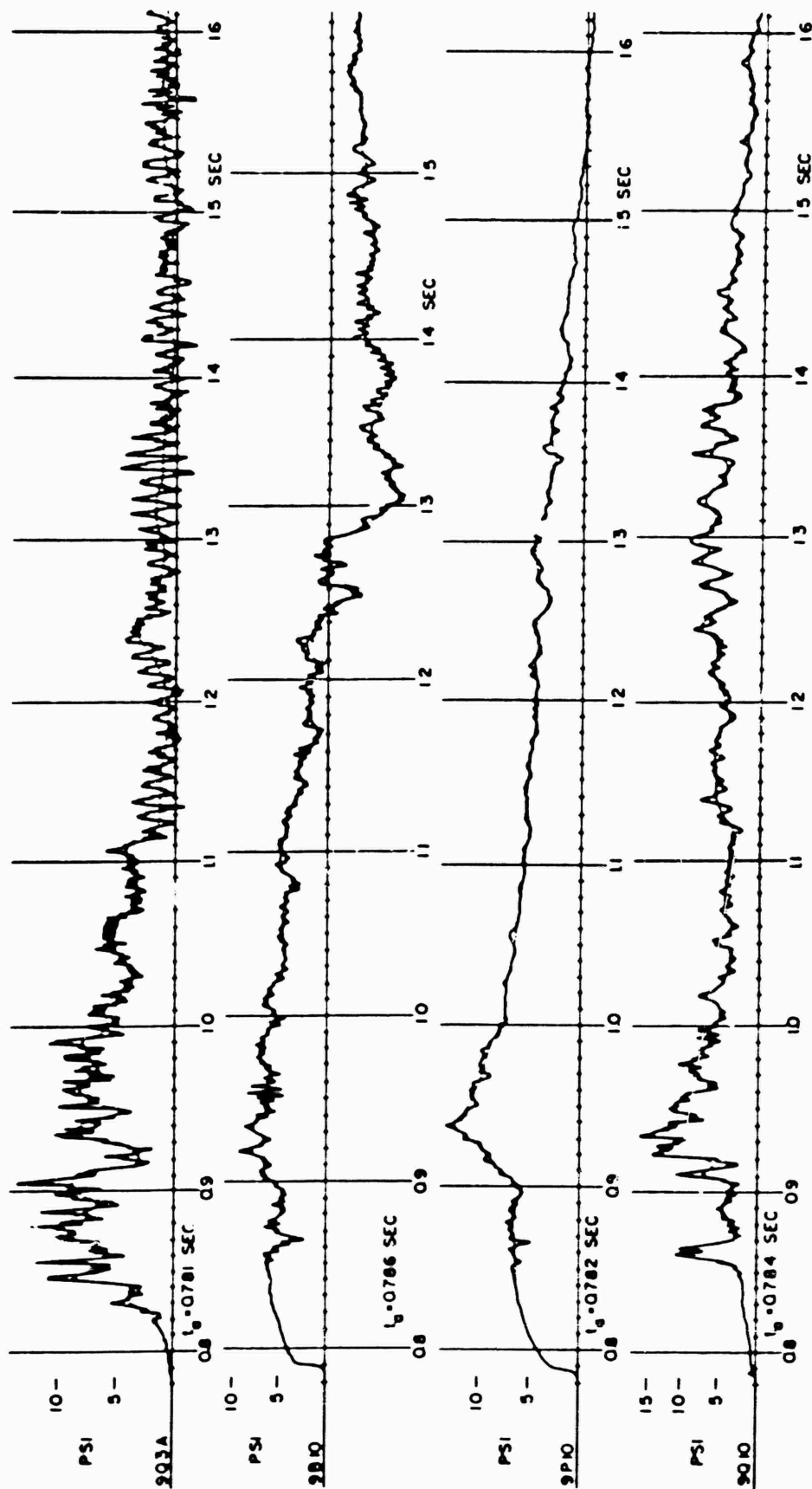


Figure B.7 Continued.

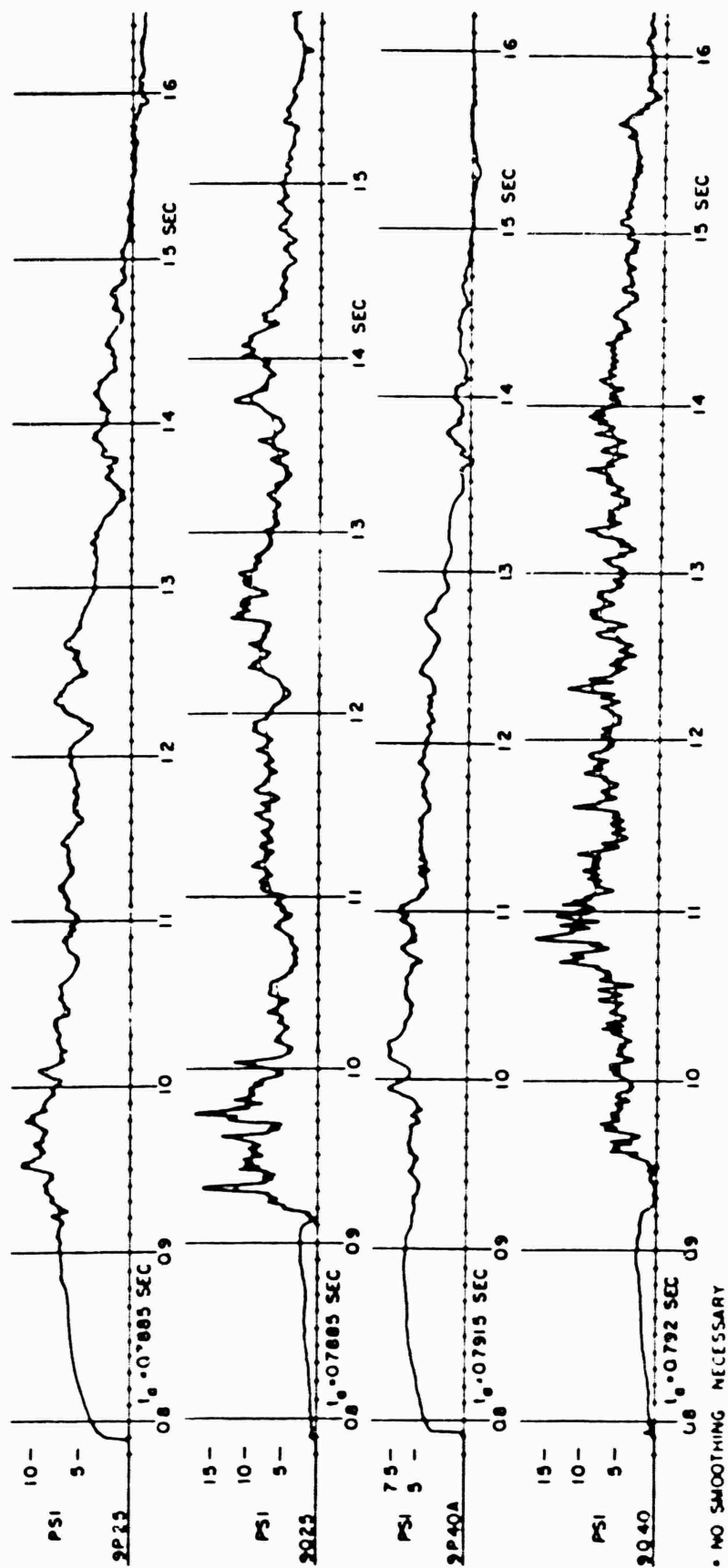


Figure B.7 Continued.

CONFIDENTIAL

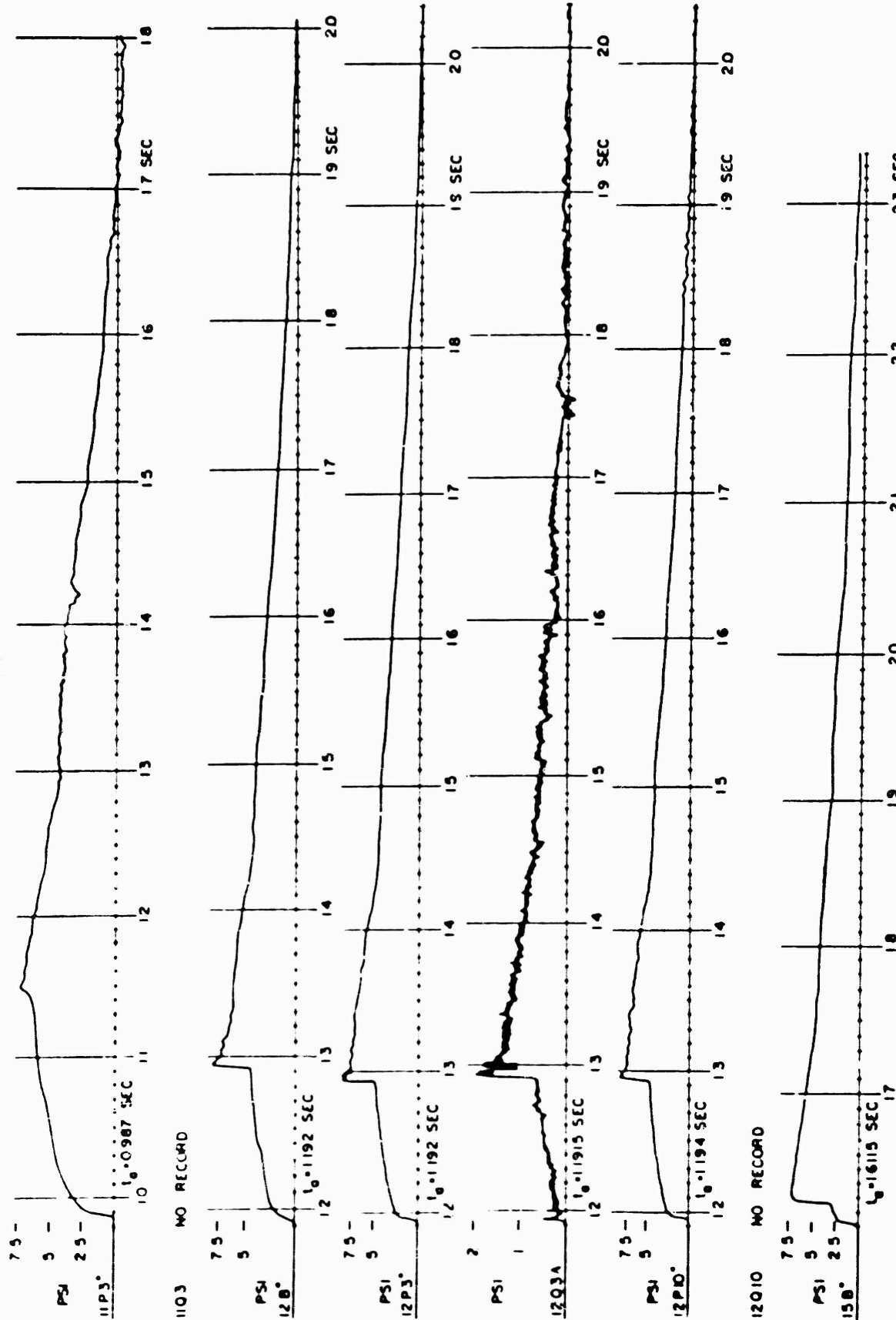
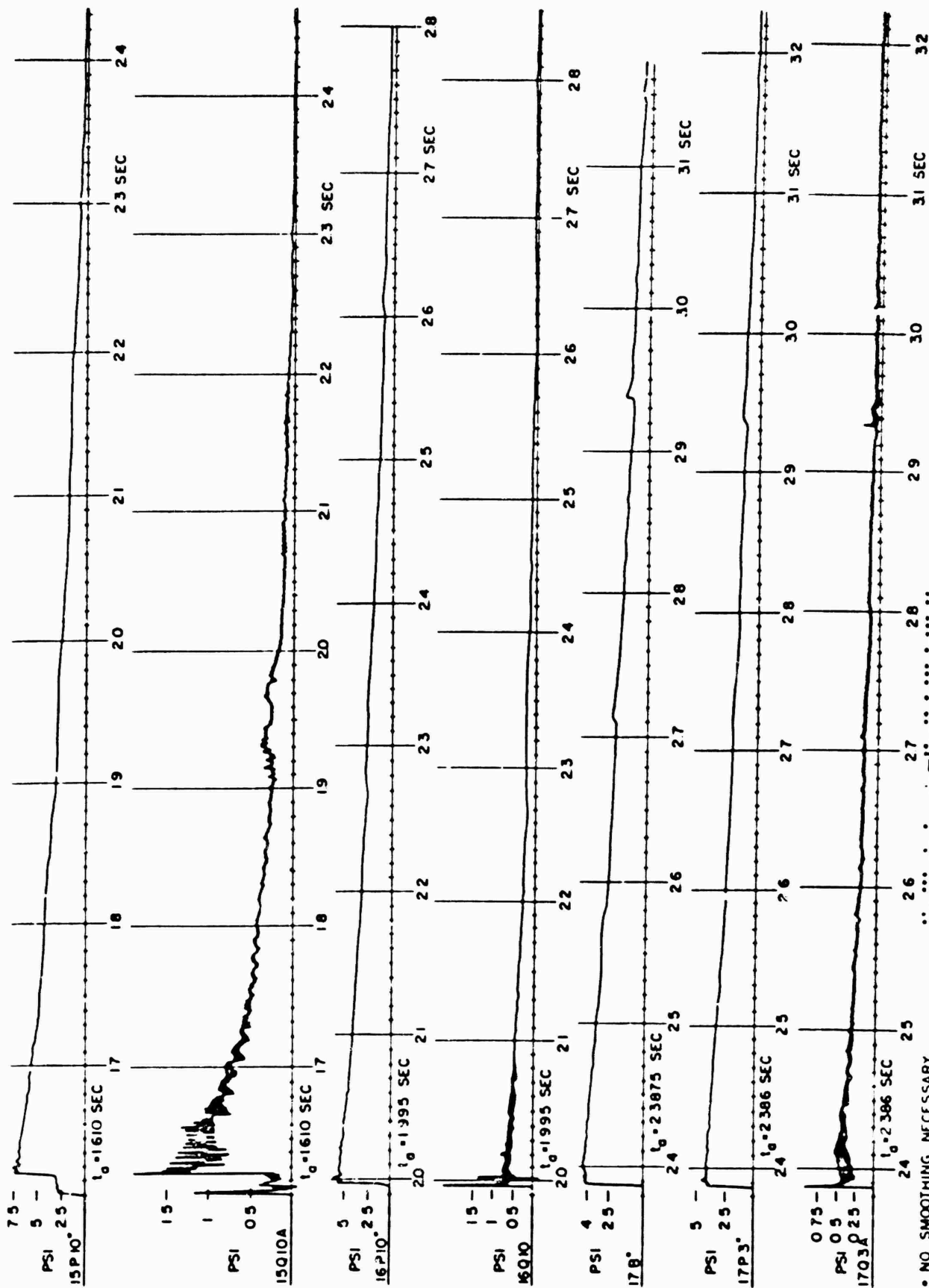


Figure B.8 Original records, Shot 12, desert line, 2,750 feet - 4,500 feet.



• NO SMOOTHING NECESSARY

Figure B.8 Continued

CONFIDENTIAL

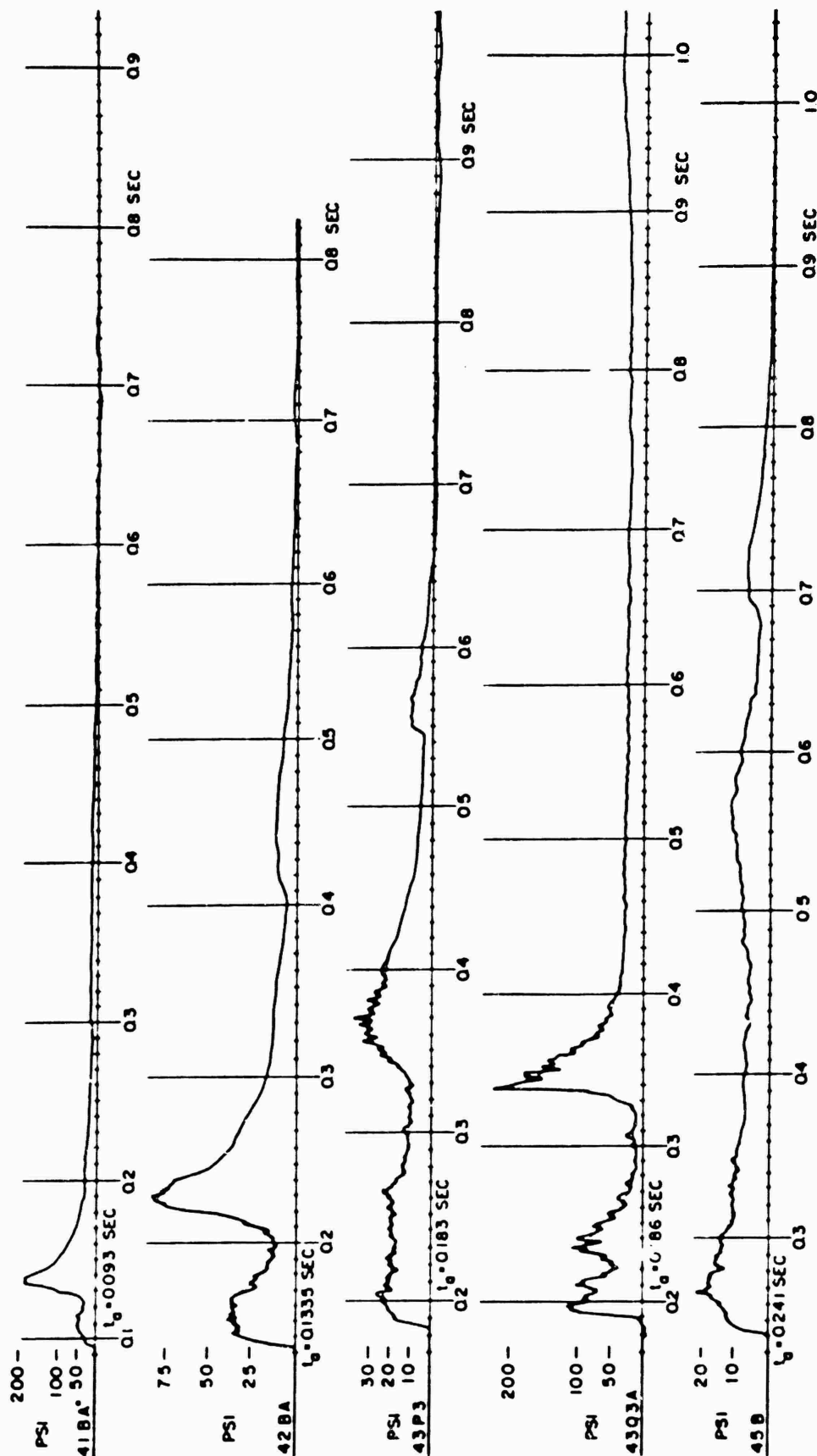


Figure B.9 Original records, Shot 12, asphalt llue, 750 feet-1,500 feet.



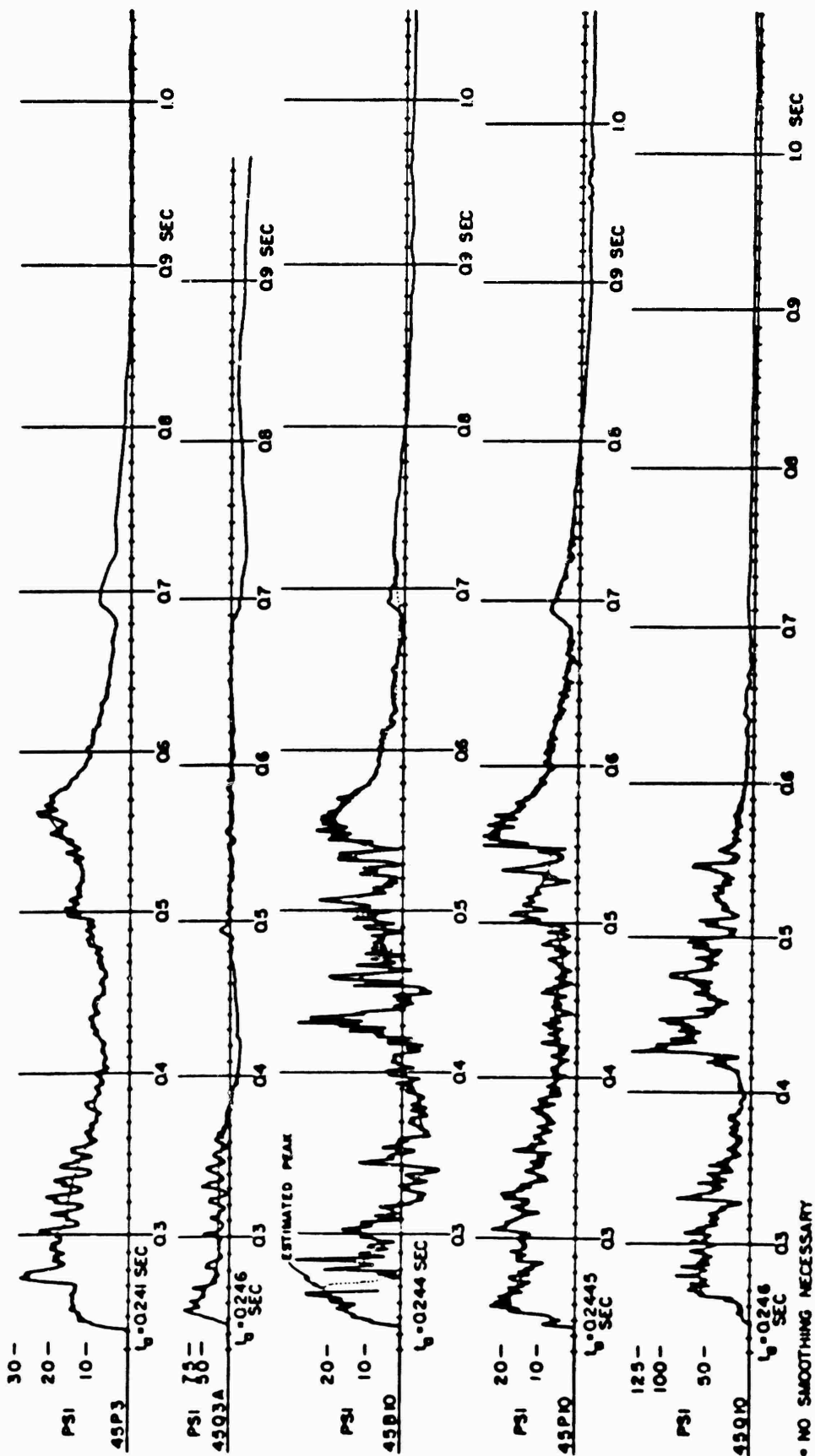


Figure B.9 Continued.

CONFIDENTIAL

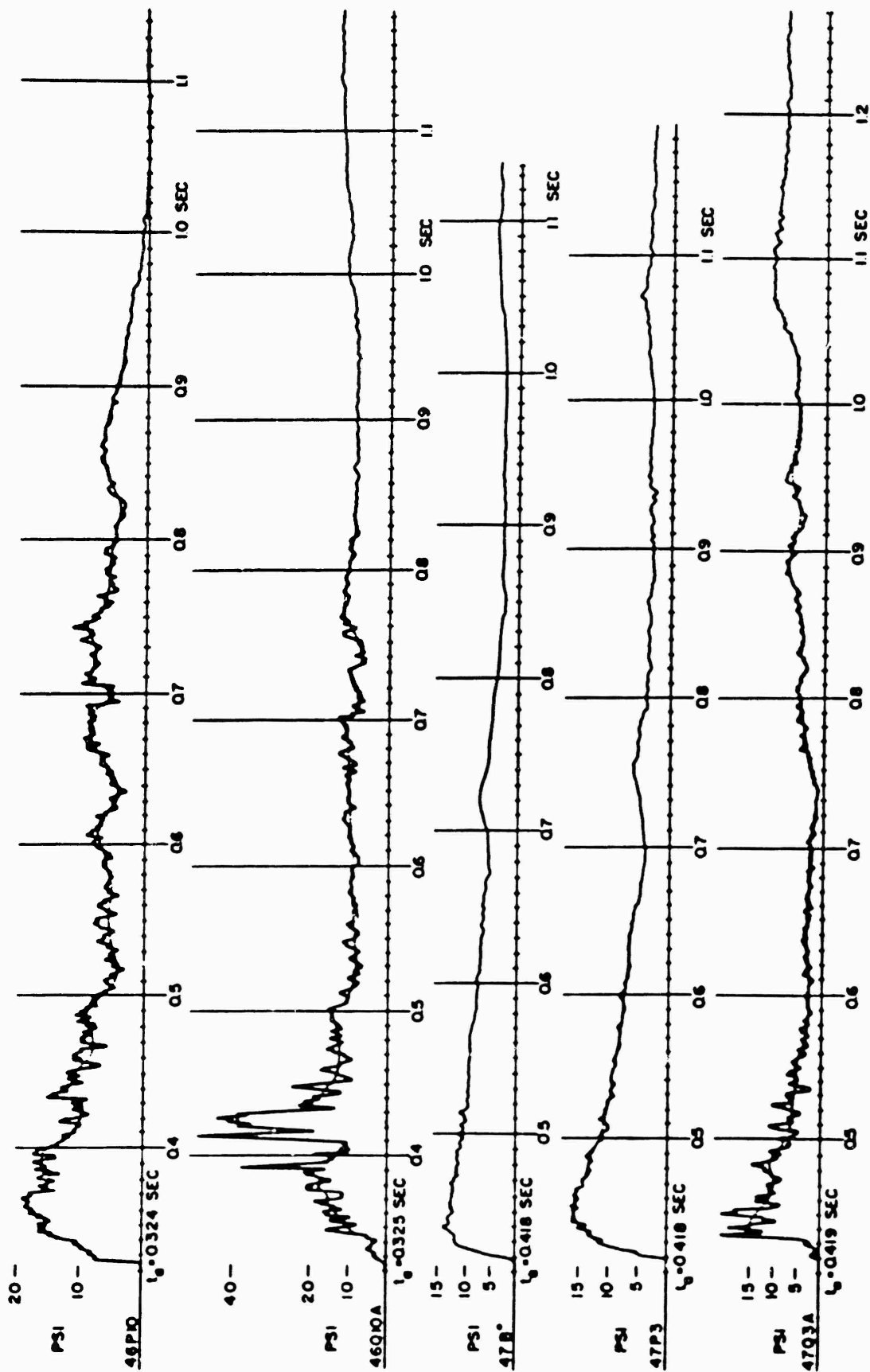


Figure B.10 Original records. Shot 12, asphalt line, 1,750 feet-2,250 feet.

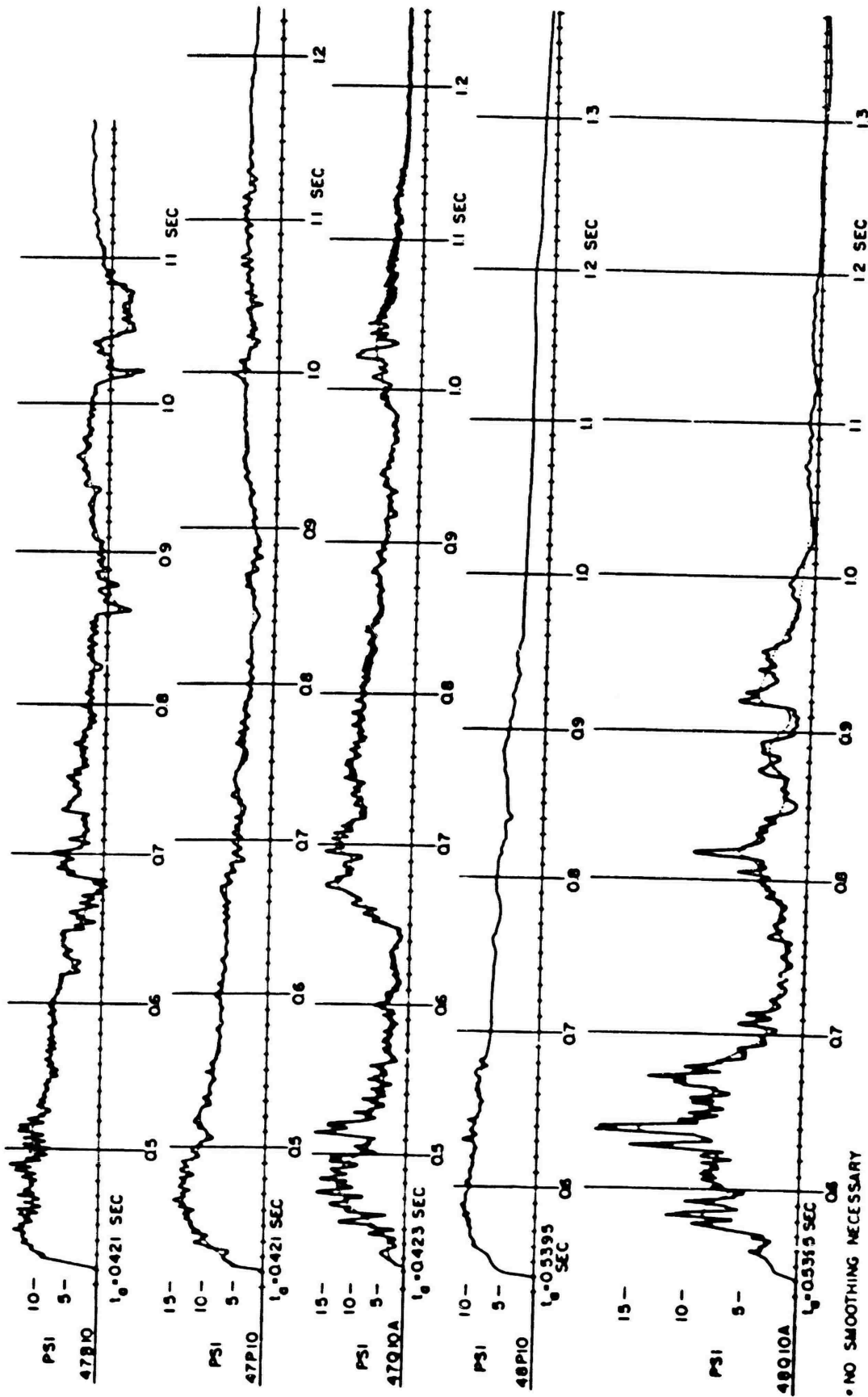


Figure B.10 Continued.

CONFIDENTIAL

CONFIDENTIAL

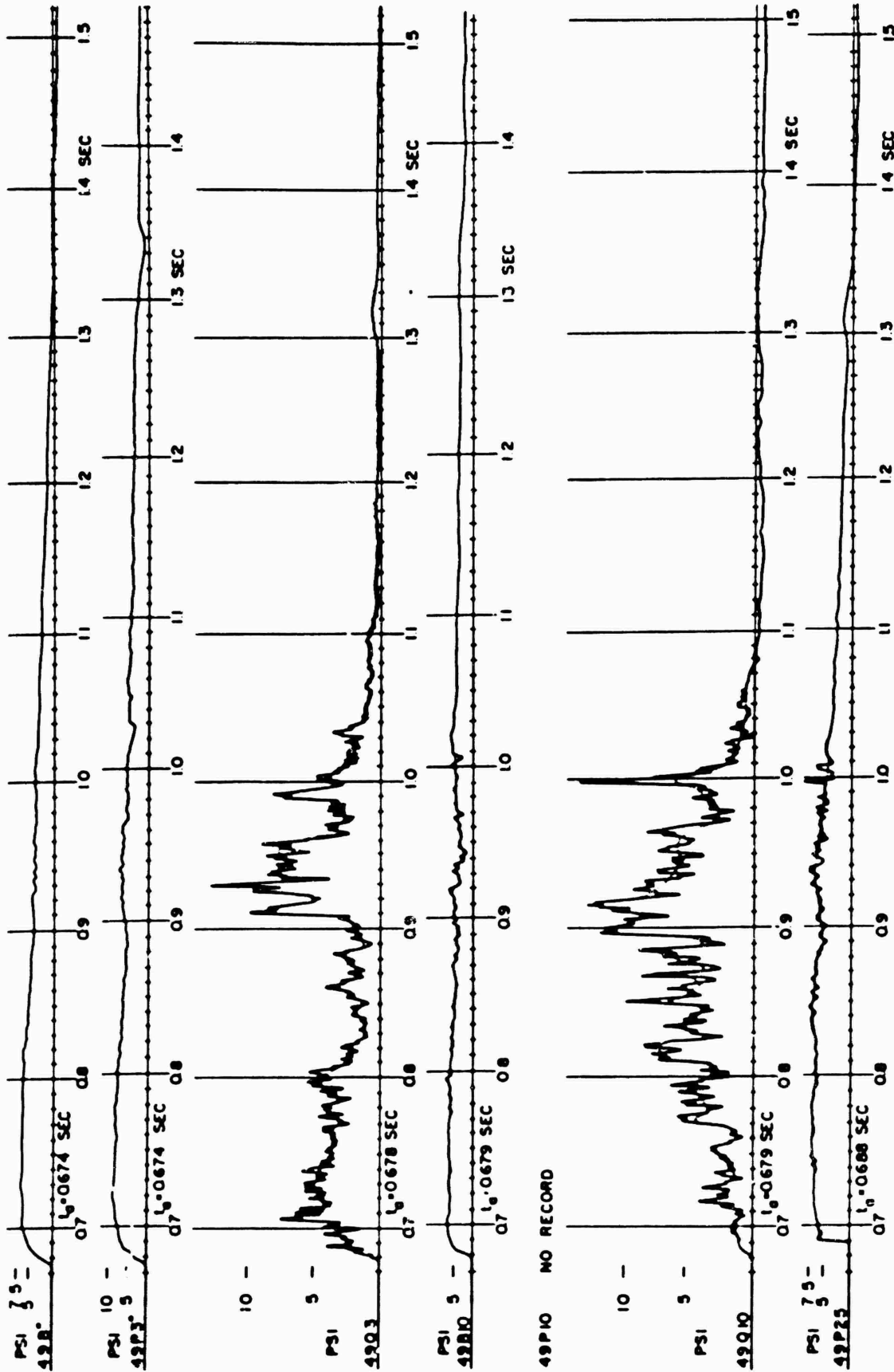
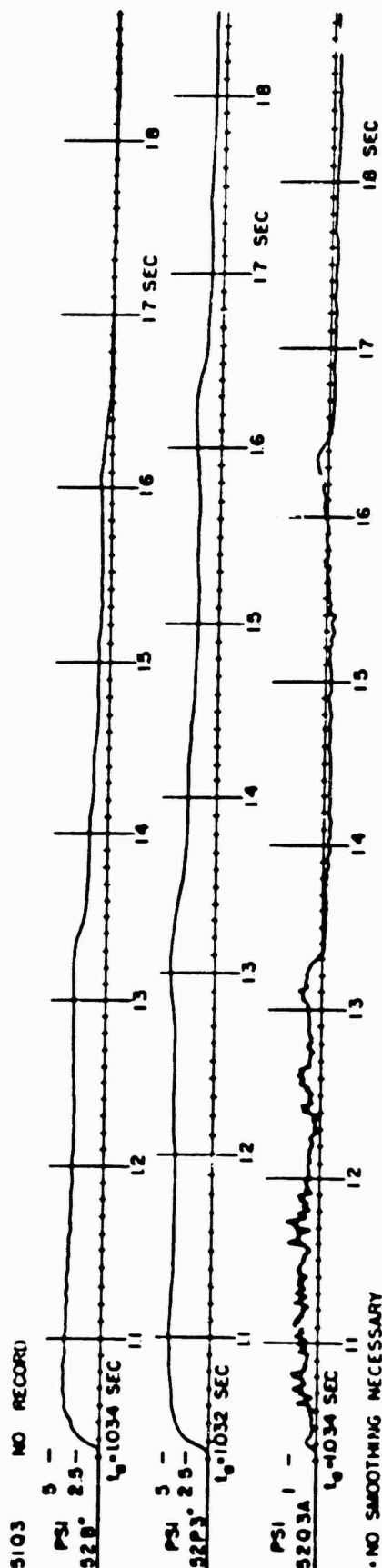
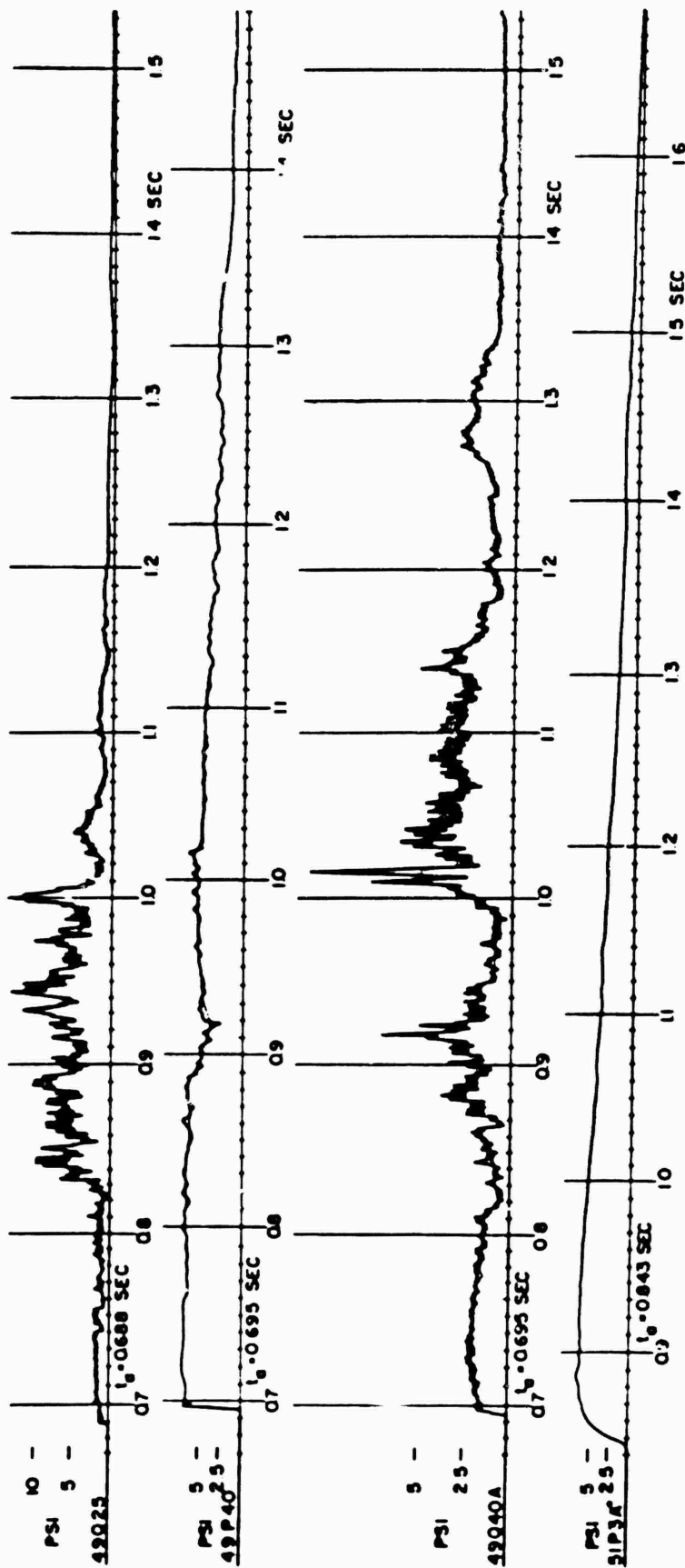


Figure B.11 Original records, Shot 12, asphalt line, 2,500 feet--3,000 feet.



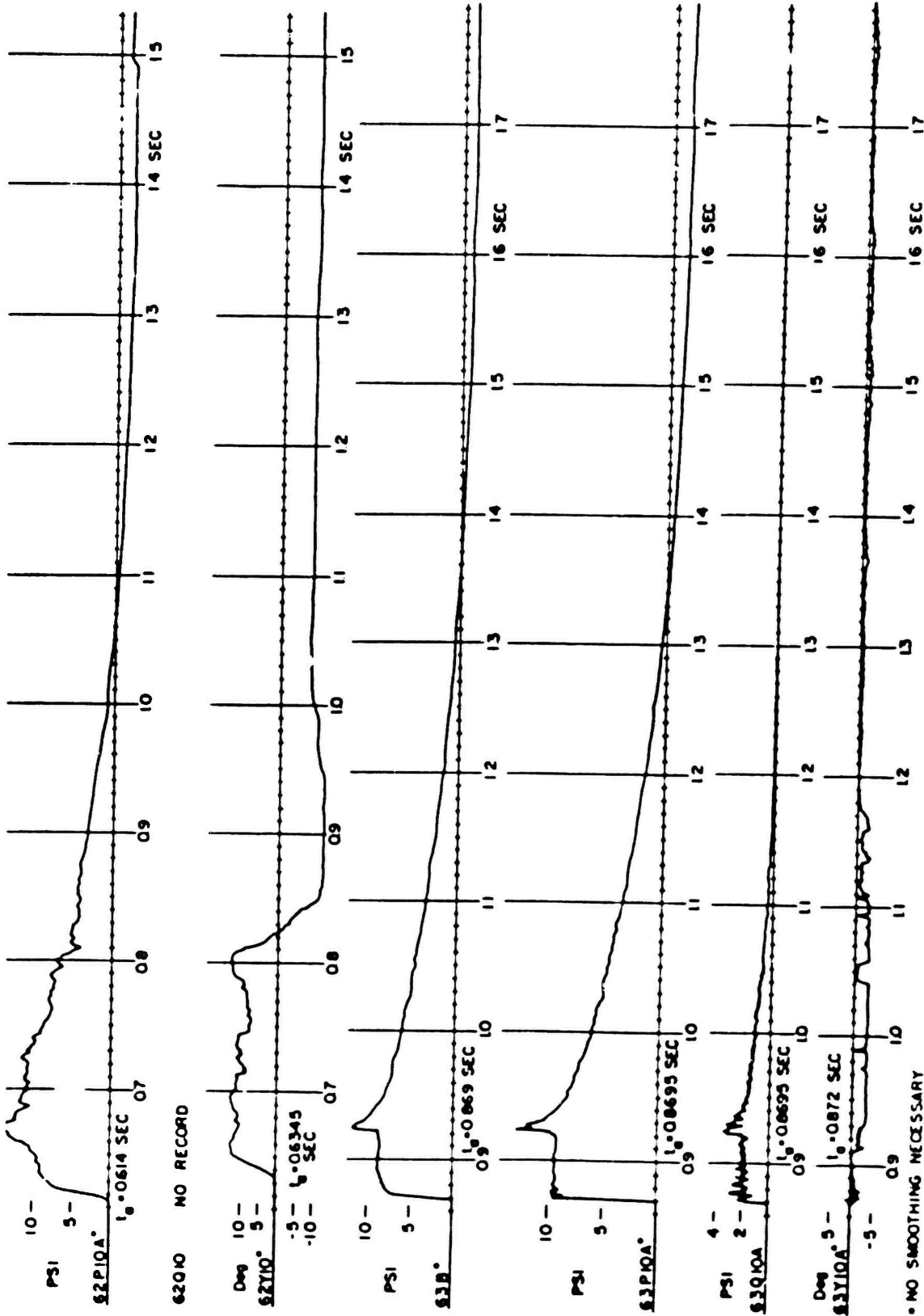
• NO SMOOTHING NECESSARY

Figure B.1. Continued.

CONFIDENTIAL

**Figure B.12 Original records, Sbot 6, desert line.**

**CONFIDENTIAL**



**Figure B.12.. Continued.**

0-218 478313

CONFIDENTIAL

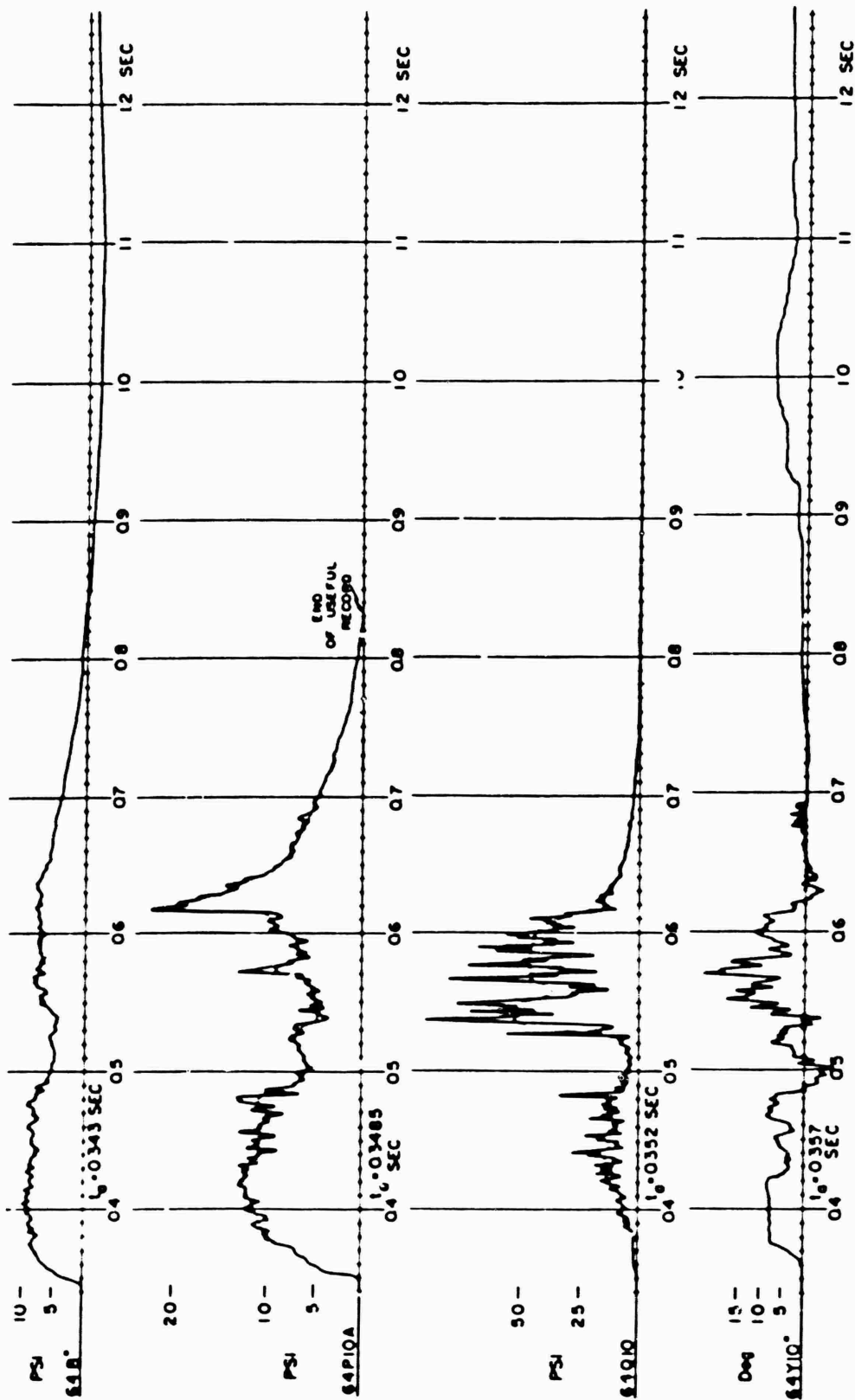


Figure B.13 Original records, Shot 6, asphalt line



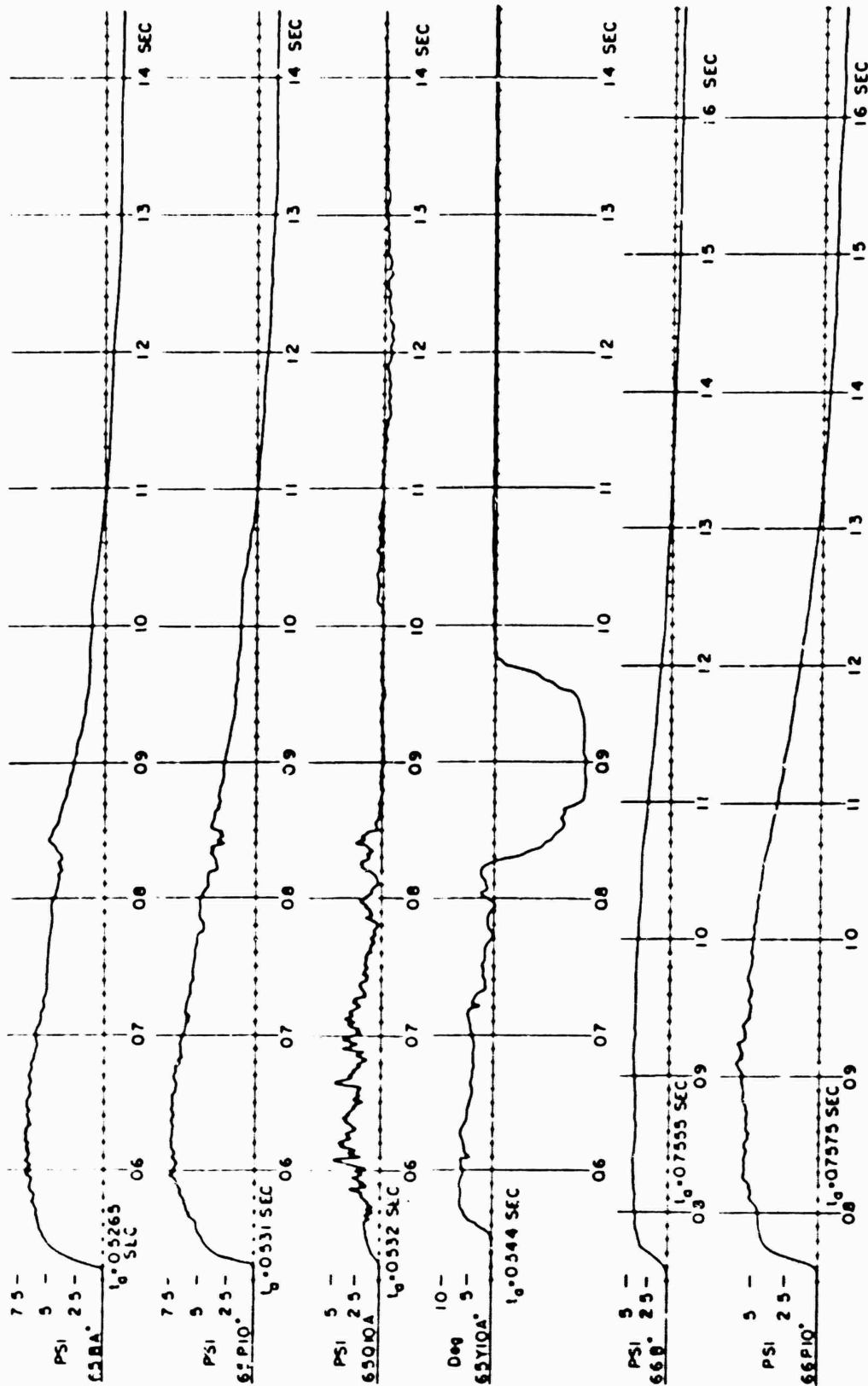


Figure B.13 Continued.

CONFIDENTIAL

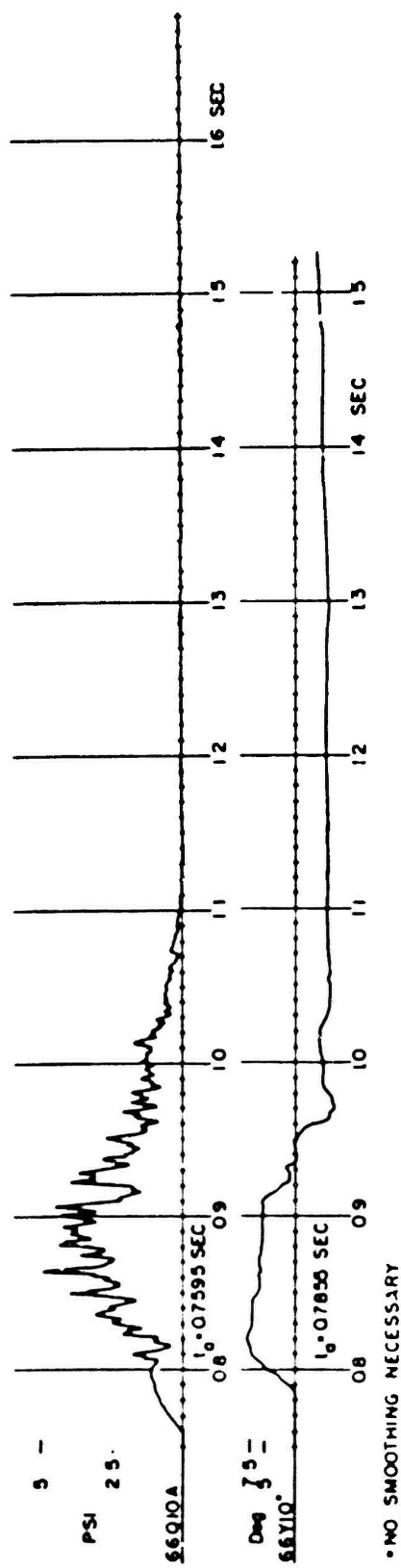


Figure B.13 Continued.

# Appendix C GAGE CALIBRATION DATA

TABLE C.1 SHOT 6 PRESSURE GAGES

Ground Range ft	Gage Number	Calibration (psi/in) ax + bx <sup>2</sup>		Ground Range ft	Gage Number	Calibration (psi/in) ax + bx <sup>2</sup>	
		A	L			A	B
Desert							
1,300	61B	8.02	0	2,000	62B	5.51	0
	61BA	7.81	-0.13		62BA	5.18	-0.08
	61P10	9.48	0.11		62P10	5.27	0
	61P10A	6.90	0		62P10A	4.35	0
	61Q10	29.29	1.30		62Q10	3.43	0.30
	61Q10A	16.17	0.06		62Q10A	3.33	0.24
	61Y10	9.76	0.14		62Y10	+13.07	0
	61Y10A	18.41	-0.36		62Y10A	+11.46	0
1,650	62B	4.72	0				
	62BA	4.02	-0.07				
	62P10	2.53	0.05				
	62P10A	5.94	0				
	62Q10	14.72	-0.39				
	62Q10A	8.83	-0.11				
	62Y10	+12.27	0				
	62Y10A	+14.14	0				
Asphalt							
1,300	64B	8.22	0	2,000	66B	6.30	0
	64BA	8.37	0		66BA	4.55	0
	64P10	8.42	0.07		66P10	3.77	0
	64P10A	5.21	0		66P10A	5.74	0.07
	64Q10	21.57	0.19		66Q10	4.09	0.09
	64Q10A	15.96	0.18		66Q10A	1.97	0
	64Y10	+11.27	0		66Y10	+9.00	0
	64Y10A	+11.33	0		66Y10A	+16.65	0
1,650	65B	5.34	0.08				
	65BA	4.40	0.07				
	65P10	4.30	0.07				
	65P10A	5.66	0.12				
	65Q10	6.42	0				
	65Q10A	5.23	0				
	65Y10	+12.23	0				
	65Y10A	+9.96	0				

TABLE C.3 SHOT 12 PRESSURE GAGES

Ground Range ft	Gage Number	Calibration (psi/in) $ax + bx^2$		Ground Range ft	Gage Number	Calibration (psi/in) $ax + bx^2$	
		A	B			A	B
Desert							
730	1B	138.1	2.4	2,500	9B	4.06	0.17
	1BA	98.7	1.7		9P3	5.24	0
1,000	2B	55.8	-0.8		9Q3	7.31	0
	2BA	56.4	-1.2		9Q3A	4.34	0
1,250	3P3	25.13	0.23		9B10	5.39	0
	3P2A	20.68	0		9P10	4.97	0.03
	3Q3	125.7	0		9Q10	5.96	0.48
	3Q2A	57.0	1.7		9Q10A	6.87	0.51
1,500	5B	12.33	-0.37		9P25	4.79	0.29
	5P3	11.31	0.18		9Q25	7.09	0.28
	5Q3	51.9	-6.5		9P40	4.64	0
	5Q2A	31.2	0		9P40A	5.37	0
	5B10	11.87	-0.10		9Q40	5.59	0.38
8	5P10	12.33	-0.18	2,750	11P3	3.42	0
	5Q10	78.0	0		11P3A	6.02	0
	5Q10A	25.7	0		11Q3	2.28	0.06
1,750	6P10	9.94	0		11Q3A	3.95	0.21
	6P10A	6.63	0	3,000	12B	4.77	-0.25
	6Q10	34.64	1.98		12P3	4.26	0
	6Q10A	18.04	0.38		12Q3	1.76	0.15
2,000	7B	8.19	0.58		12Q3A	0.921	0.034
	7P3	6.13	0.40		12P10	5.32	-0.10
	7Q3	16.88	-0.15		12Q10	2.08	0.01
	7Q2A	12.87	0	3,500	15B	4.75	0
	7B10	8.60	-0.28		15P10	4.28	0.11
	7P10	8.17	0.16		15Q10	1.08	0
	7Q10	24.61	0.37		15Q10A	0.519	-0.009
	7Q10A	12.32	0	4,000	16P10	4.93	-0.23
2,250	8P10	6.52	0.24		16Q10	1.09	0.02
	6P10A	3.91	0	4,500	17B	3.17	0.05
	8Q10	15.14	0.25		17P3	3.61	0
	8Q10A	6.10	0		17Q3	0.830	0
					17Q2A	6.887	0
				1,500	4BX	12.01	-0.11
					4BY	12.71	-0.36
Water							
750	21B	182.7	-6.6	2,500	29B	11.13	0.21
	21BA	191.6	-7.6		29BA	9.22	-0.19
1,000	22B	77.9	-1.3		29P3	9.54	0
	22BA	68.8	-1.8		29Q3	3.29	0.04
1,250	23P2	74.7	1.2		29Q3A	2.01	0
	23P2A	74.6	-2.4		29B10	10.86	-0.31
	23Q3	78.6	4.9		29P10	11.68	-0.32
	23Q2A	59.0	0		29Q10	1.84	0.04
					29Q10A	4.02	0.21
					29P25	10.71	0.24
					29Q25	2.65	0.02
					29Q25A	2.01	-0.03
					29P40	9.30	0
					29P40A	8.89	0.06
					29Q40	5.89	0
					29Q40A	2.70	-0.04

TABLE C 2 CONTINUED

Ground Range ft	Gage Number	Calibration (psi/in) $ax + bx^2$		Ground Range ft	Gage Number	Calibration (psi/in) $ax + bx^2$	
		A	B			A	B
1,500	25B	41.06	0	2,750	31P3	4.52	0.17
	25BA	35.94	-0.68		31P3A	7.98	0.31
	25P3	32.18	-1.05		31Q3	3.09	0.71
	25Q3	43.90	-0.44		31Q3A	1.31	0.27
	25Q3A	21.26	-0.29	3,000	32B	7.85	0.39
	25B10	20.81	0.07		32BA	6.60	0.28
	25B10A	33.49	0.67		32P3	5.72	0.14
	25P10	34.33	-2.44		32Q3	2.04	0.16
	25Q10	29.94	-0.19		32Q3A	2.30	0.22
1,750	25Q10A	18.06	-0.11	1,500	25P3X	33.82	-1.77
	26P10	15.98	0		25Q3X	37.71	0.45
	26P10A	26.63	0		25Q3XA	24.41	0
	26Q10	14.30	0.33		25P3Y	25.88	-0.60
	26Q10A	18.1	-0.13		25Q3Y	33.19	1.63
2,000	27B	13.04	0	2,500	25Q3YA	20.65	-0.14
	27BA	17.68	-0.37		29P3X	9.64	-0.22
	27P3	18.20	-0.45		29Q3X	2.42	0.05
	27Q3	8.76	0.89		29Q3XA	3.17	0.07
	27Q3A	6.60	0.31		29P3Y	9.09	-0.15
	27B10	19.70	-0.98		29Q3Y	3.74	0.32
	27B10A	17.11	-0.74		29Q3YA	2.80	0.22
	27P10	16.28	-0.80				
	27Q10	11.01	1.12				
	27Q10A	6.60	0.44				
2,250	28P10	11.39	0				
	28P10A	11.06	- 10				
	28Q10	5.43	0.27				
	28Q10A	3.29	0.09				
Asphalt							
750	41B	109.3	0	2,250	48P10	6.82	0.21
	41BA	127.0	0		48P10A	6.36	0
1,000	42B	48.8	4.1		48Q10	7.32	0.41
	42BA	26.6	0.7		48Q10A	4.16	0.06
1,250	43P3	24.0	-0.4	2,500	49B	9.99	-0.80
	43P3A	42.3	-0.86		49P3	11.98	0
	43Q3	110.6	0		49Q3	3.50	0.06
	43Q3A	74.2	0		49Q3A	4.40	0.10
1,500	45B	13.20	1.13		49B10	13.24	-0.96
	45P3	10.79	1.00		49P10	5.97	0.28
	45Q3	285.2	-68.2		48Q10	3.23	0.14
	45Q3A	89.1	7.73		49Q10A	4.60	0.11
	45B10	14.18	-0.46		49P23	8.96	-0.42
	45P10	13.66	0.14		49Q23	6.46	0.20
	45Q10	85.27	0.96		49Q23A	2.90	0
	45Q10A	25.98	-0.26		49P40	5.72	0.20
					49P40A	7.79	0.30
1,750	46P10	7.23	0		49P40	8.91	0
	46P10A	10.36	0		49P40A	2.93	0
	46Q10	30.25	1.52	2,750	51P3	4.99	0.18
	46Q10A	11.96	0		51P3A	6.31	0.20
2,000	47B	9.51	-0.34		51Q3	3.17	0.32
	47P3	8.18	-0.22		51Q3A	2.73	0.22
	47Q3	21.70	-0.59	3,000	52B	5.80	0.51
	47Q3A	10.08	-0.16		52P3	5.94	0
	47B10	7.48	0		52Q3	1.09	0.04
	47P10	7.68	0		52Q3A	1.91	0.12
	47Q10	15.91	-0.20				
	47Q10A	8.70	-0.18				

TABLE C.3 SHOT 12 STRAIN GAGES (H-BEAM)

Ground Range	Gage Number	Calibration	
		A	B
ft		lb-force/in <sup>2</sup> /in	lb-force/in <sup>2</sup> /in
2,000	7F3	38.40	-1.66
2,000	7F3A	17.08	-0.93
2,500	9F3	20.59	-2.25
2,500	9F3A	19.69	-1.80